THE MICROIONIZER – A SOLID STATE ION SOURCE FOR
HIGH PRESSURE MASS SPECTROMETRY

Craig A. Cavanaugh

A dissertation submitted to the faculty at the University of North Carolina at Chapel Hill
in partial fulfillment of the requirements of Doctor of Philosophy in the Department of
Applied Physical Sciences.

Chapel Hill
2016

Approved by:

J. Michael Ramsey

Michael R. Falvo

Gary L. Glish

Scott C. Warren

Sean Washburn

ABSTRACT

Craig A. Cavanaugh: The Microionizer – A Solid State Ion Source for
High Pressure Mass Spectrometry
(Under the direction of J. Michael Ramsey)

This work describes the development of a novel, microfabricated solid-state ionization

source (a "microionizer") for use with high pressure mass spectrometry (HPMS). HPMS is

intended for miniature, low-cost, portable instrumentation. As such, the microionizer is

designed as a small, low-power ion source compatible with the 1 Torr air-based environment

of HPMS. The microionizer is a field effect device based upon silicon-on-insulator

technology that functions as a dual-source, producing field emission for internal electron

impact ionization (EI) and external field ionization.

External ion injection into the miniature cylindrical ion trap (mCIT) was performed in

helium, nitrogen, or air buffer gases at 1 Torr using traditional ion sources (thermionic

emitter and glow discharge) for proof-of-concept experiments. Further studies in helium and

air examined the effects of pressure, ion kinetic energy, and ion trap potential well depth

changes with drive radiofrequency (RF) signal frequency and amplitude. Results indicated

that mass spectral signal intensity can be maximized at pressures ranging from 10 to

1000 mTorr by tuning ion kinetic energy between 20 to 250 eV and increasing potential well

depth aids external ion injection.

Nine generations of microionizers were fabricated to optimize microionizer performance.

The first generation microionizer was coupled with HPMS as a field emission source and

generated helium and air-based high pressure mass spectra. However, high current draw

limited the microionizer lifetime and prevented field strengths necessary for field ionization. Generations two through nine encompassed processing variations of device fabrication procedures, development of robust electrical contacts, and microionizer device incorporation into the ion trap electrode stack, leading to improved microionizer signal intensity and low power (< 1 mW average power) consumption.

The ninth generation microionizer demonstrated operation as both a field emission and field ionization source in air buffer gas at 1 Torr. Electric field strengths for field emission were near 1 MV/cm, while field ionization required greater than 1.8 MV/cm. The microionizer generated mass spectra of volatile organic compounds (such as benzene and dimethylaniline) in both modes and lifetime was found to be 9 h for field emission and 490 h for field ionization under continuous mass spectral acquisition.

To my family

ACKNOWLEDGEMENTS

TABLE OF CONTENTS

LIST OF TABLES

LIST OF FIGURES

LIST OF ABBREVIATIONS AND SYMBOLS

APCI   atmospheric pressure chemical ionization

APGDI   atmospheric pressure glow discharge ionization

ARDE   aspect ratio dependent etch

ASU   Arizona State University

CFE   cold field emission

CHANL   Chapel Hill Analytical and Nanofabrication Laboratory

CI   chemical ionization

CID   collision induced dissociation

CIT   cylindrical ion trap

cm   centimeter

CWA   chemical warfare agent

CWS   chemical warfare simulant

Da/s   Dalton/second

DAPI   discontinuous atmospheric pressure inlet

DART   direct analysis in real time

DESI   desorption electrospray ionization

DIMP   diisopropylmethane phosphonate

DMA   dimethyl aniline

DMMP   dimethyl phosphonate

DRIE   deep reactive ion etching

EI   electron (impact) ionization

EMT   electron multiplier tube

ESI	electrospray ionization
ETE	edge-to-edge emitter
eV	electron-Volt
FI	field ionization
FE	field emission
FEA	field emission array
FED	field effect device
FET	field effect transistor
GC	gas chromatography
GD	glow discharge
GDe	negative mode GD
GDi	positive mode GD
HPMS	high pressure mass spectrometry
IE	ionization energy
ITMS	ion trap mass spectrometry
L	liter
LD	laser desorption
LOD	limit of detection
lpi	lines per inch
MALDI	matrix assisted laser desorption ionization
m	meter
MEMS	microelectromechanical systems
μL	microliter

mL	milliliter
μm	micrometer, micron
mm	millimeter
mW	milliwatt
MS	mass spectrometry
MS^n	tandem mass spectrometry
m/z	mass to charge ratio
ni	nitride
nm	nanometer
ORNL	Oak Ridge National Laboratory
ox	silicon dioxide
PCB	printed circuit board
ppm	part per million
QIT	quadrupole ion trap
RIE	reactive ion etching
RIT	rectilinear ion trap
RF	radio frequency
RVMD	Rogue Valley Micro Devices, Inc
sccm	standard cubic centimeter per minute
scfh	standard cubic foot per hour
SEM	scanning electron micrograph
SIM	soft ionization membrane
SIMS	secondary ion mass spectrometry

SLIT	stretched length ion trap
SOI	silicon-on-insulator
SC	single crystal
SNR	signal-to-noise ratio
SWaP	size, weight, and power
TIC	toxic industrial compound
TOF	time of flight
UA	University of Arizona
UHP	ultrahigh purity
UNC	University of North Carolina
V	Volt
V_p	pulse voltage
V_b	bias/float voltage
V_{pp}	peak-to-peak voltage
V_{0-p}	zero-to-peak voltage
VME	vacuum microelectronics
VOC	volatile organic compound

CHAPTER 1: INTRODUCTION – HIGH PRESSURE MASS SPECTROMETRY AND THE MICROIONIZER

1.1 Motivation for Handheld Mass Spectrometry

Among analytical instrumentation, mass spectrometry (MS) offers a unique combination of selectivity, sensitivity, and speed and is often considered the gold standard for chemical analysis.[1] On-site, rapid chemical identification is important in many fields from environmental protection to national security with analytes of interest including: toxic industrial compounds (TIC); volatile organic compounds (VOC); explosives; and chemical warfare agents (CWA).[2] Mass spectrometry is the ideal technique for in-field analysis, especially when informed (and potentially costly) decisions need to be made in a timely manner for health and safety reasons. A recent example of this occurred in 2014 when Freedom Industries spilled 10,000 gal of methylcyclohexane-methanol into the Elk River in West Virginia.[3] The Kanawha Valley water treatment plant attempted to process the unknown, excess organics that suddenly appeared at the upstream side of the plant. However, the carbon filtration system was quickly overwhelmed and a 'Do Not Use' order was issued until these could be regenerated, leaving 300,000 residents without tap water for weeks.[4] Had the operators at the treatment plant access to a rapid, detailed chemical analysis, quicker, informed decisions could have been made potentially avoiding the extended downtime. Mass spectrometry would have been ideal for this situation; however, it is typically confined to the laboratory because of size (kitchen refrigerator), weight (hundreds of pounds), and power (kilowatts) as well as cost considerations.

Miniature mass spectrometers have been investigated for decades; the first suitcase-sized, field portable mass spectrometer was disclosed in 1995[5] and currently, there are several commercial systems available.[6] Moreover, there is a demonstrated need for in-field mass analysis.[7] Despite availability and demand, mass spectrometry has yet to become ubiquitous in the field because of size, cost, lack of robustness, and operator skill required. Many of the field portable systems on the market share an important trait with their lab-sized counterparts – cost both in capital (> $100k) and trained personnel to operate the instrument and interpret data.

The Ramsey group at the University of North Carolina at Chapel Hill has focused on bridging the divide – attempting to move mass spectrometry out of the laboratory and into the field in a cost-friendly manner. The primary method for accomplishing this is to operate the mass spectrometer at pressures negating the need for the most expensive, highest power-consuming component, the turbomolecular pump. This pump elimination requires operation at pressures greater than 100 mTorr. In comparison, traditional mass spectrometry requires ≤ 1 mTorr vacuum conditions and uses a two-stage pumping system, typically roughing + turbo pumps. Operating the mass spectrometer at pressures ≥ 100 mTorr is referred to as high pressure mass spectrometry (HPMS), which can be accomplished using simple miniature-roughing pump with reasonable flow rates and continuous, atmospheric sampling.

Operating under HPMS conditions and atmospheric sampling requires that the three major subsystems of the mass spectrometer (mass analyzer, ion detector, and ion source) be compatible with a vacuum environment composed of ambient air. Because portability is a key goal, these subsystems should each have small footprints and low-power consumption. The work presented in this dissertation focuses on one subsystem – the ion source. The main

objective was the development of a silicon-based solid state, field effect ionization source or microionizer. Incorporating the microionizer within the HPMS system requires an understanding of internal and external ion trapping under HPMS conditions, which was performed with currently available MS ionization sources. HPMS with the microionizer additionally required developing silicon microfabrication procedures; general instrument design and construction; ion trap mass spectrometry (ITMS); and finally generating ions and characterizing performance.

This chapter introduces the background necessary to understand the need for a low power, field effect microionizer as well as the principle of operation behind the device. Section 1.2 begins with a survey of current, miniaturized mass spectrometers. Section 1.3 highlights important theoretical details for HPMS as well as the current state of system components used in HPMS research. Section 1.4 covers traditional ion sources that have been coupled with mass spectrometry, including field effect devices; providing context for the microionizer. Section 1.5 introduces field effect theory and highlights the progression of field emission and field ionization devices. The microionizer is formally introduced in Section 1.6. Finally, Section 1.7 provides an outline of the objectives for this dissertation.

1.2 Current Technology in Miniaturized Mass Spectrometers

Miniaturization of a mass spectrometer balances the needs of the intended application (instrument performance) with the requirements for portability (size, weight, and power, SWaP).[6] This performance-portability trade-off covers a broad spectrum. On one end, when resolving power is paramount then portability is sacrificed as seen with the refrigerator-sized, miniature Fourier transform ion cyclotron resonance mass spectrometer (FT-ICR).[8] On the other end, where portability is key, instrument performance is tuned to the lowest possible

necessary to accomplish the task, such as the palm portable mass spectrometer which samples at 0.02 Hz.[9] The focus of HPMS is to raise instrument performance on the portability end of the spectrum where SWaP is a premium. HPMS does this not only by miniaturizing the hardware but also by adapting mass analysis in the high pressure regime (1 Torr vs. 1 mTorr).[6, 10] To better understand the HPMS approach, a brief survey of miniaturized mass analyzers is useful.

1.2.1 Miniaturized Mass Analyzers

Nearly every form of mass analyzer has been miniaturized[8] and includes time of flight (ToF);[11] electric and magnetic sectors;[12] linear quadrupole;[13-14] and three-dimensional ion traps.[15-17] ToF and sector-based analyzers use static (or field-free) regions and require high vacuum (less than 10^{-6} Torr) to maintain mass to charge ratio (m/z) separation. Linear quadrupoles use both static DC and dynamic RF voltages to generate electric fields where a single m/z is contained in two-dimensions and travels along the third to the detector. Since ions are actively guided, linear quadrupoles can operate at higher pressures than TOF and sectors; up to 0.01 Torr for highly miniaturized analyzers.[18] Three-dimensional ion traps use RF voltages to maintain a stable trapping volume at the center of the trap. Ion traps naturally operate at high pressure (10^{-3} Torr) because the ion trajectory is completely defined by the electric field, thus performance is less susceptible to ion-neutral scattering than the previously mentioned mass analyzers.[19] This has lead them to be the mass analyzer of choice for the majority of miniaturized MS with portability as the key design factor.

1.2.2 Portable Ion Trap Mass Spectrometers

The pressure tolerance of three-dimensional ion traps is ideal for portable applications because the vacuum systems can be reduced in size, power, and complexity. In addition to

pressure tolerance, ion traps have two more desirable properties: mass resolution is independent of trap size[20] and the ability to perform tandem mass spectrometry (MS[n]).[21-22] As such, considerable efforts have been placed into miniaturizing quadrupole ion traps (QIT).[23] One issue with the QIT is that it uses hyperbolic electrodes that become difficult to fabricate at smaller scales (radius < 1 cm),[24] which translates into higher costs for the mass analyzer. An example is the toroidal ion trap, which has a large charge capacity (and hence improved sensitivity) relative to a standard QIT, but is more difficult to fabricate.[25] Geometric variants have been developed to overcome this issue including the rectilinear ion trap (RIT)[26] and the cylindrical ion trap (CIT).[27] Each variant has been incorporated into a miniature mass spectrometer such as: Guardion GC-MS (Smith Detection, Inc) based upon the toroidal ion trap;[28] the Mini-series of instruments from Purdue based upon the RIT;[29-30] and the MMS-1000 (1st Detect, Inc) based upon the CIT.[31-32] The Guardion GC-MS is a ruggedized, briefcase-sized system which weighs > 30 lb and has less than 8 h battery life, while the MMS-1000 is a small, lightweight benchtop system designed to be used with wall power, thus it is best for stationary settings such as airport security checkpoints. The Mini-series has variants covering the spectrum from hand-portable[26] to benchtop.[30]

The Mini-instruments offer an interesting view into the miniaturization of the remaining subsystems of the mass spectrometer: the vacuum system, ion detector, and ion source. The vacuum system required is defined by the choice of mass analyzer and detector. The resolution of the RIT is best at lower pressures (< 10 mTorr),[33] which requires the use of a turbo pump. Miniature turbo pumps have been developed specifically for portable MS use, but they are specialized, expensive, and fragile.[34-35] Despite miniaturization, these pumps still consume a significant portion of the power and space budget of the instrument.[36] While

5

the inclusion of a turbo pump increases SWaP, the low pressure enables the use of electron multiplier tubes (EMT) or microchannel plates (MCP) for ion detection. Because these devices have high sensitivity and bandwidth,[37] there has yet to be a significant emphasis on incorporating alternative (pressure tolerant) ion detectors.[26, 30]

Ion sources are a different matter because each source has strengths and weaknesses for particular applications. Most miniature mass spectrometers are geared towards detecting gaseous analytes, thus electron impact ionization (EI) is a staple and can be achieved via thermionic emitters[26] or plasma generators.[29] Lower volatility analytes require ambient ionization techniques and the Mini-instruments have been adapted for several methods including low temperature plasma (LTP)[35] and desorption electrospray ionization (DESI).[38] However, each of these techniques requires sampling at atmospheric pressure, which strains the vacuum system. The discontinuous atmospheric pressure interface (DAPI) was introduced to counteract the increased power consumption caused by a constant gas load on a turbo pump.[39] In DAPI, an inlet is opened and a high gas load is imposed for sampling. The inlet is then closed and a pump-down time is added to achieve < 10 mTorr operating range for the RIT and EMT. Low pressure during mass analysis improves resolution and the discontinuous gas flow improves battery life. However, DAPI limits data acquisition to about 1 Hz as well as the maximum RF trapping voltage amplitude during ionization. This is an example of a trade-off made to bridge the gap between person-portable and hand-portability when a turbo pump is required for operation.[6]

The palm-portable mass spectrometer (PPMS) is an extreme example of DAPI. Similar to other fieldable systems it uses a low pressure ITMS, but maintains pressure with a miniature two-stage vacuum system (roughing + getter pump).[9] Baseline pressure ($\approx$

10^{-6} Torr) is achieved with a standard benchtop pumping system, then the PPMS is taken into the field for use. The maximum sample rate is only 0.2 Hz. However, this rate exhausts the getter's limited capacity in under an hour. In order to achieve day-long operation, the sampling rate is further reduced to just 0.02 Hz ($\approx$ 1 sample/minute). The acquisition rate and small sampling volume negatively impacts sensitivity and limits the applications available to the PPMS. However, the PPMS represents a functional departure from dependence on high-cost, fragile turbo pumping systems.[30, 35]

HPMS departs even further from the miniaturization efforts of the past and has been successfully realized in a commercial mass spectrometer. The M908, introduced in 2014 by 908 Devices, Inc. fulfills the promise of a truly handheld mass spectrometer. This system is based upon the theory of HPMS and is licensed technology from the Ramsey group.[40] The pumping system relies upon a custom, miniature roughing pump that maintains HPMS conditions for a CIT-based trap design and pressure tolerant ion generation and detection. The end result is a rugged, low-cost unit coming in at just 22.5 x 18.5 x 7.6 cm^3 and 2.0 kg (including battery)[41] which is already being used in the field for threat detection such as explosives and CWAs.[42] The realization of handheld mass spectrometry has guided research efforts to improve the three major subsystems (mass analyzer, ion detector, and ion source) in order to continue lowering the cost and expand the utility and ubiquity of HPMS.

1.3 High Pressure Mass Analysis

To successfully develop an ionization source, an understanding of how ion traps work at higher pressures is necessary. The historical and theoretical groundwork for ion trap-based HPMS has been thoroughly described elsewhere.[43-45] Key topics regarding quadrupole ion trap theory pertinent to ionization are highlighted here. The QIT consists of three electrically

insulated electrodes – two grounded endcaps and a center ring electrode. For a QIT, the electrodes follow a hyperbolic geometry, while a CIT is a cylindrical approximation. A cross sectional view of the QIT vs. CIT can be seen in Figure 1.1. The critical dimensions of the trap are defined as the radius of the ring electrode, r_0, and the endcap-to-trap center spacing, z_0. A radio frequency (RF) potential applied to the center ring generates a quadrupolar electric field and ions can oscillate in stable trajectories inside the field according to axial (a_z and q_z) and radial (a_r and q_r) stability parameters. These parameters are proportional to the DC offset of the RF waveform (a_n) as well as the RF voltage amplitude (q_n).[46] Regions of stable ion trajectory can be viewed using a stability diagram, shown by plotting the axial stability parameters, a_z vs. q_z.[47] The stability diagram for a QIT is plotted in Figure 1.2, which highlights the trapping conditions where ions exhibit both stable radial and axial trajectories. HPMS utilizes mass selective instability mode developed by Stafford et al.[48] which sets $a_z = 0$ and accumulates ions of various m/e (m/z) values inside the trap at low RF amplitude according to:

$$q_z = \frac{8eV}{m(r_0{}^2 + 2z_0{}^2)\Omega^2} \tag{1.1}$$

Where the variables are the zero-to-peak RF voltage amplitude, *V*; RF angular frequency, Ω; ion trap critical dimensions, r_0 and z_0; and inverse mass-to-charge, *e/m*. The RF amplitude is linearly ramped and ions eject in order of their *m/e* when $q_z = 0.908$. Goeringer et al.,[49] theoretically determined the proportional relationship between mass resolution, *Δm/m;* pressure, *P,* and RF angular frequency to be:

$$\frac{\Delta m}{m} \propto \frac{P}{\Omega} \tag{1.2}$$

suggesting that mass resolution could be maintained as buffer gas pressure increases (>
1 mTorr), provided RF frequency was increased. Whitten, et al. extended the theoretical
work to higher pressures and showed resolution could be maintained at pressures upwards of
1 Torr by reducing the ion trap dimensions and increasing drive RF frequency.[50] This is the
core concept underpinning HPMS.

These theoretical investigations were followed by experimental confirmation.
Cylindrical ion traps, with sub-millimeter critical dimensions (mCIT, $r_0 \leq 0.5$ mm) were
chosen because the QIT geometry is difficult to fabricate in miniature. Mass spectrometry
was performed at low pressure helium (≈ 1 mTorr) using a mCIT with $r_0 = 0.5$ mm, a 20-fold
decrease compared to a standard QIT ($r_0 = 10.0$ mm), and the drive RF frequency was
5.8 MHz (f = 1.0 MHz for a standard QIT).[15, 19, 51] These studies confirmed the theoretical
relationships predicted by Whitten et al.; showing improved resolution and sensitivity by
increasing RF frequency.[15, 51] Subsequently, double resonant ejection was shown to reduce
ejection voltage at both the 1/3 and 2/3 drive RF frequency resonances.[52] More recently,
HPMS has been demonstrated at 1 Torr helium,[53] nitrogen, and air;[54] confirming the mass
analyzer is capable of high pressure operation.

1.3.1 System Components for HPMS – Mass Analyzer

The initial high pressure studies used a mCIT with $r_0 = 0.5$ mm and RF drive frequencies
ranging from 6 to 9 MHz.[43, 45] They showed that with a constant RF frequency, peak widths
will increase (as predicted by Equation 1.2) as pressure increases. This loss in mass
resolution however can be regained by increasing the RF frequency.[45] In order to maintain
stable ion trajectories, Equation 1.1 shows that increased RF frequency must be balanced
with either increased RF voltage (*V*) or decreased ion trap size (*r_0*, *z_0*). Ideally, only the RF

9

amplitude would be increased with the trap size maintained for charge capacity considerations. However, there is a limit to the RF amplitude that can be applied at 1 Torr due to electrical breakdown concerns.[55] Experimentally, using smaller traps reduced the applied RF amplitude needed with sub-dalton peak widths attained at 1 Torr in air buffer gas at a drive frequency near 60 MHz with an mCIT of $r_0 = 100$ μm.[45]

A trade-off here is that the reduction in trap size negatively impacts the potential well of the ion trap leading to less sensitivity. For a QIT, the potential well depth, D_z, can be approximated for q_z less than 0.4:[56]

$$D_z \approx \frac{q_z V}{8} \qquad (1.3)$$

where V is the same RF amplitude used in Equation 1.1.   The potential well depth of a QIT is a measure of its charge capacity, the maximum number of ions that can be trapped.   For reference, a typical, commercial ITMS has $r_0 = 1.00$ cm and $z_0 = 0.783$ cm and operates with an RF frequency of 1.05 MHz with amplitude, 757 V_{0-p}. While, a mCIT has $r_0 = 0.0500$ cm and $z_0 = 0.0645$ cm and operates with an RF frequency of 6 MHz with amplitude near 150 V_{0-p}. These values yield (roughly) a 4-fold decrease in well depth (10.5 vs. 42.5 V) for the mCIT relative to a standard QIT. Assuming ion ejection and detection are equivalent, the sensitivity of the mCIT is reduced compared to a standard QIT.

Charge capacity and thus sensitivity can be increased through the use of arrays of ion traps[57-58] as well as novel, QIT-based geometries.[17, 25] Both strategies were used in HPMS development: 7 and 19-element arrays of mCITs have demonstrated improved sensitivity over single-element ion traps.[44-45] However to maintain resolution, each element of the array must be identical to ensure simultaneous ion ejection. In order to alleviate this fabrication constraint the stretched length ion trap (SLIT) was developed by Schultze and Ramsey and

subsequently shown to improve charge capacity over a single-element mCIT under HPMS conditions.[44, 59] Materials and fabrication techniques have also been investigated for improved trap operation.[45]

1.3.2 System Components for HPMS – Ion Detector

The operational pressure for HPMS, 1 Torr air buffer gas, is a demanding environment in which to detect ions. To date, HPMS has relied upon two types of charge detectors: electron multiplier tubes and faraday plates. While other charge detectors exist, such as image current detectors, these have not been pursued (to date) due to long integration times.[60] The EMT is a staple detector for mass spectrometry because it has high gain, low noise, and high bandwidth.[61] Modern EMTs are continuous dynodes, where a large negative bias (typically -1600 V) causes ions to impact the surface of the EMT which generates secondary electrons.[62] These electrons are driven by the electric field into the tube, constantly colliding with the surface and generating further secondary electrons ultimately yielding gains on the order of 10^6 electrons/ion.[37, 63] Ion feedback, the generation of ions inside the EMT via EI, limits the upper bounds of the pressure range to 10 mTorr.[64] Despite the incompatible pressure range, the EMT has been used extensively for HPMS development. This detector utilization was accomplished by using a differentially pumped system with the EMT housed in a separate detector vacuum chamber away from the mass analyzer (ion source and mCIT). Thus the EMT can be held at pressures < 100 mTorr while the ion source and mCIT can operate at 1 Torr. This approach allows high pressure ion trap operation and decouples ion detector development from that of the ion source and mass analyzer.[43] Despite operating above the recommended pressure limit, stable, low-noise operation in helium, nitrogen, and air at

11

pressures approaching 100 mTorr[65] were performed by decreasing the applied voltage (thus gain) applied to the EMT.[45, 53]

In addition to the EMT, pressure tolerant detectors have been shown to work at 1 Torr in helium and air.[43-44] These detectors collect charge using a faraday plate, then amplify and convert the charge to a voltage, capable of direct measurement via a standard data acquisition system (DAQ). Unfortunately, these detectors are more sensitive to electrical and mechanical sources of noise (such as RF and vibrations) and have lower gains than EMTs.[61] To combat these problems, HPMS specific amplifiers have been developed which reduce noise, enabling higher gain operation.[44, 66] There is also considerable interest in a solid state equivalent to an EMT, which should combine the pressure tolerance of a faraday plate with the high gain and bandwidth of an EMT.[67-68]

1.3.3 System Components for HPMS – Ion Source

Figure 1.3 shows images of the workhorse ionization sources (tungsten filament and glow discharge) used to bring HPMS from a concept to a functional technique. Due to the ease with which internally generated ions are trapped, internal EI was the preferred ionization method during HPMS development.[69] HPMS development progressed in increments: mass spectrometry with mCITs were first demonstrated at low pressure helium;[51] followed by high pressure helium (1 Torr);[43] then high pressure nitrogen; and finally in high pressure air.[54] No single electron source is compatible over this pressure range and buffer gas compositions. Thermionic emitters, such as the tungsten filament (Figure 1.3a) are ideal for low-pressure (1 mTorr) inert environments. They rely upon a heating current to overcome the potential barrier (work function) of a material such that electrons in the conduction band can escape the surface into vacuum. To shift the Fermi distribution of the electrons enough to overcome

the work function, temperatures must exceed 1000 $^{\circ}$C.[70] Thus, thermionic emitters operate best at low pressure (due to collisional cooling effects), with gas compositions that avoid oxidative reactions. For HPMS studies, thermionic emitters were pushed to high pressure (1000 mTorr) in both helium and nitrogen for proof-of-concept studies but they suffered reduced lifetimes – likely a result of surface sputtering caused by ion back streaming.[71] Air-based operation required the shift to glow discharge (Figure 1.3b). The source used for HPMS was designed for 1 Torr operation in air, with a 1 cm electrode separation and 1 cm electrode radius. However, a practical operational window of 250 to 2000 mTorr was achieved by tuning the voltage.[54] An image of the characteristic purple glow of air-based operation can be seen in Figure 1.3c.

1.4 Advanced Ion Sources

To date, HPMS has focused on detecting airborne analytes (e.g. CWAs and VOCs) via atmospheric sampling, thus EI via glow discharge-generated electrons has been the workhorse ion source. Glow discharge is a serviceable ionization source for HPMS, but there are inconvenient properties from a miniature, HPMS perspective. GD requires > 500 V and a relatively large empty volume (≈ 0.8 cm^3) to generate the conditions necessary for discharge.[72] While the direct power consumption is on the order of 10 mW, the large volume acts as a reservoir increasing the load on the vacuum pump and hence overall power consumption of the instrument.

Alternatives to GD ionization are limited, but field effect devices (FED) hold promise as ionization sources that are not only low power but also small in size thus reducing pumping volume. The field effect refers to the behavior of electrons under intense electric fields and encompasses both field emission and field ionization. Field emission describes the tunneling

of electrons from a surface into vacuum; while field ionization covers electron tunneling from a gas phase neutral into a surface.[73] The quantum mechanical nature of the field effect requires no energy outside of that required to generate the electric field and a small displacement current which makes it very attractive for portable and low-power applications.[74-75] The electric field strength necessary for field emission is near 10 MV/cm,[76] while the threshold for field ionization is dependent upon the ionization potential of the neutral and ranges from 50 MV/cm for volatile organic molecules[77] to 100 MV/cm for helium.[78] Electric field strengths of this order are achieved via localized geometric field enhancement. A voltage is applied to a surface with a sharp tip creating an electric field between it and a counter-electrode. The presence of the high radius of curvature (< 1 nm) locally enhances the electric field and creates a field emission/ionization site dependent upon the amplitude and polarity of the applied potential. Early devices relied upon electrochemically sharpened wires or edges that required greater than 5 kV to achieve field emission or ionization.[79-80]

The use of FEDs does not come without a price. Due to the small surface area, the emission current density at the tip can become very large, thus Joule heating limits the overall emission intensity.[81-82] To overcome this, arrays of emission sites can be fabricated but require each tip to be nearly identical in order to ensure even field emission across the array. The precision required to produce identical emission tips across the array often incorporate time consuming or highly specialized steps into a complicated fabrication process. The end results are devices that are functional but expensive to fabricate, especially at commercialized scales.[83]

The microionizer is a solid state, FED designed specifically with ease of fabrication in mind and geared toward HPMS operation. Proposed to fill this role by Dr. Stanley Pau, a collaborator at the University of Arizona, it offers two methods of ionization: direct field ionization and field emission-based EI. As designed, the microionizer does not rely upon the formation of an array of identical sharp tips. Instead the inherent surface roughness from the microfabrication process generates a massively redundant array of emission sites. Thus, fabrication is based upon standard techniques, such as photolithography and deep reactive ion etching.[84] This should allow the microionizer to be produced at a fraction of the time and cost of other microfabricated field effect devices. In order to better understand the microionizer, it is useful to discuss current ionization techniques as well as field effect devices used for mass spectrometry.

1.4.1 Internal vs. External Ionization

A host of ionization techniques have been developed in order to introduce analytes for mass spectral analysis.[85] To date, HPMS has been focused on threat detection, for example CWAs and VOCs, which are typically volatile. Thus, neutral gas is sampled from the atmosphere into the mass analyzer where it is subsequently ionized. Depending on the technique, ion generation occurs either internal or external to the trap. For an ion trap-based mass spectrometer, there is an important distinction between whether an ion is generated internal or external of the trapping volume due to the pseudopotential well depth.[86] In addition to defining the charge capacity of the ion trap, it places an upper bound on the kinetic energy an externally generated ion can have and still be successfully injected and captured by the trap. Internally generated ions typically have thermal kinetic energies that are near 0.025 eV at room temperature. Even with the reduced well depth of the mCIT ($\approx$ 5

to 10 V), these ions are easily trapped. However, externally generated ions must be transferred from the source into the trapping volume. Due to the dynamic nature of the three-dimensional trap, this means that the ion must not only be of low enough energy for capture, but it must also arrive at the proper phase of the RF cycle. For a traditional QITMS, estimates for the successful capture of externally generated ions are roughly 5%.

This capture percentage can be increased by several methods and include: 1) Synchronization of the ion injection with the phase of the RF thereby minimizing the chances ions are scattered by the electric field as they pass into the ion trap.[87-88] 2) Modulation of the drive RF amplitude to better trap ions across a large mass range.[89-90] 3) Use of enhanced ion optics, such as ion funnels to increase the flux through the ion trap.[91-92] 4) Raise the buffer gas pressure as more buffer gas molecules act as a frictional force to cool ions into the potential well of the ion trap[48, 93 94] Of these techniques, the final one is most pertinent for HPMS since elevated buffer gas pressure is ever-present.

1.4.2 Ionization Methods for High Volatility Analytes

In-vacuum, ions are commonly generated using techniques such as electron impact ionization (EI), photoionization, chemical ionization (CI), plasma, and field ionization. Electron impact ionization is widely used throughout mass spectrometry; for example, NIST mass spectral standards are recorded with EI.[95] However, EI requires neutrals to be easily introduced to vacuum (i.e. high vapor pressure), making it most useful for gas chromatography-mass spectrometry (GC-MS); thermal desorption; headspace sampling; and continuous flow monitoring. It was used as a staple ionization source for the development of ITMS because it is capable of producing ions with thermal energy (25 meV assuming room temperature) within the trapping volume of the analyzer.[69] Ionization occurs through

electron loss; an electron beam (typically 70 to 200 eV) is generated by a thermionic emitter, plasma, or cold cathode (field emitted) and guided through the ion trap. Electrons that interact with neutral analytes can impart enough energy to overcome the ionization potential and eject an electron from the neutral. The result is a positively charged molecular ion and two low energy electrons. Since the interaction is random, the molecular ion typically rearranges to access lower energy conformations resulting in a high degree of fragmentation; earning EI the status of a hard ionization source. EI based upon field emission is a considered a viable route towards miniaturization.[96]

Chemical ionization (CI) was developed as an extension to EI. A gas, usually methane, is introduced to the vacuum in excess relative to the analyte. Subsequent EI of the methane produces ions (mainly CH_5^+ and $C_2H_5^+$) that react with neutrals by proton or hydride reactions yielding ionized products.[97] CI increases the range of analytes accessible to mass spectral analysis, but still requires a highly volatile analyte. It also requires a consumable (methane), which makes it less amenable to miniaturization. However, atmospheric pressure chemical ionization (APCI) holds promise as an ionization technique for portable instrumentation since it relies upon ion-driven chemical reactions with nitrogen-based radicals generated from ambient air.[98-99]

Photoionization utilizes photons to ionize neutral molecules - a photon of energy greater than the ionization potential of the neutral (typically ultraviolet) must be absorbed for ionization. To generate mass spectra, high intensity light sources, such as discharge lamps or lasers are necessary. The mass spectra resulting from photoionization are similar to those observed with EI (i.e. hard ionization).[100] Due to the added complexity of the light source, photoionization is generally not suitable for miniaturization.

In addition to its utility as an electron source for EI, glow discharge plasmas can be used as external ion sources as well by directly sampling the plasma.[101] Two electrodes are immersed in a gas (noble, nitrogen, or air) and a voltage is applied between them initiating a Townsend discharge.[99, 102] The discharge will sustain if the field strength, separation between electrodes, and pressure meet the Paschen breakdown conditions.[103] Ions can be generated in several ways using GD. Gaseous analyte can be ionized and sampled directly from the plasma or a material can be placed on the cathode and ablated via ion bombardment.[101] GD has gained popularity in mass spectrometry due to its simplicity – a feature that translates well to portable instrumentation.[29, 104-105]

Field ionization relies upon the behavior of electrons at high electric field strengths, where electrons can tunnel from a neutral analyte into vacuum in the presence of a sufficient electric field (> 50 MV/cm).[78] The electric field strengths are achieved by applying a large voltage (> 5 kV) to a chemically sharpened wire or razor blade (with radius of curvature measured in nanometers).[79] As neutral molecules pass near the tip, the most loosely bound electrons can tunnel into the ionization tip, yielding singly charged, positive ions.[77, 106] This technique has been successfully coupled with mass spectrometry,[107-108] and it is considered soft because of the dominant molecular ion peak and lack of fragmentation.[109]

1.4.3 Field Effect Devices for Mass Spectrometry

Both field emission and field ionization have been used as ionization methods for mass spectrometry for a number of years.[110] Images of FEDs that have been successfully coupled with mass spectrometers are shown in Figure 1.4. For example, Spindt cathodes (Figure 1.4a) used as an electron source were first coupled with a linear quadrupole in 1968.[111] More recently, field emitter arrays, based upon Spindt-like emitters, were used as the EI source of

an ITMS for the European Space Agency's Rosetta mission that was launched in 2004 and began providing results in 2014.[112-113] Applications of FEDs aimed towards field portability include diamond-coated silicon whiskers coupled with a mCIT (Figure 1.4b)[114] and a carbon nanotube-based EI source for a handheld magnetic sector MS (Figure 1.4c).[12, 115] Field ionization sources gained traction with mass spectrometry as the first known soft ionization source.[116] This helped obtain spectra of complex samples using lower resolution instrumentation.[109]

Modern microfabrication procedures (photolithography, reactive ion etching, and thin film deposition) have led to the rise of vacuum microelectronics (VME). Previous FEDs were typically sharpened wires or edges and required ≥ 5 kV to generate field strengths necessary for the field effect.[76] At these high potentials, the ions formed acquire significant kinetic energy (on the order of keVs) resulting in significant transmission losses into the mass analyzer. With the advent of VMEs, lower potentials (near 500 V) can generate the same field strengths, improving ion transmission and opening up the possibility of coupling with ITMS.[107] Microfabricated field ion sources for mass spectrometry have been studied, though not quite as prolifically as field emission-based sources.[110] The micro-volcano (Figure 1.4d)[107] was the first VME field ionizer to be coupled with mass spectrometry.[110]

The final property of field effect devices that is pertinent is their ability to act as a dual-role source. If a structure is capable of field ionization, then it is also capable of field emission.[76, 79] Thus, a single source could be used for both EI and field ionization, which could provide two complementary fragmentation patterns. Such a source would be the ideal for a fieldable, handheld mass spectrometer, where sample preparation should be minimal.

The combination of small size, low-power, and the ability to perform both EI (based upon field emitted electrons) as well as field ionization have made field effect devices a prime target for combining with mass spectrometry. Despite these advantages, field effect devices have not displaced traditional sources such as thermionic-based EI because of economics. FEDs are simply too expensive relative to their traditional counterparts, except where circumstances prioritize performance over price, such as the Rosetta comet exploratory mission.[112-113]

1.5 Field Effect Applications and Theory

Mass spectrometry is only one of many potential applications for field effect devices. Charge generation is important in many research areas and field emission has been applied to field effect displays;[83] x-ray tubes;[117] field effect transistors;[118] and vacuum RF amplifiers such as the traveling wave tube.[119] While thermionic emitters suffice for these technologies, the general push towards smaller, more efficient devices makes FEDs highly desirable. For example, the power required for the average cellular phone tower could drop by orders of magnitude if the microwave amplifiers could utilize cold cathodes in place of thermionic electron sources.[119] Field ionization also has several applications beyond mass spectrometry including high resolution ion microscopy;[78, 120] ion sources;[121-122] gas detectors;[123-124] portable neutron generators;[121] and ion thrusters for microsatellites.[125] Given the array of applications that FEDs can help revolutionize, it is important to understand the theory behind them.

1.5.1 Field Emission

Field emission is often referred to as cold field emission (CFE) because it occurs at room temperature and only shows limited dependence upon temperature.[126] In 1928, Fowler and

Nordheim used a triangular barrier approximation for electron emission to quantify field emission current density from a planar, metallic surface as a function of electric field strength and work function.[127] The standard, temperature independent form is as follows:[128]

$$j_0 = \frac{a}{t_F^2 \varphi} F^2 e^{\frac{-v_F\, b\, \varphi^{3/2}}{F}} \tag{1.10}$$

where, the subscript '0' refers to the temperature and the variables are: φ, surface work function; F, the electric field; t_F^{-2} and v_F are elliptical functions referring to the Schottky-Nordheim barrier;[129] a and b are the Fowler-Nordheim constants which are defined as:[128, 130]

$$a \equiv \frac{e^3}{8\pi h_p} \approx 1.541 \; \frac{A\;eV}{V^2} \tag{1.11}$$

$$b \equiv \frac{8\pi e h_p}{3\sqrt{2m_e}} \approx 6.831 \; x \; 10^7 \; \frac{V}{eV^{3/2} cm} \tag{1.12}$$

and e is the elementary charge; h_p is Plank's constant; and m_e is the mass of the electron.

In 1956, Murphy and Good generalized electron emission from a metallic surface to include temperature and found that Fowler-Nordheim was the zero-temperature limit of their expression.[129] In 1976, Spindt approximated the elliptical functions, t_F^{-2} and v_F in order to use field emission current measurements to extract the emitter surface area, α and field enhancement factor, β where:[131]

$$j = \frac{I}{\alpha} \tag{1.13}$$

$$F = \beta V \tag{1.14}$$

The variables are: local current density, j (Eq 1.10) and the measured current at the detector, I. This approximation has been widely used throughout field emission research.[132] However, its accuracy is best for 'flatter' emission surfaces with a radius of curvature greater than 10 nm.[133]

The theory presented to this point is also specific to metallic surfaces. Semiconductor-based field emission requires additional consideration and depends upon the doping.[76] Deviations from standard Fowler-Nordheim field emission are observed for p-type and lightly-doped ($< 10^{18}$ dopants/cm^3 in silicon) n-type semiconductors. For p-type semiconductors, electron emission into vacuum creates an inversion layer at the surface. While the surface work function is typically lower for a p-type semiconductor,[134-135] it does not compensate for the alteration of the electric field due to penetration into the crystal and emission is reduced relative to an analogous structure in metal.[136] For lightly doped (high resistivity) n-type semiconductors, the rate of carrier (electron) generation is limited and is often smaller than the rate at which electrons are emitted into vacuum, again resulting in reduced emission relative to a metal surface.[136] For highly-doped n-type semiconductors ($>$ 10^{18} dopants/cm^3 in silicon), field emission typically follows standard Fowler-Nordheim theory.[74] For this reason, highly-doped silicon was predominately used for microionizer fabrication.

A note regarding field emission in general: due to the highly-localized nature of emission sites, quantitative analysis has been described as 'messy' by experts in the field.[73] More often than not, several variables in the Fowler-Nordheim (even the elementary version) are unknown such as the work function and radius of curvature of the emission site. As such, calculated field enhancement factors, work functions, and emission current densities (especially for field emitting arrays) are dependent upon estimates. While determining β and α values may be useful in comparing FEDs within a research group, it is often improper to compare values between completely different FEDs or to blindly trust the values reported.[137]

For many field emission sources, the microionizer included, Fowler-Nordheim analysis is used simply to verify field emission as the mechanism behind observed electron currents.

1.5.2 Field Ionization

Field ionization is a complement to field emission, where an electron from a neutral atom or molecule can tunnel into a surface.[76] Since the Fermi level is nearly full in a conductor, the electron must tunnel into an energy level above this, and a simple one-dimensional model is used to describe the energy of the neutral orbital, ϵ, relative to the Fermi level:[73]

$$\epsilon = (I_1 - \varphi) + eFx \tag{1.15}$$

where the variables are: the first ionization potential of the neutral, I_1 and the separation distance between the nucleus of the neutral and ionization tip, x. A critical distance, x_c, is defined when $\epsilon = 0$. The electron cannot tunnel directly when $x < x_c$, since this would place it below the Fermi level of the conductor. Thus, field ionization occurs outside of this critical distance while field desorption and/or tunneling through an adsorbed layer is believed to occur within the critical distance:[116]

$$x_c \cong \frac{(I_1 - \varphi)}{eF} \tag{1.15}$$

Ionization can be estimated to occur with 1 nm of the critical distance and the efficiency is dependent upon the time a neutral spends within this distance of the surface.[124] Field ionization demonstrates a threshold behavior, where neutrals with different ionization potentials demonstrate ionization at differing field strengths.[77] After the appearance potential is reached, ionization efficiency quickly approaches unity, and the ion current from the emitter saturates.[108]

1.5.3 Pressure Tolerance and Lifetime

For field emission a large negative potential is typically required to generate the requisite electric field. Many field emitters are designed to be operated at high vacuum ($< 10^{-6}$ Torr), and can maintain >50% emission of their original emission intensity after more than 10,000 h of operation.[74] This mark is especially important for applications where the FED cannot be easily serviced and/or replaced such as computer displays.[83] High vacuum reduces sputtering damage at the emission site due to ion back streaming. Back streaming involves ions formed via EI events near the FED that are accelerated opposite of the electrons and crash into the surface. This backstream of ions will gain energy equal to the potential applied to the tip, thus they can easily hit the threshold for ion-induced surface damage and sputtering[138] degrading the emission tip.[81] Tip degradation is of concern, because it can lead to emission-induced failure. The emission current density has an exponential dependence upon work function and emitter tip geometry; thus small changes such as adsorbed gases or emitter tip deformation can cause large deviations in the field emission current, resulting in emitter damage.[139-140] If the emission is spread across an array (as is common) the failure of a single tip results in outgassing which will briefly increase the rate of ion backstream sputtering as well as neutral adsorption leading to premature failure in the surrounding tips.[75, 81] This problem can be avoided by adding a current limiting (ballast) resistor in series with each tip, which adds complexity and cost to the fabrication process.[141] At higher pressure, 10^{-3} to 10^{-5} Torr, surface flashover becomes a concern. As the name implies, it is a surface effect, where charge buildup on the insulator layer of a gated field emitter can aid in the formation of a plasma that can result in an arc discharge between the anode and cathode of the field emitter.[142-143]

Field ionizers can suffer from many of the same failure mechanisms as field emission sources, such as dielectric breakdown and surface flashover.[80, 124, 144] Due to the increase in field strength for field ionization, dielectric breakdown is a more common occurrence than in field emission. Breakdown is accelerated by electron injection into the dielectric, which can degrade the insulator over time.[145-147] Additionally, field desorption can gradually erode the tip leading to reduced signal intensity over time.[144] Despite the greater difficulty of working at higher field strengths, field ionization has one advantage over field emission: the opposite polarity of the applied potential prevents ion back streaming damage since ions flow away from the ionization tip.[124] Thus, pressure limitations are more likely to originate from standard Paschen-type breakdowns to any nearby ground planes. Similar to field emission sources, well designed field ionization sources have demonstrated lifetimes longer than 10,000 h.[110]

1.5.4 Fabrication

Both field emission and field ionization devices have functional limitations, with some materials better suited than others. For example, refractory metals have high melting points, making them ideal for high current density applications where localized Joule heating can induce premature tip erosion.[139] As such a host of materials have been studied including: carbon nanotubes;[148-149] porous silicon carbide;[150] thin-film semiconductors;[151-152] metal and diamond coated semiconductors;[131, 153-154] CVD diamond;[137] among many other examples.[132]

Prior to the advent of modern microfabrication techniques, FEDs typically required > 5 kV to be applied to a chemically sharpened wire or razor-like edge.[79] The Spindt Cathode was the first FED that used modern microfabrication techniques and is considered the beginning of vacuum microelectronics (VME).[75, 111] Microfabrication offers two

important properties: first, the spacing between the emission tip and counter-electrode can be precisely controlled on the micrometer scale, reducing the potentials necessary for field emission below 1 kV; second, arrays of parallel emission sites or field emission arrays (FEA) with nearly identical dimensions can be fabricated.[75, 110] These FEA of single-point emitters produce more consistent field emission and field ionization compared to single points (as opposed to large edges).[79] Despite the 'ease' with which microfabrication enables arrays to be generated, the exponential dependence of the current density upon tip geometry and work function means that the process must be tightly controlled. Each tip should be identical down to the nanometer scale, which is a difficult task that adds time and cost to fabricaiton.[132] Techniques have been developed to 'burn in' devices, such as quickly ramping the field strength up and down in order to burn off the sharpest tips, but the array fabrication must still be tightly controlled.[155]

1.6 Solid State Microionizer

1.6.1 Design and Operation

The microionizer is a solid state, field effect device designed specifically for HPMS operation. The key to successful operation is that the spacing between electrodes, the high-field region of the device, must be smaller than the mean free path of both electrons and ions at the operational pressure. This smaller geometry suppresses electrical breakdown by avoiding the ionizing collisions necessary for Paschen-type breakdowns.[156-157] A hard sphere collision model using collisional cross sections for electrons[158-159] and toluene[160-161] (a common VOC) was used to determine the critical dimensions for the microionizer. At 1 Torr, the mean free paths are on the order of 10 mm and 100 μm for electrons and toluene molecules, respectively. This places an upper bound on the spacing between electrodes (the

high field region) of about 100 μm. At this thickness, an electric field strength of 1 MV/cm necessary for field emission would require a potential of 10 kV. As the goal is to minimize the applied voltage, preferably below 100 V, the spacing between electrodes should be on the order of 1 μm or less to produce 1 MV/cm field strengths.

The microionizer relies upon silicon-on-insulator (SOI) substrates to achieve ≤ 1 μm spacing for the high field region. SOI is a layered structure, where an insulator, typically oxide, separates two, parallel silicon layers (the device and handle).[162] A cross sectional schematic of the microionizer is shown in Figure 1.5; the SOI layers as well as the high-field region are highlighted. SOI can be made-to-order and the thicknesses of all three layers are customizable as well as dopant type and concentration. A 150 mm (6") SOI substrate can have device layers ranging from 2 to 150 μm; insulator layers from 0.1 to 10 μm; and handle layers from 400 to 650 μm.[163] SOI has been primarily used for low-power microprocessors because the electrical isolation of the device layer reduces parasitic capacitance during high speed switching.[164-165] However, the wide range of layer thicknesses has also positioned SOI as an invaluable substrate in applications ranging from photonics to microelectromechanical systems (MEMS).[166-168] For the microionizer, the insulator layer thicknesses available are ideal for sub-100 V operating voltages.

The first generation microionizer utilized SOI with highly-doped, n-type silicon, separated by a 0.5 μm oxide. The original layout is shown in Figure 1.6a and consists of a 1 cm^2 die with a 4 x 4 array of active features; the device and handle layers are 2 and 400 μm thick, respectively. The vias shown in Figure 1.6b and c are cylindrical with a 20 μm diameter. Other variants (not shown) are cylindrical with 10 and 100 μm diameters as well as rectangular trenches with a 2 x 90 μm^2 footprint. The operational voltages, pulse and bias,

applied to the microionizer are shown in Figure 1.5. The pulse voltage initiates field emission or field ionization while the bias voltage controls the electron/ion energy relative to the mCIT. For the 0.5 µm thick insulating layer, only 50 V is needed to achieve 1 MV/cm electric field strength. Geometric field enhancement due to surface roughness generated by the etch process (seen in Figure 1.6c) should boost the macroscopic field into the 10 to 100 MV/cm necessary for field emission and field ionization.[150]

1.6.2 Examples of Similar FEDs

There is precedent in the literature for similar FED devices, but none combine the ease of fabrication and dual-role nature of the microionizer. Planar devices using thin insulating layers have been fabricated for field ionization and field emission. A soft ionization membrane (SIM) proposed by Hartley achieves field ionization using the same principles as the microionizer but relies upon nanofabrication techniques to form vias in gold-on-silicon nitride substrates.[169] It is capable of generating streams of 100% ionized particles, but the nanofabrication techniques and specialized substrates used for the SIM are not amenable to mass production. The edge-to-edge emitter (ETE) is a layered-field emission device, proposed by Short, et al. It uses two tungsten electrodes separated by a composite insulator of CVD silicon oxide/nitride/oxide. While the device is better suited for mass production, it showed limited lifetime due to delamination of the tungsten layers during testing.[170] A similar layered structure has been used to produce metal-oxide-semiconductor field effect transistors (MOSFET) specifically to increase transistor switching speed through ballistic electron transport in the vacuum channel.[118, 171] While turn on/off potentials have been reduced through the use of sub-100 nm insulators, the devices are not suited for electron/ion extraction for ionization purposes.

1.6.3 Advantages of the Microionizer

The key to success for the microionizer relative to other FEDs lies in its design. It is specifically meant for HPMS, which means pressure tolerance, power consumption, and fabrication costs were key design considerations. Other field emission devices rarely operate at pressures higher than 10^{-6} Torr due to ion back streaming.[132] For the microionizer, back stream-induced sputtering should be minimized. The thinner insulating layer between handle and device layer of the SOI wafer requires smaller potentials to generate the macroscopic electric field strengths necessary for field emission. Thus, ions formed due to EI will only be able to gain limited kinetic energy (< 100 eV). Moreover, the difference in mean free paths of electrons and ions means that most of the back stream ions generated by EI will undergo collisions prior to impact with the emitter tip. This should retard their ability to sputter the emission tip. While thinner insulating layers lead to improved pressure tolerance, they also reduce power consumption. Reduction of the insulating layer thickness yields similar macroscopic field strengths at lower operating voltages. Since the displacement current is a function of electric field strength, lower voltages will yield lower power consumption. Ultimately, the circuitry required to generate the pulse can be simplified as the voltage amplitude decreases which will also reduce secondary power consumption.[172]

The microionizer achieves field effect by geometric enhancement due to the surface roughness of the device sidewalls. Many other FED's use arrays of identically sharpened tips. By relying upon the surface roughness, the stringent fabrication requirements for nanometer-level precision are not necessary. This also means the process is less susceptible to variations in etches and depositions across the entire surface area of a single wafer. Additionally, the SOI-based process flow does not require any time consuming or specialized

fabrication steps (a list of the tools and techniques used for microionizer fabrication can be found in Appendix A). The end result is that microionizer fabrication can use more surface area of the wafer while simultaneously maintaining a better overall yield than other FEDs. Thus, the cost per device should be lower for the microionizer.

1.7 Objectives and Roadmap

The work presented in this dissertation focuses on developing a pressure and oxygen tolerant ion generation source (microionizer) for use with high pressure mass spectrometry. The original specific aims proposed in 2012, were: 1) demonstrate field emission and field ionization-based high pressure mass spectrometry using a microionizer; 2) determine lifetime and controlling parameters for the microionizer; and 3) integrate the microionizer into a mCIT trap electrode stack.

The work began with investigating traditional ionization sources under HPMS conditions and finished with successful microionizer-based HPMS. Chapter 2 reports the results of internal and external ionization under HPMS conditions using traditional ionization sources. Chapter 3 covers proof of concept experiments with the initial microionizer design providing important design and operational condition insights for successful field emission and field ionization. Chapter 4 documents the development of the fabrication process flow for producing microionizers capable of field emission and field ionization. Chapter 5 is devoted to HPMS utilizing the microionizer in both field emission and field ionization modes. The final chapter presents conclusions and future directions.

1.8 Figures
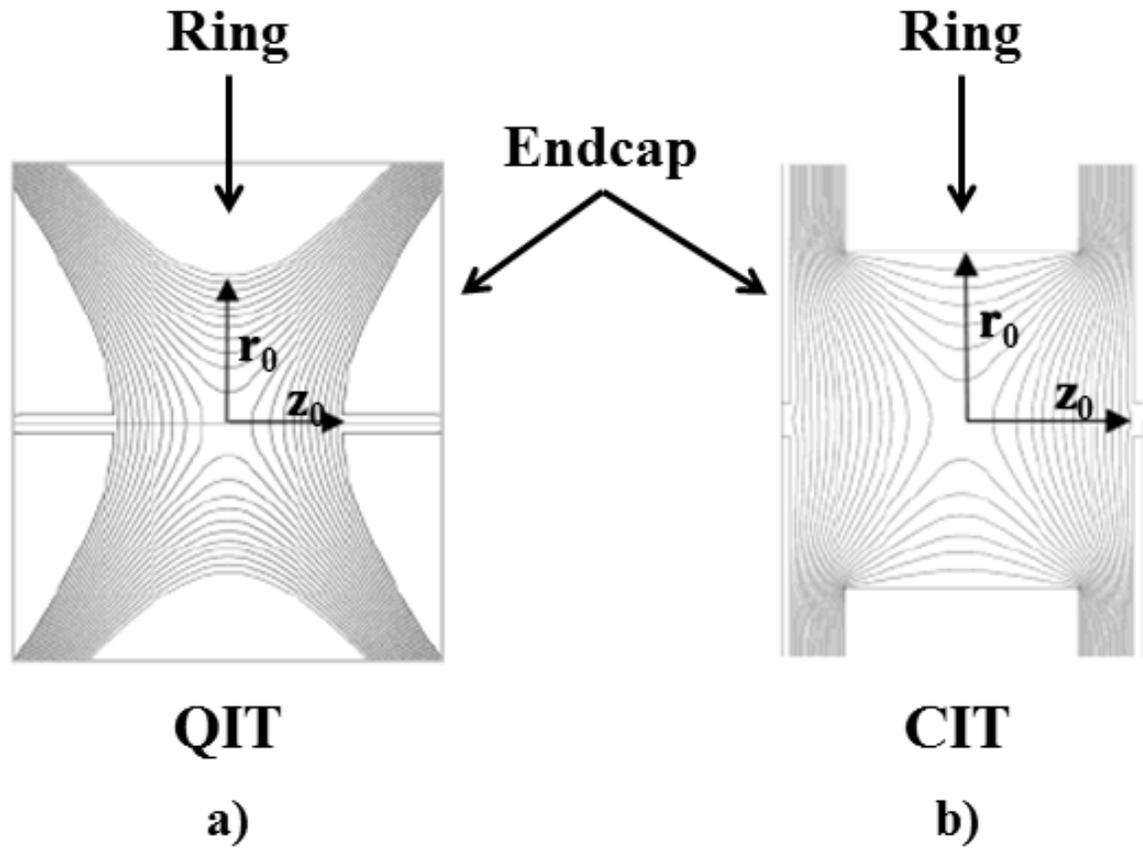
Figure 1.1: Cross sectional schematic of three-dimensional ion traps: a) QIT and b) CIT.[17] The equipotential lines are shown to highlight the differences between the QIT and CIT. Both display quadrupolar fields at the center of the trapping volume, but the CIT has higher order fields particularly near the electrode boundaries, introduced by the sharp transitions due to the geometry simplification.
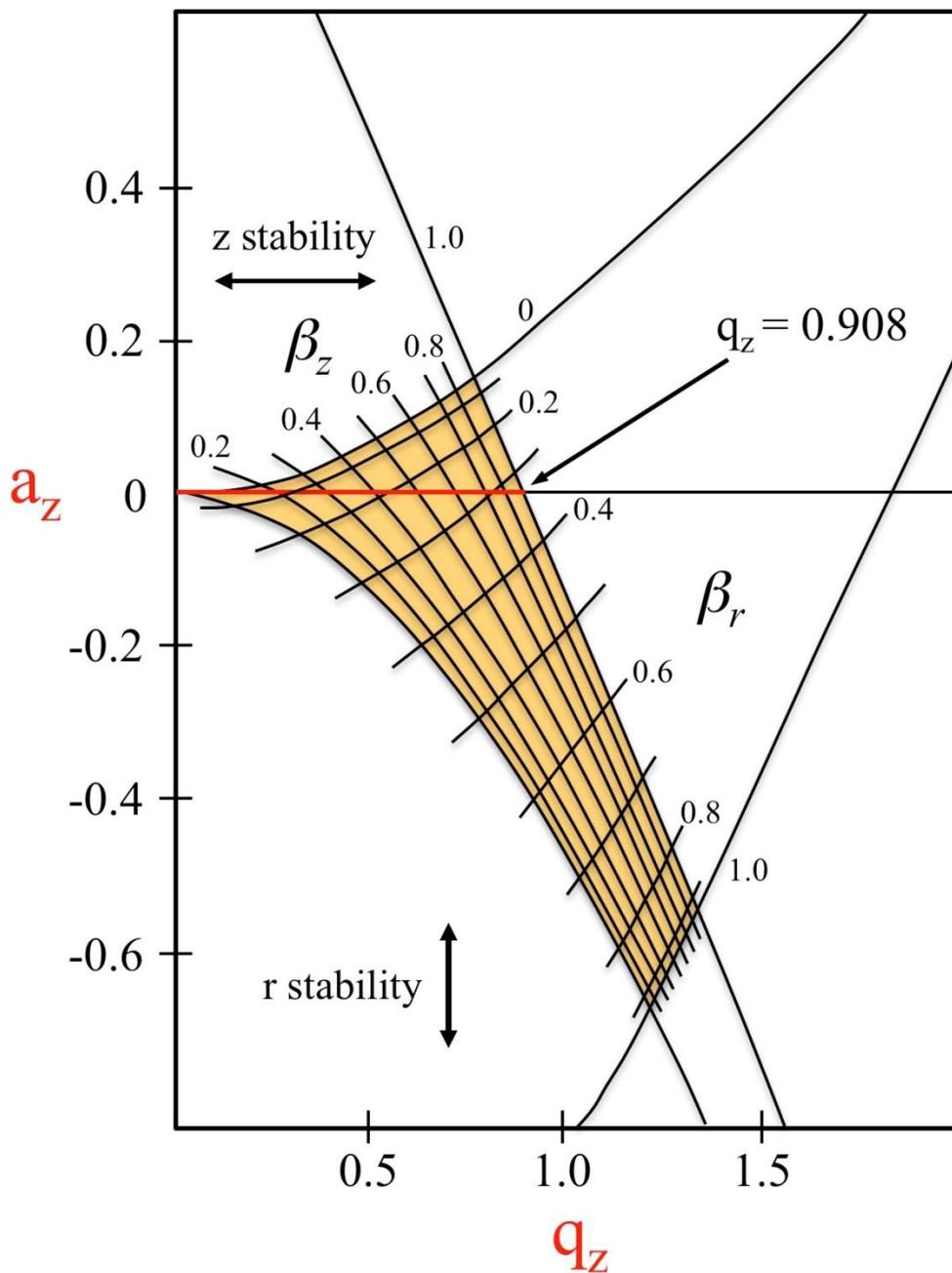
Figure 1.2: Stability diagram for the z-dimension of a QIT. The axes are the stability parameters where a_z is proportional to the DC offset and q_z to the RF amplitude. The β lines are thresholds between stable, periodic motion in each direction. The red line at $a_z = 0$ is the typical region over which a QITMS operates in mass selective instability mode. Ions order themselves inversely proportional to q_z; as the RF amplitude is increased ions eject axially from smallest to largest m/z.
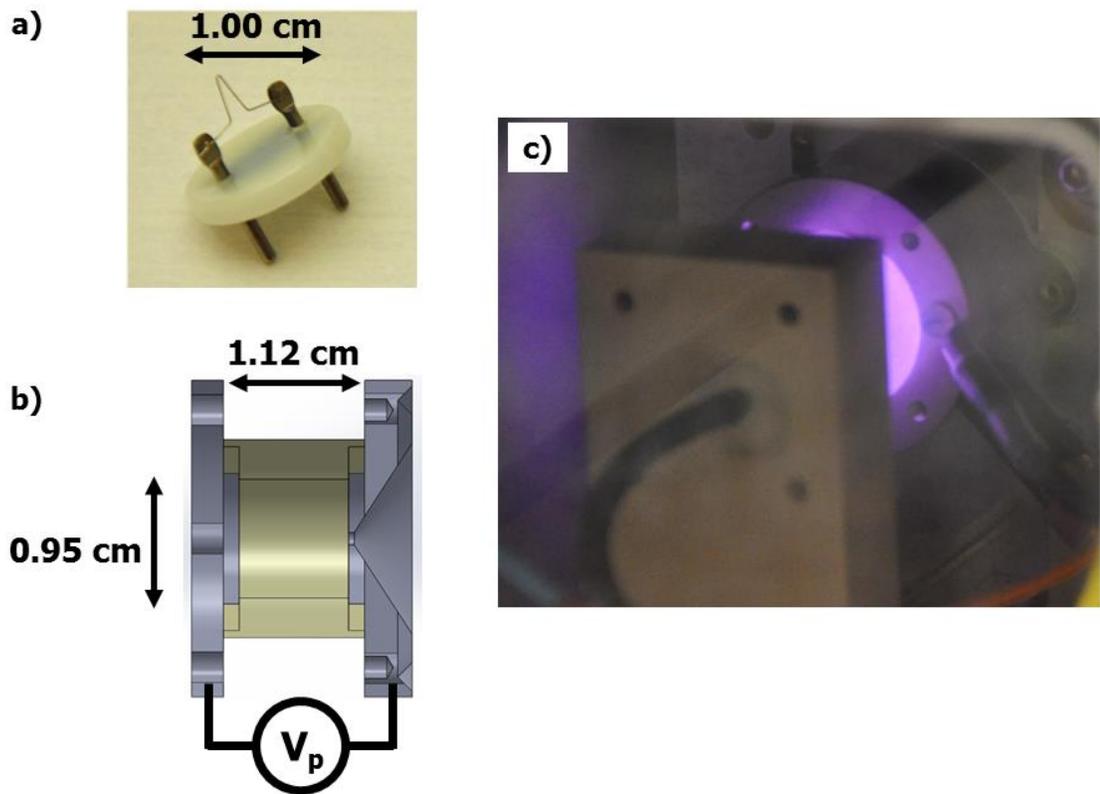
Figure 1.3: Thermionic and glow discharge sources used for HPMS. a) Image of a tungsten filament (Kimball Physics, ES-020). A biased, heating current, $\approx$ 1.2 A at -70 to -250 V, flows through the wire to produce electrons for EI. b) Schematic of the GD source used in the differential chamber. A pulse voltage, $\approx$ 500 to 750 V, strikes a DC plasma, a bias potential applied to the pulse selects the mode GDe, 0 to -250 V, and GDi, 0 to +250 V. c) Image of the GD source operating at 1 Torr.
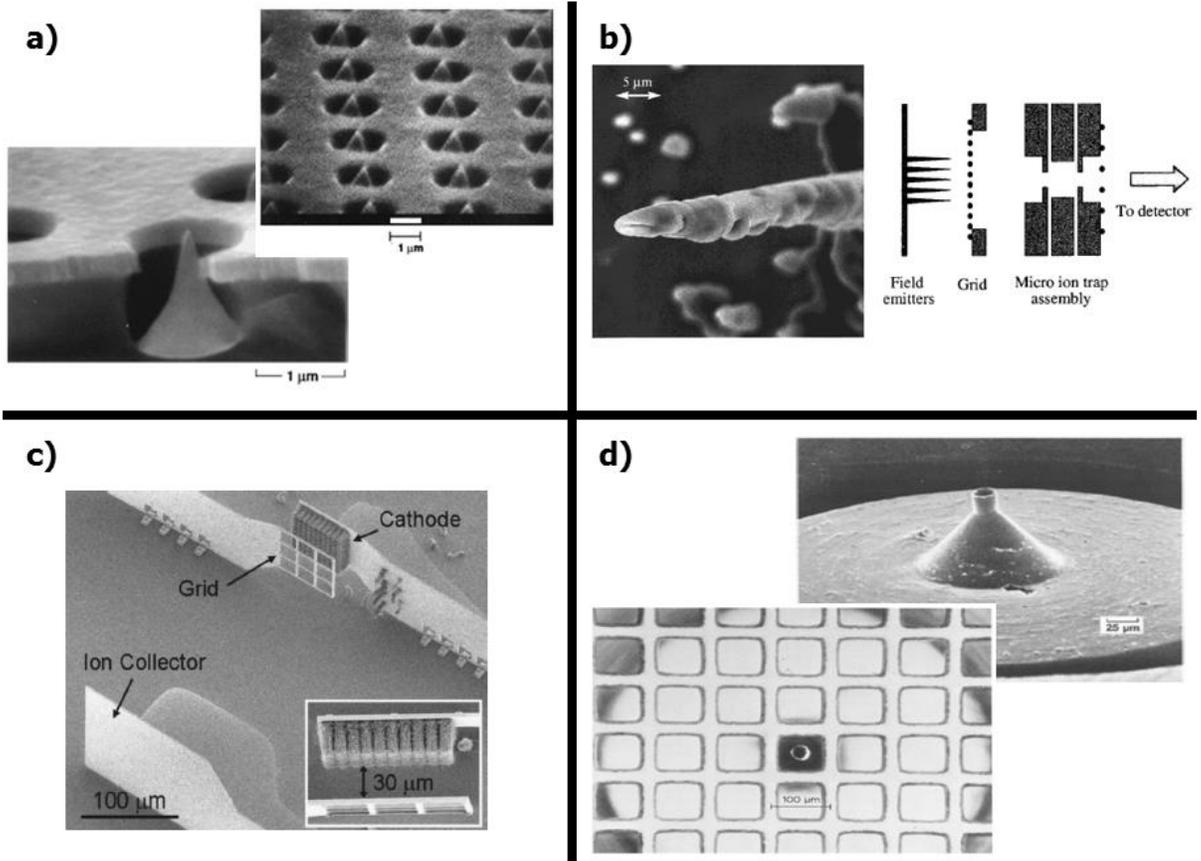
Figure 1.4: Examples of field effect devices used for mass spectrometry. a) An array of Spindt cathodes used as an electron source for EI with a linear quadrupole.[75] b) CVD diamond-coated silicon whiskers used as an EI source for a CIT.[114] c) Carbon nanotube array used as an EI source for a magnetic sector.[115] d) Field ionization 'volcano' used as an field ion source for a linear quadrupole.[107]
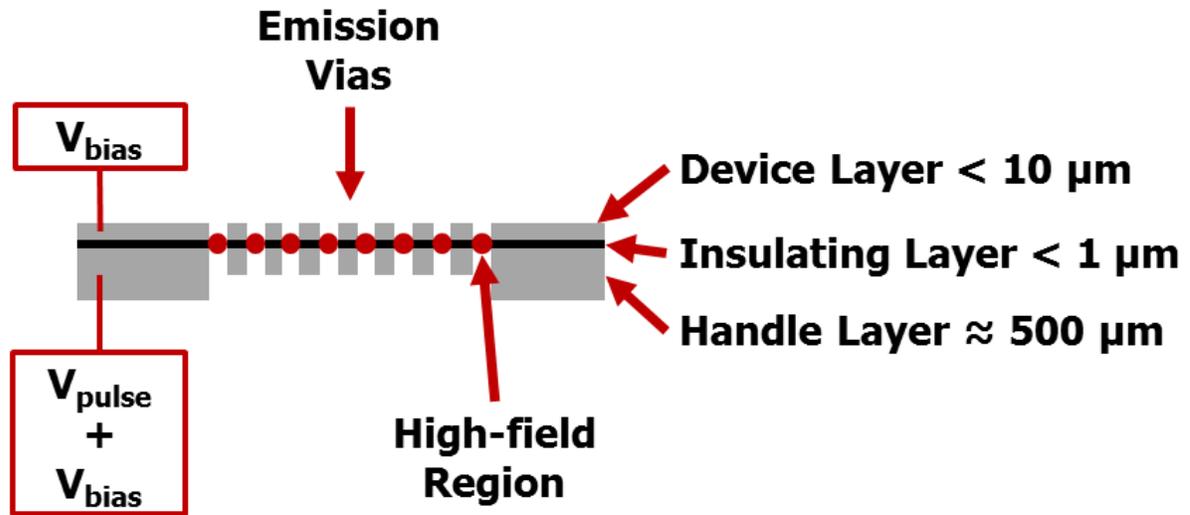
Figure 1.5: A cross-sectional schematic of the microionizer (not to scale). The SOI layers, device, insulator, and handle are indicated along with their typical thicknesses. The location of the high-field region (●) within each via is also highlighted. Field emission and field ionization mode are selected by the polarity of the pulse and bias voltages: negative voltages access field emission and positive voltages are used for field ionization. The bias voltage controls the electron/ion energy by floating the potential of the microionizer relative to the mCIT.
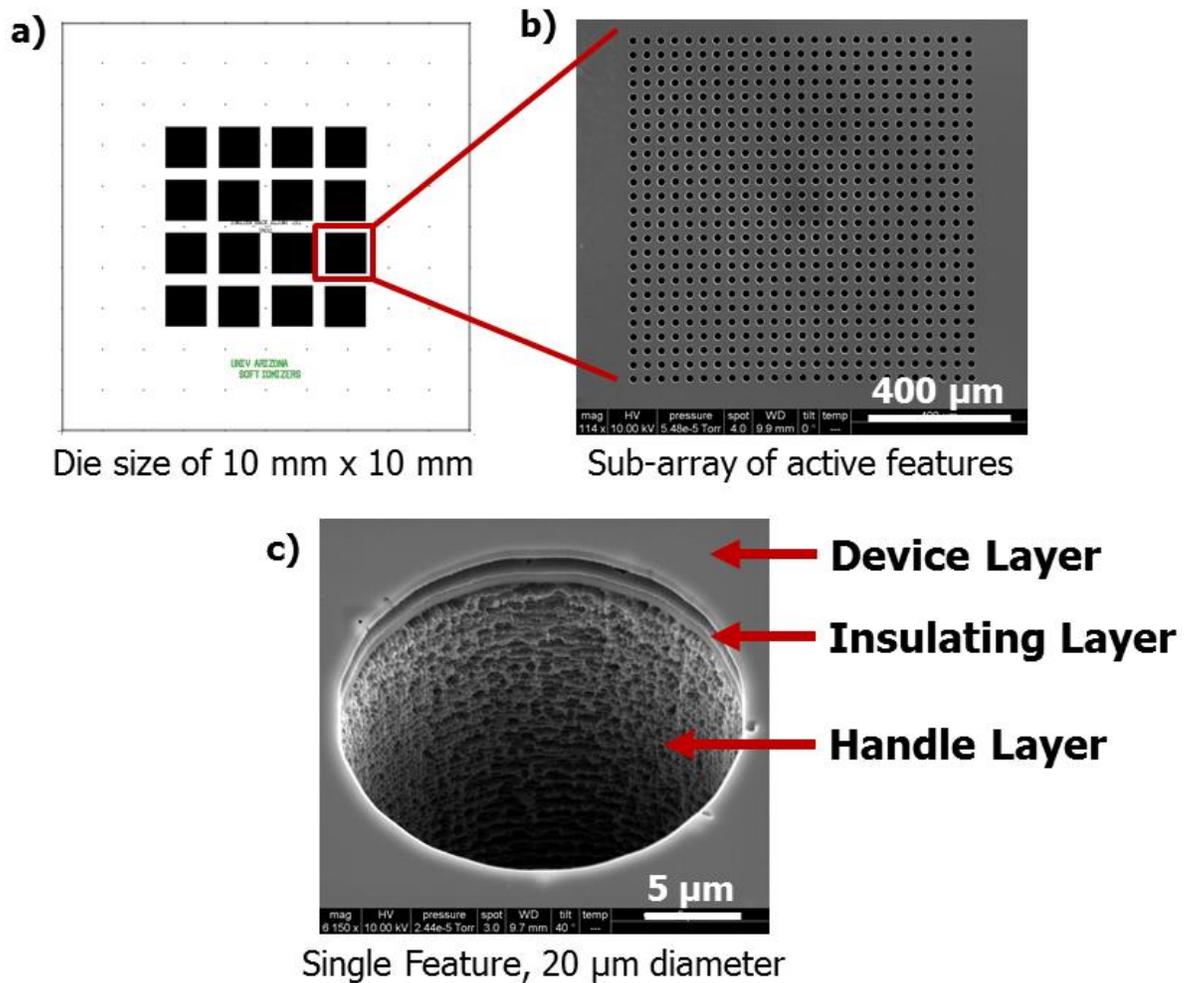
Figure 1.6: Introduction to the microionizer. a) CAD diagram of the original microionizer design provided by Dr. Pau. b) SEM of a sub-array of 20 µm diameter features and c) a single via. The device layer is the front surface of the device, while the handle layer is only seen as the rough, cylindrical sidewalls of the feature. The insulating layer is 0.5 µm thick and separates the device and handle.

1.9 REFERENCES

1.   de Hoffmann, E.; Stroobant, V., *Mass Spectrometry Principles and Applications*. 3rd ed.; John Wiley & Sons: West Sussex, England, 2009; p 489.

2.   McClennen, W. H., et al., Field-portable hypenated instrumentation: the birth of the tricorder? *Trends in Analytical Chemistry* **1994,** *13* (7), 286-293.

3.   McGuire, M. J., et al., An unwanted licorice odor in a West Virginia water supply. *J Am Water Works Ass* **2014,** *106* (6), 72-82.

4.   Manuel, J., Crisis and Emergency Risk Communication: Lessons from the Elk River Spill. *Environ Health Persp* **2014,** *122* (8), A214-A219.

5.   Bryden, W. A., et al., The Tiny-Tof Mass-Spectrometer for Chemical and Biological Sensing. *J Hopkins Apl Tech D* **1995,** *16* (3), 296-310.

6.   Lammert, S. A., Field Portable Mass Spectrometry. In *Detection of chemical, biological, radiological and nuclear agents for the prevention of terrorism : mass spectrometry and allied topics*, Banoub, J., Ed. Springer: New York, 2014; p 291.

7.   Hoffmann, W. D.; Jackson, G. P., Forensic Mass Spectrometry. In *Annual Review of Analytical Chemistry, Vol 8*, Cooks, R. G.; Pemberton, J. E., Eds. Annual Reviews: Palo Alto, 2015; Vol. 8, pp 419-440.

8.   Badman, E. R.; Cooks, R. G., Special feature: Perspective - Miniature mass analyzers. *J. Mass Spectrom.* **2000,** *35* (6), 659-671.

9.   Yang, M., et al., Development of a Palm Portable Mass Spectrometer. *J. Am. Soc. Mass Spectrom.* **2008,** *19* (10), 1442-1448.

10.   Ouyang, Z., et al., Handheld Miniature Ion Trap Mass Spectrometers. *Analytical chemistry* **2009,** *81* (7), 2421-2425.

11.   Bryden, W. A., et al., Tiny-TOF-MALDI mass spectrometry for particulate drug and explosives detection. *Law Enforcement Technologies: Identification Technologies and Traffic Safety* **1995,** *2511*, 153-164.

12.   Gilchrist, K. H., et al. In *A Novel Ion Source and Detector for a Miniature Mass Spectrometer*, IEEE Sensors, 2007; pp 1372-1375.

13.   Orient, O. J., et al., Miniature, high-resolution, quadrupole mass-spectrometer array. *Review of Scientific Instruments* **1997,** *68* (3), 1393-1397.

14.   Taylor, S., et al., Silicon based quadrupole mass spectrometry using microelectromechanical systems. *Journal of Vacuum Science & Technology, B: Microelectronics and Nanometer Structures* **2001,** *19* (2), 557-562.

15.   Kornienko, O., et al., Micro ion trap mass spectrometry. *Rapid Commun. Mass Spectrom.* **1999,** *13* (1), 50-53.

16.   Badman, E. R., et al., A miniature cylindrical quadrupole ion trap: simulation and experiment. *Analytical chemistry* **1998,** *70* (23), 4896-4901.

17.   Ouyang, Z., et al., Rectilinear Ion Trap: Concepts, Calculations, and Analytical Performance of a New Mass Analyzer. *Anal. Chem.* **2004,** *76* (16), 4595-4605.

18.   Ferran, R. J.; Boumsellek, S., High-pressure effects in miniature arrays of quadrupole analyzers for residual gas analysis from 10-9 to 10-2 Torr. *Journal of Vacuum Science Volume A* **1996,** *14* (3, Pt. 1), 1258-1265.

19.   March, R. E., An Introduction to Quadrupole Ion Trap Mass Spectrometry. *Journal of Mass Spectrometry* **1997,** *32* (4), 351-369.

20.   March, R. E.; Todd, J. F. J., *Quadrupole ion trap mass spectrometry*. 2nd ed.; J. Wiley: Hoboken, N.J., 2005.

21.   Louris, J. N., et al., Instrumentation, applications, and energy deposition in quadrupole ion-trap tandem mass spectrometry. *Analytical chemistry* **1987,** *59* (13), 1677-1685.

22.   Moxom, J., et al., Analysis of volatile organic compounds in air with a micro ion trap mass analyzer. *Anal. Chem.* **2003,** *75* (15), 3739-3743.

23.   Orient, O. J.; Chutjian, A., A compact, high-resolution Paul ion trap mass spectrometer with electron-impact ionization. *Rev. Sci. Instrum.* **2002,** *73* (5), 2157-2160.

24.   Wells, J. M., et al., A Quadrupole Ion Trap with Cylindrical Geometry Operated in the Mass-Selective Instability Mode. *Analytical chemistry* **1998,** *70* (3), 438-444.

25.   Lammert, S. A., et al., Miniature Toroidal Radio Frequency Ion Trap Mass Analyzer. *J. Am. Soc. Mass Spectrom.* **2006,** *17* (7), 916-922.

26.   Gao, L., et al., Handheld Rectilinear Ion Trap Mass Spectrometer. *Anal. Chem.* **2006,** *78* (17), 5994-6002.

27.   Bonner, R. F., et al., The cylindrical ion trap. Part I. General introduction. *Int. J. Mass Spectrom. Ion Phys.* **1977,** *24* (3), 255-269.

28.   Contreras, J. A., et al., Hand-portable gas chromatograph-toroidal ion trap mass spectrometer (GC-TMS) for detection of hazardous compounds. *J. Am. Soc. Mass Spectrom.* **2008,** *19* (10), 1425-1434.

29.   Gao, L., et al., Design and Characterization of a Multisource Hand-Held Tandem Mass Spectrometer. *Anal. Chem.* **2008,** *80* (19), 7198-7205.

30.   Li, L. F., et al., Mini 12, Miniature Mass Spectrometer for Clinical and Other Applications-Introduction and Characterization. *Analytical chemistry* **2014,** *86* (6), 2909-2916.

31.   Cylindrical Ion Trap. http://1stdetect.com/technology/cylindrical-ion-trap/ (accessed 10/15/2015).

32.   Rafferty, D., Driving a mass spectrometer ion trap or mass filter. Google Patents: 2011.

33.   Song, Q. Y., et al., Ion trap mass analysis at high pressure: an experimental characterization. *Journal of Mass Spectrometry* **2010,** *45* (1), 26-34.

34. Johnson, M. C., et al. Miniature turbomolecular pump. US6412173 B1, Jul 2, 2002, 2002.

35. Chen, C. H., et al., Design of Portable Mass Spectrometers with Handheld Probes: Aspects of the Sampling and Miniature Pumping Systems. *Journal of the American Society for Mass Spectrometry* **2015,** *26* (2), 240-247.

36. Ouyang, Z.; Cooks, R. G., Miniature Mass Spectrometers. *Annu. Rev. Anal. Chem.* **2009,** *2*, 187-214.

37. Allen, J. S., The detection of single positive ions, electrons and photons by a secondary electron multiplier. *Physical review* **1939,** *55* (10), 0966-0971.

38. Keil, A., et al., Ambient mass spectrometry with a handheld mass spectrometer at high pressure. *Anal. Chem.* **2007,** *79* (20), 7734-7739.

39. Gao, L., et al., Breaking the Pumping Speed Barrier in Mass Spectrometry: Discontinuous Atmospheric Pressure Interface. *Anal. Chem.* **2008,** *80* (11), 4026-4032.

40. Ramsey, J. M. Microscale mass spectrometry systems, devices and related methods. 20140263999 A1, 9/18/2014, 2014.

41. M908 Spec Sheet. http://908devices.com/wp-content/uploads/2014/10/SpecSheet-908_2014_v21.pdf (accessed 11/3/2015).

42. Nanos, J., 908 Devices has a hand-held approach to thwarting chemical attacks. *Boston Globe* 4/20/2015, 2015.

43. Wolfe, D. W. High-Pressure Cylindrical Ion Trap Mass Spectrometry. Dissertation, University of North Carolina, Chapel Hill, 2012.

44. Schultze, K. P. Advanced System Components for the Development of a Handheld Ion Trap Mass Spectrometer. Dissertation, University of North Carolina at Chapel Hill, Chapel Hill, NC, 2014.

45. Blakeman, K. H. Development of High Pressure Mass Spectrometry for Handheld Instruments. Dissertation, University of North Carolina at Chapel Hill, Chapel Hill, NC, 2015.

46. Paul, W.; Steinwedel, H., A New Mass Spectrometer without a Magnetic Field. *Zeitschrift fuer Naturforschung* **1953,** *a8*, 448-450.

47. Mather, R. E., et al., Some operational characteristics of a quadrupole ion storage mass spectrometer having cylindrical geometry. *International Journal of Mass Spectrometry and Ion Physics* **1980,** *33* (3), 201-230.

48. Stafford Jr, G. C., et al., Recent improvements in and analytical applications of advanced ion trap technology. *Int. J. Mass Spectrom. Ion Processes* **1984,** *60* (1), 85-98.

49. Goeringer, D. E., et al., Theory of high-resolution mass spectrometry achieved via resonance ejection in the quadrupole ion trap. *Analytical chemistry* **1992,** *64* (13), 1434-1439.

50. Whitten, W. B., et al., High-pressure ion trap mass spectrometry. *Rapid Commun. Mass Spectrom.* **2004,** *18* (15), 1749-1752.

51. Kornienko, O., et al., Electron impact ionization in a microion trap mass spectrometer. *Rev. Sci. Instrum.* **1999,** *70* (10), 3907-3909.

52. Moxom, J., et al., Double resonance ejection in a micro ion trap mass spectrometer. *Rapid Commun. Mass Spectrom.* **2002,** *16* (8), 755-760.

53. Blakeman, K. H., et al., High-Pressure Mass Spectrometry at Pressures Exceeding 1 Torr in a Microscale Cylindrical Ion Trap. *Manuscript in preparation* **2015**.

54. Blakeman, K. H.; Ramsey, J. M., High Pressure Mass Spectrometry in Nitrogen and Air. *Manuscript in preparation* **2014**.

55. Tian, Y., et al., How far can ion trap miniaturization go? Parameter scaling and space-charge limits for very small cylindrical ion traps. *Journal of Mass Spectrometry* **2014,** *49* (3), 233-240.

56.   Dehmelt, H. G., Radiofrequency Spectroscopy of Stored Ions I: Storage. *Advances in Atomic and Molecular Physics* **1968,** *3*, 53-72.

57.   Badman, E. R.; Cooks, R. G., A parallel miniature cylindrical ion trap array. *Analytical chemistry* **2000,** *72* (14), 3291-3297.

58.   Pau, S., et al., Microfabricated quadrupole ion trap for mass spectrometer applications. *Phys. Rev. Lett.* **2006,** *96* (12), 120801.

59.   Ramsey, J. M.; Schultze, K., Miniature charged particle trap with elongated trapping region for mass spectrometry. Google Patents: 2014.

60.   Badman, E. R., et al., Fourier Transform Detection in a Cylindrical Quadrupole Ion Trap. *Analytical chemistry* **1998,** *70* (17), 3545-3547.

61.   Koppenaal, D. W., et al., MS detectors. *Anal. Chem.* **2005,** *77* (21), 418A-427A.

62.   Goodrich, G. W.; Wiley, W. C., Continuous Channel Electron Multiplier. *Review of Scientific Instruments* **1962,** *33* (7), 761-762.

63.   Yellin, E., et al., Ion Detection Using a Continuous Channel Electron Multiplier. *Review of Scientific Instruments* **1970,** *41* (1), 18-19.

64.   Andresen, R. D.; Page, D. E., On Ion Feedback in a Straight Channel Multiplier. *Nucl. Instrum. Methods* **1970,** *85* (1), 141-142.

65.   Gilliland, W. M., et al., Coupling Microchip Electrospray Ionization Devices with High Pressure Mass Spectrometry. *Manuscript in preparation* **2015**.

66.   Wolfe, D., et al., High-Pressure CIT Mass Spectrometry with a Solid-State CTIA Detector. UNC at Chapel Hill: 2012; p 28.

67.   Johnson, M. S., et al., Solid-State Impact-Ionization Multiplier with P-N Junction Injection Node. *IEEE Transactions on Electron Devices* **2009,** *56* (6), 1360-1364.

68.   Johnson, M. S., et al. In *Improving Gain Efficiency in Planar Impact Ionization Devices*, 218th ECS Meeting, 2010.

69.   Todd, J. F. J.; March, R. E., A retrospective review of the development and application of the quadrupole ion trap prior to the appearance of commercial instruments. *International Journal of Mass Spectrometry* **1999,** *191*, 9-35.

70.   Jenkins, R. O., A Review of Thermionic Cathodes. *Vacuum* **1969,** *19* (8), 353-359.

71.   Stuart, R. V.; Wehner, G. K., Sputtering Yields at Very Low Bombarding Ion Energies. *J Appl Phys* **1962,** *33* (7), 2345-2352.

72.   Lisovskiy, V. A.; Yakovin, S. D., Experimental study of a low-pressure glow discharge in air in large-diameter discharge tubes: I. Conditions for the normal regime of a glow discharge. *Plasma Phys Rep+* **2000,** *26* (12), 1066-1075.

73.   Forbes, R. G., Field electron and ion emission from charged surfaces: a strategic historical review of theoretical concepts. *Ultramicroscopy* **2003,** *95* (1-4), 1-18.

74.   Fursey, G., *Field emission in vacuum microelectronics*. Kluwer Academic/Plenum Publishers: New York, 2005; p 205.

75.   *Vacuum Microelectronics*. 1 ed.; Wiley-Interscience: 2001; p 408.

76.   Gomer, R., *Field emission and field ionization*. Harvard University Press: Cambridge,, 1961; p 195.

77.   Heinen, H. J., et al., Appearance Potentials of Field Ions. *Z Naturforsch A* **1974,** *A 29* (5), 773-781.

78.   Muller, E. W.; Bahadur, K., Field Ionization of Gases at a Metal Surface and the Resolution of the Field Ion Microscope. *Physical review* **1956,** *102* (3), 624-631.

79.   Beckey, H. D., et al., Comparison of Tips Thin Wires and Sharp Metal Edges as Emitters for Field Ionization Mass Spectrometry. *J Phys E Sci Instrum* **1968,** *1* (2), 118-120.

80.   Muller, E. W.; Nishikaw.O, Increased Image Brightness in a Field Ion Microscope. *Review of Scientific Instruments* **1965,** *36* (4), 556.

81.   Charbonnier, F., Arcing and voltage breakdown in vacuum microelectronics microwave devices using field emitter arrays: Causes, possible solutions, and recent progress. *J Vac Sci Technol B* **1998,** *16* (2), 880-887.

82.   Bonard, J.-M., et al., Degradation and failure of carbon nanotube field emitters. *Physical Review B* **2003,** *67* (11), 115406.

83.   Talin, A. A., et al., Field emission displays: a critical review. *Solid-State Electronics* **2001,** *45* (6), 963-976.

84.   Madou, M. J., *Fundamentals of microfabrication and nanotechnology*. 3rd ed.; CRC Press: Boca Raton, FL, 2012.

85.   Alberici, R. M., et al., Ambient mass spectrometry: bringing MS into the "real world". *Anal Bioanal Chem* **2010,** *398* (1), 265-294.

86.   Kishore, M. N.; Ghosh, P. K., Trapping of Ions Injected from an External Source into a 3-Dimensional Rf Quadrupole Field. *International Journal of Mass Spectrometry and Ion Processes* **1979,** *29* (4), 345-350.

87.   Qin, J.; Chait, B. T., Matrix-assisted laser desorption ion trap mass spectrometry: Efficient trapping and ejection of ions. *Analytical chemistry* **1996,** *68* (13), 2102-2107.

88.   Appelhans, A. D.; Dahl, D. A., Measurement of external ion injection and trapping efficiency in the ion trap mass spectrometer and comparison with a predictive model. *International Journal of Mass Spectrometry* **2002,** *216*, 269-284.

89.   Doroshenko, V. M.; Cotter, R. J., Injection of externally generated ions into an increasing trapping field of a quadrupole ion trap mass spectrometer. *Journal of Mass Spectrometry* **1997,** *32* (6), 602-615.

90.   Doroshenko, V. M.; Cotter, R. J., Linear Mass Calibration in the Quadrupole Ion-Trap Mass-Spectrometer. *Rapid Commun Mass Sp* **1994,** *8* (9), 766-776.

91.   Shaffer, S. A., et al., A novel ion funnel for focusing ions at elevated pressure using electrospray ionization mass spectrometry. *Rapid Commun Mass Sp* **1997,** *11* (16), 1813-1817.

92.   Laiko, V. V., et al., Atmospheric pressure MALDI/ion trap mass spectrometry. *Analytical chemistry* **2000,** *72* (21), 5239-5243.

93.   Louris, J. N., et al., Injection of Ions into a Quadrupole Ion Trap Mass-Spectrometer. *International Journal of Mass Spectrometry and Ion Processes* **1989,** *88* (2-3), 97-111.

94.   McLuckey, S. A., et al., Ion Trap Mass Spectrometry of Externally Generated Ions. *Analytical chemistry* **1994,** *66* (13), 689-696.

95.   Stein, S. E., "Mass Spectra". in *NIST Chemistry WebBook, NIST Standard Reference Database Number 69* [Online] Linstrom, P. J.; Mallard, W. G., Eds. National Institute of Standards and Technology, Gaithersbrug, MD, http://webbook.nist.gov, (accessed 10/2/2015).

96.   Felter, T. E., Cold cathode field emitter array on a quadrupole mass spectrometer: Route to miniaturization. *J Vac Sci Technol B* **1999,** *17* (5), 1993-1996.

97.   Munson, M. S. B.; Field, F. H., Chemical Ionization Mass Spectrometry I General Introduction. *J Am Chem Soc* **1966,** *88* (12), 2621-2630.

98.   Siefering, K., et al., Improved Atmospheric-Pressure Ionization Mass Spectroscopic Methods .2. Extending the Range of Accuracy through Nonlinear Calibration Techniques. *Journal of the Electrochemical Society* **1993,** *140* (4), 1165-1168.

99.   Tendero, C., et al., Atmospheric pressure plasmas: A review. *Spectrochim Acta B* **2006,** *61* (1), 2-30.

100.   Chait, E. M., Ionization Sources in Mass-Spectrometry. *Analytical chemistry* **1972,** *44* (3), A77-A91.

101.   Harrison, W. W., et al., Glow-Discharge Techniques in Analytical-Chemistry. *Analytical chemistry* **1990,** *62* (18), A943-A949.

102. Fridman, A. A., *Plasma chemistry*. First paperback edition. ed.; Cambridge University Press: Cambridge, 2012; p 978.

103. Lisovskii, V. A.; Yakovin, S. D., A modified paschen law for the initiation of a DC glow discharge in inert gases. *Tech Phys+* **2000,** *45* (6), 727-731.

104. Handberg, E. S. Atmospheric sampling glow discharge ionization (ASGDI) using a quarter-sized cylindrical ion trap mass spectrometer (CIT-MS) for explosives detection in air. Purdue University, West Lafayette, IN, 2006.

105. Rubinshtein, A. A., et al., Characterization of a third-generation Faraday-strip array detector coupled to a Mattauch-Herzog geometry mass spectrograph with a dc-glow discharge ionization source. *J. Anal. Atom. Spectrom.* **2010,** *25* (5), 735-738.

106. Beckey, H. D., et al., Über die Feldstärkeabhängigkeit der Winkelverteilung feldemittierter Elektronen und Ionen. In *Zeitschrift für Naturforschung A*, 1966; Vol. 21, p 141.

107. Aberth, W.; Spindt, C. A., Characteristics of a Volcano Field-Ion Quadrupole Mass-Spectrometer. *International Journal of Mass Spectrometry and Ion Processes* **1977,** *25* (2), 183-198.

108. Beckey, H. D., *Principles of field ionization and field desorption mass spectrometry*. 1st ed.; Pergamon Press: Oxford Eng. ; New York, 1977; p 335.

109. Abramson, F. P.; Howard, R. F., Some Operational Principles of Field Ionization Mass Spectrometry. *Org Mass Spectrom* **1968,** *1* (3), 488.

110. Spindt, C. A., Microfabricated field-emission and field ionization sources. *Surface Science* **1991,** *266*, 145-154.

111. Spindt, C. A., A Thin-Film Field-Emission Cathode. *J Appl Phys* **1968,** *39* (7), 3504-3505.

112. Huq, S. E., et al., Field emitters for space application. *J Vac Sci Technol B* **2001,** *19* (3), 988-991.

113. Balsiger, H., et al., Rosina - Rosetta orbiter spectrometer for ion and neutral analysis. *Space Sci Rev* **2007,** *128* (1-4), 745-801.

114. Kornienko, O., et al., Field-Emission Cold-Cathode EI Source for a Microscale Ion Trap Mass Spectrometer. *Analytical chemistry* **2000,** *72* (3), 559-562.

115. Bower, C. A., et al., On-chip electron-impact ion source using carbon nanotube field emitters. *Appl. Phys. Lett.* **2007,** *90* (12), 124102.

116. Robertson, A. J. B., Field ionization mass spectrometry. *Journal of Physics E: Scientific Instruments* **1974,** *7*, 321-327.

117. Sprenger, F., et al., Distributed source x-ray tube technology for tomosynthesis imaging. In *Medical Imaging 2010: Physics of Medical Imaging*, Samei, E.; Pelc, N. J., Eds. Spie-Int Soc Optical Engineering: Bellingham, 2010; Vol. 7622.

118. Srisonphan, S., et al., Metal-oxide-semiconductor field-effect transistor with a vacuum channel. *Nat Nanotechnol* **2012,** *7* (8), 504-508.

119. Whaley, D. R., et al., 100 W Operation of a Cold Cathode TWT. *Ieee Transactions on Electron Devices* **2009,** *56* (5), 896-905.

120. Tsong, T. T.; Muller, E. W., Current-Voltage Characteristics by Image Photometry in a Field-Ion Microscope. *J Appl Phys* **1966,** *37* (8), 3065-3070.

121. Johnson, B. B., et al., Field ion source development for neutron generators. *Nucl Instrum Meth A* **2012,** *663* (1), 64-74.

122. Rao, K. A., et al., A Combination Electron-Ion Field-Emission Source. *J Vac Sci Technol B* **1989,** *7* (6), 1793-1797.

123. Ghodsian, B., et al., Gas Detector with Low-Cost Micromachined Field Ionization Tips. *IEEE Electron Device Letters* **1998,** *19* (7), 241-243.

124. Fomani, A. A., et al., Low-Voltage Field Ionization of Gases Up to Torr-Level Pressures Using Massive Arrays of Self-Aligned Gated Nanoscale Tips. *Ieee Transactions on Electron Devices* **2014,** *61* (5), 1520-1528.

125.   Hartley, F. T., Miniature Free-Space Electrostatic Ion Thrusters. Stephens, J. B., Ed. NASA: NASA Technology Briefs, 2006; p 29.

126.   Benilov, M. S.; Benilova, L. G., Field to thermo-field to thermionic electron emission: A practical guide to evaluation and electron emission from arc cathodes. *J Appl Phys* **2013,** *114* (6).

127.   Fowler, R. H.; Nordheim, L., Electron Emission in Intense Electric Fields. *Proceedings of the Royal Society A: Mathematical, Physical and Engineering Sciences* **1928,** *119* (781), 173-181.

128.   Forbes, R. G., Physics of generalized Fowler-Nordheim-type equations. *Journal of vacuum science & technology. B, Microelectronics and nanometer structures processing, measurement and phenomena* **2008,** *26* (2), 788-793.

129.   Murphy, E. L.; Good, R. H., Thermionic Emission, Field Emission, and the Tranistion Region. *Physical review* **1956,** *102* (6), 1464-1473.

130.   Burgess, R., et al., Corrected Values of Fowler-Nordheim Field Emission Functions v(y) and s(y). *Physical review* **1953,** *90* (4), 515-515.

131.   Spindt, C. A., et al., Physical Properties of Thin-film Field Emission Cathodes with Molybdenum Cones. *J Appl Phys* **1976,** *47* (12), 5248-5263.

132.   Xu, N. S.; Huq, S. E., Novel cold cathode materials and applications. *Mat Sci Eng R* **2005,** *48* (2-5), 47-189.

133.   Forbes, R. G., et al., Improved approach to Fowler-Nordheim plot analysis. *Journal of Vacuum Science and Technology B* **2013,** *31* (2), 1-8.

134.   Allen, F. G.; Gobeli, G. W., Work Function, Photoelectric Threshold, and Surface States of Atomically Clean Silicon. *Physical review* **1962,** *127* (1), 150-158.

135.   Novikov, A., Experimental measurement of work function in doped silicon surfaces. *Solid-State Electronics* **2010,** *54* (1), 8-13.

136. Baskin, L. M., et al., General Features of Field Emission from Semiconductors. *Phys Status Solidi B* **1971,** *47* (1), 49-62.

137. Zhu, W., et al., Electron field emission from chemical vapor deposited diamond. *J Vac Sci Technol B* **1996,** *14* (3), 2011-2019.

138. Wu, S. M., et al., Sputtering yields of Ru, Mo, and Si under low energy Ar+ bombardment. *J Appl Phys* **2009,** *106* (5).

139. Browning, J., et al., Experimental Observations of Gated Field Emitter Failures. *IEEE Electron Device Letters* **1992,** *13* (3), 167-169.

140. Browning, J., et al., Gated Field Emitter Failures: Experiment and Theory. *IEEE Transactions on Plasma Science* **1992,** *20* (5), 499-506.

141. Levine, J. D., Benefits of the lateral resistor in a field effect display. *J Vac Sci Technol B* **1996,** *14* (3), 2008-2010.

142. Pillai, A. S.; Hackam, R., Surface Flashover of Solid Insulators in Atmospheric Air and in Vacuum. *J Appl Phys* **1985,** *58* (1), 146-153.

143. Miller, H. C., Surface Flashover of Insulators. *IEEE T Electr Insul* **1989,** *24* (5), 765-786.

144. Johnson, B. B., et al., Field ionization characteristics of an ion source array for neutron generators. *J Appl Phys* **2013,** *114* (17).

145. Osburn, C. M.; Weitzman, E. J., Electrical-Conduction and Dielectric Breakdown in Silicon Dioxide Films on Silicon. *Journal of the Electrochemical Society* **1972,** *119* (5), 603-609.

146. Demey, G.; Dewilde, W., Influence of Mobile Ions on Electronic Conduction in Silicon-Oxide Films. *Thin Solid Films* **1974,** *23* (3), 301-304.

147. Chiu, F. C., A Review on Conduction Mechanisms in Dielectric Films. *Adv Mater Sci Eng* **2014**.

148.   Cheng, Y.; Zhou, O., Electron field emission from carbon nanotubes. *Comptes Rendus Physique* **2003,** *4* (9), 1021-1033.

149.   Ding, M. Q., et al., Fabrications of Spindt-type cathodes with aligned carbon nanotube emitters. *Appl. Surf. Sci.* **2005,** *251* (1-4), 201-204.

150.   Kang, M., et al., Stable field emission from nanoporous silicon carbide. *Nanotechnology* **2013,** *24*, 1-5.

151.   Sowers, A. T., et al., Thin films of aluminum nitride and aluminum gallium nitride for cold cathode applications. *Appl. Phys. Lett.* **1997,** *71* (16), 2289.

152.   Chung, M. S., et al., Tip-geometry enhanced cooling of field emission from the n-type semiconductor. *Appl. Phys. Lett.* **2014,** *104* (8).

153.   Fomani, A. A., et al., Toward Amp-Level Field Emission With Large-Area Arrays of Pt-Coated Self-Aligned Gated Nanoscale Tips. *Ieee Transactions on Electron Devices* **2014,** *61* (7), 2538-2546.

154.   Chang, Y., et al., Enhanced field emission characteristics in metal-coated Si-nanocones. *Physical Chemistry and Chemical Physics* **2013,** *15* (10), 761-766.

155.   Purcell, S. T., et al., Nanoprotrusion model for field emission from integrated microtips. *J Vac Sci Technol B* **1997,** *15* (5), 1666-1677.

156.   Wallash, A.; Levit, L., Electrical breakdown and ESD phenomena for devices with nanometer-to-micron gaps. *Reliability, Testing, and Characterization of MEMS/MOEMS II* **2003,** *4980*, 87-96.

157.   Slade, P. G.; Taylor, E. D., Electrical breakdown in atmospheric air between closely spaced (0.2 mu m-40 mu m) electrical contacts. *IEEE T Compon Pack T* **2002,** *25* (3), 390-396.

158.   Kauppila, W. E., et al., Measurements of total scattering cross sections for intermediate-energy positrons and electrons colliding with helium, neon, and argon. *Physical Review A* **1981,** *24* (2), 14.

159. Dalba, G., et al., Absolute Total Cross-Section Measurements for Intermediate Energy Electron-Scattering .2. N-2 O-2 and No. *J Phys B-at Mol Opt* **1980,** *13* (23), 4695-4701.

160. Sielemann, S., et al., Quantitative analysis of benzene, toluene, and m-xylene with the use of a UV-ion mobility spectrometer. *Field Anal Chem Tech* **2000,** *4* (4), 157-169.

161. Lin, S. N., et al., Dependence of Polyatomic Ion Mobilities on Ionic Size. *J Chem Phys* **1974,** *60* (12), 4994-4999.

162. Celler, G. K.; Cristoloveanu, S., Frontiers of silicon-on-insulator. *J Appl Phys* **2003,** *93* (9), 4955-4978.

163. Ultrasil Product Information. http://www.ultrasil.com/our_products_details.aspx?ID=6 (accessed 12/21/2015).

164. Nguyen, B. Y., et al., A Review of SOI Technology and its Applications. *Journal of Integrated Circuits and Systems* **2009,** *4* (2), 51-54.

165. Mitani, K.; Gosele, U. M., Wafer Bonding Technology for Silicon-on-Insulator Applications - a Review. *J Electron Mater* **1992,** *21* (7), 669-676.

166. Plossl, A.; Krauter, G., Wafer direct bonding: tailoring adhesion between brittle materials. *Mat Sci Eng R* **1999,** *25* (1-2), 1-88.

167. Geear, M., et al., Monolithic MEMS quadrupole mass spectrometers by deep silicon etching. *Journal of Microelectromechanical Systems* **2005,** *14* (5), 1156-1166.

168. Bower, C. A., et al., Microfabrication of fine-pitch high aspect ratio Faraday cup arrays in silicon. *Sensors and Actuators, A: Physical* **2007,** *A137* (2), 296-301.

169. Hartley, F. T.; Kanik, I. In *A nanoscale soft-ionization membrane: A novel ionizer for ion mobility spectrometers for space applications*, Proceedings of SPIE, The International Society for Optical Engineering, 2002; pp 1-7.

170. Van Amerom, F. H. W., et al., Microfabrication of Cylindrical Ion Trap Mass Spectrometer Arrays for Handheld Chemical Analyzers. *Chem. Eng. Commun.* **2008,** *195* (2), 98-114.

171. Lim, H. J., et al., Impact of the crystallization of the high-k dielectric gate oxide on the positive bias temperature instability of the n-channel metal-oxide-semiconductor field emission transistor. *Appl. Phys. Lett.* **2013,** *102* (23).

172. Huang, P. C., et al., High Efficiency and Smooth Transition Buck-Boost Converter for Extending Battery Life in Portable Devices. *2009 IEEE Energy Conversion Congress and Exposition, Vols 1-6* **2009**, 2342-2345.

CHAPTER 2: THERMIONIC AND GLOW DISCHARGE SOURCES FOR HPMS APPLICATIONS

2.1 Introduction

Expanding mass spectrometry beyond the lab environment and making it a ubiquitous analytical technique is the collective goal of the research performed developing high pressure mass spectrometry (HPMS). HPMS provides a vehicle for miniaturizing the systems (ionizer, mass analyzer, detector) of the ion trap mass spectrometer to achieve an inexpensive, small form factor (handheld or benchtop) instrument. Ion traps are the chosen mass analyzer because they have several characteristics that are ideal for miniaturization: mass resolution does not depend upon their size;[1] they can operate at higher pressures than other mass analyzers;[2-3] and they have the ability to perform MS^n.[4-5] HPMS operates miniature cylindrical ion traps at 1 Torr (mCIT, $r_0 \leq 500$ μm) at high frequency (f > 6 MHz). By doing so, the turbo pump is eliminated from the vacuum system decreasing the size, weight, and power (SWaP) as well as the cost.[3] Additionally, HPMS relies upon ambient air as the buffer gas, removing the need for an external helium tank further reducing the size and weight. While there are many positive qualities to ion traps, external ion injection is a weak point for quadrupole ion traps (QIT); typically as few as 5% of the ions generated external to the trapping volume are successfully injected into a 3D trap.[6-8] With this in mind, early HPMS studies relied exclusively upon electron impact ionization (EI). Mass spectrometry with the mCIT was performed in modest pressure helium buffer gas and worked towards the 1 Torr goal[2-3, 9-10] before moving to nitrogen and air[11] buffer gases. Having achieved these

milestones, development of an external ion injection source would add ambient ionization methods to the HPMS toolbox.

A standard QIT has a 1 cm radius and operates at 1 MHz RF with amplitudes ramping from 0.5 to 10 kV_{0-p} and helium buffer gas at ≤ 1 mTorr pressure.[12] Because efficient ion injection is difficult to achieve under these conditions, early commercial ITMS systems relied upon *in situ* (internal) ionization such as EI and chemical ionization (CI) and were mainly employed as gas chromatograph detectors.[13] Studies showed that external ion injection is particularly dependent upon the ion kinetic energy and drive RF phase[14] as well as higher order fields due to geometric imperfections of the QIT.[15] In order to expand the analyte range of ITMS beyond small molecules, much research was devoted to coupling external ionization techniques such as atmospheric pressure glow discharge ionization (APGDI), electrospray ionization (ESI), atmospheric pressure chemical ionization (APCI), secondary ion mass spectrometric source (SIMS), laser desorption (LD), and matrix assisted laser desorption (MALDI) with the QIT.[16-19] This research pushed the boundaries of ITMS and expanded its utility well beyond volatile, low mass analytes to include peptides and proteins.[20]

Several techniques were found to boost the efficacy of external ion injection into QITs. Maximizing ion transmission makes the most of the low trapping efficiency inherent to QIT operation and is typically used in conjunction with either waveform modulation or collisional cooling. The RF ion funnel is a particularly successful example of ion optics that can be employed to this end.[21] Waveform gating is employed with pulsed sources such as LD[22] and MALDI,[23] where ion injection is precisely synchronized to the pulsed or modulated RF drive field which improves external trapping efficiency.[24] Finally, buffer gas pressure can simply

be increased.[13] Collisional cooling due to ion-neutral interactions acts like friction on the walls of the ion trap's potential well improving trapping efficiency.[6, 25] Of these techniques, collisional cooling is a natural consequence of operating at high pressures so it does not require additional instrumentation to implement.

Prior to the studies presented in this chapter, external ion injection under HPMS conditions had not been attempted with a mCIT. Internal EI is a more predictable method for producing ions and generally better suited for demonstrating mass analysis at 1 Torr. However, external ion injection should expand the utility of the technique, so the efficacy of ion injection with a mCIT at both high (1 Torr) and low (< 250 mTorr) pressures was undertaken. A custom, off-axis EI source was developed for the purpose of generating external ions for injection into the mCIT. It was used to probe the low pressure properties of ion injection with the mCIT and helium buffer gas. Furthermore, external ion injection across a wide range of pressures, ion kinetic energies, and trapping conditions was done with an on-axis glow discharge (GD) ionization source. The GD source was used in both positive (GDi) and negative (GDe) modes. These experiments lay the groundwork for coupling ambient ionization techniques such as ESI with HPMS.

2.2 Experimental Section

A custom, high pressure mass spectrometer similar to that used for previous HPMS studies was employed.[3, 26] Figure 2.1a shows an exploded view of the differentially pumped vacuum chambers with the location of the ion source, mass analyzer, and detector highlighted. The components of the 'trap-side' vacuum chamber are shown in Figure 2.1b. It is maintained at high pressure (≈1000 mTorr) and houses the ionization source and mass analyzer (mCIT). The 'detector-side' is shown in Figure 2.1c. It houses the electron

multiplier (EMT) and is held at low pressures (< 50 mTorr) suitable for EMT operation. Each chamber was pumped with an Agilent TPS Benchtop pumping system consisting of an SH110 scroll pump and TV-81M turbomolecular pump. With this configuration, the pressure on the mass analyzer-side can be ranged from 1 to 1000+ mTorr while the EMT pressure remains below 50 mTorr preventing autoionization within the detector.[27] Pressure in each chamber was monitored with a full range pressure gauge (FRG-700, Agilent, Inc). In addition, trap-side pressure was measured absolutely using a NIST traceable capacitance manometer (Baratron 627D, MKS Instruments, Inc).

The miniature cylindrical ion trap had critical dimensions of $r_0 = 500$ μm and $z_0 = 645$ μm. The ring electrode was electrochemically etched from 790 μm thick copper (Towne Labs, Somerville, NJ). Two types of endcaps were used: aperture and mesh. Standard apertures were etched from 250 μm thick beryllium copper with a radius of 200 μm (Towne Labs). Mesh endcaps were assembled by soldering 400 lpi copper mesh TEM grids (SPI, Inc) over a 3 mm diameter aperture in a printed circuit board endcap (Advanced Circuits, Inc). The mCITs were assembled with 125 μm polyimide washers (#002, McMaster-Carr, Inc). An image of an assembled, aperture-endcap mCIT is shown in Figure 2.1b.

The RF trapping potential was generated using an Agilent E4428C signal generator driving a custom, tanked amplifier arrangement. The trap was driven at 8.0 ± 1.5 MHz. The amplitude of the drive potential (RF voltage) is frequency dependent. RF amplitude ranged from 200 to 800 V_{0-p}, depending on the RF frequency and mass range. The RF amplitude was ramped during mass analysis with scan speeds between 15 to 25 kDa/s. Both boundary ejection (mass selective instability) and double resonant ejection were used. For boundary

ejection, both endcaps were grounded, while axial RF was applied asymmetrically near 1/3

drive frequency for resonant ejection. Axial RF was applied to the detector side endcap only

at 2.5 ± 0.5 MHz and pressure-dependent amplitude 2.5 to 10 $V_{pp.}$ The drive RF and axial RF

were both monitored with 10X probes and a 4-channel, digital oscilloscope (P6139A and

TDS 3034B, Tektronix).

Helium and nitrogen buffer gases (UHP Grade, National Welders, Inc) were introduced

to the chamber via a 0-50 sccm mass flow controller (FMA 5402, Omega, Inc). Ambient

air was also used as a buffer gas and introduced through a needle valve inlet to the mass

spectrometer. Pressure was controlled by a combination of flow rate and conductance limits.

The analyte, mesitylene (1, 3, 5-trimethyl benzene) from Sigma Aldrich (St Louis, MO), was

introduced to the chamber at 0.01 mTorr via an ultrahigh vacuum leak valve (MDC, Inc).

Two ion sources were used for this study: a custom off-axis, EI source and an on-axis

glow discharge (GD). Both were placed approximately 10 mm from the mCIT. A schematic

of the off-axis, EI source and its pertinent operating voltages is shown in Figure 2.2a. A

tungsten filament (ES-020, Kimball Physics, Inc) was used to generate ions via EI internal to

the chassis volume. Thermionic emission was powered with a continuous, current controlled

voltage, 1.9 to 2.1 A with a bias voltage, -20 to -70 V applied to control electron kinetic

energy. In addition to the filament, the external ion source has three controlling voltages:

the repeller, chassis, and gate. The repeller plate, situated opposite the gate, collected excess

electrons and provided a field to direct ions towards the gate. Ion flux to the mCIT was

controlled by the gate electrode. Nominally, the gate voltage equaled the chassis voltage and

was pulsed below the chassis to illuminate the mCIT. The gate voltages defined the field

between the source and ion trap and were used to control the ion kinetic energy. Typical

values for the repeller and chassis were +110 and +90 V and the gate was pulsed 40 V below the chassis, giving the ions 50 eV (ignoring collisional cooling).

The second source employed was a glow discharge. This source has been used extensively for HPMS operations.[11, 26, 28] It consists of two, 1.5 cm radius plates (either steel or brass) with a small aperture between 0.1 to 0.5 mm in radius at the center of each plate. They are placed on either end of a 1 cm long hollow, cylindrical Teflon spacer. The glow discharge is capable of either positive (GDi) or negative (GDe) mode.[26] The glow was struck by applying a 500 to 750 V pulse across the plates, where the pulse length determines the ion accumulation time. Positive mode applied a positive float to the entire source, while a negative float was applied for negative mode. Both GDi and GDe were studied using the ion trap as a faraday plate. In this configuration, the ring electrode acted as the collector while the endcap was used to shield the current preamplifier (SR570, Stanford Research) from capacitive coupling. It was also biased to perform gating studies to determine ion kinetic energy. The electric field between the GD and mCIT was controlled by the float voltage and dominated ion and electron kinetic energy. The float voltage ranged from -250 to +250 V relative to the mCIT (ground). Assuming singly-charged ions and electrons, the kinetic energy is directly proportional to the bias voltage, thus +100 V_{bias} yields ion energies of 100 eV and -100 V_{bias} corresponds to 100 eV electrons.

Ion detection was performed using an electron multiplier (Model 2300, Detech) pulsed to -1600 V during the RF ramp. A current preamplifier voltage converted and amplified the EMT current output. Hardware control and data collection were performed with a custom LabVIEW program interfaced with analog/digital I/O cards (PXIe-6356 and PXI-6733, National Instruments). Data acquisition was performed at 500 kHz. After acquisition, the

data was low pass filtered at 30 kHz to remove high frequency noise. Mass to charge conversions used two-point calibration based upon NIST standards.[29] Baseline corrected signal integration and signal-to-noise calculations were performed with a custom LabVIEW program.

2.3 Results and Discussion

Pressure, buffer gas composition, and ion kinetic energy all play roles in the efficacy of external ion injection. However, these parameters also impact the operation of the ion source. As such, a single ion source is unable to cover the range from low to high pressure (≈ 0.01 to 1 Torr) in helium, nitrogen, and air. The off-axis, EI source is based upon thermionic emission and can operate in helium across the entire pressure range but it suffers reduced lifetime above 100 mTorr in nitrogen and is incompatible with air. As such, proof-of-concept and low pressure studies utilized the off-axis source. The on-axis GD source used a fixed geometry that was optimized for 1 Torr air operation and therefore unsuitable for helium-based operation using reasonable voltages.[30] Thus, GD operation was limited to 0.25 to 1.0 Torr in nitrogen and air. High pressure studies in these buffer gases utilized on-axis GD.

Ion injection into an aperture-based mCIT was undertaken with both helium and nitrogen buffer gases. The drive RF was 7.24 MHz held at 190 V_{0-p} during ion accumulation and ramped to 350 V_{0-p} for the mass instability scan. Resonant ejection was utilized with axial RF at 2.46 MHz at 3.0 V (helium) and 7.4 V (nitrogen). The off-axis EI source was pulsed for 10 ms during ion accumulation and the chassis, repeller, and gate voltages were adjusted for optimal mass spectral signal strength at each pressure. Representative spectra using the off-axis EI source are shown in Figure 2.3 with both helium and nitrogen buffer gases. The

helium spectrum was recorded at 1030 mTorr using 60 eV ions, while the nitrogen spectrum was recorded at 405 mTorr and 40 eV. Filament lifetime concerns at higher pressures limited the operational pressure for nitrogen. Both spectra display strong signal for the molecular ion at 120 m/z, with SNR of 455 and 1100 in helium and nitrogen, respectively. The nitrogen spectrum is unable to detect fragments smaller than 91 m/z and peak broadening is observed. Both of these effects were also observed using internal EI across a constant drive RF frequency when increasing the buffer gas mass.[26] While the differences in pressure make direct comparisons difficult, these spectra demonstrate that external ion injection at least functions under HPMS pressures.

In order to better compare the buffer gas mass effects, the gases were studied at low pressure. Mesitylene mass spectra were recorded as a function of pressure using the same ion trap and ion source parameters as described for Figure 2.3. Figure 2.4 shows the integrated mass spectral intensity vs. buffer gas pressure in both helium and nitrogen. The pressure range was 1 to 500 mTorr; the high end was limited in order to suppress pressure-dependent ion source variations from the results. Both helium and nitrogen show a linear increase in signal intensity with pressure. Mass spectra are only observed above 200 mTorr in helium, while external ion injection yielded mass spectra starting at 20 mTorr in nitrogen. For each point, the mass spectra were optimized and the kinetic energy for helium at the cutoff was 20 eV vs. 15 eV in nitrogen. There is a 10-fold difference in the lowest pressure observable for external ion injection between helium and nitrogen buffer gases. This is likely a result of helium and nitrogen's mass relative to mesitylene, which are 4, 28, and 120 amu, respectively. Nitrogen can remove more kinetic energy per ion-neutral interaction than helium. Thus, at pressures below 200 mTorr, nitrogen is able to trap externally injected ions

whereas in helium there is insufficient collisional cooling and the ions pass directly through the ion trap. Only when the pressure has been increased by 10-fold does a mesitylene ion interact with enough helium neutrals for successful trapping. Assuming mesitylene ion generation via EI is constant in helium and nitrogen buffer gases, the absolute signal intensity as well as the relative rate of increase of signal observed in Figure 2.4 support the conclusions regarding buffer gas mass. The nitrogen-based signal intensity at 100 mTorr exceeds helium's at 500 mTorr by a factor of 3. Unfortunately, nitrogen's external ion injection efficacy comes at the cost of resolution (relative to helium). However, as seen in Figure 2.3, despite the loss in resolution the overall increase in signal intensity leads to improved SNR in nitrogen versus helium under identical trapping conditions. Since nitrogen and ambient air operate interchangeably from an HPMS standpoint;[11, 26] this increase in SNR is an advantage for a handheld, portable system that would utilize air as the buffer gas.

Having used the off-axis EI source to validate external ion injection with the mCIT, several studies were performed using air buffer gas since it is the preferred buffer gas for HPMS operation due to SWaP concerns. For these studies, an on-axis GD source was used in place of the off-axis thermionic source as the thermionic source is not oxygen tolerant. GD is capable of operating as both an electron (GDe) and ion (GDi) source.[30] Pulsed GDe is a simple, strong-intensity, long-lifetime electron source for EI and has been relied upon heavily for HPMS studies.[26] Reversing the source's bias voltage from negative to positive polarity changes it from GDe to GDi. The bias controls the electric field between the source and ion trap; gating experiments (data not shown) determined that the ion and electron kinetic energy is directly proportional to the electric field strength. A faraday plate study was performed with the GD source in both positive and negative modes at 1015 mTorr of air.

The current density as a function of particle kinetic energy (read bias voltage) is plotted in

Figure 2.5. Negative mode (GDe) operation shows a linear, 16-fold increase in current

density (more negative signal) to -1.0 μA/cm^2 from 10 to 125 eV. Beyond 120 eV, the signal

rate changes to an exponential with a final current density approaching -10 μA/cm^2. This is

likely due to the production of secondary electrons via EI interactions between the source and

faraday plate, which is a consequence of operating an electron beam at high buffer gas

pressures. The mean free path for electrons at 1 Torr in nitrogen (surrogate for air) is

approximately 10 mm. There is a non-zero chance of an EI event between the source and

detector. Upon occurrence, any ions generated will be pulled into the negatively biased GD

front plate while secondary electrons will be accelerated towards the detector. The

exponential rise in signal is a sign that electrical discharge is approaching (which was

observed above 250 eV).[31] The current density in positive mode (GDi) has the opposite

polarity and behavior. It ramps quickly at lower energies; increasing by over 4-fold to

4.7 μA/cm^2 from 5 to 50 eV before leveling off at 5.6 μA/cm^2. This indicates the current

density is limited by scattering between the source and detector. Similar to GDe mode, the

ion beam interacts with the buffer gas between the source and detector. Below 50 eV, ions

have insufficient energy and can be scattered/lost without being collected – likely in the

small (250 μm) field free-region between the endcap and ring electrode. Above 50 eV, ion

kinetic energy is sufficient to overcome the interactions between the source and detector and

most ions are collected at the detector with varying degrees of residual kinetic energy. Thus,

the current density will asymptotically approach the maximum ion flux the GDi source is

capable of producing.

The GD source proved to be more reproducible (and simple) to operate across pressure ranges than the off-axis EI source. As such, external ion injection was explored using mesitylene across the GD source's operable pressure range. Mesitylene mass spectra in air buffer gas were recorded as a function of ion energy at 375, 630, and 1015 mTorr. The mCIT RF frequency was 9.24 MHz with resonant ejection at 2.98 MHz. The axial RF for double-resonance ejection has been shown to be pressure dependent.[2, 32] Axial RF amplitude was adjusted to maximize resolution at each pressure with voltages of 3.75, 6.25, and 10.00 V_{pp}, respectively going from low to high pressure. The mass spectra with maximum signal intensity at each pressure, corresponding to 30, 35, and 70 eV, respectively, are plotted in Figure 2.6a. Typical HPMS behavior can be identified by a couple of observations about the mass spectra. The peak width increases as pressure increases due to the increased collisional frequency.[1, 33] Second, the mCIT's low mass cutoff decreases with pressure,[11] which is seen by the appearance of a fragment peak at approximately 78 m/z at 375 mTorr.

The integrated mass spectral signal intensity as a function of kinetic energy for each pressure is shown in Figure 2.6b. The plot is normalized to focus on the interaction of pressure and energy with external ion injection. At low energy, all three pressures show a steady increase from low signal intensity upwards to a maximum. This feature can be attributed to the ramp of the GDi output as a function of energy, seen in Figure 2.5. The rate of increase during the GDi ramp at 1015 mTorr is slower than the lower pressures, which is attributed to the reduced mean free path. The maximum signal intensity for each pressure represents the balance between ion kinetic energy and the mCIT's potential well depth; the ions have enough energy to overcome scattering between the source and ion trap, but not so much energy that the collisional cooling – the frictional forces on the sidewalls of the

potential well – cannot reduce the energy for a successful trapping event. As energy increases beyond the maximum, ions start to skip through the ion trap and external trapping efficacy decreases. The rate of decay is also pressure dependent. At 150 eV, the signal intensity at 375 mTorr is just 10.8% of the maximum while at 675 mTorr only 30.1% of its maximum signal is retained. The signal at 1015 mTorr maintains 71.8% of its maximum signal. This shows that external ion injection is actually more efficient as pressure increases. This ion injection behavior is consistent with observations made regarding the discontinuous atmospheric inlet (DAPI) on the Mini-series of miniature MS instruments from Purdue.[34] However, by performing the mass analysis at high pressure, HPMS with the mCIT avoids the loss in sampling rate that DAPI imposes on the Mini system.

Having demonstrated ion injection into the mCIT under optimal HPMS conditions, 1 Torr in air buffer gas, it is informative to compare with the more traditional HPMS ion source, GDe. Mesitylene mass spectra were recorded at 1015 mTorr of air buffer gas using both GDi and GDe ionization as a function of kinetic energy (bias voltage). The mCIT was operated at 8.13 MHz using boundary ejection (grounded endcaps). Ion accumulation was held at 5 ms for both GDi and GDe. The mass spectra plotted in Figure 2.7a show the strongest signal intensity for each mode of operation: for GDi, the ion kinetic energy is 150 eV, while GDe peaks at 175 eV. The mass spectra themselves are nearly identical in terms of fragmentation pattern, except the integrated signal for external ion injection is 69% that of internal GDe. Examining the integrated mass spectra vs. kinetic energy plotted in Figure 2.7b, GDi shows a similar pattern as seen at 1015 mTorr in Figure 2.6b. From 5 to 110 eV, mass spectral intensity increases (roughly) linearly before rolling off and peaking at 150 eV, after which signal decays because collisional cooling is no longer sufficient for the

highest energy ions. The rate of decay is slow though as by 250 eV, the signal is still 76.6%

of the maximum. GDe on the other hand demonstrates a rapid rise in signal intensity from

10 to 50 eV before it plateaus, eventually showing maximum signal at 175 eV. The reason

for the strong increase is the EI mechanism; EI requires sufficient energy transfer between

the ion and neutral to ensure ionization.[35] At low kinetic energy, electrons survive the transit

between source and detector (as seen in Figure 2.5) but with insufficient kinetic energy for

EI. As the GDe bias is increased, the population of electrons arriving at the trap with

sufficient energy increases and the trap approaches saturation above 60 eV. While the peak

signal intensity of GDi is 31% lower than GDe, both modes operate on the same order of

magnitude under these controlled conditions. In a practical application, the ionization time

of GDi could easily be increased to compensate for the difference in signal intensity. The

cost is a slight loss in sampling rate (less than 1 Hz), which is reasonable for the added utility

ambient ionization brings to HPMS.

In addition to pressure and buffer gas effects, it is important to understand how ion trap

operation affects trapping efficacy. Studies documented in Chapter 1 showed dynamic ion

trapping is a relatively involved process; operation is dependent upon RF frequency, RF

amplitude, ion trap critical dimensions, as well as the analyte mass to charge ratio (among

many parameters). Thus, studying external ion injection with respect to voltage and

frequency is a difficult endeavor. However, this does not prevent a general analysis of trap

operation in order to place guidelines for implementing external ion injection. External ion

trapping was shown to yield improved signal intensity with increased pressure (Figure 2.6).

It is believed that signal improved because of the collisional frequency: increased ion-neutral

interactions results in a greater degree of collisional cooling leading to more ions falling into

the trap's potential well. Adjusting the voltage and frequency of the drive RF alters the potential well depth of the ion trap. While the q_z and well depth of the mCIT cannot be absolutely calculated, it should still follow the same general trends of QIT theory. Mainly, at the same frequency, the well depth should increase with voltage.

Mesitylene mass spectra were recorded using on-axis GD in air buffer gas with a total pressure of 1020 mTorr. The mCIT was operated at 7.46 MHz using boundary ejection conditions with two different RF amplitude ramps. Two voltage ramps were chosen to highlight a 'low' and 'high' potential well depth (280-610 V_{0-p} and 340 to 660 V_{0-p}). Internal ion generation, GDe at 250 eV, was used to saturate the ion trap in order to highlight the effects of altering the low and high ramps on mass spectral quality. The mass spectra plotted in Figure 2.8a represent the best-case scenario for mCIT operation under these conditions. It is apparent that increasing the operating voltage positively impacts the signal intensity. If the mass spectra are integrated (20.5 and 70.0 au, respectively), the high voltage ramp has 3.6-times more ions than the low voltage ramp; all as a result of a 20% increase in RF amplitude on the potential well depth of the mCIT.

To understand the RF amplitude effects on external ion injection, the ion source was switched to GDi and mesitylene mass spectra were recorded vs. kinetic energy. These spectra for the high and low ramps were integrated and plotted in Figure 2.8b. Compared with the internal ionization, a similar difference in signal intensities is observed between the two RF ramp amplitudes; the ratio of the maximum recorded signal in high and low voltage ramps is 3.9, which is within 10% of that observed in saturated, internal mode. The key difference between the RF amplitudes is observed at higher ion kinetic energies. The high voltage ramp shows a linear increase through 250 eV, while the low voltage rolls off; ions

with 250 eV are trapped at the high RF amplitude, while at lower voltages they are not. This suggests that the mCIT well depth has been increased because there is no change in the collisional frequency or energy of these ions between the two RF amplitudes. At no point did signal intensity prove insufficient to produce high pressure mass spectra, but the RF amplitude study does indicate that external ionization should be re-optimized for signal intensity when the RF amplitude is changed.

The final trapping parameter studied was RF frequency. The frequency is an important parameter for HPMS because the more often the electric field interacts with the ion, the less likely it is to be affected by ion-neutral scattering. Unfortunately, increased frequency comes at two costs: RF amplitude and power both scale to the 2nd power with respect to frequency. The increased voltage leads to deeper potential well depth at the same q_z-value, but it also brings the possibility of electrical arcing (especially as pressure approaches and exceeds 1 Torr). Practically, the RF amplitude is limited to 0.8 kV$_{0-p}$ by HPMS conditions. The high power draw is also not attractive for portable applications. In order to keep the RF amplitude in check, 1.0 mm diameter mCIT frequency is typically held between 6 and 10 MHz.

The same experimental setup used to study RF amplitude (Figure 2.8) was used for testing frequency effects. In order to compare mass spectra across frequencies, the q_z-values should be as similar as possible. This was achieved by aligning the m/z ejection times at the two frequencies. Mesitylene mass spectra vs. kinetic energy were recorded at 8.89 MHz using boundary ejection in air buffer gas at 1020 mTorr total pressure. The RF ramp at 8.89 MHz was 440 to 770 V$_{0-p}$, which overlaps temporally with the low-voltage mass spectra recorded at 7.46 MHz (Figure 2.8b). The integrated mass spectra for each frequency are plotted in Figure 2.9a. The 8.89 MHz data increases linearly with ion kinetic energy. This

mimics the trend observed for the high RF amplitude data shown in Figure 2.8b. And indeed, it is due to the same reason, the potential well depth. While q_z was tuned to be as similar as possible between the two frequencies, the well depth is proportional to the RF amplitude, which is about 37% larger at 8.89 MHz.

With this in mind, the low and high RF voltage test was repeated at 8.89 MHz. The RF ramps were 410 to 740 and 470 to 800 V_{0-p}, respectively. Again, internal EI was used to saturate the ion trap in order to detect mCIT differences across the ramp, and the integrated mass spectral signal intensity ratio of high RF voltage to low was 1.4 (data not shown). Recall, this ratio for 7.46 MHz was 3.6. The decrease in this ratio at 8.89 MHz is because the mass spectra generated at low RF amplitudes lose less signal intensity relative to the high RF amplitude spectra. This is attributable to the increased well depth at 8.89 MHz; suggesting the mCIT should display improved ion injection characteristics as well. The integrated mass spectra vs. ion kinetic energy are plotted in Figure 2.9b. The integrated intensities of both high and low RF amplitude increases across the entire kinetic energy range, and only at 250 eV does the low-voltage ramp show signs of a plateau. Given that 250 eV requires GD bias voltages that verge on electrical discharge at 1 Torr, 8.89 MHz represents a minimum RF drive frequency to ensure a predictable response across RF amplitudes. While this is a single study for a small m/z range, it highlights the importance of ion trap operation, particularly well depth, on the efficacy of external ion injection and the same reasoning presumably extends to the larger m/z values available by ambient ionization techniques.

2.4 Conclusions

External ion injection was studied using mCITs under HPMS conditions and found to be dependent upon the ion kinetic energy, buffer gas composition, buffer gas pressure, and ion

trap potential well depth. Collisional cooling, the friction on the sidewalls of the ion trap's potential well, is key to ion injection. Cooling is increased by raising the buffer gas pressure and/or using a heavier buffer gas. Pressure increases the ion-neutral interaction rate while buffer gas composition alters the energy change per collisions. Buffer gas composition had a significant impact on overall signal amplitude, showing superior amplitude in nitrogen and air vs. helium at the cost of resolution. Moreover, ion kinetic energy had a less significant impact on overall signal intensity as pressure increased towards 1 Torr. This final observation is a welcome result from an HPMS perspective. Much of the development of HPMS has been devoted to overcoming some of the tradeoffs necessary in order to operate at 1 Torr with loss in resolution a primary one. It is nice to have a property of ITMS (ion injection) that scales positively with the high pressure operation required for portable, HPMS. Additionally it was shown that higher RF frequencies (and their corresponding amplitudes) are preferable for ion injection. This ensures a predictable signal across the range of kinetic energies due to the differing m/z values of ions in a given scan range.

Finally, studies using on-axis, glow discharge showed ion injection can operate with similar signal intensity as internal EI. This is an important observation because it opens up the possibility of coupling HPMS with ambient ionization. Prior to the implementation of the off-axis EI source, HPMS was limited to internal ionization via EI. This limited the range of analytes detectable with HPMS to easily volatilized chemicals. Ambient ionization offers multiple ionization routes for larger molecules with efforts already proving successful in coupling nano-electrospray ionization with HPMS.[36]

2.5 Figures

a) HPMS Schematic

Ion Source

External Ion Source

Mass Analyzer

mCIT

≈1000 mTorr

b) Trap-side Chamber

Detector

EMT

< 50 mTorr

c) Detector-side Chamber
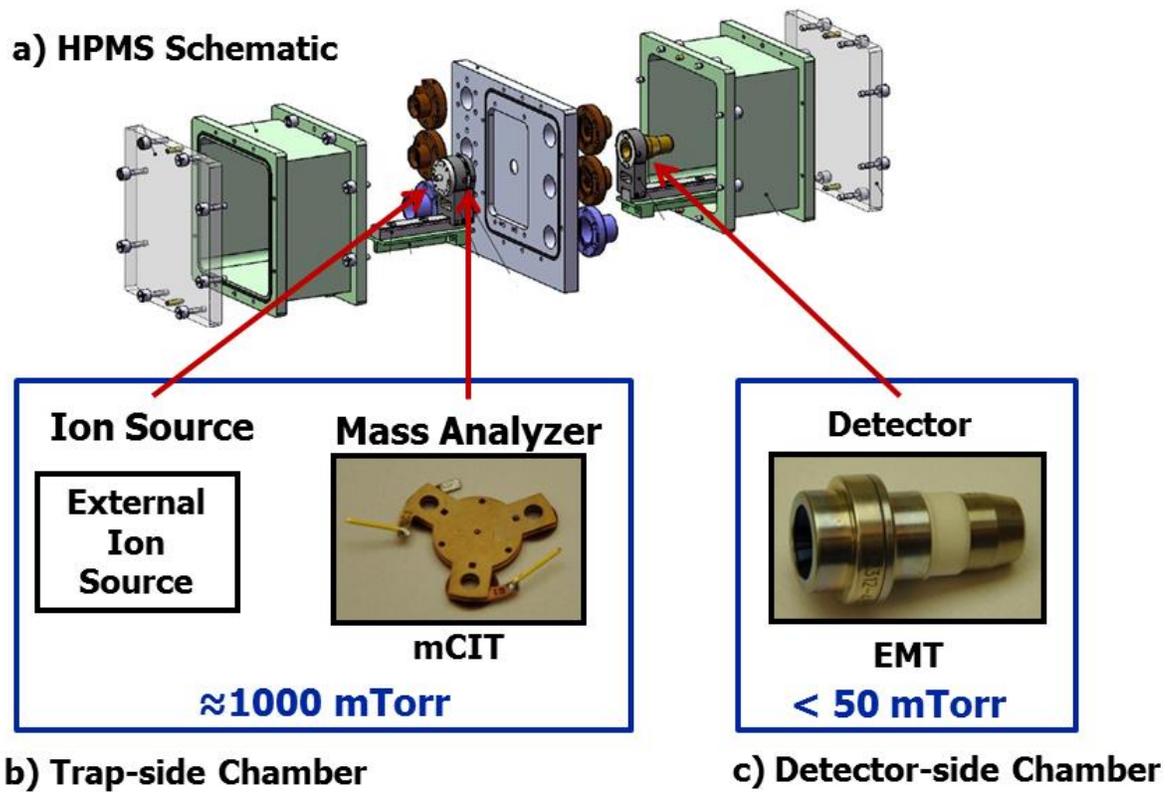
Figure 2.1: a) An exploded rendering of the differentially pumped mass spectrometer (HPMS). This setup decouples ion source/mass analyzer development from ion detection. b) A schematic of the high pressure, trap-side of the HPMS. A standard (r_o = 500 μm and z_o = 645 μm) mCIT is shown. c) Schematic of the detector-side of the HPMS. EMT detectors are used for their superior bandwidth and signal amplification relative to a faraday cup-based detector.

a) Off-axis EI Source

Gate Bias Pulse
$V_{gate} < V_{chassis}$

Repeller Bias
$V_{rep} > V_{chassis}$

CIT

e⁻

$V_{chassis}$

Filament

b) On-axis Glow Discharge

$\Delta V \approx 500\ V$

$V_{bias} > 0\ V$

or

CIT

$V_{bias} < 0\ V$
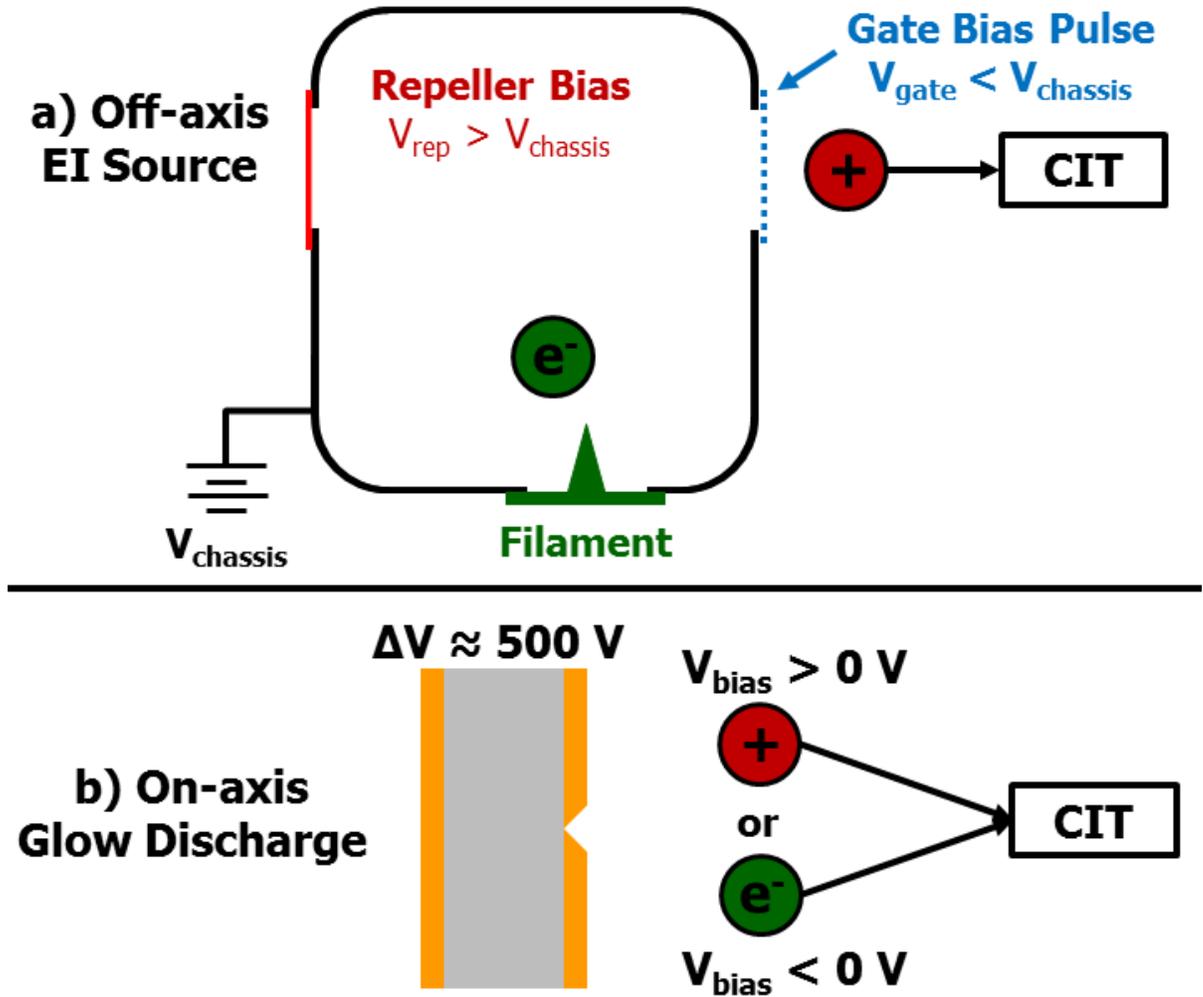
Figure 2.2: a) Schematic of the off-axis EI source. Ions are generated internal to the chassis via EI and gated to the CIT by a pulse at the gate mesh. b) Schematic of the on-axis GD source. The polarity of the source is controlled by the bias which is used to float the entire source relative to the CIT.
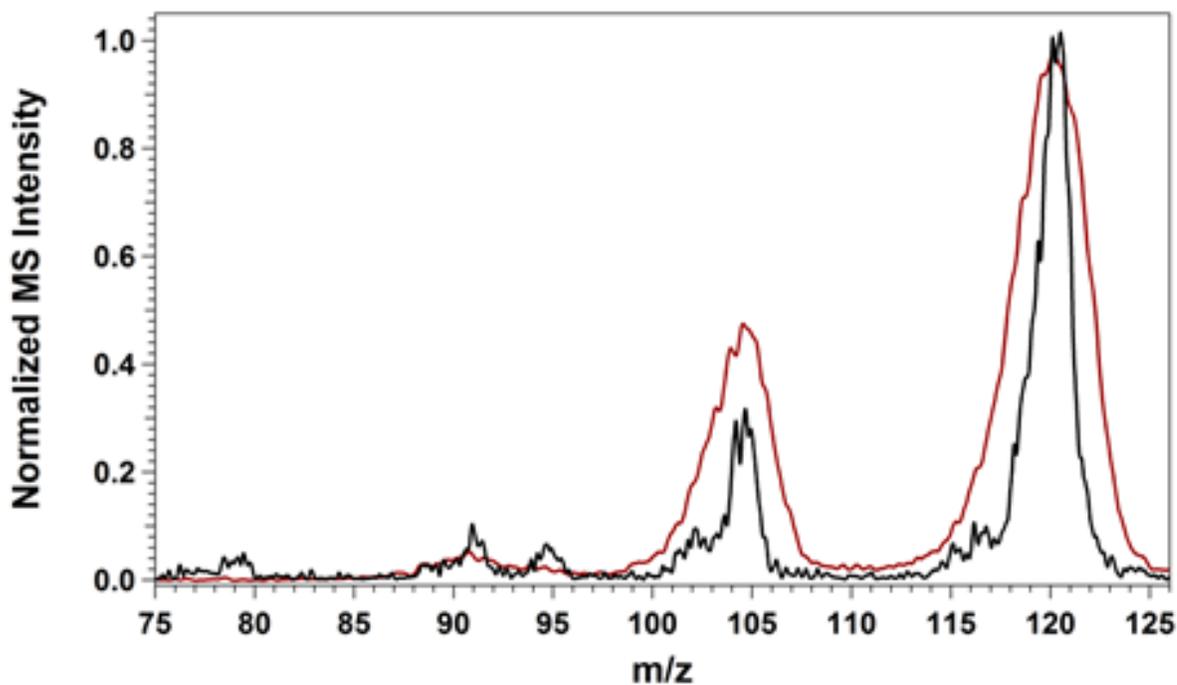
Figure 2.3: Normalized mass spectra of mesitylene generated using the off-axis EI source.
a) Helium buffer gas at 1030 mTorr (—) and nitrogen buffer gas at 405 mTorr (—).
Nitrogen pressure was limited by the off-axis EI source's pressure instability. The helium
SNR is 455 while nitrogen is 1100 suggesting nitrogen is a better buffer gas for external ion
injection, but with reduced resolution and low mass cutoff.
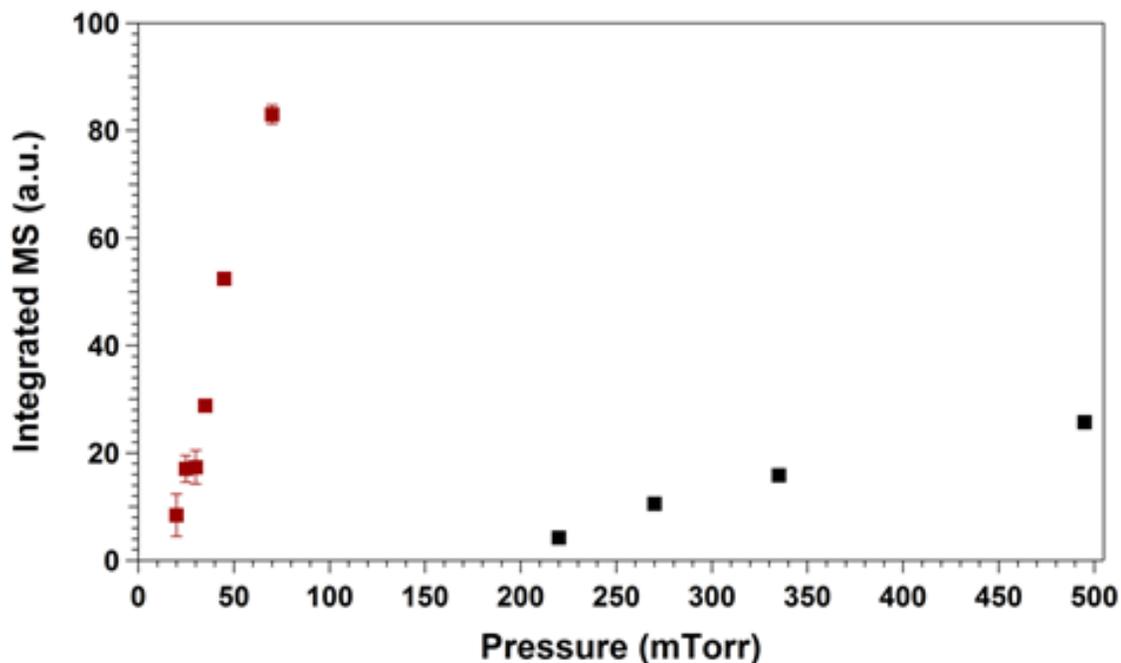
Figure 2.4: Mass spectral pressure series of mesitylene in helium (■) and nitrogen (■) buffer gases recorded using the off-axis EI source, optimized for maximum signal at each pressure. Each buffer gas displayed a different low-pressure cutoff under these trapping conditions; mass spectral intensity was lost below 200 mTorr in helium, while mass spectra were observed down to 20 mTorr in nitrogen. Nitrogen's efficacy as a buffer gas for external ion injection is highlighted by the mass spectral signal intensity relative to helium.
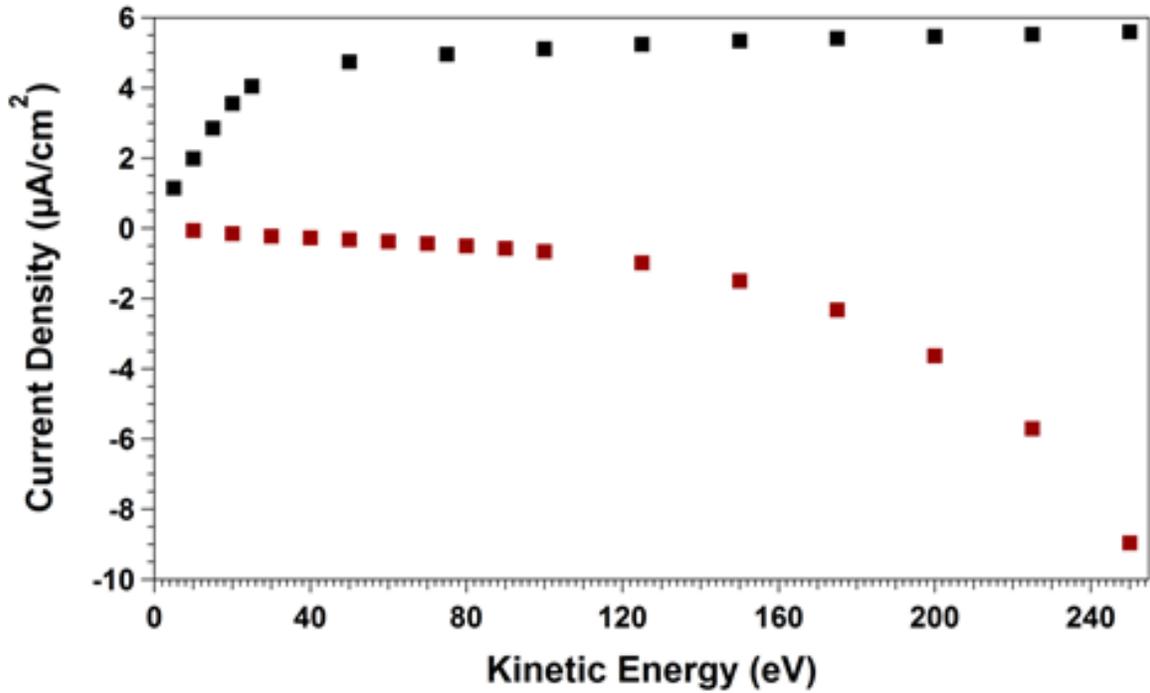
Figure 2.5: Faraday plate measurement of the current density as a function of GD bias in both ion (■) and electron (■) modes at 1015 mTorr in air buffer gas. Ion mode ramps towards a steady intensity as ions overcome scattering between the source and detector. Electron mode current density increases in magnitude linearly from 10 to 120 eV, after which signal begins an exponential increase towards discharge above 250 eV.
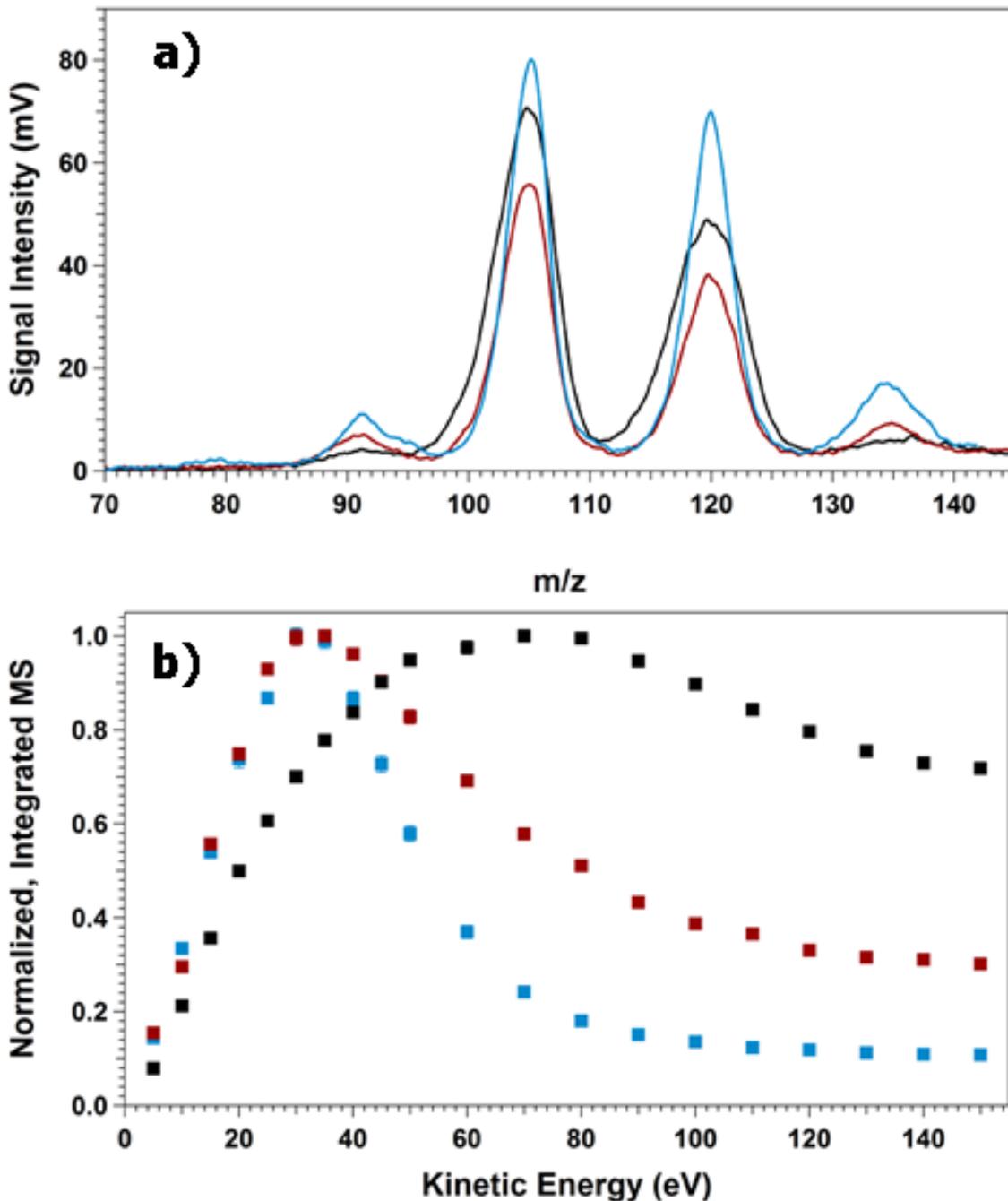
Figure 2.6: a) Plot of the strongest amplitude mesitylene mass recorded during a pressure vs. kinetic energy experiment: 1015 mTorr (■, 70 eV); 630 mTorr (■, 35 eV); and 375 mTorr (■, 30 eV). Despite a 3-fold buffer gas pressure change, all spectra are within 45% of one another. b) Integrated mass spectral signal intensity of mesitylene in air buffer gas at 1015, 630, and 375 mTorr recorded with on-axis GDi. Normalization removes variation due to pressure-dependent GD operation. As pressure increases, externally injected ions of larger kinetic energy can be trapped and the range beyond the maximum signal intensity extends as well.
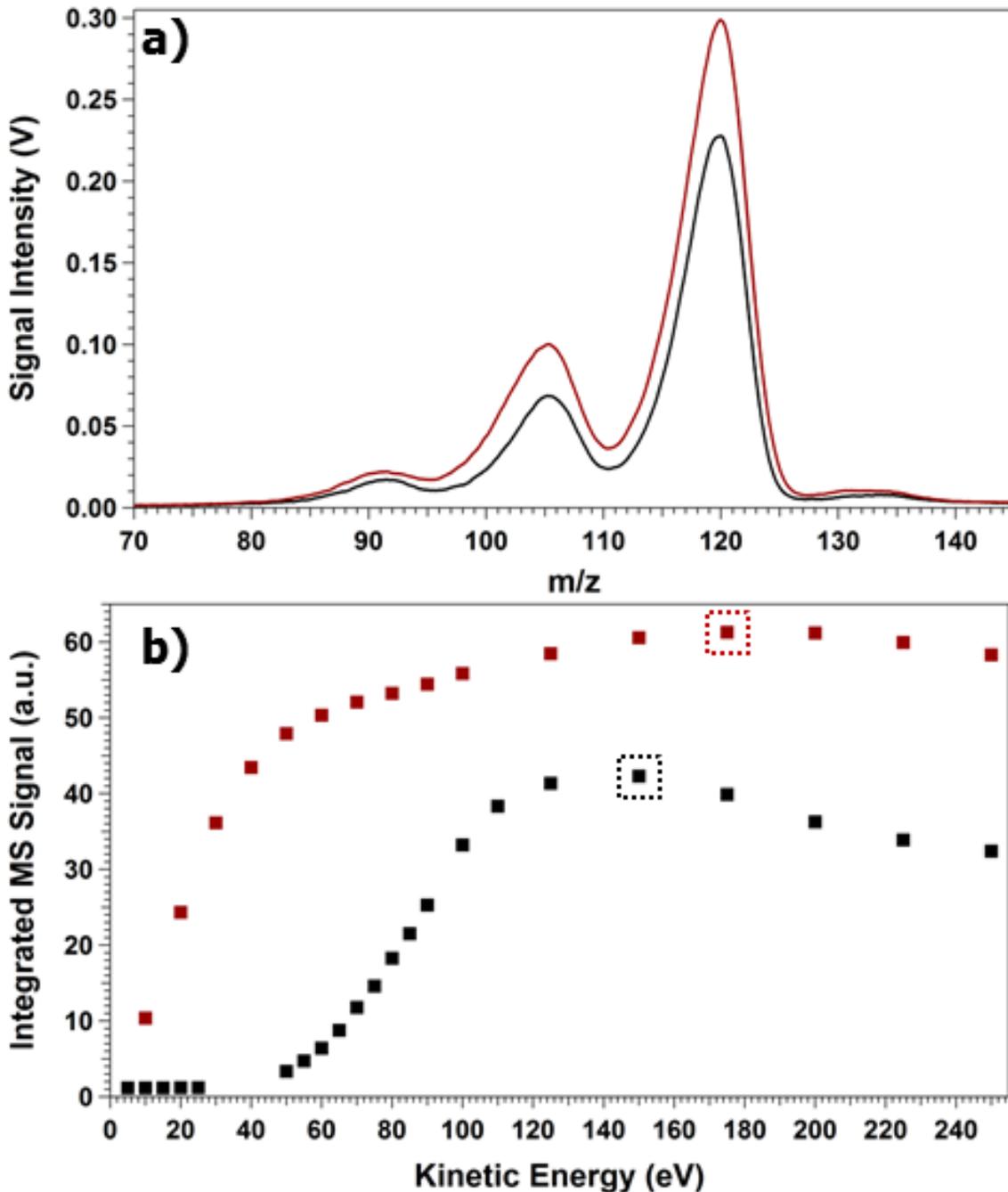
Figure 2.7: a) Comparison of mesitylene mass spectra recorded with GDi (—) vs. GDe (—) under identical HPMS conditions at 1015 mTorr. The GD bias was optimized for maximum signal intensity for each spectrum, which directly corresponds to kinetic energy (assuming singularly charged species). The maximum signal in GDi was observed at 150 eV (+150 V_{bias}) and GDe peaked at 175 eV (-175 V_{bias}). b) Integrated mass spectral data of mesitylene for GDi (■) and GDe (■) across multiple kinetic energies. GDi is limited by the trapping efficiency of external generated ions, peaking near 150 eV, while GDe saturates the ion trap near 70 eV.

76
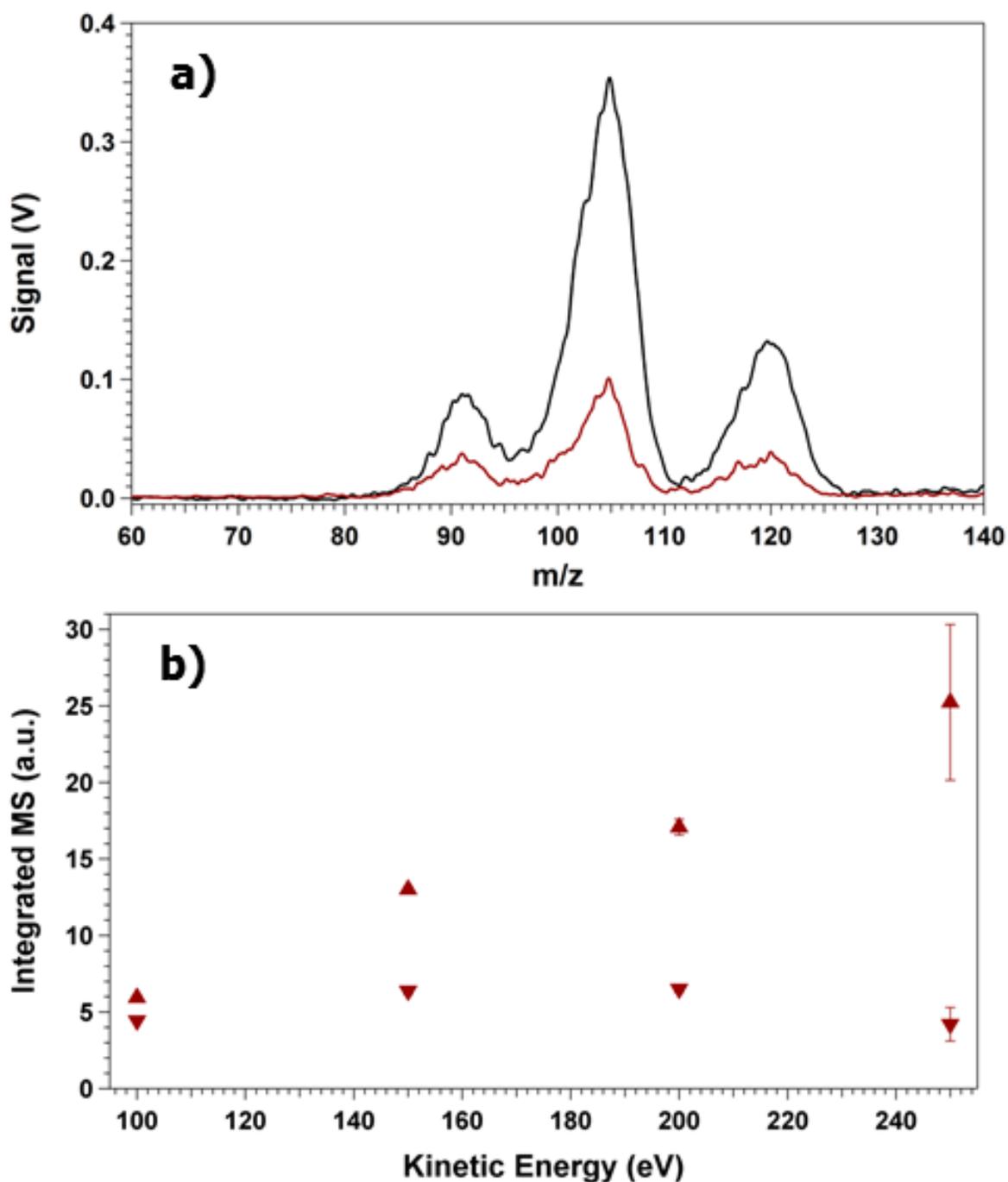
Figure 2.8: Drive RF amplitude effects on ion injection with the mCIT. a) Mesitylene mass spectra recorded via GDe using low voltage RF ramp (━) and high voltage RF ramp (━) at 7.46 MHz. The 3.4 ratio of high:low integrated signal intensity highlights drive RF amplitude effects when the trap is saturated. b) Integrated mass spectra using GDi with high (▲) and low (▼) RF amplitude. The high RF amplitude has a larger potential well and shows a linear increase in signal intensity across kinetic energies; while the decreased potential well depth at low RF amplitude limits the mCIT response above 150 eV.
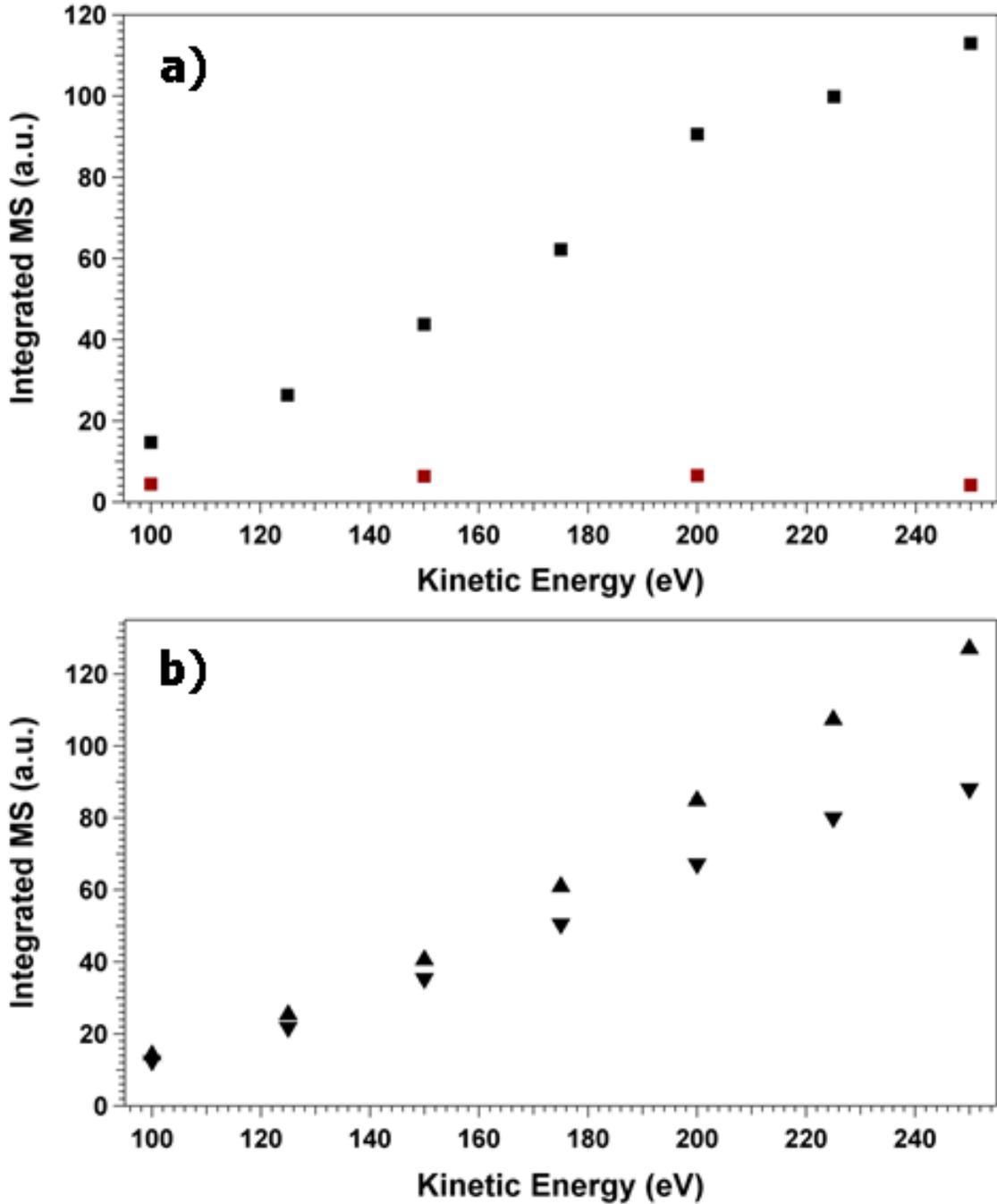
Figure 2.9: Drive RF frequency effects on ion injection with the mCIT. a) Integrated mass spectra recorded at similar q_z-values for two different RF frequencies: 8.89 MHz (■) and 7.46 MHz (■). Signal intensity is increased across the entire ionic kinetic energy range at the higher potential well depth afforded by 8.89MHz. b) Integrated mass spectra recorded at high (▲) and low (▼) RF amplitudes at 8.89 MHz. The linear response across the entire ionic kinetic energy range shows improved ion injection over 7.46 MHz, especially at the lower RF amplitude.

2.6 REFERENCES

1.   Goeringer, D. E., et al., Theory of high-resolution mass spectrometry achieved via resonance ejection in the quadrupole ion trap. *Analytical chemistry* **1992,** *64* (13), 1434-1439.

2.   Wolfe, D. W. High-Pressure Cylindrical Ion Trap Mass Spectrometry. Dissertation, University of North Carolina, Chapel Hill, 2012.

3.   Blakeman, K. H., et al., High-Pressure Mass Spectrometry at Pressures Exceeding 1 Torr in a Microscale Cylindrical Ion Trap. *Manuscript in preparation* **2015**.

4.   Kornienko, O., et al., Micro ion trap mass spectrometry. *Rapid Commun. Mass Spectrom.* **1999,** *13* (1), 50-53.

5.   Moxom, J., et al., Analysis of volatile organic compounds in air with a micro ion trap mass analyzer. *Anal. Chem.* **2003,** *75* (15), 3739-3743.

6.   McLuckey, S. A., et al., Ion Trap Mass Spectrometry of Externally Generated Ions. *Analytical chemistry* **1994,** *66* (13), 689-696.

7.   McLuckey, S. A., et al., Coupling of an Atmospheric-Sampling Ion Source with an Ion-Trap Mass Spectrometer. *Analytica Chimica Acta* **1989,** *225*, 25-35.

8.   Qin, J.; Chait, B. T., Matrix-Assisted Laser Desportion Ion Trap Mass Spectrometry: Efficient Isolation and Effective Fragmentation of Peptide Ions. *Analyltical Chemistry* **1996,** *68*, 2108-2112.

9.   Kornienko, O., et al., Electron impact ionization in a microion trap mass spectrometer. *Rev. Sci. Instrum.* **1999,** *70* (10), 3907-3909.

10.   Kornienko, O., et al., Field-Emission Cold-Cathode EI Source for a Microscale Ion Trap Mass Spectrometer. *Analytical chemistry* **2000,** *72* (3), 559-562.

11.   Blakeman, K. H.; Ramsey, J. M., High Pressure Mass Spectrometry in Nitrogen and Air. *Manuscript in preparation* **2014**.

12.   March, R. E., An Introduction to Quadrupole Ion Trap Mass Spectrometry. *Journal of Mass Spectrometry* **1997,** *32* (4), 351-369.

13.   Louris, J. N., et al., Injection of Ions into a Quadrupole Ion Trap Mass-Spectrometer. *International Journal of Mass Spectrometry and Ion Processes* **1989,** *88* (2-3), 97-111.

14.   Appelhans, A. D.; Dahl, D. A., Measurement of external ion injection and trapping efficiency in the ion trap mass spectrometer and comparison with a predictive model. *International Journal of Mass Spectrometry* **2002,** *216*, 269-284.

15.   Quarmby, S. T.; Yost, R. A., Fundamental studies of ion injection and trapping of electrosprayed ions on a quadrupole ion trap. *International Journal of Mass Spectrometry* **1999,** *190*, 81-102.

16.   Liang, X. R., et al., Alternately pulsed nanoelectrospray ionization/atmospheric pressure chemical ionization for ion/ion reactions in an electrodynamic ion trap. *Analytical chemistry* **2006,** *78* (9), 3208-3212.

17.   Handberg, E. S. Atmospheric sampling glow discharge ionization (ASGDI) using a quarter-sized cylindrical ion trap mass spectrometer (CIT-MS) for explosives detection in air. Purdue University, West Lafayette, IN, 2006.

18.   Van Berkel, G. J., et al., Established and emerging atmospheric pressure surface sampling/ionization techniques for mass spectrometry. *J Mass Spectrom* **2008,** *43* (9), 1161-1180.

19.   Laiko, V. V., et al., Atmospheric pressure MALDI/ion trap mass spectrometry. *Analytical chemistry* **2000,** *72* (21), 5239-5243.

20.   Aebersold, R.; Mann, M., Mass spectrometry-based proteomics. *Nature* **2003,** *422* (6928), 198-207.

21.   Shaffer, S. A., et al., A novel ion funnel for focusing ions at elevated pressure using electrospray ionization mass spectrometry. *Rapid Commun Mass Sp* **1997,** *11* (16), 1813-1817.

22.   Hand, O. W., et al., Depth Profiling of Multilayered Samples and Comparisons of Secondary Ion and Laser Desorption Mass-Spectra in the Same Instrument. *International Journal of Mass Spectrometry and Ion Processes* **1989,** *90* (2), 97-118.

23.   Doroshenko, V. M.; Cotter, R. J., Injection of externally generated ions into an increasing trapping field of a quadrupole ion trap mass spectrometer. *Journal of Mass Spectrometry* **1997,** *32* (6), 602-615.

24.   Doroshenko, V. M.; Cotter, R. J., A New Method of Trapping Ions Produced by Matrix-Assisted Laser-Desorption Ionization in a Quadrupole Ion-Trap. *Rapid Commun Mass Sp* **1993,** *7* (9), 822-827.

25.   Gao, L., et al., Characterization of a discontinuous atmospheric pressure interface. Multiple ion introduction pulses for improved performance. *International Journal of Mass Spectrometry* **2009,** *283* (1-3), 30-34.

26.   Blakeman, K. H. Development of High Pressure Mass Spectrometry for Handheld Instruments. Dissertation, University of North Carolina at Chapel Hill, Chapel Hill, NC, 2015.

27.   Allen, J. S., The detection of single positive ions, electrons and photons by a secondary electron multiplier. *Physical review* **1939,** *55* (10), 0966-0971.

28.   Schultze, K. P. Advanced System Components for the Development of a Handheld Ion Trap Mass Spectrometer. Dissertation, University of North Carolina at Chapel Hill, Chapel Hill, NC, 2014.

29.   Stein, S. E., "Mass Spectra". in *NIST Chemistry WebBook, NIST Standard Reference Database Number 69* [Online] Linstrom, P. J.; Mallard, W. G., Eds. National Institute of Standards and Technology, Gaithersbrug, MD, http://webbook.nist.gov, (accessed 10/2/2015).

30.   Fridman, A. A., *Plasma chemistry*. First paperback edition. ed.; Cambridge University Press: Cambridge, 2012; p 978.

31.   Lisovskiy, V. A.; Yakovin, S. D., Experimental study of a low-pressure glow discharge in air in large-diameter discharge tubes: I. Conditions for the normal regime of a glow discharge. *Plasma Phys Rep+* **2000,** *26* (12), 1066-1075.

32.   Arnold, N. S., et al., Extended Theoretical Considerations for Mass Resolution in the Resonance Ejection Mode of Quadrupole Ion-Trap Mass-Spectrometry. *Journal of the American Society for Mass Spectrometry* **1994,** *5* (7), 676-688.

33.   Whitten, W. B., et al., High-pressure ion trap mass spectrometry. *Rapid Commun. Mass Spectrom.* **2004,** *18* (15), 1749-1752.

34.   Gao, L., et al., Breaking the Pumping Speed Barrier in Mass Spectrometry: Discontinuous Atmospheric Pressure Interface. *Anal. Chem.* **2008,** *80* (11), 4026-4032.

35.   Märk, T. D.; Dunn, G. H., *Electron impact ionization*. Springer-Verlag: Wien ; New York, 1985; p 383.

36.   Gilliland, W. M., et al., Coupling Microchip Electrospray Ionization Devices with High Pressure Mass Spectrometry. *Manuscript in preparation* **2015**.

CHAPTER 3: INITIAL MICROIONIZER DEVELOPMENT

3.1 Introduction

Handheld high pressure mass spectrometry (HPMS) requires the major components (ion source, mass analyzer, and detector) to be: small in size, low power, pressure tolerant (upwards of 1 Torr), and oxygen compatible.[1] Mass analyzers and detectors for HPMS described elsewhere[2-4] are components that would be complementary with the microionizer source investigated here. The microionizer was conceived as a field effect device (FED), capable of both field emission and field ionization, and as such, is compatible with the stringent requirements of HPMS.

The intrinsic properties of FEDs align with the first two requirements of HPMS – small size and low power. In terms of size, the active features of silicon FEDs easily scale to micron-dimensions and microfabrication methods are well established.[5-6] They are also capable of low voltage operation[7] which can reduce the size and complexity of the supporting electronics.[8] For power concerns, they are attractive for portable applications because their power consumption is lower than comparable thermionic devices thus extending operational runtime.[9-10] The remaining two requirements, the degree of pressure and oxygen tolerance, is unknown and the idea that they can be pressure and oxygen tolerant is not obvious based on current applications of FEDs. Most research involving field emission and ionization maintains pressures well below 1 Torr, in the 10^{-6} to 10^{-9} Torr range.[11-12] Additionally, many researchers' definition of atmospheric compatibility is whether the device can be exposed to atmosphere and still operate when placed under vacuum again.[13] Despite this, there have

been strides in producing high pressure tolerant FEDs.[14-15] It has been shown that pressure

tolerance can be designed into the device if the length scale over which the electric field is

generated is reduced below the mean free path of the intended operating pressure (roughly

100 μm at 1.0 Torr). With this design feature, Paschen breakdown can be avoided while still

generating high electric fields.[16] In terms of oxygen tolerance, there has been some limited

success operating carbon nanotube-based field emission sources in a low-pressure, oxygen

containing environment.[17] There are also reports of field effect transistors (FET) that boost

switching frequency through ballistic transport of electrons through conduction channels at

virtual vacuum.[7] The critical dimensions are below 50 nm, the mean free path of electrons at

atmospheric pressure, such that the FETs can operate at atmospheric pressure.[18] Combining

the small size and low power operation with pressure and oxygen tolerance were primary

motivators for the microionizer's design.

Conceptually, the microionizer is similar to a parallel plate capacitor – two electrodes

separated by a thin insulating layer. However, unlike a capacitor, the microionizer is

perforated to expose as much of the interfacial layer as possible. If the insulating layer is

made thin enough (< 1 μm), then a modest voltage (on the order of 10 to 100 V) can be

applied between the electrodes to generate electric fields on the order of 1 MV/cm. For the

first generation microionizer, the device layer was 2 μm and the insulating layer was 0.5 μm.

These values were chosen because of the mean free path at the intended operating pressure of

1 Torr. Hard sphere calculations yield mean free paths on the order of 10 mm for electrons

and 100 μm for ions. Electrical breakdown in micron-sized gaps can be enhanced by field

emitted electrons.[19] By reducing the thickness of the layers, ion generation due to EI in the

vicinity of the emission site can be minimized which should suppress electrical discharge via

plasma formation.[20] Silicon-on-insulator substrates (SOI) with their micron to submicron

insulating layer between silicon layers were chosen to implement this design. Bonded SOI

was chosen over buried oxide (such as SIMOX) wafers for superior insulating layer

uniformity and quality.[21] A typical wafer has a single, thin (< 200 μm) Si device layer

separated from a thick Si handle wafer (> 400 μm) by a thin insulating layer (< 2 μm).

Moreover, the choice of SOI as a substrate opens up all standard microfabrication techniques

for development of the microionizer.

Utilizing an SOI wafer, a first generation microionizer was designed at the University of

Arizona (UA). The die was 1 cm^2, and contained a 4x4 array of through-etched features (or

vias) with either 5, 20, or 100 μm radius circular features as well as one design that used 5 x

90 μm^2 rectangular trenches. A representative die with 20 μm features is shown in Figure

3.1a. The SOI substrate had 2 μm of n-type (Sb) silicon (0.01 to 0.02 1 Ω-cm); 500 nm of

silicon oxide insulator and 400 μm of n-type (Sb) silicon (0.01 to 0.02 Ω-cm) handle. The

highlight in Figure 3.1a shows one of the 20 μm circular via subarrays and the subsequent

SEM images show one subarray (Figure 3.1b) plus magnification of an individually etched

via (Figure 3.1c). Also shown in Figure 3.1d is a cross sectional SEM of a trench device,

where the three SOI layers are identified.

The operating conditions of the SOI-based microionizer depend on the desired ionization

mechanism. The field mechanisms are complimentary – field emission (FE) generates ions

inter-trap via electron impact ionization (EI) while field ionization (FI) produces ions

external to the trap via direct electron removal.[22] The onset of FE is expected at field

strengths on the order of 10 MV/cm, and is affected by the work function of the emitting

material. Field ionization can require field strengths upwards of 100 MV/cm for helium

ions.[23] However, the ionization potential of helium is 24.6 eV while for many VOCs and CWAs this value is closer to 9 eV,[24] reducing the needed field strength closer to 50 MV/cm. The microionizer field strength is fundamentally limited by the dielectric breakdown of the insulating layer; for silicon dioxide it is in the range of 5 to 11 MV/cm[25-26] and depends on many factors including device area,[27] oxide thickness,[28] insulator quality,[29] as well as the method of testing.[30] Therefore, to operate as a low-voltage FED, the microionizer needs to rely upon geometric field enhancement to generate ions.[31-32] Typically, a low voltage FED has a carefully crafted emission tip, which is separated by microns from its counter electrode[23, 33] with the geometric field enhancement a function of the radius of curvature of the tip and its height.[11] A modest bias (< 200 V) is applied and the macroscopic field between the tip and counter electrode is enhanced to generate field strengths in excess of 10 MV/cm. Field enhancement in the microionizer differs in that the macroscopic field is maximized requiring only modest geometric enhancement at the emission site. This approach has been shown to work in nanoporous silicon carbide.[34] The microionizer does not use crafted tips, instead it relies upon the surface roughness left behind by the deep reactive ion etch process.[35] Thus, the emission 'tips' are randomly distributed at the interface of the silicon and silicon dioxide layers, which can be seen in Figure 3.1c. With this surface roughness, voltages of 10 to 100 V that generate electric fields of 0.1 to 1.0 MV/cm can be enhanced to the larger field strengths necessary for field emission and ionization.[36]

Design, fabrication, and initial testing of the first generation of microionizers were performed at UA and Oak Ridge National Laboratory (ORNL). This collective effort produced the first generation of microionizers capable of ion generation using the field ionization mode at low pressures. Further integration and testing of the first generation

86

microionizer as an ionization source for HPMS with a focus on lifetime, power draw, size, and pressure tolerance is explored in this chapter.

3.2 Experimental

The first generation microionizer was used as the ion source with the high pressure mass spectrometer described in Chapter 2. Six microionizers fabricated at Arizona State University's Nanofab Laboratory were delivered to UNC for testing. The six devices had the following features: two with 100 μm, two with 20 μm, and one with 5 μm circular features, and one with 5 x 90 μm^2 trench features. A rail mounted holder, similar to that used at ORNL, shown in Figure 3.2a, was used for mounting the microionizer. Electrical contact to the front and backsides were made by pressure mounting the die to printed circuit boards (PCB) (not shown in figure). The devices proved sensitive to mounting force, and spring loading was used to ensure a strong clamp without over-tightening the die.

A schematic of the electrical connections as well as the identifying terminology used regarding the microionizer is shown in Figure 3.2b with the voltages used to operate the microionizer. Ionization was initiated using a pulse voltage, V_p, applied to the ionizer. V_p ranged from $\pm$ 20 to 50 V depending upon microionizer geometry and length of use. V_{bias}, a constant voltage placed on the entire microionizer, controlled the electric field between ionization source and ion trap. Bias strengths of -70 to -150 V were used to control electron energy for optimal mass spectrometry signal strength. Field emission mode operated optimally with a negative V_{bias} constantly applied to both sides of the microionizer and a negative V_p applied for less than 5 ms during ionization.

The voltage pulse was generated with a simple relay circuit. A control signal from the LabVIEW interface triggered an arbitrary waveform generator (AFG3022B, Agilent). The

generator provided a square wave to drive a PVA3354N phototransistor that switched the pulse supply between the microionizer and the bias supply. The power supply current and voltages for both pulse and bias were read directly from the digital readout of the supplies (E3612A, Agilent). Both the voltage pulse and the bias were monitored with 10X probes and a digital oscilloscope (P6139A and TDS 2022B, Tektronix).

The differentially pumped mass spectrometer setup as described in Chapter 2 was used, except the thermionic emitter was replaced with a microionizer. Buffer gases included helium (UHP grade, National Welders) and ambient air. Helium was introduced by a mass flow controller while air was introduced by an atmospheric inlet and metered with a needle valve. Analytes included xenon gas (99.999%, Nova Gas Technologies) and mesitylene (Sigma Aldrich, Milwaukee, WI) and were introduced at 0.01 to 0.1 mTorr (uncalibrated).

Hardware control and data collection were performed with a custom LabVIEW program interfaced with analog/digital I/O cards (PXIe-6356 and PXI-6733, National Instruments). Ion detection was performed with an electron multiplier tube (EMT) (EMT2300, DeTech) pulsed to -1600 V during the RF ramp. EMT signal was amplified and converted at 200 nA/V with a preamplifier (SR570, Stanford Research). Data acquisition was performed at 500 kHz. After acquisition, the data was low pass filtered at 30 kHz to remove high frequency noise. Mass to charge conversions used two-point calibration based upon NIST standard mass spectra.[37] Baseline corrected signal integration and signal-to-noise calculations were performed with a custom LabVIEW program.

3.3 Results and Discussion

As the results from the experiments performed at ORNL with the microionizer helped define this project a brief summary of their results is beneficial. The microionizer was

clamped in a pressure-mounted holder, where the clamping plates provided electrical contact to the device and ion counts were monitored with an EMT. The microionizer was operated in field ionization mode (positive voltages relative to the detector) with a 10% duty cycle using a 10 ms pulse length.[38] The results are presented in Figure 3.3. Ion count vs. microionizer pulse voltage were measured for the analytes triethylamine (Figure 3.3a), diisopropylmethane phosphonate (DIMP) (Figure 3.3b) and toluene Figure 3.3c). Finally, the current draw as a function of voltage is shown in Figure 3.3d. As would be expected, the ion counts for all three analytes increased with microionizer voltage amplitude. The voltages explored correspond to field strengths from 0.4 to 1.4 MV/cm. Triethylamine and DIMP, Figure 3.3a and b, showed pressure independent ionization while toluene, Figure 3.3c did not. Signal from a field ionization source should only depend upon the partial pressure of the analyte, provided the field strength does not ionize background gas.[39] The IE for helium,[24] triethylamine,[40] toluene[41], and DIMP [42] are 24.6, 7.5, 8.5, and < 10.6 eV. The toluene ion counts are thus inconsistent with field ionization. Moreover, the current draw of the device approached 150 mA at 40 V_{pulse}. This current draw was unexpected, because the corresponding power is 6 W, which is equivalent to a thermionic emission source. While these results were not ideal, the microionizer showed signs of what appeared to be field ionization during this initial evaluation. The testing performed at ORNL was the springboard for microionizer work and impacted the trajectory followed at UNC for integrating the microionizer with HPMS.

3.3.1 1st Generation Microionizer as a Field Emission Source

Initial work with the microionizer emulated the ORNL experiments and placed the ionizer directly in line with the EMT. Xenon analyte was leaked into the chamber at

0.01 mTorr with a balance of helium buffer gas to less than 10 mTorr, near traditional ion trap operating pressures.[43] The microionizer was operated in field ionization mode and ion signal was observed for pulses of +25 to +35 V applied to the front side of the device. Having confirmed signal in a field ionization mode similar to that seen at ORNL, HPMS was attempted with a full-size, $r_o = 500$ μm and $z_o = 645$ μm, CIT. The microionizer was able to generate ions, but efforts to trap these ions with the ion trap MS (ITMS) system proved unsuccessful. Trapped ions were never observed.

As a field ionization source, the ions are generated externally and then injected into the ion trap. At traditional ITMS pressure near 1 mTorr, ion injection efficiency is low ($\approx 5\%$) and is dependent upon the ion kinetic energy; buffer gas pressure; and the ion trap potential well depth.[44] Ion kinetic energy is particularly important because of the reduced potential well depth of the miniature CIT.[2] A simple DC gating experiment was performed with the microionizer in order to determine the kinetic energy distribution of the generated ions, where a gate lens was placed between the microionizer and the EMT. Xenon was leaked into the chamber at 0.1 mTorr. A positive 25.5 V_p was applied to the gate-side of a 20 μm microionizer and the gate potential varied from 0 to +125 V. The pulse was 2.5 ms long at a 6% duty cycle. Interestingly, no signal was observed between 0 and +27 V. Starting at +27 V, a few ions reach the detector and as the gate voltage is increased, signal continued to rise until it saturated near +125 V_{gate}. This trend is opposite of what is expected for a field ionization source since the field between the source and gate lens is tilted in favor of negative charge transport. A negative ion current was ruled out because of xenon and helium electron affinity values (-1894 and -5 kJ/mol, respectively)[24] and the electric field polarity. The most plausible explanation is that the microionizer was instead acting as a field emission source.

The emitted electrons were accelerated towards the gate lens and underwent EI in the vicinity

of the gate lens, with the resulting positively charged ions detected by the EMT. In terms of

power consumption, the signal was being produced with an average of 4.5 mA measured

between the microionizer conductive layers. Extrapolated for duty cycle, this represents a

peak current and power of 75 mA and 1.9 W which is on the same order of magnitude as a

thermionic source.[45] While the power draw was not much improved compared to the results

obtained at ORNL, the conditions for ion generation and thus potential HPMS were

identified.

3.3.2 Mass Spectrometry in Helium Buffer Gas

Once the conditions for consistent electron-mode operation were determined; the

microionizer was integrated into an HPMS instrument as a drop-in replacement for the

thermionic emission source. The mass spectra shown in Figure 3.4 are of xenon in helium

buffer gas at 4.9 and 960 mTorr. Both were taken with a 20 μm microionizer in electron

mode using a -34.0 V_{pulse} of 1.0 ms at a 1.2% duty cycle and -75 V_{bias}. This operating mode

resulted in the peak power approaching 17 W but averaging approximately 180 mW. In the

low pressure spectrum, six of xenon's seven isotopic peaks are easily identified with 250

scan averaging. As buffer gas pressure is increased to 960 mTorr, the peaks broadened as

expected for a constant RF frequency, but still retained five isotopic peaks.[2, 46] Signal

intensity decreased at the higher pressure so averaging was increased to 500 scans to

compensate. It is worth noting that this was the very first ca. 1 Torr high pressure mass

spectrum produced at UNC, and was an important step towards developing handheld HPMS.

The pressure for this mass spectrum was two orders of magnitude higher than previously

reported for ITMS[47] and three orders of magnitude above other field emission-based mass

spectrometers.[12, 23, 48] The diamond-coated silicon whiskers used by Kornienko *et al*. are the closest in operating pressure at 1 mTorr, however these devices require upwards of 700 V to operate.[14]

3.3.3 Mass Spectrometry in Air Buffer Gas

The mass spectra recorded in helium buffer gas proved the microionizer is pressure tolerant in an inert environment. However, air is the preferred buffer gas for HPMS operation because it eliminates the need for an external tank of buffer gas. Air buffer gas would help reduce the size, weight, and complexity of a handheld instrument. Using a 5 μm microionizer and ambient air as the buffer gas, a mesitylene mass spectrum was generated and shown in Figure 3.5. In this case, mesitylene was introduced via a UHV leak valve and room air was leaked into the chamber to 510 mTorr (pressure was limited by the detector). The microionizer was operated in field emission mode with a 0.3% duty cycle. The -40 V pulse was 0.25 ms in length and biased to -140 V. The peak current was limited to 10 mA, yielding peak powers of 0.4 W. These results are significant, because they demonstrate microionizer oxygen tolerance. Oxygen tolerance was attributed to the pressure itself and to the low duty cycle. The mean free path of electrons at 0.5 Torr is on the order of 10 millimeters, while for ions it is on the order of 200 μm. The maximum energy an ion could attain was 180 eV, which is capable of physical sputtering.[49] However, the ions would likely be generated many mean free paths away from the electrode surface and be subject to collisions prior to reaching the microionizer surface. This would reduce the ion kinetic energy and protect the surface from bombardment damage.[50]

3.3.4 1st Generation Microionizer Characterization

With the proven ability to generate ions and thus mass spectra, HPMS was used to study properties of interest, mainly signal intensity as a function of pulse and bias voltages. Fowler-Nordheim tunneling describes electron behavior in high fields and predicts an exponential increase in field emission with field strength.[51] Signal intensity of xenon ions as a function of field strength is shown in Figure 3.6 for a 20 μm microionizer. The data points represent the integrated ramp portion of the mass spectrum in helium buffer gas. The field range, 0.53 to 0.70 MV/cm, corresponds to the onset of observable mass spectral signal and the maximum field strength attempted during these experiments. The voltage pulses ranged from 26.5 to 35.0 V. There is a 60-fold signal increase for the 32% increase in field strength with a relatively linear trend over the range. This is contrary to the exponential trend predicted by Fowler-Nordheim. This discrepancy is believed to be an experimental artifact because field emission intensity does not necessarily translate one-to-one with mass spectral signal intensity. Unfortunately, the ionization pulse intensity was not recorded at the time due to potential damage to the EMT.[52] Subsequent studies with improved devices addressed this issue (see Chapter 4), but for the first generation microionizer the primary focus was placed upon function, i.e. generating mass spectra.

Beyond the electric field strength, a second adjustment for improving ion production with an EI source is the electron energy.[46, 53] The bias voltage of the microionizer controls the electric field between the electron source and the cylindrical ion trap (CIT). Larger bias voltages impart more energy to electrons. The mean free path increases as a result because the collisional cross section with the helium buffer gas decreases with energy.[54] This has two consequences – both of which increase mass spectral signal intensity. First for a fixed

source-to-CIT distance, the electron flux through the trap will increase due to fewer collisions.   Second, the electrons that arrive at the trap will have more energy, providing a greater chance of a successful EI event.[55-56] A 20 μm microionizer operated in field emission mode with increasing microionizer bias generated xenon mass spectra in helium buffer gas with the integrated mass spectra signal plotted in Figure 3.7. The ionizer was pulsed for 1.0 ms with -34 V, and the bias was varied from ground to -125 V. The integrated signal had a general upward trend with bias; increasing over 7.5-fold between ground and -125 V_{bias}. There was a dip in intensity between -50 and -100 V and while tempting to explore the physics that may be responsible for the dip, the reality was that the signal intensity from the first generation microionizers was inconsistent. Trends could be observed in the short term using single scan modes but upon averaging, the microionizer did not maintain steady emission on the minutes time scale. The most likely explanations for these variations were geometry changes in individual emitter tips;[57] adsorbed gases on the tips surface;[58] and thermal fluctuations induced by the oxide leakage current.[59]

With only six devices and a focus on generating active mass spectra, microionizer lifetime was difficult to characterize as potential lifetime was used up in optimizing conditions. The devices however showed similar patterns where field emission would begin strongly and then drop to unusable levels; this process typically took about ten hours of instrument time – translating to only 6 min of ionizer lifetime at a 1% duty cycle. Another drawback was that the duty cycles were short and the mass spectrometer acquisition had to be slowed down in order to provide the ionizer sufficient time to recover between scans. Thermionic emitters yielded acquisition rates near 65 Hz, while the microionizer required 60 ms of cool time slowing the rate to 14 Hz.   Once a device's signal level decayed below

where mass spectrometry was no longer feasible, it was found that an RCA, silicon cleaning[60-61] could regenerate the device for another few hours of instrument runtime but this process is time intensive and only delays the inevitable – a short across the insulating layer. Once a device developed a major breakdown and short, there was less than 1 kΩ of resistance across the electrodes and ionizers would be unrecoverable.

3.4 Conclusions

Handheld HPMS requires an ion source that is small, low-power, pressure tolerant, and oxygen compatible. Preliminary results at ORNL with a first generation microionizer helped identify stable-operating conditions transferable for potential use with UNC's differentially pumped HPMS. Mass spectra were demonstrated in helium at both low and high pressures, as well as high pressure air; and the first generation microionizer satisfied the pressure and oxygen tolerances needed for HPMS along with a small instrumental footprint. The power draw was comparable to thermionic levels by operating at reduced duty cycles. This came at the price of mass spectral acquisition rate and was the main area targeted for future development.   Additionally, studies of the microionizer's emission properties revealed other, less desirable aspects – in particular, the lack of field ionization, short lifetime, and poor emission stability. It was postulated that excess heat generated by the current flowing during the ionization pulse contributed to these issues. Field ionization was inaccessible due to device overheating before sufficient field strengths could be attained. Lifetime was shortened by the excess heat which could accelerate emitter tip degradation as well as oxide breakdown.[62] Field emission is also a function of temperature, thus uncontrolled thermal runaways could be more likely with the microionizer operating at elevated temperature in vacuum.[63] While heat sinking could potentially solve these issues, it would not increase the

appeal of the microionizer as an ion source for a handheld HPMS. Thus, armed with the

early success of the microionizer and the goal of reducing the power draw; improved designs

and fabrication techniques were undertaken in developing HPMS compatible microionizers.

3.5 Figures
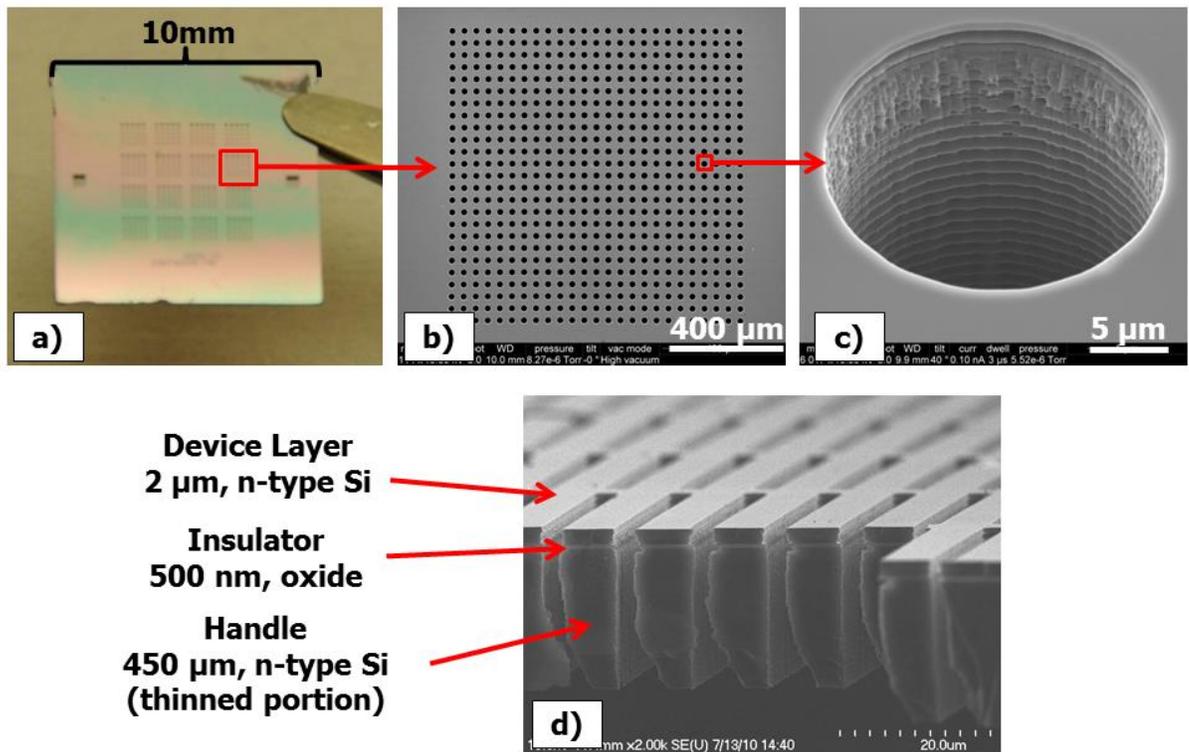
Figure 3.1: a) Optical image of a microionizer. The device layer is only 2 μm thick and transparent to optical frequencies. The iridescence is due to interference from reflections off the oxide surface. b) SEM of the highlighted sub-array of 20 μm vias in the SOI. c) SEM of a single, 20 μm feature. d) A cross sectional SEM of a microionizer, where the three layers of the SOI are identified. This ionizer is a trench device featuring an array of rectangular vias that are 5 x 90 μm^2.
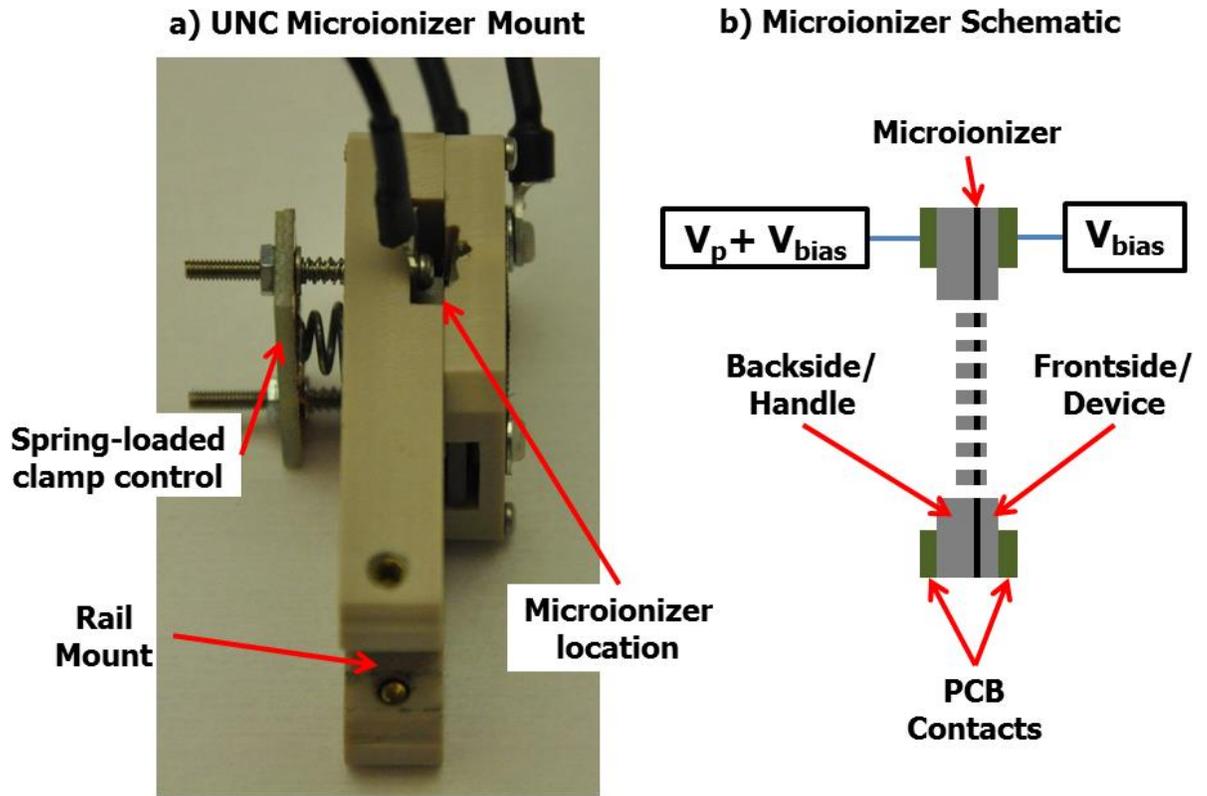
Figure 3.2: a) Image of the microionizer mount used at UNC. The device is pressure-mounted between two PCB for electrical contact. b) Diagram of the microionizer electrical connections; voltage pulse was applied to the handle or backside and bias voltage was applied to both sides. Note - the front side is facing the ion trap.
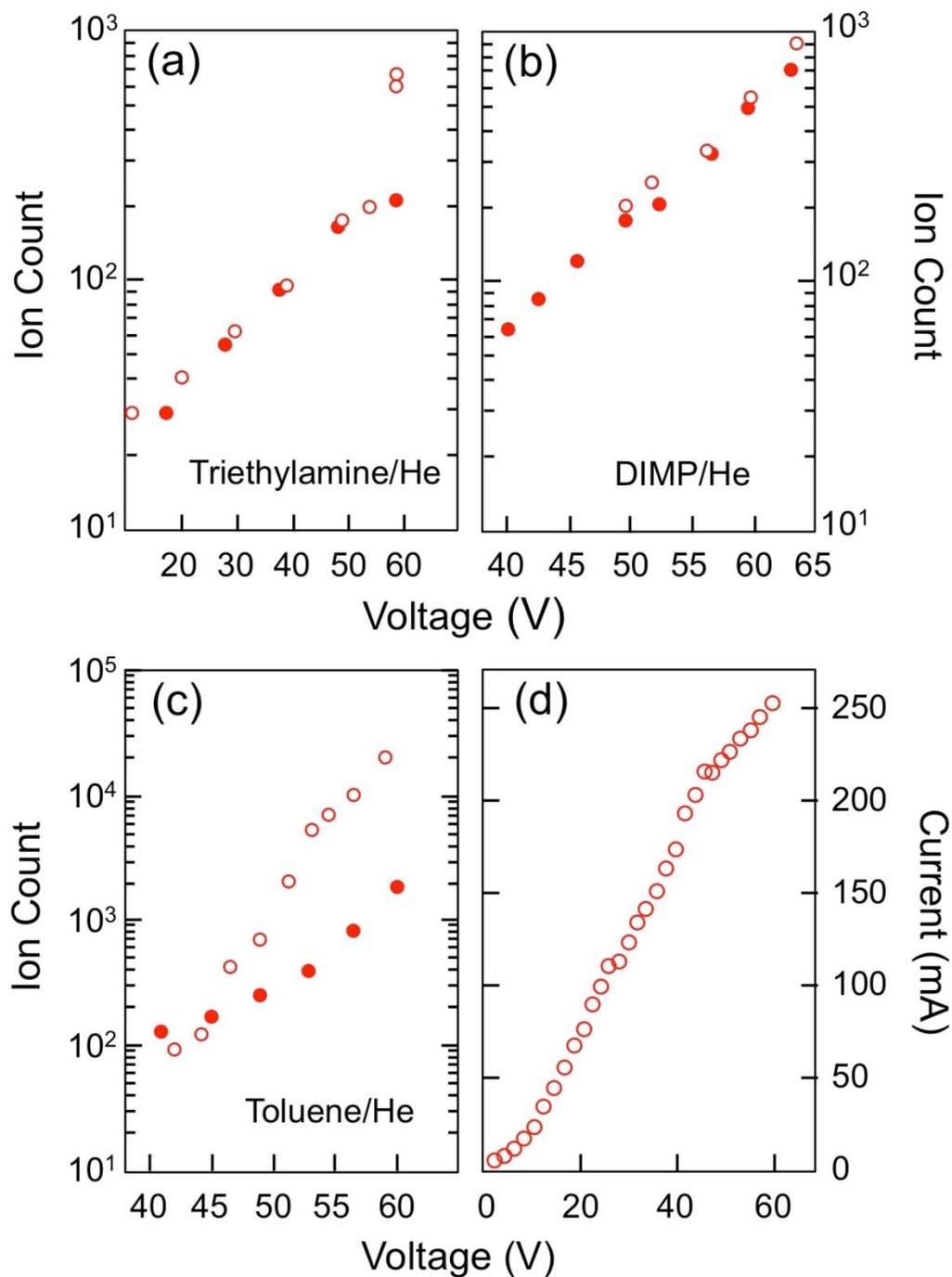
Figure 3.3: Summary of ORNL microionizer results for a single trench device operated at various bias voltages. Analyte concentrations were held constant and helium bath gas pressure was changed for: a) Triethylamine ion count at 16 mTorr helium (●) and 36 mTorr helium (○); b) DIMP ion count at residual pressure (●) and 13 mTorr helium (○); c) Toluene ion count at 25 mTorr helium (●) and 80 mTorr helium (○); and d) current versus voltage trace.
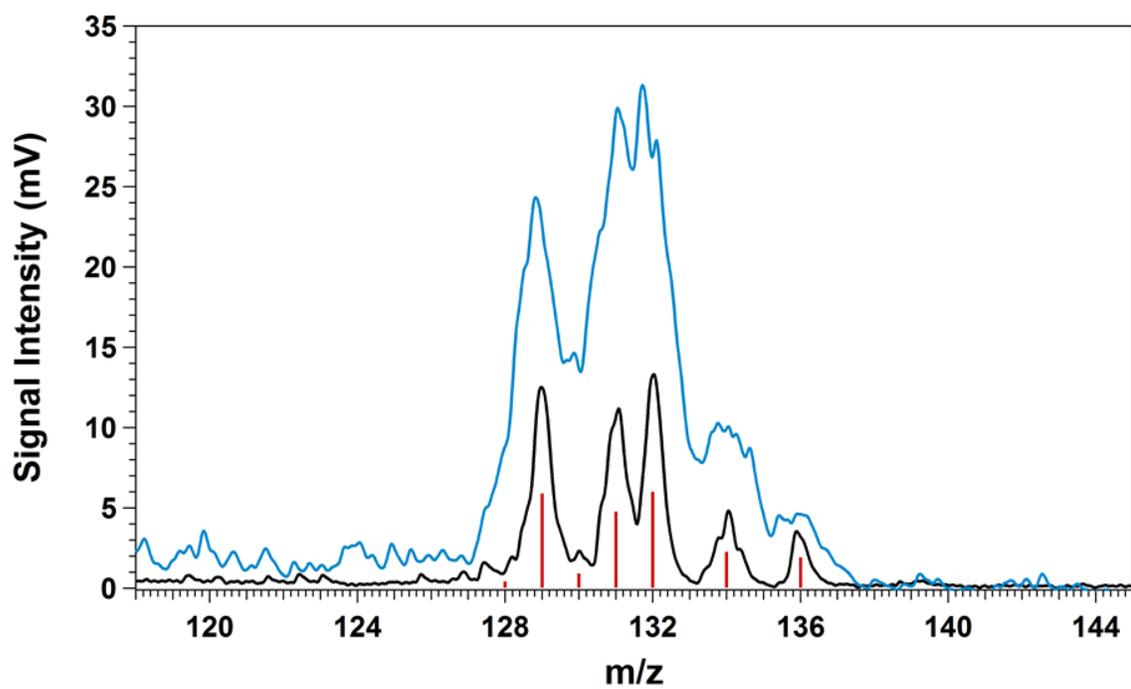
Figure 3.4: Mass spectra of xenon in helium buffer gas at 4.9 mTorr (━) and 960 mTorr (━) as well as the NIST standard (▌). The microionizer field strength was 0.68 MV/cm and was biased to -75 V. A full-size CIT (r_0 = 500 μm and z_0 = 645 μm) was driven at 6.62 MHz with resonant ejection at 4.44 MHz at 0.7 and 5.5 V_{pp} (4.9 and 960 mTorr).
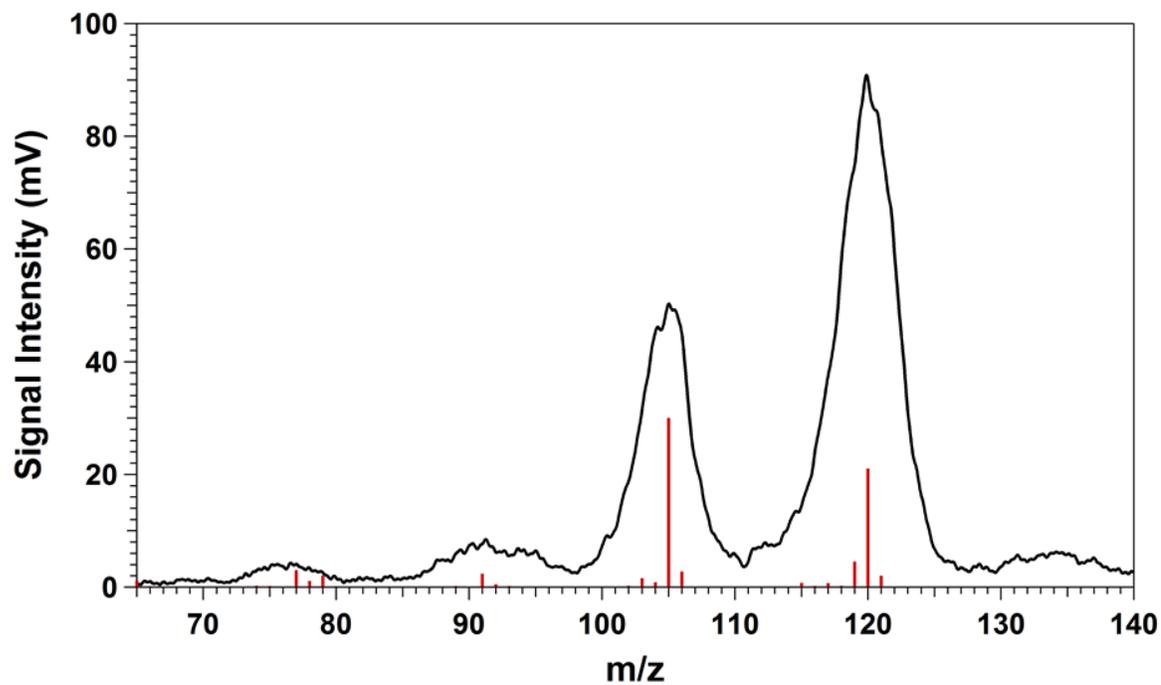
Figure 3.5: Mass spectrum of mesitylene in 510 mTorr of room air (——) and the NIST mesitylene standard (|). The microionizer was pulsed at 0.8 MV/cm for 0.25 ms. The full-size CIT was operated at 8.28 MHz with axial resonance at 2.79 MHz at 2.6 V_{pp} .
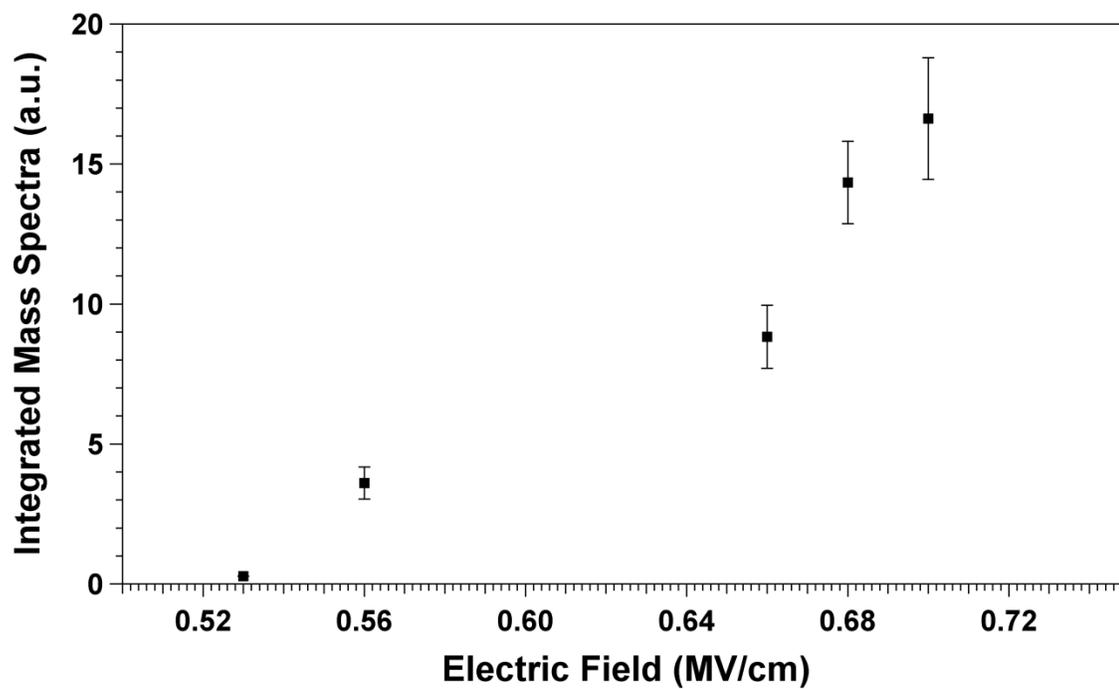
Figure 3.6: Integrated mass spectral signal intensity versus microionizer electric field strength. For a 500 μm insulating layer, these fields correspond to voltage pulses of 26.5 to 35 V. The spectra were of xenon analyte in helium buffer gas at 3.1 mTorr.
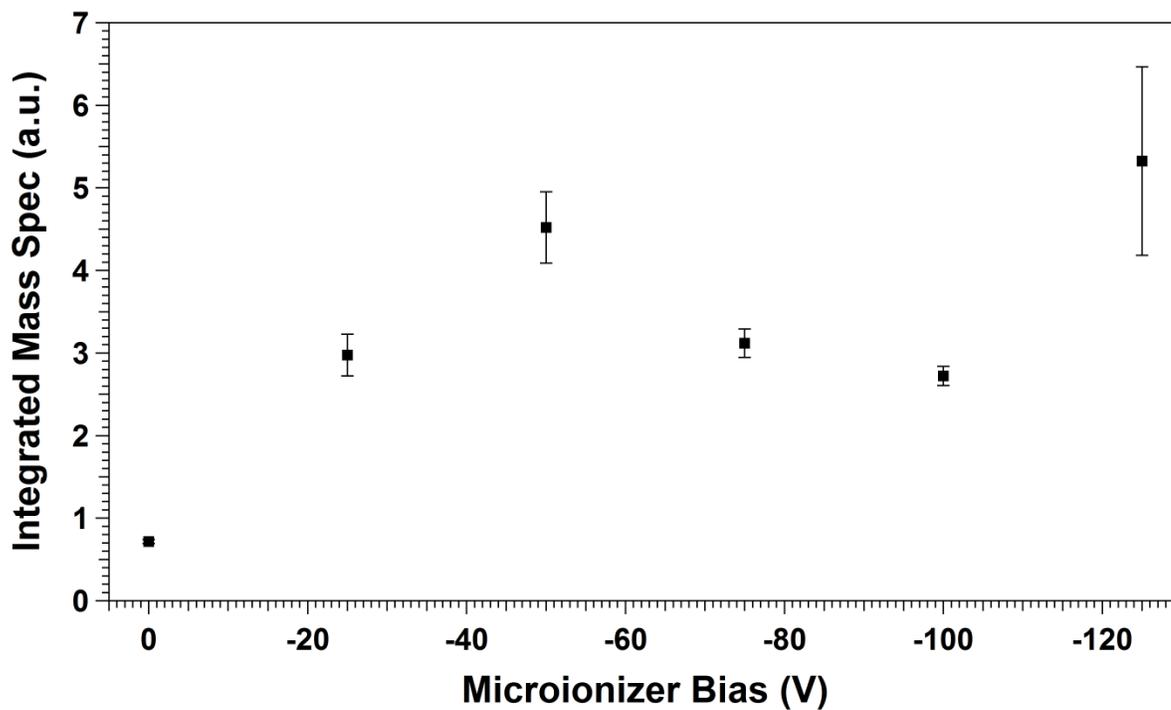
Figure 3.7: Integrated mass spectral signal intensity versus microionizer bias potential. Signal intensity generally increases with electron energy, however this data highlights the inconsistent operation of the first generation microionizer. Spectra are xenon analyte in helium buffer gas at 960 mTorr. The microionizer field strength was pulsed at 0.68 MV/cm for 1 ms.

3.6 REFERENCES

1.   Whitten, W. B., et al., High-pressure ion trap mass spectrometry. *Rapid Commun. Mass Spectrom.* **2004,** *18* (15), 1749-1752.

2.   Wolfe, D. W. High-Pressure Cylindrical Ion Trap Mass Spectrometry. Dissertation, University of North Carolina, Chapel Hill, 2012.

3.   Blakeman, K. H., et al., High-Pressure Mass Spectrometry at Pressures Exceeding 1 Torr in a Microscale Cylindrical Ion Trap. *Manuscript in preparation* **2015**.

4.   Kornienko, O., et al., Micro ion trap mass spectrometry. *Rapid Commun. Mass Spectrom.* **1999,** *13* (1), 50-53.

5.   Johnson, B. B., et al., Field ion source development for neutron generators. *Nucl Instrum Meth A* **2012,** *663* (1), 64-74.

6.   Johnson, S., et al., Field emission properties of self-assembled silicon nanostructures on n- and p-type silicon. *Appl. Phys. Lett.* **2004,** *85* (15), 3277.

7.   Srisonphan, S., et al., Metal-oxide-semiconductor field-effect transistor with a vacuum channel. *Nat Nanotechnol* **2012,** *7* (8), 504-508.

8.   Huang, P. C., et al., High Efficiency and Smooth Transition Buck-Boost Converter for Extending Battery Life in Portable Devices. *2009 IEEE Energy Conversion Congress and Exposition, Vols 1-6* **2009**, 2342-2345.

9.   Whaley, D. R., et al., 100 W Operation of a Cold Cathode TWT. *Ieee Transactions on Electron Devices* **2009,** *56* (5), 896-905.

10.   Gilchrist, K. H., et al. In *A Novel Ion Source and Detector for a Miniature Mass Spectrometer*, IEEE Sensors, 2007; pp 1372-1375.

11.   Xu, N. S.; Huq, S. E., Novel cold cathode materials and applications. *Mat Sci Eng R* **2005,** *48* (2-5), 47-189.

12. Felter, T. E., Cold cathode field emitter array on a quadrupole mass spectrometer: Route to miniaturization. *J Vac Sci Technol B* **1999,** *17* (5), 1993-1996.

13. Deheer, W. A., et al., A Carbon Nanotube Field-Emission Electron Source. *Science* **1995,** *270* (5239), 1179-1180.

14. Kornienko, O., et al., Field-Emission Cold-Cathode EI Source for a Microscale Ion Trap Mass Spectrometer. *Analytical chemistry* **2000,** *72* (3), 559-562.

15. Fomani, A. A., et al., Toward Amp-Level Field Emission With Large-Area Arrays of Pt-Coated Self-Aligned Gated Nanoscale Tips. *Ieee Transactions on Electron Devices* **2014,** *61* (7), 2538-2546.

16. Hartley, F. T.; Kanik, I. In *A nanoscale soft-ionization membrane: A novel ionizer for ion mobility spectrometers for space applications*, Proceedings of SPIE, The International Society for Optical Engineering, 2002; pp 1-7.

17. Bower, C. A., et al., On-chip electron-impact ion source using carbon nanotube field emitters. *Appl. Phys. Lett.* **2007,** *90* (12), 124102.

18. Driskill-Smith, A. A. G., et al., The "nanotriode": A nanoscale field-emission tube. *Appl. Phys. Lett.* **1999,** *75* (18), 2845-2847.

19. Slade, P. G.; Taylor, E. D., Electrical breakdown in atmospheric air between closely spaced (0.2 mu m-40 mu m) electrical contacts. *IEEE T Compon Pack T* **2002,** *25* (3), 390-396.

20. Ono, T., et al., Micro-discharge and electric breakdown in a micro-gap. *Journal of Micromechanics and Microengineering* **2000,** *10*, 445-451.

21. Cristoloveanu, S.; Li, S. S., *Electrical characterization of silicon-on-insulator materials and devices*. Kluwer Academic: Boston, 1995; p 381.

22. Gomer, R., *Field emission and field ionization*. Harvard University Press: Cambridge,, 1961; p 195.

23.   Spindt, C. A., Microfabricated field-emission and field ionization sources. *Surface Science* **1991,** *266*, 145-154.

24.   Haynes, W. M., *Handbook of Chemistry and Physics*. 95th ed.; CRC Press: 2014; p 2693.

25.   Sze, S. M.; Ng, K. K., *Physics of semiconductor devices*. 3rd ed.; Wiley-Interscience: Hoboken, N.J., 2007; p 815.

26.   Osburn, C. M.; Weitzman, E. J., Electrical-Conduction and Dielectric Breakdown in Silicon Dioxide Films on Silicon. *Journal of the Electrochemical Society* **1972,** *119* (5), 603-609.

27.   DiMaria, D. J.; Stathis, J. H., Ultimate limit for defect generation in ultra-thin silicon dioxide. *Appl. Phys. Lett.* **1997,** *71* (22), 3230-3232.

28.   Stuart, M., Conduction in Silicon Oxide Films. *Brit J Appl Phys* **1967,** *18* (11), 1637-1640.

29.   Osburn, C. M.; Ormond, D. W., Dielectric Breakdown in Silicon Dioxide Films on Silicon: II Influence of Processing and Materials. *Journal of the Electrochemical Society* **1972,** *119* (5), 597-603.

30.   Osburn, C. M.; Ormond, D. W., Dielectric Breakdown in Silicon Dioxide Films on Silicon: I Measurement and Interpretation. *Journal of the Electrochemical Society* **1972,** *119* (5), 591-597.

31.   Talin, A. A., et al., Field emission displays: a critical review. *Solid-State Electronics* **2001,** *45* (6), 963-976.

32.   Spindt, C. A., A Thin-Film Field-Emission Cathode. *J Appl Phys* **1968,** *39* (7), 3504-3505.

33.   Ding, M. Q., et al., Fabrications of Spindt-type cathodes with aligned carbon nanotube emitters. *Appl. Surf. Sci.* **2005,** *251* (1-4), 201-204.

34.   Kang, M., et al., Stable field emission from nanoporous silicon carbide. *Nanotechnology* **2013,** *24*, 1-5.

35.   Purcell, S. T., et al., Nanoprotrusion model for field emission from integrated microtips. *J Vac Sci Technol B* **1997,** *15* (5), 1666-1677.

36.   Fursey, G., *Field emission in vacuum microelectronics*. Kluwer Academic/Plenum Publishers: New York, 2005; p 205.

37.   Stein, S. E., "Mass Spectra". in *NIST Chemistry WebBook, NIST Standard Reference Database Number 69* [Online] Linstrom, P. J.; Mallard, W. G., Eds. National Institute of Standards and Technology, Gaithersbrug, MD, http://webbook.nist.gov, (accessed 10/2/2015).

38.   Pau, S.; Whitten, W. B., Personal Communication. 2011.

39.   Muller, E. W.; Bahadur, K., Field Ionization of Gases at a Metal Surface and the Resolution of the Field Ion Microscope. *Physical review* **1956,** *102* (3), 624-631.

40.   Mathis, J. E.; Compton, R. N., Single and multiple photon ionization of triethylamine. *J Chem Phys* **1996,** *104* (21), 8341-8347.

41.   Lu, K. T., et al., Toluene Cation - Nearly Free Rotation of the Methyl-Group. *J Phys Chem-Us* **1992,** *96* (24), 9742-9748.

42.   Sielemann, S., et al., IMS with non radioactive ionization sources suitable to detect chemical warefare agent simulation substances. *International Journal of Ion Mobility Spectrometry* **2002,** *5* (3), 143-148.

43.   March, R. E., An Introduction to Quadrupole Ion Trap Mass Spectrometry. *Journal of Mass Spectrometry* **1997,** *32* (4), 351-369.

44.   McLuckey, S. A., et al., Ion Trap Mass Spectrometry of Externally Generated Ions. *Analytical chemistry* **1994,** *66* (13), 689-696.

45.   Jenkins, R. O., A Review of Thermionic Cathodes. *Vacuum* **1969,** *19* (8), 353-359.

46.   Blakeman, K. H. Development of High Pressure Mass Spectrometry for Handheld Instruments. Dissertation, University of North Carolina at Chapel Hill, Chapel Hill, NC, 2015.

47.   Song, Q., et al., Ion trap mass analysis at high pressure: an experimental characterization. *J. Mass Spectrom.* **2010,** *45* (1), 26-34.

48.   Huq, S. E., et al., Field emitters for space application. *J Vac Sci Technol B* **2001,** *19* (3), 988-991.

49.   Wu, S. M., et al., Sputtering yields of Ru, Mo, and Si under low energy Ar+ bombardment. *J Appl Phys* **2009,** *106* (5).

50.   Stuart, R. V.; Wehner, G. K., Sputtering Yields at Very Low Bombarding Ion Energies. *J Appl Phys* **1962,** *33* (7), 2345-2352.

51.   Fowler, R. H.; Nordheim, L., Electron Emission in Intense Electric Fields. *Proceedings of the Royal Society A: Mathematical, Physical and Engineering Sciences* **1928,** *119* (781), 173-181.

52.   Andresen, R. D.; Page, D. E., On Ion Feedback in a Straight Channel Multiplier. *Nucl. Instrum. Methods* **1970,** *85* (1), 141-142.

53.   Märk, T. D.; Dunn, G. H., *Electron impact ionization*. Springer-Verlag: Wien ; New York, 1985; p 383.

54.   Kauppila, W. E., et al., Measurements of total scattering cross sections for intermediate-energy positrons and electrons colliding with helium, neon, and argon. *Physical Review A* **1981,** *24* (2), 14.

55.   Asundi, K. K.; Kurepa, M. V., Ionization Cross Sections in He, Ne, A, Kr and Xe by Electron Impact†. *Journal of Electronics and Control* **1963,** *15* (1), 41-50.

56.   Stephan, K.; Märk, T. D., Absolute partial electron impact ionization cross sections of Xe from threshold up to 180 eV. *The Journal of Chemical Physics* **1984,** *81* (7), 3116.

57.   Bonard, J.-M., et al., Degradation and failure of carbon nanotube field emitters. *Physical Review B* **2003,** *67* (11), 115406.

58.   Wei, Y., et al., Surface chemical changes on field emitter arrays due to device aging. *J Vac Sci Technol B* **1999,** *17* (1), 233-236.

59.   Wallash, A.; Levit, L., Electrical breakdown and ESD phenomena for devices with nanometer-to-micron gaps. *Reliability, Testing, and Characterization of MEMS/MOEMS II* **2003,** *4980*, 87-96.

60.   Kern, W., The Evolution of Silicon-Wafer Cleaning Technology. *Journal of the Electrochemical Society* **1990,** *137* (6), 1887-1892.

61.   Kern, W.; Puotinen, D. A., Cleaning Solutions Based on Hydrogen Peroxide for Use in Silicon Semiconductor Technology. *RCA Review* **1970,** *31* (2), 187.

62.   Reynolds, F. H., Thermally Accelerated Aging of Semiconductor Components. *Proceedings of the Ieee* **1974,** *62* (2), 212-222.

63.   Levine, J. D., Benefits of the lateral resistor in a field effect display. *J Vac Sci Technol B* **1996,** *14* (3), 2008-2010.

CHAPTER 4: MICROIONIZER FABRICATION AND DEVELOPMENT

4.1 Introduction

The integration of the first generation microionizer with HPMS was considered successful enough to warrant further development. Both positive and negative aspects of the first generation's performance were considered in designing subsequent ionizer generations. The most important aspect of the initial integration was that it successfully generated ions for HPMS. An ion source for HPMS must be small, low-power, and oxygen tolerant in pressures upward of 1 Torr. The first generation with a small footprint achieved two out of three objectives by generating mass spectra in high pressure air, but with high power consumption and inconsistent performance from device-to-device. This chapter documents an in-house developed fabrication process and improvements to both the device interface and HPMS for lowering power consumption and increasing consistency of operation between microionizers.

Thermal fluctuations in the first generation caused by high power consumption lead to suboptimal performance in terms of achieving field ionization, device-to-device reproducibility, and lifetime. The microionizer should behave as an ideal capacitor with only displacement current and no leakage current. However, the first generation microionizer easily pulled milliamp-levels of leakage current. There are several mechanisms responsible for this leakage current into and through thin film dielectrics and they can be broken down into either interfacial or bulk-related phenomena.[1] Current and dielectric breakdown studies of thin film insulators are most often considered in terms of field effect transistors where a

110

'large' device area is 0.0005 cm^2.[2] The microionizer, on the other hand, has a 1 cm^2 surface area, thus insulator quality (bulk conduction) is paramount for reducing the leakage current. Higher quality insulators offer fewer traps, defects, and ions for field-driven current conduction.[3-4] Given the encouraging field emission results of the first generation, subsequent generations focused on reduction of leakage current through the choice of insulating layer.

The initial microionizer was designed with simplicity in mind so that fabrication costs could be held to a minimum. This fabrication approach relies upon deep reactive ion etching (DRIE) and is straightforward compared with other field effect device fabrication methods. DRIE utilizes a two-step process (passivation and etch) developed by engineers at Bosch, GMBH.[5] The Bosch process alternates passivation and etching to generate anisotropic features with aspect ratios approaching 50.[6] A single, simple field effect transistors (FET) commonly requires an extensive process flow.[7] Spindt-emitters for field emission have an ever more complex flow due to the addition of arrays of carefully crafted field enhancing tips.[8-9] By contrast, the microionizer perforates a silicon-on-insulator (SOI) substrate using DRIE and relies upon minor field enhancements of a macroscopically generated field (~ 1 MV/cm) across the thin insulating layer. The surface roughness of the silicon sidewalls at the interface of the insulating layer is responsible for the geometric enhancement necessary to achieve 10 to 100 MV/cm electric fields.

The general process for fabrication of the first generation microionizer (Gen 1) is shown in Figure 4.1a. The process starts with a SOI substrate consisting of three layers: device, insulator, and handle. In step 1, a photoresist masking layer is deposited on the handle layer and patterned via photolithography, defining an open window area (~ 1 mm^2). 2) The

111

window is etched by DRIE into the handle to within approximately 20 μm of the insulator layer after which the photoresist is stripped and the wafer cleaned. 3) A masking layer is deposited on the device side and patterned with the active ionizer features and aligned with the backside window using fiducial marks. 4) The wafer is through-etched from the device side layer-by-layer: DRIE through the device layer; DRIE or wet chemical etch through the insulator; and DRIE through the handle layer and finally, 5) the wafer is cleaned and diced. A cross-section SEM of a completed device is shown in Figure 4.1b. The device/insulator/handle layers form a membrane on the order of 25 μm thick. The device layer (2 μm) and insulator (0.5 μm) are located at the top of the SEM. The active region is the silicon-insulator interface with the handle layer for mechanical support. An optical image of the front side of a 100 μm Gen 1 device is shown in Figure 4.1c. The color is due to bonding fringes that are a result of optical interference from reflections off the insulating layer.

Microionizer development at UNC using this process flow as a starting point was undertaken and can be divided into three stages: Early, Optimization, and Final. Early development focused on reproducing Gen 1 devices however with one departure from the design – the through-etch. A single-side etch (starting at step 3 in Figure 4.1a) exposes the silicon-insulator interface where field emission or field ionization occur. Etching through the remainder of the handle layer would only act to enhance field ionization when forcing neutral analyte molecules to pass through the active region (from handle to device layer) on their way to the ion trap (rather than relying upon diffusion). Additionally, since Gen 1 devices were only capable of field emission, etching through the handle layer is unnecessary. This decision reduces the process development complexity and enhances the rate at which devices

can be produced and characterized. The Optimization stage was transitional as device fabrication became consistent enough to produce microionizers with similar device-to-device behavior improving characterization results. As part of the optimization process, the die layout changed and electrical contact to the device and handle layers was made to the front of the device. The through-etch was also attempted to determine the difficulties of incorporating it with the front side processing. The lessons learned from these two stages culminated in the Final development stage. The Final process was used to fabricate both single-side and through-etch microionizers characterized for their leakage current and emission intensity under HPMS conditions across an array of geometries and materials.

During the fabrication optimization time frame, the HPMS testing platform evolved as well with improvements made through the combined efforts of the research group. Most of the improvements have been documented[10-11] and were used to maximum benefit for microionizer development. A couple of advances regarding the development of a high voltage pulsing circuit and vacuum chamber miniaturization are highlighted in this chapter because they were crucial to successful implementation of the microionizer.

4.2 Fabrication

A full array of microfabrication tools, as detailed in Appendix 1, was available for device development. Access to this equipment was crucial; from photolithography mask design and fabrication to device processing up through to device bonding. Based upon the lack of field ionization seen in the Gen 1 devices at ORNL, the first UNC devices were only front side etched to just beyond the insulator layer. Since field emission is not dependent upon mass transport of neutrals through the high field region, these microionizers should operate similarly to the Gen 1 devices despite not being through-etched.

The first generation was defined as those devices fabricated at Arizona State University while the additional generations developed at UNC were divided into the three stages of fabrication: Early development (Gen 2 to 6), Optimization (Gen 7 and 8), and Final (Gen 9.1 to 9.6). A representative device from each generation is shown in Figure 4.2. Device generations were numbered when either the photolithographic mask was updated or major changes to the fabrication sequence were made. Table 4.1 displays substrate physical characteristics for each microionizer generation. There were three categories of substrates used for these studies: SOI (Ultrasil Corporation, Hayward, CA), polysilicon-on-insulator (Pau Research Group, UA), and metal-on-insulator (Rogue Valley Microdevices, Medford, OR). All substrates had four key features: the handle and device layers were always highly doped; device layer thickness never exceeded 12 μm; the insulating layer was always less than 1 μm thick; and the handle thickness was between 400 and 500 μm. The early generations attempted to reproduce Gen 1 and remained faithful to those SOI specifications until Gen 5, after which, device and insulating layer thicknesses were investigated. Thinner device layers should yield improved signal intensity, while insulating layer thickness affects the leakage current[12] and operating voltage; 1.0 μm requires 100 V to generate 1.0 MV/cm. The handle thickness balances robustness for handling and thin film stresses with etch time. The handles were 10 to 30% thinner than normal for 100 and 150 mm diameter wafers.[13]

The material choice for each layer has consequences for device operation and fabrication. Field emission is dependent upon the work function of a material;[14] for silicon it ranges from 4.7 to 4.9 eV, depending on doping type and level.[15] For reference, cesium has a work function of 2.1 eV and can be coated on electrodes to enhance field emission from devices but quickly degrades.[16] Tungsten on the other hand, has a work function near 5 eV and is

used in high power devices because of its high melting point.[17] Field emission from p-type semiconductors is more complex than metals due to carrier inversion and field penetration.[18] Both dopants were tested, but n-type silicon ($> 10^{18}$ atoms/cm^3) was the focus of this study since it exhibits metal-like field emission.[19]

Internal crystal stress is influenced by the high dopant concentrations used, however the insulating layer dominates the durability of the SOI structure.[6] Silicon wafers less than 400 μm thick can actually warp under the stress induced by thin films such as oxide and nitride. Wet, thermal oxides are preferred for bonded SOI because they grow quickly and have residual ions for anodic bonding.[20] However, they are prone to trapped charge states at the silicon interface that can lead to charge conduction at high electric field strengths.[21-22] As such, alternatives were investigated including dry thermal oxide, oxide/nitride/oxide as well as multi-layered, low-stress silicon nitride. Dry thermal oxide is of higher quality, yielding higher dielectric breakdown than wet oxide.[23] The layered materials were chosen because the additional interfaces in the insulating layer suppress leakage current[24] and with proper annealing have lower stress than a single layer of insulating material of the same thickness.[25]

4.2.1 Early Development – Generations 2 to 6

Early development focused on reproducing Gen 1 devices for continued field emission-based HPMS testing. As fabrication progressed towards Gen 6, the active ionizer feature layouts changed to better align with the cylindrical ion traps (CIT) and stretched length ion traps (SLIT) being developed in other parts of the HPMS program. The geometry of via architecture also shifted away from the variety of circular features towards trench-only layouts. A 10 μm trench width was chosen for superior etch results and to reduce variability

across the wafer. These devices adhered to the original design with the clamp-style holder

for electrical contact.

4.2.2 Optimization – Generations 7 through 8

Gen 7 and 8 were the first to depart from their predecessors in terms of device layout.

These also represent the first attempts at through-etching since Gen 1. These microionizers

used an 'island' configuration as seen in Figure 4.2g and h. The unused portions of the

device and insulator layers were removed to decrease the area available for leakage current

conduction. The island configuration encouraged a change in microionizer holder because

both device and handle layers could be accessed from the front side of the device. The

clamp-style holder was abandoned and printed circuit boards (PCBs) were employed. These

gave more flexible microionizer positioning relative to the CIT. The use of PCBs also helped

electrical contact evolve from silver epoxy to soldering and wire bonding.

4.2.3 Final Process – Generation 9

The optimization stage culminated in the final process and development of Gen 9

devices. The major steps of the final process flow can be found in Table 4.1. This process

blended every advance and lesson learned during fabrication, testing, and HPMS operation to

yield the microionizer as seen in Figure 4.2i. This design was overhauled such that the active

features, 10 x 90 μm^2 trenches were laid out lengthwise in seven, 5 x 20 rectangular arrays.

Alignment was then ensured to overlap the 4 mm SLIT (an image of which is shown in

Figure 4.4a). The die layout was also changed to 2.5 x 20 mm^2 in order to lay flat against the

compact ion trap electrodes.

Six versions of Gen 9 were fabricated, 9.1 to 9.6 with Figure 4.3a to f showing an optical

image of each. The first five versions were single-side etched starting at Step #8 in Table

116

4.2. These devices were fabricated to test the effect of device layer thickness, insulating layer thickness, and material choice. Three variants were based on SOI substrates. The remainder used layered substrates with cheaper material cost compared to bonded SOI: metal-insulator-silicon and polysilicon-insulator-silicon. The final version, Gen 9.6, was through-etched using the best performing substrate. The device layers of all variants except 9.3 and 9.5 are thin enough to be optically translucent. The colors and patterns observed in Figure 4.3 are representative of the SOI bond quality, device layer thickness, insulating material, and overall surface roughness. A Gen 9.6 device mounted and wire bonded to a PCB is shown in Figure 4.3g. The die is secured to the PCB with epoxy before wire bonding.

4.3 Experimental

4.3.1 HPMS Updates

Over the course of microionizer development, there were advances in nearly every aspect of HPMS with most of these achievements incorporated into the microionizer test bed. One key change that influenced the microionizer design was the miniaturization of the vacuum chamber. This design was implemented to minimize parasitic capacitance for optimal CIT operation at high frequencies (> 10 MHz) and was accomplished by reducing the ion trap electrode surface area as well as the amount of coaxial cabling.[11, 26] A comparison of an original ion trap electrode next to a compact ion trap electrode is shown in Figure 4.4a where the compact electrode has roughly half the surface area. The reduction in surface area brought the mounting screws closer to the center (location of the ion trap), leaving only 3 mm between the heads of the mounting screws. This limited space required a redesign of the microionizer, with the width of Gen 9 reduced from 10 to 2.5 mm. While both electrodes

can be used in the original HPMS differential chamber, shown in Figure 4.4b, only the compact electrodes are compatible with the mini-chamber and the trap-mounted chamber as shown in Figure 4.4c and d, respectively. The differential chamber was employed for the external ion trapping results presented in Chapters 2; the first generation microionizer results in Chapter 3, as well as testing Gen 2 through 7. The large volume of this chamber gave great flexibility in experimental design. However, operation was often limited by discharge (RF or DC) to the grounded chamber walls. The mini-chamber, shown in Figure 4.4c, was used to test the 8th generation microionizer. This chamber reduced the incidence of RF discharge, easing mass analyzer operation, and reduced the gas loads on the pumping system at the cost of flexibility.[11, 26] The trap-mounted chamber, Figure 4.4d, was a purpose-built version of the mini-chamber to provide room for the PCB mounted microionizer as well as its associated electrical feedthroughs.

4.3.2 Microionizer Operation

While the ion traps and vacuum chamber received improvements, the majority of the support electronics such as current preamplifier, data acquisition, and RF generation remained constant throughout the testing of the microionizer. However, the pulsing circuit received an overhaul between Gen 5 and 6. The original pulsing circuit relay was a simple photorelay IC (PVA3354N) that was upgraded to a high-voltage single-pull, double-throw switch (HV Switch). The HV Switch was custom designed and based upon N-channel MOSFETS (Model STP6N95K5). The HV switch improved every aspect of voltage pulsing over the optical relay – maximum amplitude (950 V versus 300 V), bias range (1 kV vs 300), and ease of switching pulse polarity. The improvements are demonstrated in the oscilloscope traces in Figure 4.5. The yellow traces are an 80 μs square, control pulse and the blue traces

are each circuit's attempt to reproduce the control pulse with +125 V amplitude. The photorelay response is shown in Figure 4.5a and shows a delay of 80 μs. More importantly, it only outputs +88 V due to the slow rise time and requires over 200 μs to return to baseline. Early microionizer operation used pulse lengths between 1 to 10 ms; at these time scales the relay's faults are evident but not disruptive to operation. As shorter pulse lengths were investigated, a new pulsing circuit to overcome the photorelay's limitations is required. Figure 4.5b shows the performance of the HV Switch under the same operating conditions as the relay. The HV Switch accurately reproduces the control pulse at +125 V amplitude, and it displays a 200-fold decrease in rise time and a 1000-fold decrease in fall time compared to the photorelay.

The mount interfacing the microionizer to the HPMS also evolved over the course of development. A clamp-style holder previously discussed in Chapter 3 was used exclusively with the differential chamber. As such, Gen 1 through 6 were tested with this style holder. Beginning with Gen 7, the holder was updated to a PCB mount, three versions of which are shown in Figure 4.6. The PCB shown in Figure 4.6a was used with Gen 7 and fabricated by SAE Circuits Colorado, Inc. (Gunbarrel, CO). Electrical contact between the PCB and microionizer was made by either silver epoxy, soldering, or copper tape. When the vacuum chamber was switched to the mini-chamber, the PCB was updated as seen in Figure 4.6b. This PCB was used as a vacuum bulkhead by an o-ring seal between the aluminum chamber and PCB. The white, circular ring in the soldermask of the PCB was used to guide o-ring placement when mounting the PCB to the vacuum chamber. The final version of the PCB mount is shown in Figure 4.6c and used wire bonding to make electrical contact. Fabrication was by Sierra Circuits, Inc (Sunnyvale, CA) for their superior, wire-bondable gold finish. It

was mounted in the vacuum chamber as shown in Figure 4.4d. The spacing between the microionizer and SLIT could be controlled to 50 μm.

4.3.3 Characterization and Testing

Fabrication results were primarily assessed in three ways: profilometry (P-6 Stylus Profilometer, KLA-Tencor); optical microscopy (VHX-2000, Keyence Corporation and Eclipse LV-150, Nikon Corporation); and SEM (FEI Quanta 200 ESEM or FEI Helios 600 Nanolab, FEI Corporation). Any reference to physical dimensions such as etch depth was measured with one or more of these techniques. Profilometry and optical microscopy were crucial for monitoring etch depth to gauge DRIE etch rates. Additional observations by SEM were critical in determining a number of device physical attributes including: the fidelity of the final etch features with the mask; notching at the silicon-insulator interface; and surface roughness.

Both field emission and field ionization used 1 ms voltage pulses, a 3.6% duty cycle. An operational schematic is shown in Figure 4.7a using an SEM image to highlight how the voltages are applied to the device as well. For field emission, the microionizer was pulsed and biased negatively; positive mode reversed the polarities of the pulse and bias. The voltage pulse generates the electric field across the insulating layer while the bias voltage aids in extracting the charge once emitted. Figure 4.7b shows a high-magnification SEM of the surface roughness of the handle layer at the insulator-handle interface. This roughness is likely responsible for the geometric field enhancement necessary to achieve field emission and field ionization. The voltage pulse was monitored using an oscilloscope (Model DPO3034, Tektronix, Inc), while the bias was measured with a digital multimeter (Model 179, Fluke, Inc). The pulse and bias supplies were ballasted with 100 kΩ and 1 MΩ

resistors, respectively. Average current was measured via digital multimeter (Model U1272A, Agilent, Inc.) operated in DC-Current mode on the μA scale. Microionizer operation was characterized under HPMS conditions as both a field emission and field ionization source. Air was leaked into the ionization-side chamber with a needle valve, and the pressure measured ranged from 350 to 1000 mTorr. A schematic of the ionizer test setup is shown in Figure 4.8. The ionizer was spaced approximately 100 μm from a voltage-controlled aperture electrode. The aperture mimicked a SLIT with $x_o = 100$ μm and length = 4.0 mm and was controlled between ± 250 V. The aperture throttled gas flow into the detection chamber, keeping the EMT chamber pressure below 100 mTorr. Signal was detected using an EMT (Model 2300, Detech, Inc.) biased to -1200 V; the output of which was amplified (2 nA/V) by a current preamplifier (SR570, Stanford Research, Inc). In positive mode, the detected signal was a direct measure of the microionizer's emission. In field emission mode, the signal was a measure of the ions generated via EI, where the rate of ion generation was assumed to be proportional to the field emission intensity.[27] Ambient air provided the background neutrals for both modes of operation. Signal was acquired at 250 kHz using the same interface described in Chapter 2. It was averaged over 250 scans, low pass filtered at 30 kHz, and integrated to produce data points for plotting purposes.

4.4 Results and Discussion

4.4.1 Fabrication and Leakage Current

The final process flow described in Table 4.2 evolved from the lessons learned fabricating Gen 2 through Gen 8 microionizers. In the Early development phase, these lessons pertained to developing and optimizing silicon microfabrication techniques. Eventually, procedure refinements led to reproducible device performance (Optimization

phase) and progressed towards the final process flow. While many lessons were learned, two dealing with DRIE and final device preparation in particular were crucial to success.

Deep reactive ion etching (DRIE) is a well-established technique in micro-electrical-mechanical systems (MEMS).[28-29] However, its implementation is highly specific to the fabrication tool, the loading area of the pattern, and masking material employed. In the Early and Optimization stages of device development, broken wafers in the DRIE were a common occurrence. Many reasons were posited: seeking to maximize yield the early mask design patterned the entire wafer; thinned wafers lacked robustness; and the thin films in use (chromium masking, SiO_2 insulators, etc.) simply added too much stress to the wafer causing it to break. While any combination of these issues could have contributed to wafer breakage, the real culprit was heat. When optimized, a 100 μm etch depth required 14 min of etch time at approximately 7 μm/min. The ceramic mechanical chuck of the Alcatel AMS-100 DRIE was unable to adequately remove the heat generated during this etch time, resulting in mask degradation and wafer breakage. This overheating was overcome by adding a delay step to the etch process. The final etch was a loop of 30 s of Bosch etch followed by 60 s of dead time, yielding an effective etch rate near 4 μm/min. The heat released during etching is dissipated in this 60 s dead time, greatly increasing the selectivity of the masking material (particularly towards the perimeter) and reducing the risk of wafer breakage. For reference, 15 wafers were processed for Gen 2 through 8 with most of these wafers suffering breakage during the etch process, primarily due to thinning at the perimeter. Whereas, Gen 9 that utilized the delay loop, had no wafers broken during the DRIE step. Moreover, most wafers retained sufficient structural rigidity for the follow-up wet cleaning, contact pad deposition, annealing, and dicing.

The second major obstacle overcome during development was the device to HPMS interface. Gen 1 through 6 utilized a clamp style holder, mainly because it was simple and the ionizers were capable of producing mass spectra and their inconsistent performance was thought to be a result of insulator quality. Only when the device layout was updated for Gen 7 and 8 and electrical contact made by wire bonding was poor electrical contact determined as a major issue. The disadvantage of the clamp-style holder is evident in Figure 4.9 where a comparison of current draw versus field strength for clamp-style contact and wire bonded contact is shown. The black squares in Figure 4.10a are a Gen 5 device that used the clamp-style holder and have current draws above 0.5 mA. The leakage current however was held in check using a low duty cycle (less than 1%) and by current limiting the power supply to 4 mA. The wire bonded Gen 8 (red squares) and Gen 9 (blue squares) generation devices both have a dramatic drop in leakage current compared to the clamped-style Gen 5 device. Figure 4.10b shows a magnified view of these results. Relative to the maximum current of Gen 5, Gen 8 is 2500-fold lower and Gen 9 is over 11,000-fold lower. Moreover, higher duty cycles are possible – the Gen 9 trace used a 22% duty cycle; thus increasing the mass spectral acquisition rate by more than 3-fold to 44 Hz. The current draws shown in these traces are also closer to what is expected from a FED[30-31] and are directly attributable to electrical contact by wire bonding.

Examples of wire bonds used with Gen 8 and 9 devices are shown in Figure 4.10. In manufacturing, wire bonding is a staple for establishing stable electrical contact to silicon dies.[32] It requires a metallized, contact pad be deposited onto the silicon surface. Bonding is achieved with thermosonic compression – a combination of ultrasonic agitation, compression, and heat welds the wire to the contact pad. The pad material must be chosen

such that it creates an ohmic contact with the silicon while also alloying with the wire.[32-33] The bond system used in Gen 8 shown in Figure 4.10a were titanium/copper contact pads with 1 mil aluminum wire bonded to the front and back side pads.[34] Figure 4.10b shows a Gen 9 bond system with titanium/palladium/gold metallized pads and 1.5 x 0.5 mil^2 gold ribbon.[35] The drastic reduction in current draw introduced by wire bonding suggests that the 'leakage' current had less to do with the insulating layer than the electrical contact. The likely candidate for the intermittent electrical contact with the clamp-style holder would be the native surface oxide.[36] The clamp-style holder likely functioned when a perfect balance of surface abrasion and clamp pressure was attained.

Microionizer development progress accelerated once the fabrication and electrical contact procedures were established such that wafer-level failure analysis was possible. Six variants of Gen 9 were produced, with a sample completed wafer shown in Figure 4.11a. The Gen 9 mask produces 208 devices from a single, 150 mm wafer. Operable vs. non-operable devices are distinguished by measuring the microionizer's capacitance, with operable devices measuring nF capacitance and non-operable devices measured as short circuits. Thirty devices from a wafer processed for a single variant were chosen at random across and measured. The device yield and average capacitance categorized by variant were determined and are shown in Figure 4.11b. Gen 9.2 and 9.4 both show sub-standard yields compared to the others with only 43 and 73% yields, respectively. The probable cause for the low yield is that both Gen 9.2 and 9.4 have polySi device layers. SOI is a very reliable substrate, but it is also expensive from a manufacturing standpoint so alternatives were explored. Thin polySi films can be sequentially deposited on wafers in a parallel fashion reducing costs, while SOI wafers requires an anodic bonding step performed on single wafer-to-wafer pairs. The

polySi wafers pushed the boundaries in terms of maximum insulating layer thickness

(300 nm, dry-thermal SiO_2 for Gen 9.2 and 1000 nm Si_3N_4 for Gen 9.4) to try and minimize

the leakage current when it was thought to be a result of insulating layer quality.

Unfortunately, the stresses in these thin films when combined with that of the poly-Si device

layer, which was deposited at 0.5 µm thicknesses, resulted in fragile wafers. As a result, the

fabrication process for these two variants consumed multiple wafers due to breakage during

the lithography steps. Lithography is an early process step and breaks at this point are

unusual from a MEMS perspective, suggesting the thin-film induced stress was very high for

these substrates. Moreover, successfully fabricated devices broke down and shorted before

any significant ion current could be collected with some even showing visible fractures after

testing. Due to their poor yield, these devices were not further characterized.

Despite the failures of the polySi-based devices, the remaining Gen 9 devices provided

insight into the operation of the microionizer. Gen 9.5 had a titanium/chromium device layer

on oxide that was investigated as another alternative to SOI. The remaining variants, Gen

9.1, 9.3, and 9.6 were based upon Ultrasil SOI. The key features and main differences

between each variant are listed in Table 4.3. Briefly, Gen 9.1 was the first wafer to use the

trap-mounted configuration as well as gold wire bonding. Gen 9.3 used the same substrate

SOI as 9.1, only the device layer was left unaltered at 10 µm. Gen 9.6 also used the same

substrate SOI and was meant to be as similar as possible to Gen 9.1 only with a through-etch.

Gen 9.5 had the thinnest device layer and insulator of the 4 variants at 0.25 and 0.3 µm,

respectively.

4.4.2 Field Emission Mode Operation

The field emission signal intensity as a function of field strength is shown for each 9th generation microionizer in Figure 4.12. The data was collected at 1 Torr of room air buffer gas in a gated configuration (as shown in Figure 4.8). The electric field range varied from device to device, beginning where measurable emission was observed and ending short of electrical discharge. The raw signal intensity is shown in Figure 4.12a. As expected for a field emission source, the signal of all four devices increases exponentially with field strength.[37] To highlight this fact, the data is reevaluated in Fowler-Nordheim coordinates and shown in Figure 4.12b. The linear relationship indicates Fowler-Nordheim tunneling is responsible for the electron emission; assuming that the ions detected by the EMT are directly proportional to the field emission intensity. For a well-defined field emission tip (radius of curvature and aspect ratio), these plots can be used to estimate the emission area and geometric field enhancement of the device, but that would be improper for the microionizer because the emission sites are not well defined.[38]

Returning to Figure 4.12a, a range of maximum field emission strengths is observed among the variants. Gen 9.5 has the largest overall signal intensity as well as the thinnest insulating layer at 0.3 μm and the thinnest device layer at 0.25 μm. It produced a measurable signal at 1.0 MV/cm and a slow emission ramp over 0.8 MV/cm. Gen 9.3 had the next largest signal intensity and a 1 μm insulating layer and 3 μm device layer. It ranged from 1.4 to 1.8 MV/cm. Gen 9.6, which should be identical to Gen 9.1 except for the extra processing required to fabricate a through-etch; demonstrated moderate field emission at the highest field strengths observed, 1.8 to 2.2 MV/cm. Finally, Gen 9.3 showed a small amount of field emission from 1.5 and 2.0 MV/cm. This device should be identical to Gen 9.1, except with a

10 μm device layer. The observed signal intensity of Gen 9.3 was over 24-fold lower than Gen 9.1, suggesting that the device layer thickness plays an important role in charge extraction from the microionizer. Given the operating conditions, this is not surprising. The device layer is a field-free region, and electrons must drift through it. Any interactions will remove energy and reduce the electron's probability of transiting this region. Another factor that may contribute to this drop in signal is the angular dependence of the field emission.[37] Thus, the device layer may serve to 'clip' signal that does not exit the emission site orthogonal to the silicon surface.

The difference in both signal intensity and field strength between Gen 9.1 and 9.6 was unexpected because the insulating layers were identical and device layer thickness near 3 μm for both. Gen 9.6 showed a 4.8-fold reduction in maximum signal intensity, while requiring a 22% higher field strength to achieve it. The measured device layers of the two variants are 2.6 μm for Gen 9.1 and 3.1 μm for Gen 9.6. While there is a 20% difference in device layer thickness, this alone should not account for the entire disparity in signal intensity, given that a 400% difference between Gen 9.1 and 9.3 yielded a 24-fold decrease in signal intensity. Moreover, device layer thickness should not contribute to the increased field strength required in Gen 9.6. The SEMs of Gen 9.1 and Gen 9.6 shown in Figure 4.13 reveal a major difference at the insulator interface. The device layer of Gen 9.6 was notched nearly 1.5 μm from the edge of the insulating layer. This notching was likely a result of the through-etch since the other Gen 9 variants do not display it (images not shown). The overhanging insulating layer likely acts to hinder field emitted electrons from exiting the device. Thus, the larger field strength needed for emission was likely required to overcome this inefficiency. Unfortunately, this insulating layer contains a nitride which is difficult to wet

etch[39] without affecting the silicon or wire bonding pads. A pure oxide could be etched back with a simple buffered oxide etch which might then shift the field strength range back in-line with Gen 9.1.

The maximum field strengths possible are limited by electrical discharge, which is observed as an overload of signal from the electron multiplier. Comparisons of the maximum field strengths generated for each variant lend insight into the discharge mechanism. Insulator breakdown was unlikely because the ballast resistors prevent current surges capable of instantly breaking down the insulator. Moreover, after the field limit was found, each device was operated for at least 1 hour afterwards with no signs of signal degradation or increased leakage current. Thus, discharge is likely a result of a microdischarge plasma aided by surface flashover.[40-41] In a microdischarge, field emission typically contributes to atypical Paschen breakdown by generating ions (via EI) in the gap between electrodes, which in this case is the insulating layer. Gen 9.1 and 9.5 each had maximum field strengths near 1.8 MV/cm, while still producing a strong signal, meaning there is sufficient charge in the vicinity to generate a discharge pathway. However, Gen 9.3 and 9.6 have the same insulating layer as 9.1 but discharge limits that are 11 and 22% higher than 9.1. The thick device layer of 9.3 likely acted as a charge sink, suppressing the conditions for flashover and neutralizing a portion of the ions generated via EI in the vicinity of surfaces. Gen 9.6 has a nearly identical device layer thickness as gen 9.1 and the highest limit on discharge field strength. This is likely due to a geometric suppression of the surface flashover by the notch seen in Figure 4.13b.[42] While the notch was not planned for, it may have shown a way to intentionally design the microionizer to sustain higher field strengths at the cost of field emission current.

The plots in Figure 4.14 show further evidence of the microionizer working as a field emission source. The results of a gating experiment are plotted in in Figure 4.14a for a Gen 9.5 microionizer at 1 Torr. The field strength was held constant at 2.0 MV/cm by applying a voltage of -60 V across the 0.3 μm insulating layer. An additional bias of -25 V was applied, therefore the maximum kinetic energy of the electrons leaving the surface of the emission source was -85 eV. As the gate potential was changed from 0 to -75 V, the signal decreases to zero, indicating the microionizer is a source of negative charge. It is important to note that the EMT detects positive ions, thus the loss in signal is because electrons arriving at the gate electrode no longer have sufficient energy to perform EI. This conclusion is also consistent with the mass spectrometry-based results shown in Chapter 3.

While field emission has been demonstrated, one key aspect has been ignored, power consumption. Figure 4.14b plots each Gen 9 microionizer's average current draw as a function of field strength. All four variants demonstrate a similar improvement in leakage current over the Early stage microionizers as shown in Figure 4.9. In particular, Gen 9.1 and 9.5 demonstrated their maximum field emission strengths at 1.8 MV/cm, which required voltage pulses of -180 and -55 V, respectively. The corresponding current for each was 0.6 and 0.2 μA; yielding an average power consumption of 110 and 11 μW. With a duty cycle of 3.6% (1 of 28 ms), the peak powers were 3.0 and 0.3 mW. An important note is the amplitude of Gen 9.5. It had the thinnest insulating layer and was able to operate at only 55 V of amplitude. This low power consumption is advantageous for use in a portable instrument that most likely will be powered by a battery. In comparison to the alternative glow discharge ionization source operating at 1 Torr of air under identical duty cycle conditions, the GD source runs with a pulse of 625 V and draws 35 μA, yielding average and

peak powers of 21.8 and 605 mW. The glow discharge consumes over 1900 times more power than the microionizer.

4.4.3 Positive Mode Operation

Positive mode operation is believed to produce field ionization. Early stage devices were periodically operated in positive mode operation but the insulating layers typically suffered fatal breakdown before ion generation was observed. This breakdown was believed to be a consequence of the high leakage current combined with the increased field strength required for field ionization versus field emission. With the reduced leakage current of the Gen 9 devices, positive mode operation was revisited. Using the same experimental setup as described in Figure 4.8, the polarity of the pulse and bias voltages were reversed with the results plotted in Figure 4.15. Signal intensity as a function of field strength is shown in Figure 4.15a for each Gen 9 device. The applied electric field was investigated from observable signal to values just shy of electric discharge. Ambient air was leaked into the chamber to monitor ionization and assumed to be constant with time. Each device shows an exponential increase in signal strength with the electric field. This behavior is expected under low-field conditions near the threshold for field ionization. For a single analyte at low pressures (< 0.1 mTorr), one would expect to see signal plateau as the probability of ionization approaches one.[43] However, the atmospheric sample is a mixture and each compound has a different ionization potential. Thus signal is not expected to plateau under these conditions. The current draw and power requirements under positive mode were also similar to field emission mode. The largest average current was measured at 2.7 μA for Gen 9.6, yielding average and peak power of 0.68 mW and 18 mW, respectively.

The results of a gating experiment performed in positive mode are shown in Figure 4.15b. The experiment is identical to that shown in Figure 4.14b, except a positive gate voltage was used to block the ion current. The gating experiment was performed with a Gen 9.5 device, pulsed with +70 V for an electric field of 2.3 MV/cm. An additional +25 V bias yielded a maximum ion kinetic energy of +95 eV. The signal dropped to zero as the gate potential increased from ground to +90 V. These results are consistent with ion generation occurring at the microionizer. However, it cannot differentiate whether the ion current is a result of field ionization or electron impact ionization.

The mechanism behind positive ion mode is believed to be field ionization though the gate aperture experiment cannot distinguish how the ions are generated – by direct field ionization or EI localized near the microionizer's surface. The electric field strength necessary for field ionization should be five to ten times greater than field emission, however for the microionizer this is not the case. For an emitter with well-defined geometry (radius of curvature and aspect ratio), an enhancement factor can be calculated assuming the work function is known. When the emission site is not defined as in our case, only a rough estimate of the enhancement can be made.[44] Theoretically, field emission should initiate at 10 MV/cm though it can range as high as 50 MV/cm for higher work functions.[18, 37] The microionizer initiates field emission near 1.4 MV/cm, thus a field enhancement factor is estimated at 8 to 35. The field ionization threshold also depends upon the ionization potential of an analyte.[43] Many compounds of interest (VOC, CWA, and explosives) have ionization potentials from 7 to 12 eV.[45] The threshold field strengths of these compounds are closer to 50 to 70 MV/cm.[46-47] Positive mode operation only requires a 10 to 50% increase in field strength (relative to field emission) to generate ions, yielding an estimated field

131

enhancement of 25. Because field emission and field ionization sources can operate with less than an order of magnitude between the modes,[48] the exact mechanism under positive mode operation is not known. To fully determine the mechanism, HPMS experiments looking at ion generation are needed.

4.5 Conclusions

The first generation microionizer produced mass spectra under HPMS conditions – showing that the microionizer design could operate in an oxygen-containing environment at 1 Torr. However, it failed one important test: low power operation. The mA-level leakage current was thought to negatively impact device-to-device reproducibility, signal intensity, and access to field ionization mode. This chapter documented the development from mask to device testing of a process flow that is capable of producing through-etched microionizers. The leakage current was reduced to the μA-level by combining proper metal-semiconductor contact pads with wire bonding. The microionizer demonstrated consistent operation from day-to-day and device-to-device, enabling studies of field emission and positive mode operation for several Gen 9 variants. Each variant demonstrated field emission confirmed by Fowler-Nordheim and gating experiments, as well as a positive mode of operation confirmed via emission studies and gating. The variants demonstrated that a thin device layer is key to charge extraction. The best performing variant, Gen 9.1, had high fabrication yield with consistent field emission and positive mode operation. The mechanism behind positive mode operation could not be confirmed as either field ionization or device-localized electron impact ionization. Regardless, the microionizer demonstrated its utility as a dual-role ionization source. Moreover, it did so under all the requirements for portable, HPMS: 1 Torr

of atmospheric buffer gas and low power. Lifetime and mass spectral-level signal intensity

are investigated in Chapter 5 documenting microionizer use with HPMS.

4.6 Figures
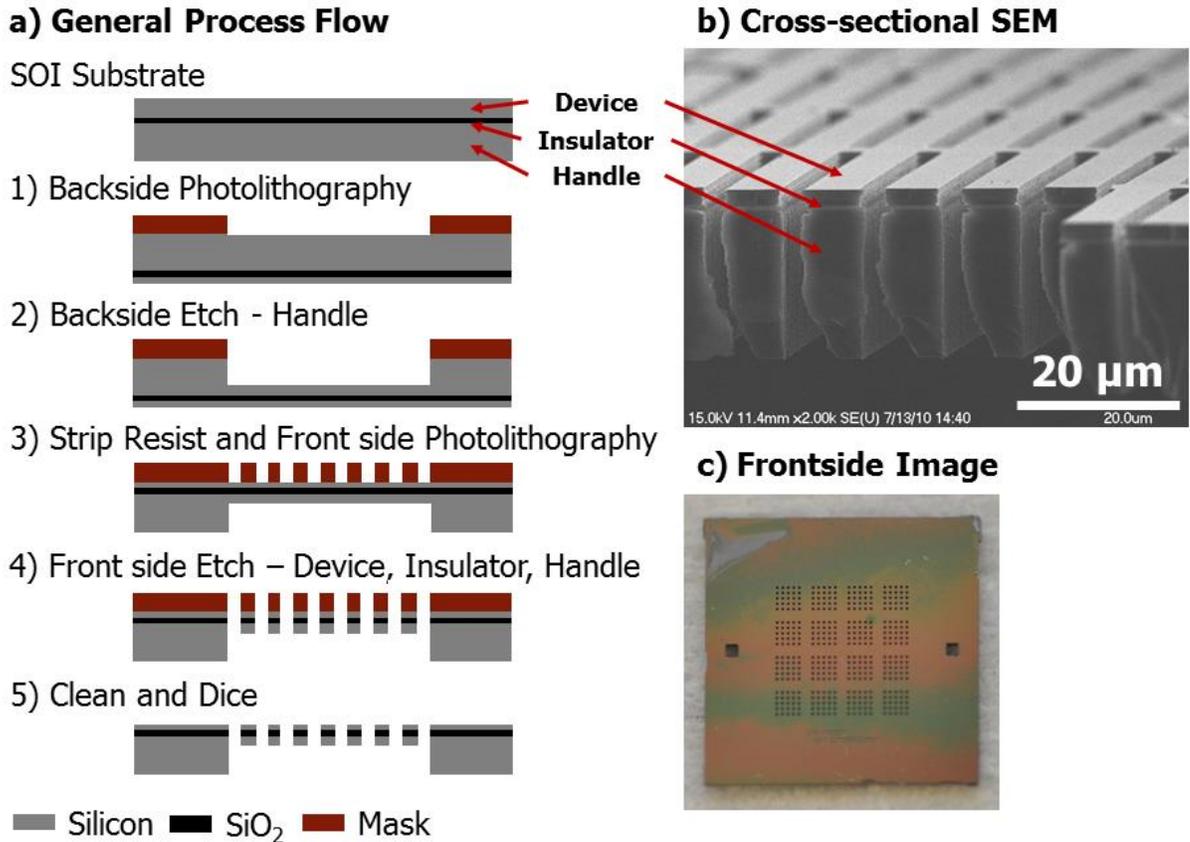
Figure 4.1: a) Process flow steps for Gen 1 devices beginning with a prime SOI substrate with device, insulator, and handle layers. 1) Handle layer mask is deposited and photolithographically patterned. 2) DRIE of handle layer window features as seen in b). 3) Resist is stripped and wafer cleaned, then the device layer mask is deposited before photolithographically defining the active features. 4) Device layer etch using DRIE for silicon and/or wet etch for insulating layer. 5) Masking removed and wafer cleaned before dicing. b) Cross-sectional SEM of the membrane produced by the fabrication process. The location of the silicon-insulator interface of the SOI is near the device layer and the supporting handle layer has been thinned to ~ 25 μm. c) Optical image of the device layer of a completed 100 μm diameter Gen 1 device.
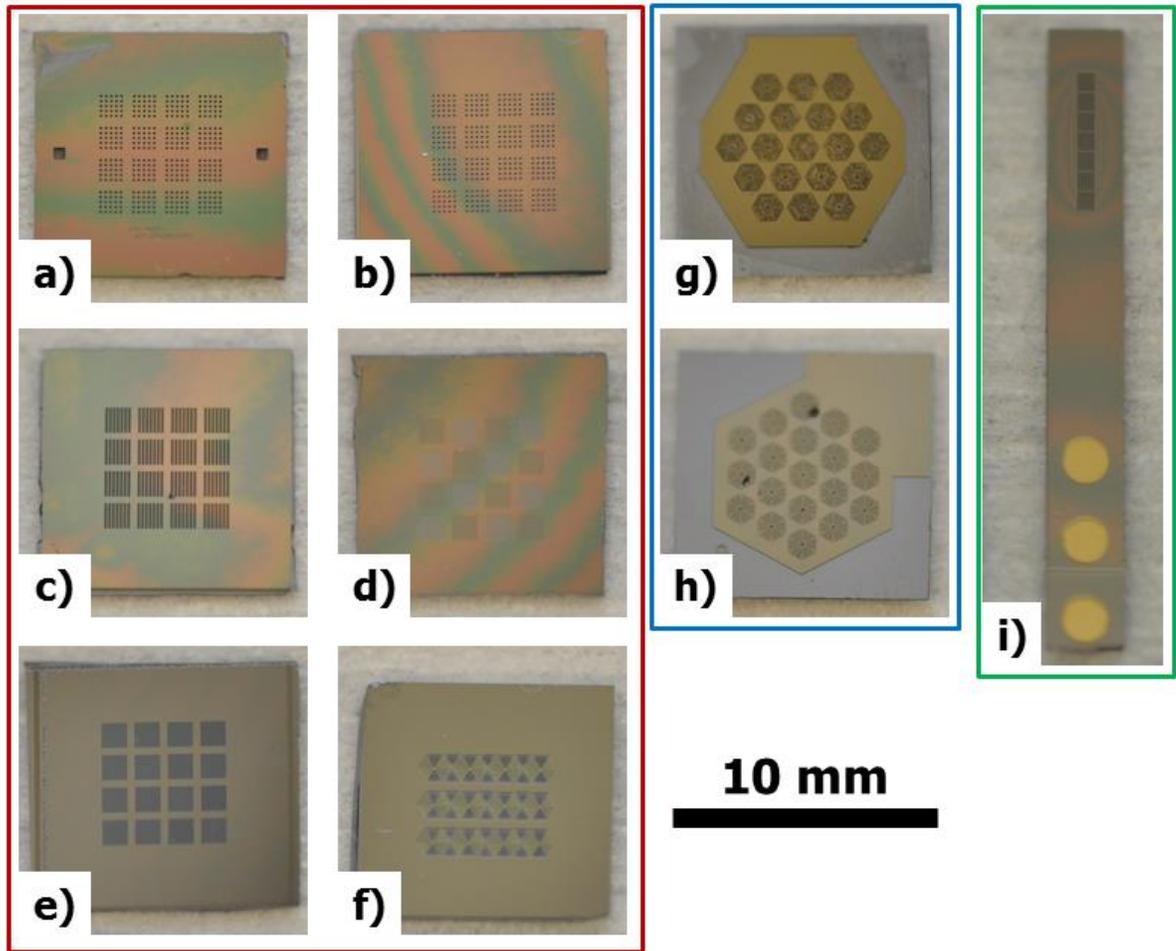
Figure 4.2: Optical image of representative microionizers. The three eras of development from UNC Chapel Hill are highlighted: Early (■); Optimization (■); and Final (■). a) Gen 1, 100 μm radius features b) Gen 2, 100 μm radius features c) Gen 3, 10 x 90 μm^2 trench d) Gen 4, 10 x 90 μm^2 trench e) Gen 5, 10 x 90 μm^2 trench f) Gen 6, 3-SLIT array of 10 μm width trenches g) Gen 7, 19-element, CIT array of 10 μm width trenches h) Gen 8 with identical elements as Gen7. The device layer is expanded (relative to Gen 7) to facilitate device layer electrical contact. i) Gen 9, single-SLIT compatible 10 x 90 μm^2 trenches. Early generations mimicked the Gen 1 with 5, 20, and 100 μm circular features as well as 5 x 90 μm^2 trenches. Subsequent generations used only trench features, 10 μm in width of varying lengths that were arrayed to match the ion traps' layout. Gen 1, 7, 8, and 9 were all through-etched.

Generation(s)	Type	Diameter (mm)	Device Type (Dopant)	Thick (μm)	Insulator Type	Thick (μm)	Handle Si (Dopant)	Thick (μm)
1	SOI	100	Si (Sb)	2	Oxide	0.5	Sb	400
2, 3, 4	SOI	76.2	Si (Sb)	2	Oxide	0.5	Sb	400
5.1	SOI	100	Si (Sb)	12	Oxide	0.5	Sb	450
5.2	SOI	150	Si (B)	5	Nitride	0.5	B	600
6, 9.1, 9.3, 9.6	SOI	150	Si (Sb)	10	Ox/Ni/Ox	0.4/0.3/0.3	Sb	450
7	Alt	150	Ti/Cr	0.015/.25	Nitride	0.6	B	500
8.1	SOI	150	Si (B)	5	Oxide	1	B	500
8.2, 9.5	Alt	150	Ti/Cr	0.015/.2	Oxide[*]	0.3	Sb	420
8.3, 8.4, 9.4	Alt	150	PolySi (As)	0.5	Nitride	1	Sb	450
9.2	Alt	150	PolySi (As)	0.5	Oxide[*]	0.3	Sb	420

Table 4.1: Substrate characteristics for each generation of microionizer.
* denotes dry, thermal oxide. Alt = alternative to SOI. All silicon is single-crystal, <100> unless specified.

Step #	Wafer Side	Description	Fab Tool	Notes
1	Back	Ti/Cr Mask Deposition	e- Beam	Pump down at least 4 h
2	Back	Photolithography - AZ9260 Resist	Lithography	Spin Coater/Mask Aligner. Resist thickness 7 μm.
3	Whole	Chrome etch	N/A	Transfer resist pattern into the chrome mask
4	Back	Isotropic Si etch of backside windows	RIE	375 μm etch depth
5	Whole	Heated Nanostrip 2X	N/A	Strip any remaining organics
6	Whole	Chrome etch	N/A	Strip chrome mask
7	Whole	RCA Cleaning	N/A	Remove particles, organics, and metals
8	Front	Photolithography - AZ9260 Resist	Lithography	Double-side aligned. Resist thickness 7 μm.
9	Front	Anisotropic Si etch of device layer	DRIE	Etch is looped for 30 s on and 35 s off. Depth depends on device layer thickness
10	Front	Anisotropic Insulator etch	DRIE	Etch is looped, mainly a physical sputtering
11	Front	Anisotropic Si etch of handle	DRIE	Same etch as device layer, ~75μm depth
12	Front	Oxygen plasma clean	DRIE	Strip photoresist
13	Front	Anisotropic Si etch, thin device layer	DRIE	Same etch as device layer, aiming for < 3 μm device layer thickness
14	Front	Oxygen plasma clean	DRIE	Strip leftover passivation fluoropolymer
15	Whole	Heated Nanostrip 2X	N/A	Strip any remaining photoresist
16	Whole	RCA Cleaning	N/A	Remove particles, organics, and metals
17	Front	Ti/Pd/Au electrical contact deposition	e- Beam	Pump down at least 5 h. Contact pads defined by kapton shadow mask (< 100 μm thick)
18	Whole	Anneal contacts at 450° C	Furnace	Under forming gas to prevent oxidation
19	Whole	Dicing	Dicer	Diced completely, 2 cuts/street
20	N/A	Affix die to PCB with epoxy	Oven	EpoTek LHC epoxy
21	N/A	Au-Ribbon Bonding	Wire Bonder	Ribbon is 0.5 x 1.5 mil^2

Table 4.2: Final process flow from wafer to microionizer.
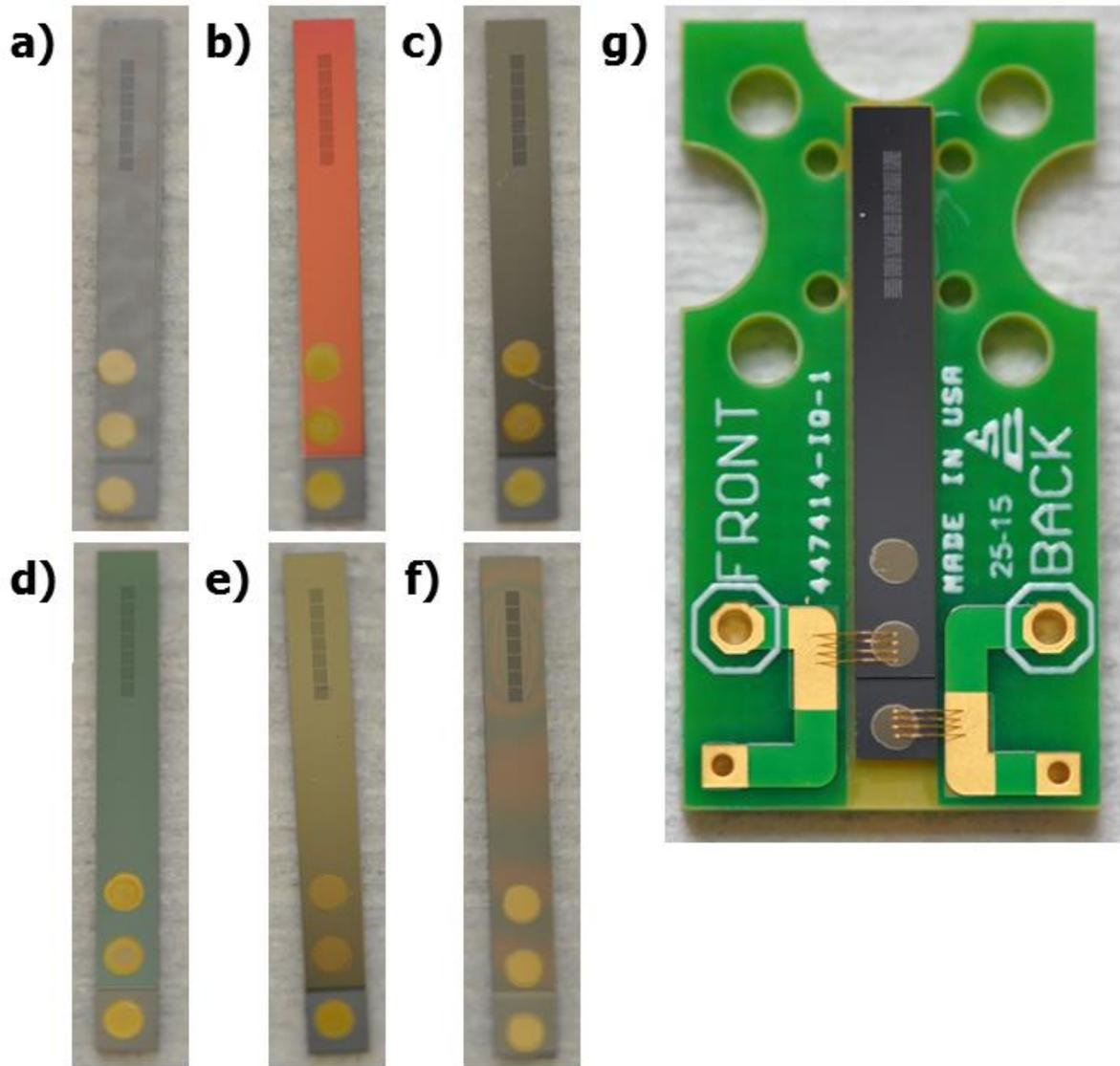
Figure 4.3: Optical images of 9th generation silicon dies (2.5 x 20 mm^2). a) through f) are Gen 9.1 to 9.6, respectively. g) Image of a wire-bonded Gen 9.6 microionizer. Gen 9.1 to 9.5 are single-side etched. Gen 9.6 is a through-etched version of the best performing variant, Gen 9.1. The active features for all six variants are 5 x 90 μm^2 trenches. The circular features are gold wire bonding pads deposited by e-beam evaporation. The pad at the bottom of each device is for handle layer electrical contact, the remaining pads are for device layer contact.

a) SLIT Ring Electrodes

b) Differential Chamber HPMS

Mass Analysis Chamber

Detector Chamber
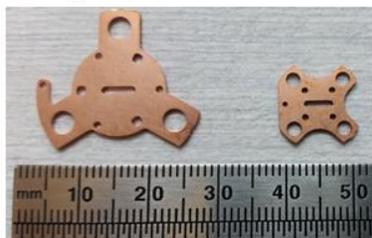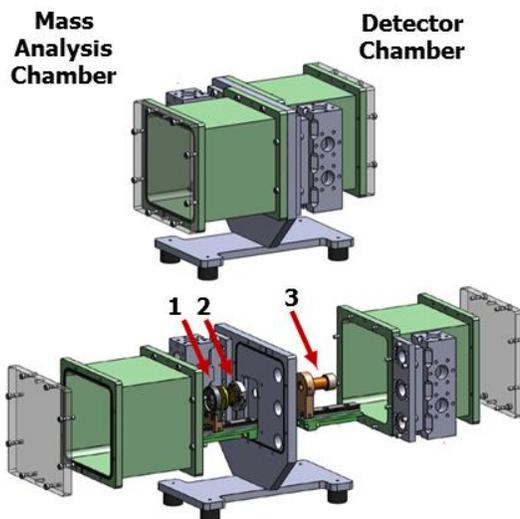
c) Mini-chamber v1.0
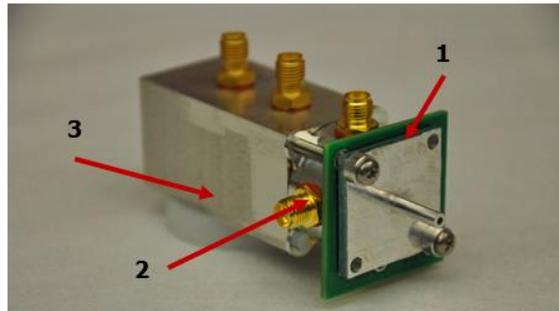
d) Trap-Mounted Chamber
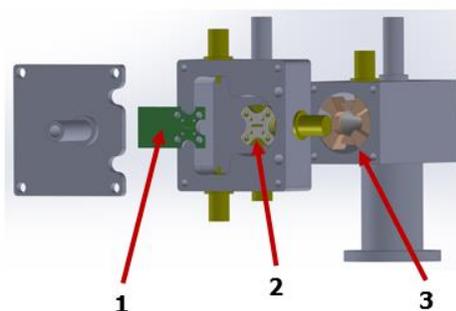
Figure 4.4: Evolution of the HPMS. a) Image of the SLIT ring electrodes used. The full-size electrode (left) was used in the differentially pumped system while the compact electrode (right) was compatible with all versions of the HPMS. b) Original differentially pumped chamber used for Chapter 2 and Chapter 3 experiments. The labeled features: 1, 2, and 3, highlight the ionization source, mass analyzer, and detector, respectively. c) The mini-chamber, shown with an electron multiplier detector housing. The SMA feedthroughs are vacuumed sealed and soldered directly to the ion trap. d) A microionizer-specific variation of the minichamber; the trap-chamber volume was adapted to include the entire microionizer-PCB-SLIT assembly.
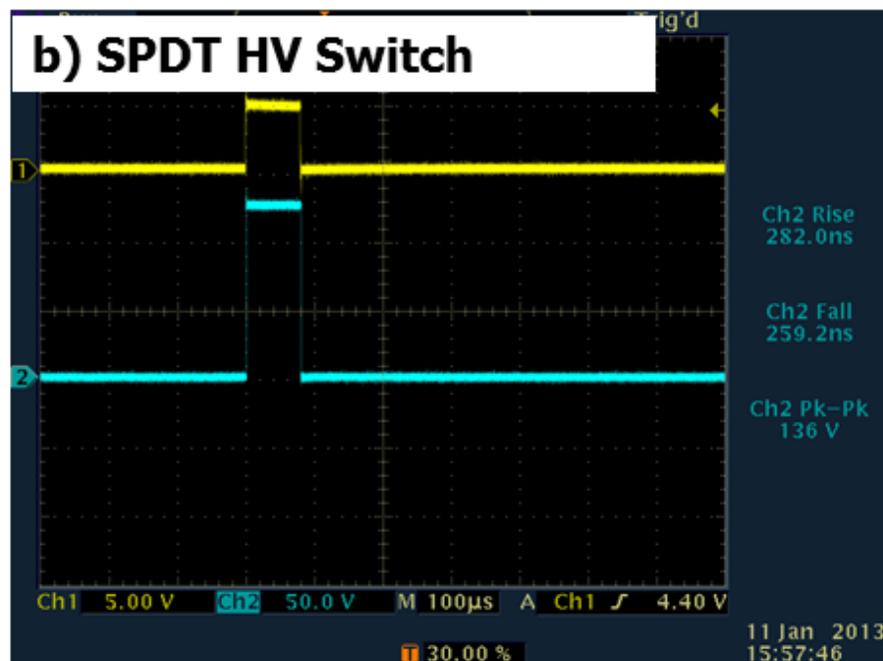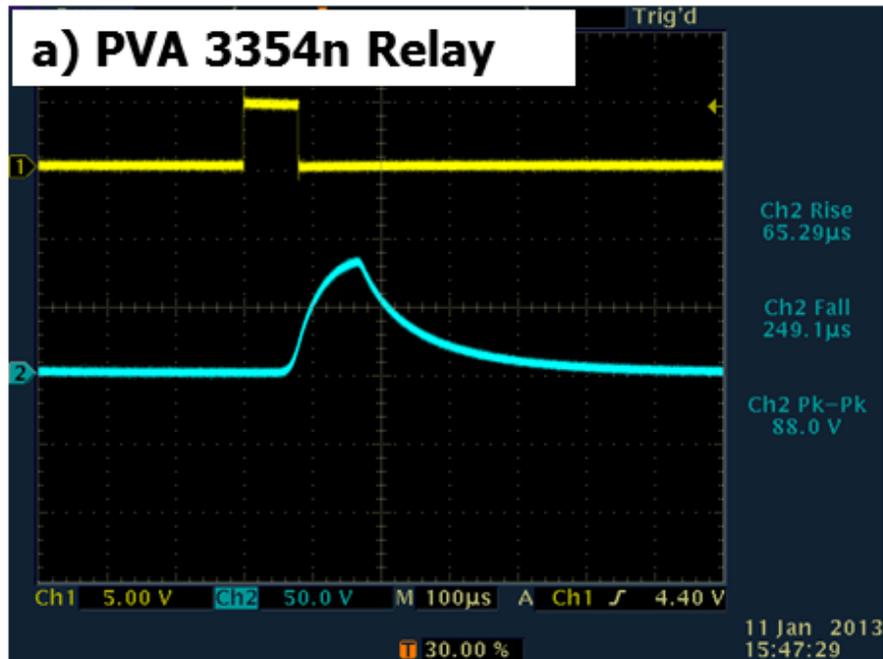
Figure 4.5: Oscilloscope screen shot of voltage pulse generation by the a) PVA 3354n relay and b) the Single-Pull, Double-Throw High-Voltage Switch. The control pulse (—) for both circuits is 80 μs TTL. The output (—) pulse is each circuits' attempt to reproduce the control pulse at +125 V amplitude. While the relay has an inherent delay of about 80 μs, the real problem is in the rise and fall times that are longer than the pulse length, preventing the pulse from achieving full amplitude. The HV Switch has virtually no delay as well as 200 to 1000-fold faster rise and fall times.
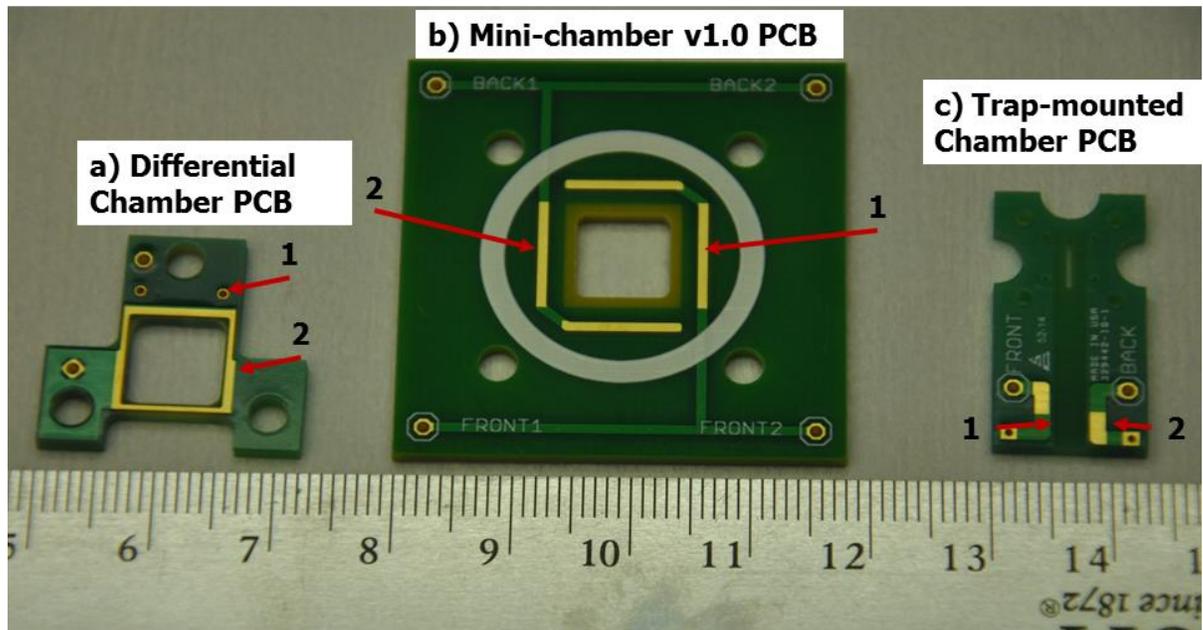
Figure 4.6: Evolution of the microionizer PCB mount. **1** and **2** refer to device layer and handle electrical contact locations, respectively. a) The PCB was used with Gen 7 inside the differential chamber. A wire was soldered at point 1, which would then be silver pasted/epoxied to the front side of the device. b) The mini-chamber compatible PCB used with the Gen 8 microionizer. It was with wire/epoxy bonding as well as wire bonding. c) The trap-mounted microionizer PCB exclusively used for Gen 9 and designed for gold wire bonding. The bond pads are approximately 1.5 cm from the ionizer features in order to clear the ion trap electrodes when laid face-down for trap mounting.
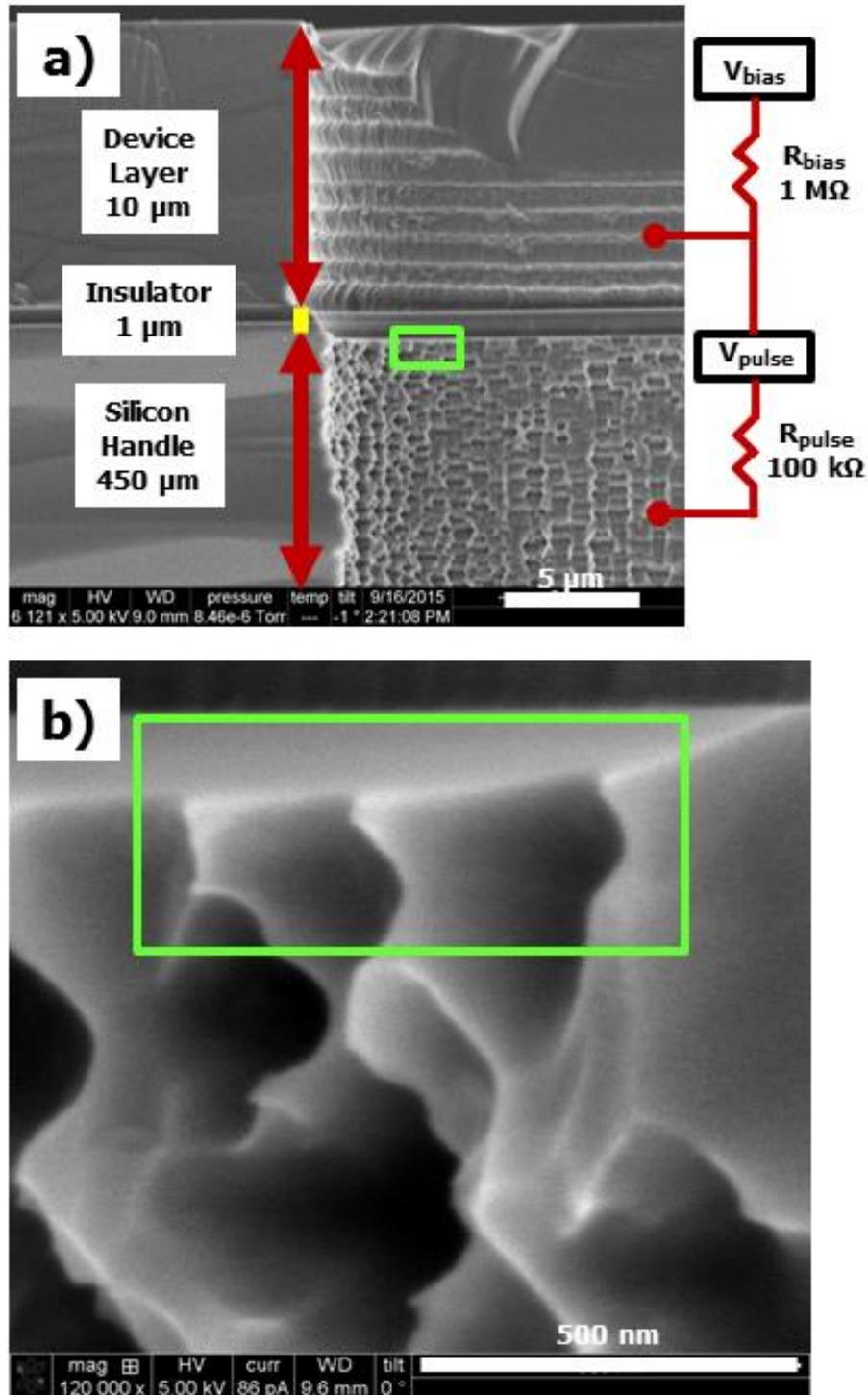
Figure 4.7: a) Cross-sectional SEM of Gen 9.3 device, the bias and pulse voltages are schematically shown. Field emission uses negative bias and pulse, while positive mode uses positive polarity. b) High-resolution SEM of field enhancement sites.
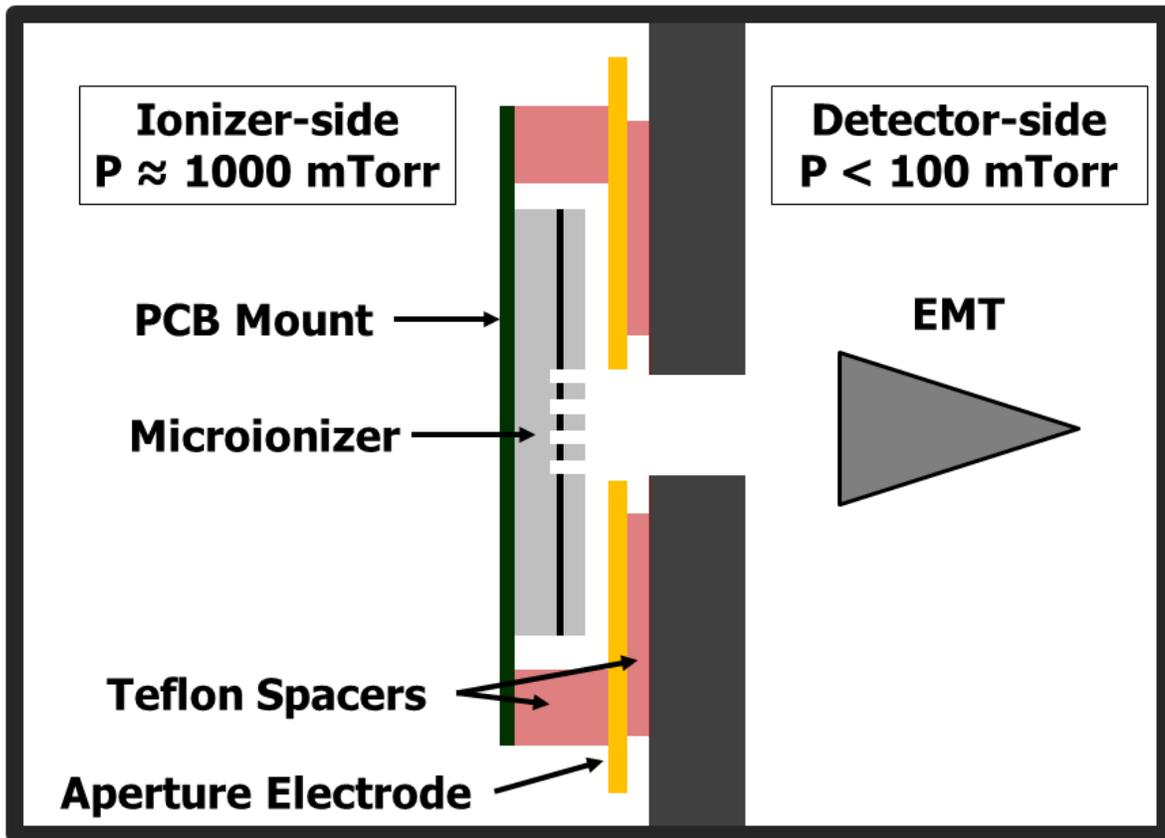
Figure 4.8: Schematic of the ionizer test setup (not to scale). An aperture was used to maintain differential pressure between two chambers, ionization and detector. The microionizer and aperture were operated at high pressure (~ 1 Torr) and the EMT detector was held at low pressure. The spacing between the ionizer and aperture was 100 μm, and the aperture was electrically isolated in order to be used as a gate electrode.
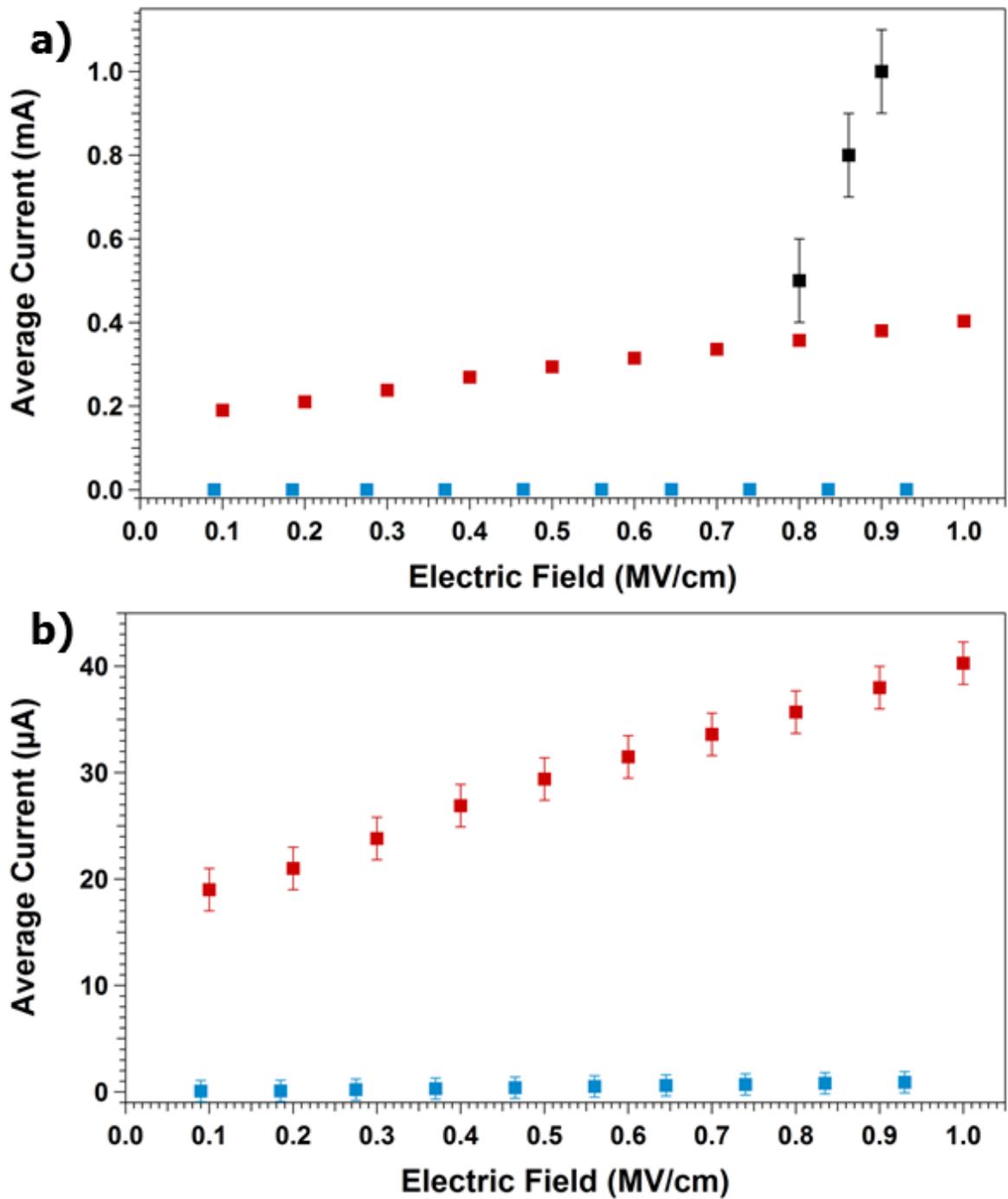
Figure 4.9: a) Representative current draws as a function of electric field strength for three generations of microionizers: Gen 5 (■); Gen 8 (■); and Gen 9 (■). b) A magnified view of Gen 8 and Gen 9 results. These traces were recorded in field emission mode and the duty cycles were 0.1, 0.2, and 4.43%, respectively.
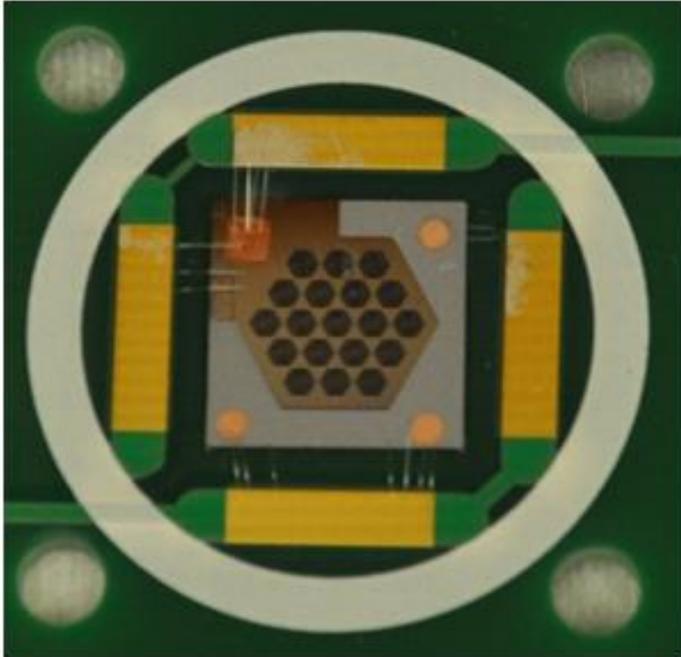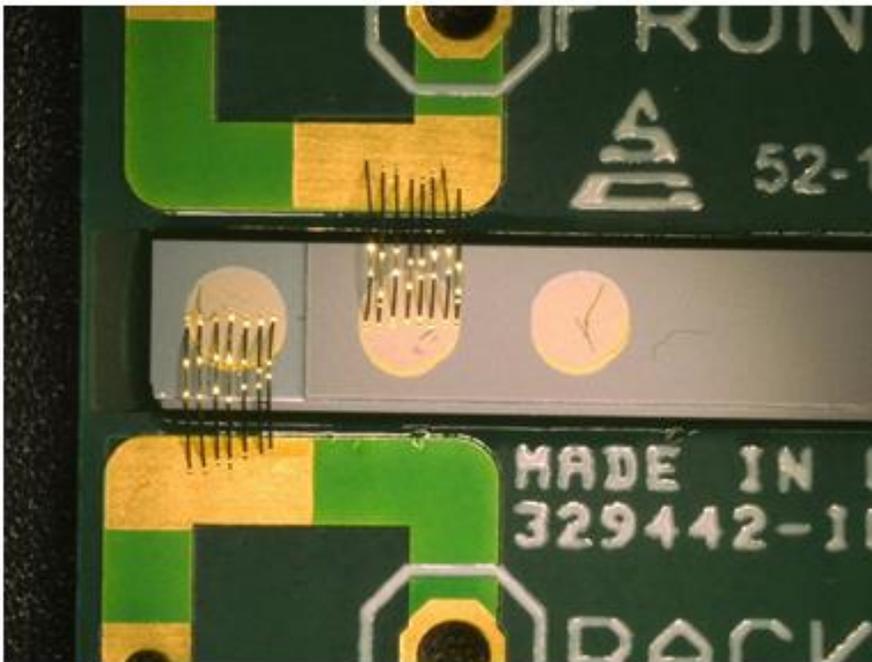
Figure 4.10: Images of a) Gen 8 wire bonds utilizing 1 mil diameter aluminum wire and titanium/copper bond pads and b) Gen 9 wire bonds consisting of 0.5 x 1.5 mil^2 gold ribbon and titanium/palladium/gold bond pads.

145
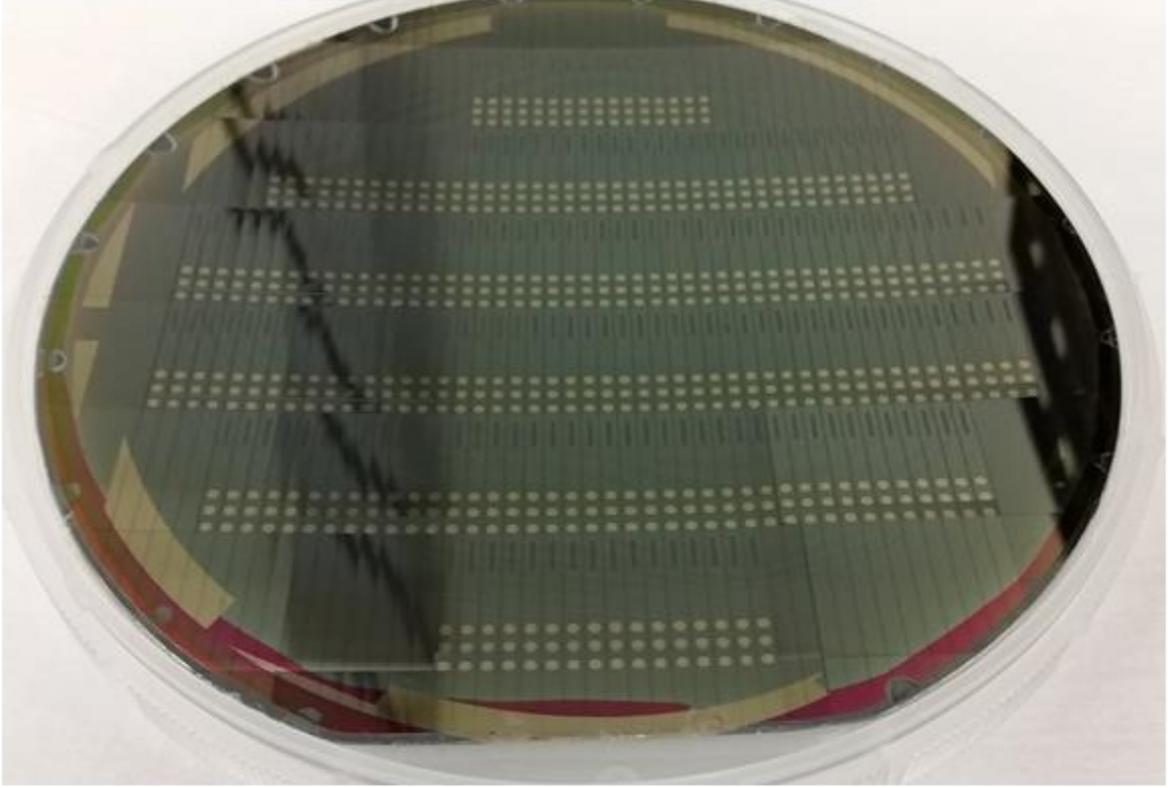
a) Processed Wafer

b) Wafer-level Analysis

Wafer Yields and Device Capacitance

- Gen 9.1: 97% and 1.42 ± 0.11 nF
- Gen 9.2: 73% and 4.44 ± 0.05 nF
- Gen 9.3: 100% and 1.52 ± 0.01 nF
- Gen 9.4: 43% and 2.21 ± 0.69 nF
- Gen 9.5: 83% and 4.46 ± 0.07 nF
- Gen 9.6: 90% and 1.48 ± 0.01 nF

Figure 4.11: a) Image of processed Gen 9.6 wafer. b) Results of wafer-level failure analysis. The Gen 9 mask afforded 208 devices per 150 mm silicon wafer. The capacitance of 30 devices from each variant was measured to determine the fabrication yield and average capacitance. Low yields were the result of shorted devices, likely due to stress fractures in the insulating layer.

Gen	Etch	Device	Insulator	Tests
9.1	Single	3 μm, SC-Si	0.3/0.4/0.3 μm, $SiO_2/Si3N_4/SiO_2$	Thinned device layer, proven insulator
9.2	Single	0.5 μm, poly-Si	0.3 μm, SiO_2	Polysilicon on proven insulator
9.3	Single	10 μm, SC-Si	0.3/0.4/0.3 μm, $SiO_2/Si3N_4/SiO_2$	Thick device layer on proven insulator
9.4	Single	0.5 μm, poly-Si	1.0 μm, Si_3N_4	Polysilicon on custom insulator
9.5	Single	0.25 μm, Cr	0.3 μm, SiO_2	Metal device layer on proven insulator
9.6	Through	3 μm, SC-Si	0.3/0.4/0.3 μm, $SiO_2/Si3N_4/SiO_2$	Through-etch of best combination

Table 4.3: List of the substrates used for Gen 9 devices. 'Tests' denotes the key feature(s) of the wafer for differentiation.

.
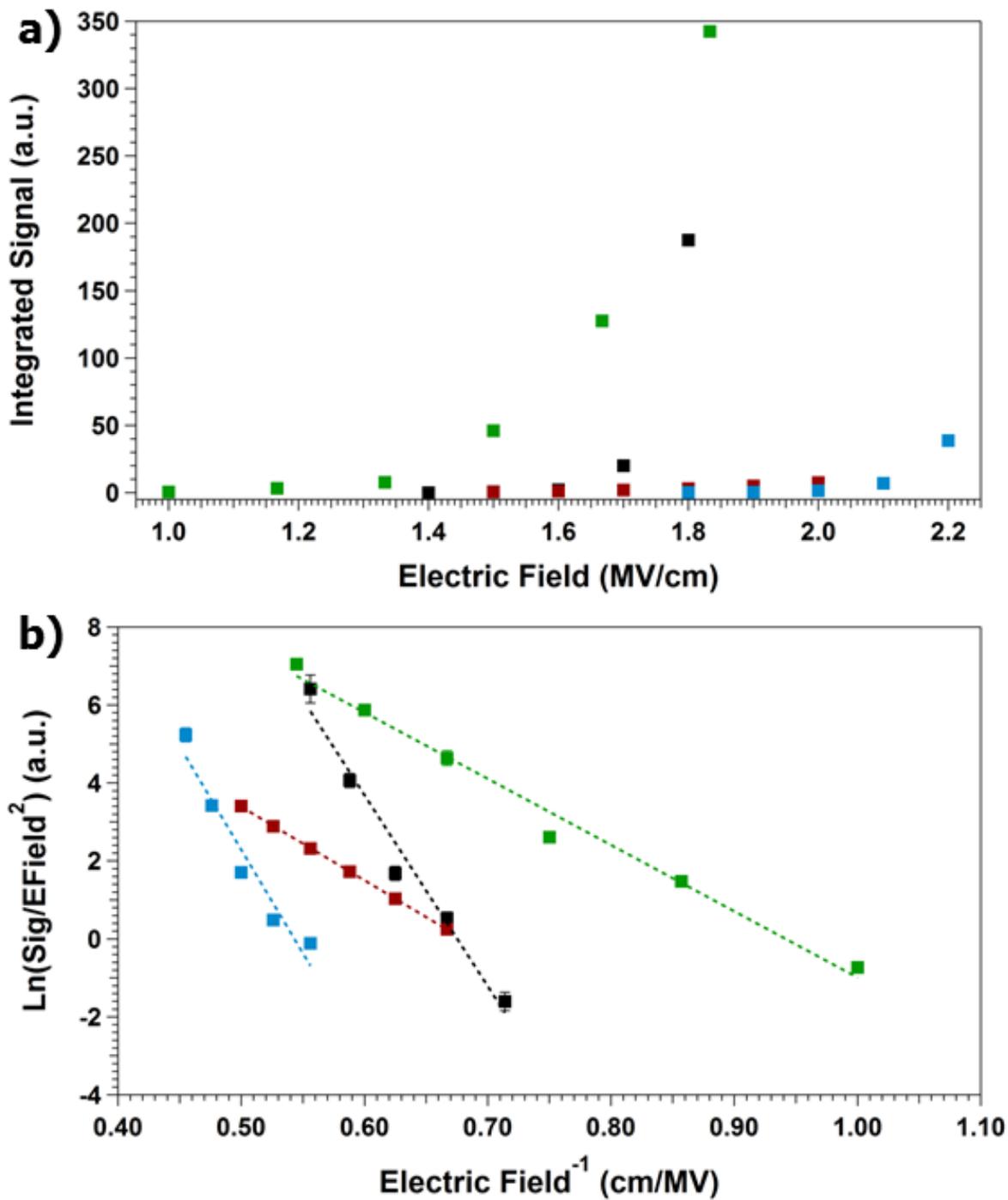
Figure 4.12: a) Field emission as a function of electric field strength for Gen 9.1 (■), 9.3 (■), 9.5 (■), and 9.6 (■). Field emission is an exponential function of applied field. b) Fowler-Nordheim plots of the field emission shown in part a). A linear fit has been applied to each (dashed lines). A linear FN relationship is indicative of field effect-based electron emission.

148
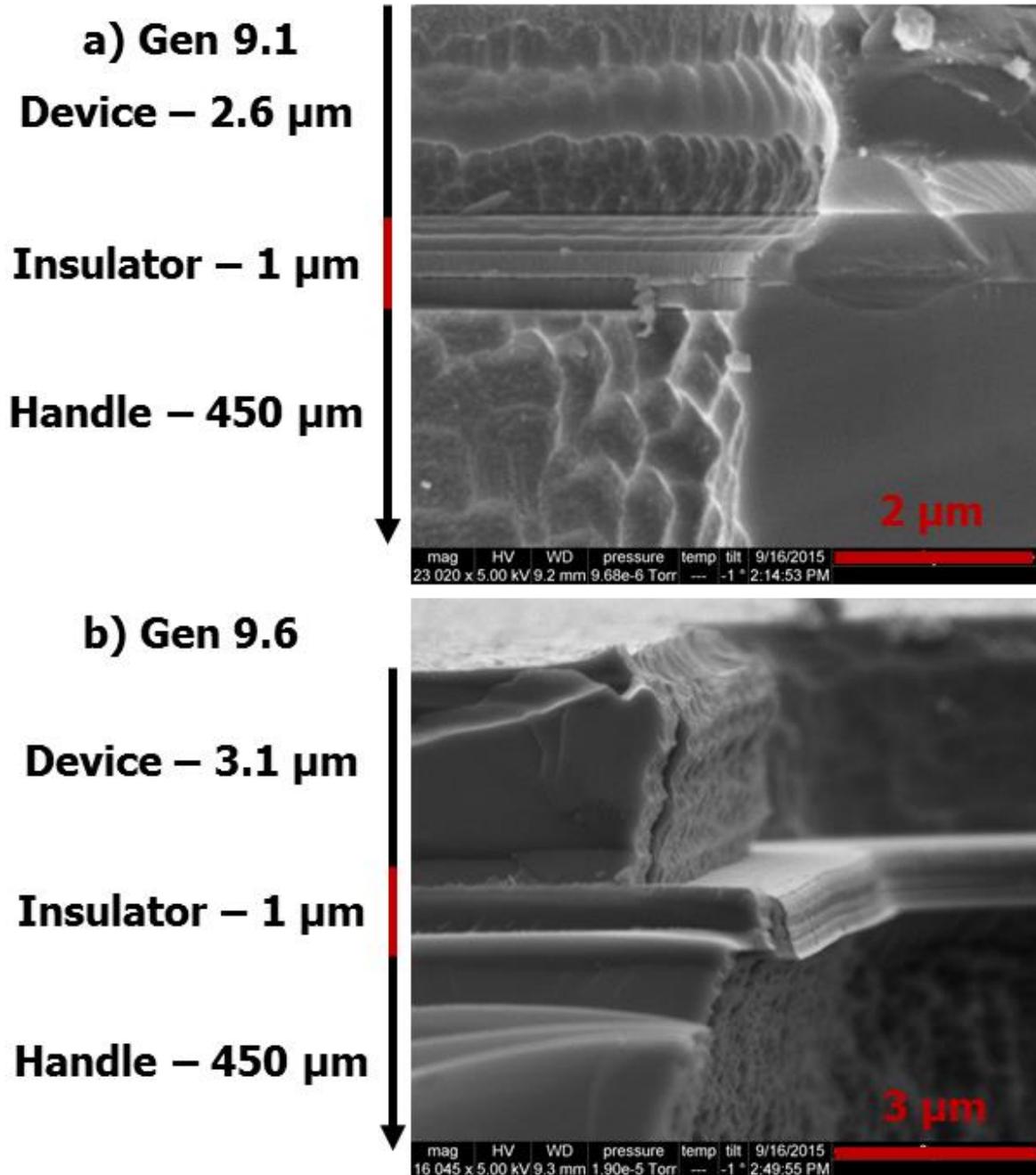
Figure 4.13: Cross sectional SEM of Gen 9.1 a) and Gen 9.6 b). There is an obvious notching as a result of the through-etch process. This is the likely cause of the increased threshold field strengths seen in the Gen 9.6 field emission and positive mode operation relative to the other variants.
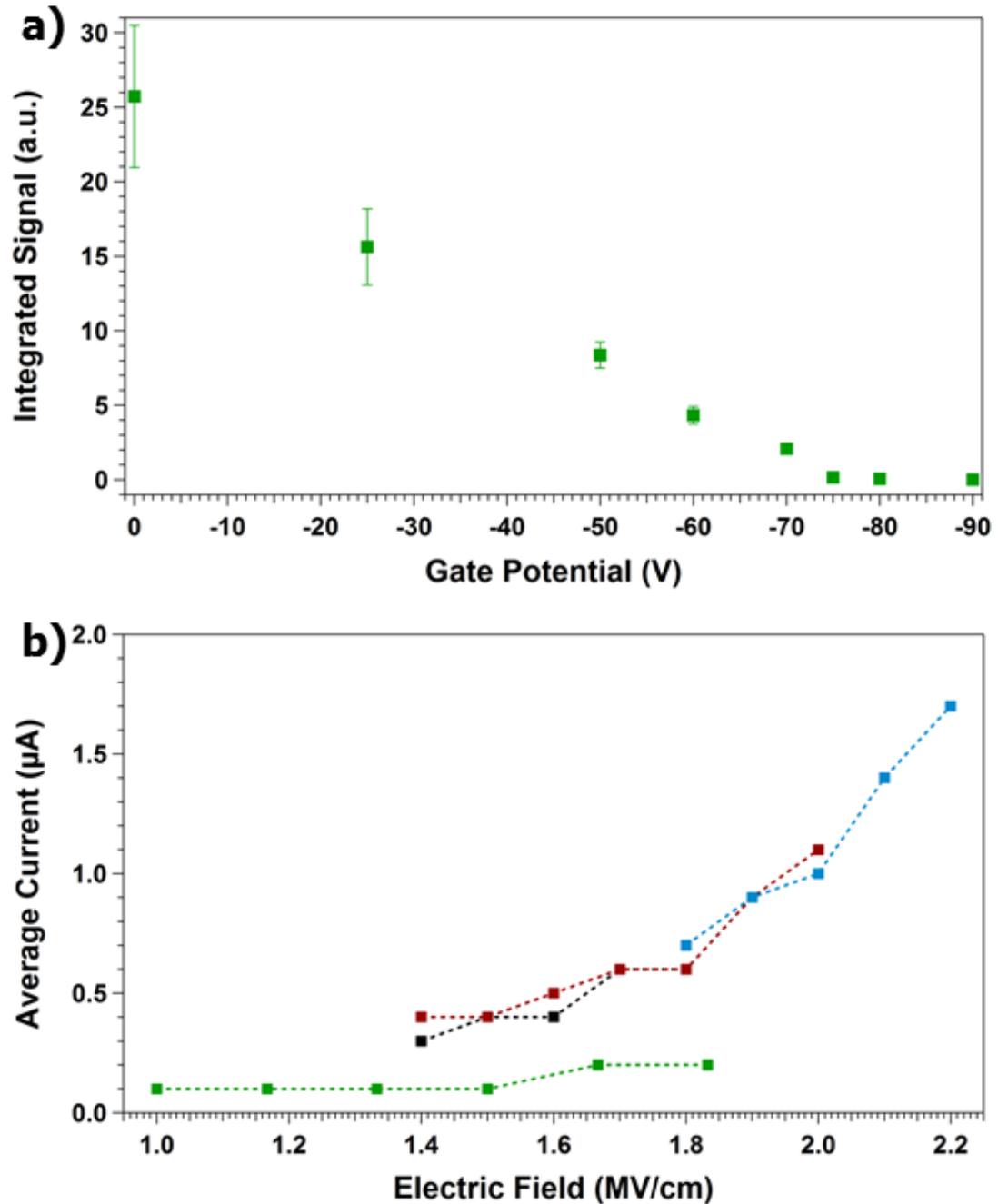
Figure 4.14: a) Field emission signal (■) as a function of a gating potential at 1 Torr for a Gen 9.5 microionizer. The electrons obtain 85 eV from the microionizer and interactions with the buffer gas decrease it. Eventually, near -75 V on the gate, electrons do not have sufficient energy to generate signal at the detector. b) Average current draws versus field emission pulse voltage as measured for representative devices from Gen 9.1 (■), 9.3 (■), 9.5 (■), and 9.6 (■). The pulse duration is 1 ms and duty cycle is 4.2%. The points are connected to aid viewing (dashed lines).
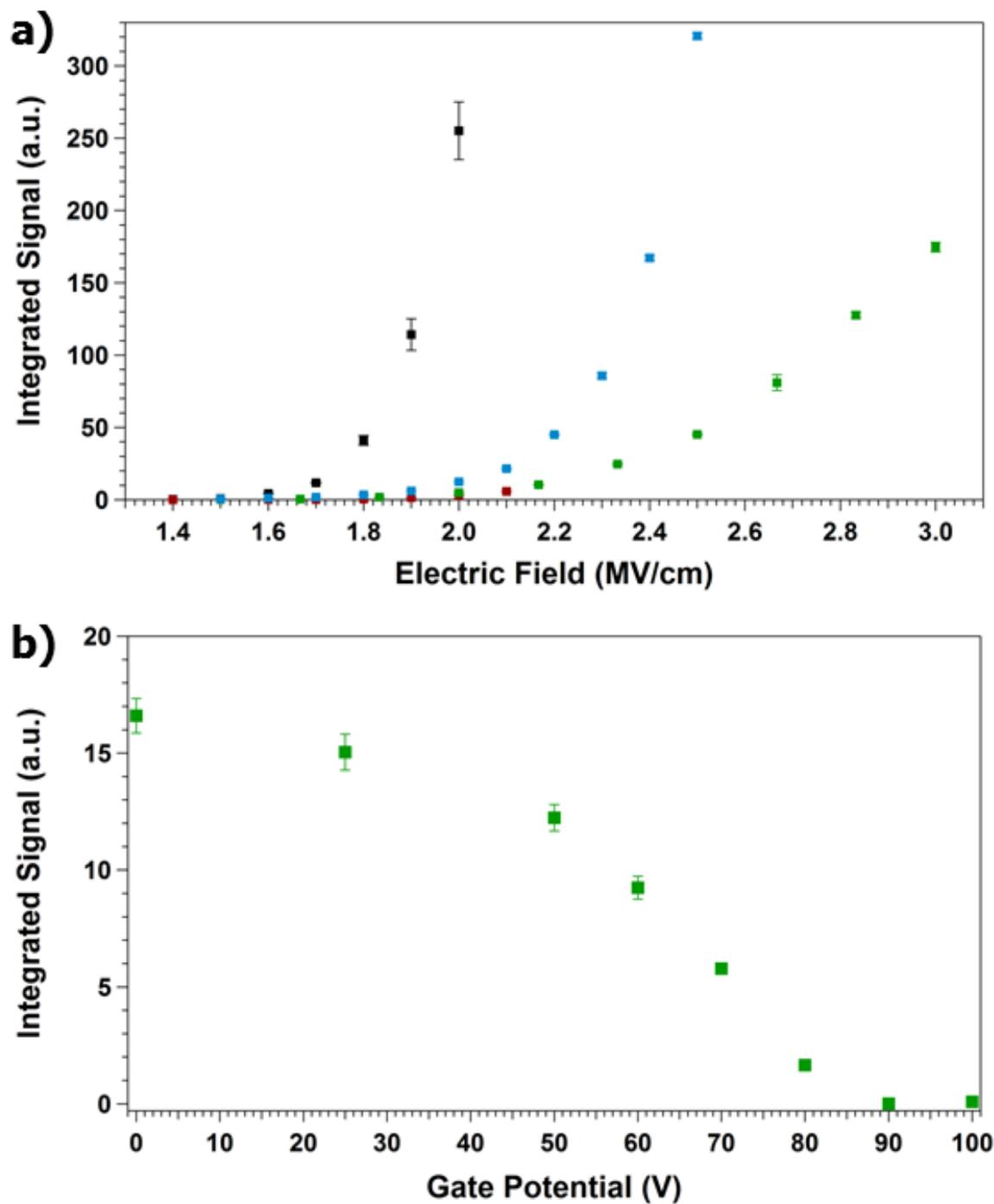
Figure 4.15: a) Field ionization signal as a function of electric field strength for Gen 9.1 (■), 9.3 (■), 9.5 (■), and 9.6 (■). a) Field ionization signal as a function of a gating potential for a Gen 9.5 microionizer at 1 Torr. The ions obtain 105 eV from the microionizer. As gate potential increases, they are deflected from the detector. The microionizer is a source of positive charge in this mode, indicative of field ionization.

4.7 REFERENCES

1. Chiu, F. C., A Review on Conduction Mechanisms in Dielectric Films. *Adv Mater Sci Eng* **2014**.

2. DiMaria, D. J.; Stathis, J. H., Ultimate limit for defect generation in ultra-thin silicon dioxide. *Appl. Phys. Lett.* **1997,** *71* (22), 3230-3232.

3. Osburn, C. M.; Weitzman, E. J., Electrical-Conduction and Dielectric Breakdown in Silicon Dioxide Films on Silicon. *Journal of the Electrochemical Society* **1972,** *119* (5), 603-609.

4. Demey, G.; Dewilde, W., Influence of Mobile Ions on Electronic Conduction in Silicon-Oxide Films. *Thin Solid Films* **1974,** *23* (3), 301-304.

5. Laermer, F.; Schilp, A., Method of anisotropically etching silicon. Google Patents: 1996.

6. Madou, M. J., *Fundamentals of microfabrication and nanotechnology*. 3rd ed.; CRC Press: Boca Raton, FL, 2012.

7. Taur, Y.; Ning, T. H., *Fundamentals of modern VLSI devices*. 2nd ed.; Cambridge University Press: Cambridge, UK ; New York, 2009; p 656.

8. Fomani, A. A., et al., Low-Voltage Field Ionization of Gases Up to Torr-Level Pressures Using Massive Arrays of Self-Aligned Gated Nanoscale Tips. *Ieee Transactions on Electron Devices* **2014,** *61* (5), 1520-1528.

9. Cruz, D., et al., Field emission characteristics of a tungsten microelectromechanical system device. *Appl. Phys. Lett.* **2005,** *86* (15), 153502.

10. Blakeman, K. H., et al., High-Pressure Mass Spectrometry at Pressures Exceeding 1 Torr in a Microscale Cylindrical Ion Trap. *Manuscript in preparation* **2015**.

11. Schultze, K. P. Advanced System Components for the Development of a Handheld Ion Trap Mass Spectrometer. Dissertation, University of North Carolina at Chapel Hill, Chapel Hill, NC, 2014.

12.   Stuart, M., Conduction in Silicon Oxide Films. *Brit J Appl Phys* **1967,** *18* (11), 1637-1640.

13.   Your Guide to SEMI Specifications for Si Wafers. http://www.virginiasemi.com/pdf/semi%20specificationsoverview71002.pdf (accessed 10/8/2015).

14.   Fowler, R. H.; Nordheim, L., Electron Emission in Intense Electric Fields. *Proceedings of the Royal Society A: Mathematical, Physical and Engineering Sciences* **1928,** *119* (781), 173-181.

15.   Allen, F. G.; Gobeli, G. W., Work Function, Photoelectric Threshold, and Surface States of Atomically Clean Silicon. *Physical review* **1962,** *127* (1), 150-158.

16.   van Gorkom, G. G. P.; Hoeberechts, A. M. E., Performance of silicon cold cathodes. *Journal of Vacuum Science and Technology B* **1986,** *4*, 108-111.

17.   Whaley, D. R., et al., 100 W Operation of a Cold Cathode TWT. *Ieee Transactions on Electron Devices* **2009,** *56* (5), 896-905.

18.   Schroder, D. K., et al., Semiconductor Field-Emission Photocathode. *Ieee Transactions on Electron Devices* **1974,** *Ed21* (12), 785-798.

19.   Baskin, L. M., et al., General Features of Field Emission from Semiconductors. *Phys Status Solidi B* **1971,** *47* (1), 49-62.

20.   Celler, G. K.; Cristoloveanu, S., Frontiers of silicon-on-insulator. *J Appl Phys* **2003,** *93* (9), 4955-4978.

21.   Lau, S. P., et al., Changes in the Poole-Frenkel coefficient with current induced defect band conductivity of hydrogenated amorphous silicon nitride. *J Non-Cryst Solids* **1998,** *227*, 533-537.

22.   Harrell, W. R.; Frey, J., Observation of Poole-Frenkel effect saturation in SiO2 and other insulating films. *Thin Solid Films* **1999,** *352* (1-2), 195-204.

23. Osburn, C. M.; Ormond, D. W., Dielectric Breakdown in Silicon Dioxide Films on Silicon: II Influence of Processing and Materials. *Journal of the Electrochemical Society* **1972,** *119* (5), 597-603.

24. Swaroop, B.; Schaffer, P. S., Conduction in Silicon Nitride and Silicon Nitride-Oxide Films. *J Phys D Appl Phys* **1970,** *3* (5), 803-806.

25. Yota, J. In *Effects of Deposition Method of PECVD Silicon Nitride as MIM Capacitor Dielectric for GaAs HBT Technology*, Electrochemical Society Meeting, Montreal, Canada, Montreal, Canada, 2011.

26. Blakeman, K. H. Development of High Pressure Mass Spectrometry for Handheld Instruments. Dissertation, University of North Carolina at Chapel Hill, Chapel Hill, NC, 2015.

27. Märk, T. D.; Dunn, G. H., *Electron impact ionization*. Springer-Verlag: Wien ; New York, 1985; p 383.

28. Wu, B. Q., et al., High aspect ratio silicon etch: A review. *J Appl Phys* **2010,** *108* (5).

29. Jansen, H. V., et al., Black silicon method X: a review on high speed and selective plasma etching of silicon with profile control: an in-depth comparison between Bosch and cryostat DRIE processes as a roadmap to next generation equipment. *Journal of Micromechanics and Microengineering* **2009,** *19* (3).

30. Talin, A. A., et al., Field emission displays: a critical review. *Solid-State Electronics* **2001,** *45* (6), 963-976.

31. Xu, N. S.; Huq, S. E., Novel cold cathode materials and applications. *Mat Sci Eng R* **2005,** *48* (2-5), 47-189.

32. Harman, G. G.; Harman, G. G., *Wire bonding in microelectronics*. 3rd ed.; McGraw-Hill: New York, 2010; p 426.

33. Rhoderick, E. H., *Metal-semiconductor contacts*. Clarendon Press: Oxford, 1978; p 201.

34. Lum, I., et al., Footprint study of ultrasonic wedge-bonding with aluminum wire on copper substrate. *J Electron Mater* **2006,** *35* (3), 433-442.

35. Poate, J. M., et al., Thin-Film Interdiffusion .1. Au-Pd, Pd-Au, Ti-Pd, Ti-Au, Ti-Pd-Au, and Ti-Au-Pd. *J Appl Phys* **1975,** *46* (10), 4275-4283.

36. Morita, M., et al., Growth of Native Oxide on a Silicon Surface. *J Appl Phys* **1990,** *68* (3), 1272-1281.

37. Gomer, R., *Field emission and field ionization*. Harvard University Press: Cambridge, 1961; p 195.

38. Zhu, W., et al., Electron field emission from chemical vapor deposited diamond. *J Vac Sci Technol B* **1996,** *14* (3), 2011-2019.

39. Vangelde.W; Hauser, V. E., Etching of Silicon Nitride in Phosphoric Acid with Silicon Dioxide as a Mask. *Journal of the Electrochemical Society* **1967,** *114* (8), 869-872.

40. Pillai, A. S.; Hackam, R., Surface Flashover of Solid Insulators in Atmospheric Air and in Vacuum. *J Appl Phys* **1985,** *58* (1), 146-153.

41. Ono, T., et al., Micro-discharge and electric breakdown in a micro-gap. *Journal of Micromechanics and Microengineering* **2000,** *10*, 445-451.

42. Miller, H. C., Surface Flashover of Insulators. *IEEE T Electr Insul* **1989,** *24* (5), 765-786.

43. Heinen, H. J., et al., Appearance Potentials of Field Ions. *Z Naturforsch A* **1974,** *A 29* (5), 773-781.

44. Au, F. C. K., et al., Electron field emission from silicon nanowires. *Appl. Phys. Lett.* **1999,** *75* (12), 1700-1702.

45. Haynes, W. M., *Handbook of Chemistry and Physics*. 95th ed.; CRC Press: 2014; p 2693.

46.   Beckey, H. D., et al., Über die Feldstärkeabhängigkeit der Winkelverteilung feldemittierter Elektronen und Ionen. In *Zeitschrift für Naturforschung A*, 1966; Vol. 21, p 141.

47.   Beckey, H. D., *Principles of field ionization and field desorption mass spectrometry*. 1st ed.; Pergamon Press: Oxford Eng. ; New York, 1977; p 335.

48.   Rao, K. A., et al., A Combination Electron-Ion Field-Emission Source. *J Vac Sci Technol B* **1989,** *7* (6), 1793-1797.

CHAPTER 5: MICROIONIZER-BASED HIGH PRESSURE MASS SPECTROMETRY

5.1 Introduction

The first generation microionizer proved capable of field emission mass spectra in high pressure helium and air (Chapter 3). However, the high power consumption, device-to-device reproducibility, and lifetime limitations posed serious obstacles for a reliable, portable HPMS ionization source. Chapter 4 documented the advances made in fabrication and operation to overcome these obstacles. These advances culminated in the 9th generation microionizer, which was shown capable of low-power, field emission and positive mode operation. This chapter will focus on applying the 9th generation (Gen 9) as the ionization source for HPMS.

While microionizer performance improved with advances in design and operation from the first generation, the realm of high pressure mass spectrometry also advanced. Some of this advancement was documented in Chapter 4 – mainly with the switch from a differentially pumped chamber to a miniature chamber.[1] This change proved effective in reducing gas loads and also simplifies ion trap installation, which helped pinpoint sources of RF discharge, increasing the uptime of the HPMS instruments. Moreover, it significantly reduces the capacitance of the drive RF electrical feedthrough enabling high frequency characterization of ion traps with smaller critical dimensions. Evidence suggests that smaller traps, $100 < r_0 < 500$ μm, driven at increased RF drive frequencies, $f > 6$ MHz, aids in trapping and retention of ions as well as increasing resolution relative to our standard $r_0 =$

500 μm traps.[2] In addition to the instrument updates, the mass analyzer was upgraded from a standard CIT to a stretched length ion trap (SLIT).[1] The SLIT trap operates identically to a CIT, only it has an expanded charge capacity relative to a CIT.[3] While these HPMS advances were not vital to the success of the microionizer as a charge source, they were key to applying the microionizer as an HPMS ion source.

As stated in Chapter 4, Gen 9 microionizers deviated from the symmetric die layout of the prior generations and corresponded with use of the mini-chamber HPMS. The mini-chamber is limited to compact ion trap electrodes only (see Chapter 4), which reduces the area available for aligning the microionizer's active features with the ion trap. Thus, alignment is critical for maximizing the signal intensity as either an electron source or ion source. It was shown in Chapter 2 that external ion trapping for HPMS is mainly a function of pressure and ion kinetic energy. Combining this experience with that from electrospray ionization[4] show external ion trapping is a balance between ensuring an ion has enough energy to enter the ion trap but not so much that it cannot be captured by the electric field. In order to maximize the microionizer's signal intensity, particularly in positive ion mode, it needs to be placed in close proximity to the ion trap. By trap-mounting the microionizer, the separation distance between ionizer and trap is controllable on the order of the mean free path length (100 μm at 1 Torr). This proximal mounting is important because the collisions that induce scattering loss outside the trap are crucial to successfully trapping an externally generated ion once inside the trap.

Four 9th gen microionizers (9.1, 9.3, 9.5, and 9.6) have successfully operated at high pressure as both air-based field emission and positive ion mode ionizers. These ionizers are further characterized for their ability to generate mass spectra under HPMS conditions. Of

the four, two (Gen 9.1 and 9.5) will be discussed here. The former was based upon Ultrasil SOI, with a 3 μm device layer and a 1 μm insulating layer, while the latter had a device layer of 0.25 μm titanium/chrome and a 0.3 μm insulating layer – both were single-side etched. Of the remaining variants, Gen 9.3 did not generate sufficient signal intensity (in either field emission or positive mode) for consistent HPMS operation. Gen 9.6 is a through-etched version of Gen 9.1, designed to be an atmospheric inlet to the mass spectrometer. In trap-mounted configuration, it operates similarly to Gen 9.1, but as an atmospheric interface it serves better as a vision into future microionizer work and as such will be discussed in Chapter 6. Mass spectral characterization of the two 9th generation microionizers drew upon all of the advances made in both microionizer and high pressure mass spectrometry development - from hardware to operation - in order to examine the ionizer's behavior under both field emission and positive ion mode.

5.2 Experimental

The 9th generation devices were tested in a trap-mounted configuration with a cross-sectional schematic of the mounted trap shown in Figure 5.1. The PCB-mounted microionizer was separated from the endcap by 200 or 400 μm Teflon spacers. It was secured in-place with the same screws and alignment pins (not shown) used to align and mount the ion trap. Figure 5.2a shows a rendering of a sample inlet plate, mass analyzer chamber and detection chamber designed to fit the entire PCB-microionizer-trap assembly into a compact vacuum system. The mass analyzer chamber was an adaptation of the mini-chamber HPMS,[1] designed to fit the entire ionizer-trap assembly inside the vacuum. Figure 5.2b shows an image of the assembly inside the compact system with the sample inlet plate removed.

The ion traps employed for these studies were two SLITs: full-size and half-size. The full-size SLIT had critical dimensions $x_0 = 500$ μm, $y_0 = 4.0$ mm, and $z_0 = 645$ μm, while the half-size SLIT had $x_0 = 250$ μm, $y_0 = 4.0$ mm, and $z_0 = 320$ μm. Two types of endcaps were used: mesh endcaps with 250 lpi spacing and aperture endcaps with $x_0 = 100$ μm. All trap electrodes were electrochemically etched beryllium copper (Towne Labs). The full-size SLIT was operated near 9 MHz ($\pm$ 0.5 MHz), and the half-size SLIT was driven at near 20 MHz ($\pm$ 0.5 MHz). Operation of the SLIT for HPMS is identical as for the CIT as previously described.

Three methods of analyte introduction were used. The UHV leak valve and atmospheric sampling methods were previously described. The third method utilized Tedlar sampling bags (10 L w/septum, Fisher Scientific). These gas-sampling bags were used in order to introduce known concentrations of gas to the mass spectrometer. The bags were filled, heated, and purged three times with nitrogen to reduce trace contaminants.[5] Bags were filled to capacity with nitrogen or air (UHP, National Welders), then heated to about 70 °C with a heat gun, and the gas was expelled. The bag was then filled just above capacity with buffer gas and allowed to equalize to room pressure. A syringe and septum were used to introduce volatile, liquid analytes. Concentrations were calculated by volume in parts per million (ppm). The analytes included benzene, toluene, *o*-xylene, *p*-xylene, mesitylene, aniline, methylaniline, and dimethylaniline (Sigma-Aldrich, Milwaukee, WI). Trap chamber pressure was maintained near 1.0 Torr by metering flow rate with a needle valve.

The 9th generation microionizer was employed as both field emission-based EI and positive mode ion source. They were mechanically secured to the PCB with epoxy and wire bonded for electrical contact. Charge production from the microionizer was electrically

gated with a voltage pulse (V_p) placed on the handle layer (farthest from trap) of the microionizer. An additional bias potential (V_b) was continuously applied to aid in control of the electrons or ions. Previous characterization showed that electron and ion energy are equal to the total potential during generation: bias + pulse voltages. The pulse and bias were ballasted with 0.1 to 1 MΩ, 1/2 W resistors. Power supplies for the pulse and bias were high voltage (Series 230, Bertan-Spellman) and moderate voltage (E3612A, Agilent) models. Pulse polarity was negative for field emission mode and positive for field ionization mode and ranged from -300 V to +300 V. Typical field strengths for field emission were near 0.8 MV/cm and for field ionization mode near 2.0 MV/cm. A 4.5 digit multimeter (U1272A, Agilent) was placed in series with the voltage pulse and operated in DC, μA mode to monitor the current. The reading varied due to duty cycle, thus the maximum value observed over a three second visual window was recorded as the average value. This method of measurement was checked by measuring the voltage across a series resistor (R = 10 kΩ) using an oscilloscope and found to be within close agreement. Peak current was back calculated by dividing by the duty cycle of the pulse. Average and peak powers were calculated by taking the product of the appropriate current and the voltage pulse.

Instrument and data acquisition under LabVIEW control has been described previously. For the HPMS studies, mass spectra were recorded at 500 kHz acquisition rate for at least 250 averaging and then low pass filtered at 30 kHz. Mass axis calibration was performed with a LabVIEW program and based upon NIST EI standards. For lifetime studies, file size became a consideration; therefore signal averaging was increased to 1000 and data acquisition rate was slowed to 250 kHz. Data was processed with a LabVIEW program, (SignalIntegrator_v4.vi). The time axis (abscissa) was constructed from the timestamp of

each averaged spectrum. MS signal was low pass filtered at 30 kHz and baseline subtracted assuming a linear offset. The signal-to-noise ratio (SNR) was calculated using the maximum signal intensity divided by the root mean square noise value calculated between two user-controlled cursors. Integration of the signal during the ionization pulse and RF ramp portions of the scan was also performed. Due to the use of an EMT detector, negative charge was not directly measured. For field emission mode, the integrated ionization pulse was considered to be directly proportional to the electron emission intensity.

5.3 Results and Discussion

The microionizer was evaluated at 1 Torr air buffer gas in both field emission-based EI as well as positive ion source mode. Each mode successfully generated mass spectra but with differing operating characteristics, particularly in regards to emission stability and lifetime. As such, the results for each mode are discussed separately.

5.3.1 Field Emission HPMS Characterization

Chapter 3 documented mass spectral results with the Gen 1 microionizer operating as a field emission source in high pressure helium and air buffer gases – though with power draws on the order of watts and at low duty cycles (less than 2%). Before fully characterizing the Gen 9 devices, the ability to achieve HPMS with field emission and air buffer gas was undertaken. Figure 5.3 shows a mass spectrum of *o*-xylene, sampled via the atmospheric inlet, where a sample vial was held at the needle valve inlet to the mass spectrometer for 1-2 s. The valve was throttled to 1.0 Torr of room air. This spectrum was taken with a full-size SLIT at 8.84 MHz. The Gen 9.1 microionizer was trap mounted and spaced 200 μm from the trap endcap. Field emission was initiated with five, 1 ms pulses of -80 V, yielding a field strength of 0.8 MV/cm, and a -100 V bias was applied to the ionizer. The average

current draw was less than 3 μA, consuming an average of 240 μW. The duty cycle of the

microionizer was 22%, which scales the peak current and power to 13.5 μA and 1.1 mW,

respectively. These power figures represent a decrease of over four orders of magnitude

compared to a thermionic emitter.[6] However, they also contrast the Gen 9 microionizer

operation relative to Gen 1. For comparison, Gen 1 microionizers drew a peak of 10 mA of

current (limited by the supply) requiring a low duty cycle of 0.3% to generate field emission

at 0.8 MV/cm. Gen 9 devices accomplished the same role while drawing nearly 400 times

less power. Moreover, because the power draw is low, the duty cycle can be increased. In

this case, the Gen 9 duty cycle is 73 times greater than the Gen 1, meaning there is less dead

time for each mass spectral scan length. This decreased dead time directly impacts the

acquisition rate of the mass spectrometer, which was 12 Hz for Gen 1 and 44 Hz for Gen 9.

The improved acquisition rate is crucial in time sensitive applications such as chemical

warfare agent detection[7] as well as when the HPMS is coupled to a rapid separation

techniques such as gas chromatography where higher DAQ rates are needed to accurately

define peaks.[1]

Generating consistent, predictable mass spectra scan-to-scan is necessary for an

ionization source that will be used in a setting requiring not only detection but quantification;

as a result the source must also present a predictable signal decay in order to compare mass

spectra over time.[8] Prior to the 9th generation, microionizers rarely exceeded more than a few

hours of mass spectral acquisition. Their lifetime was difficult to quantify, because much of

operational time was spent in search for signal intensity, which typically ended in device

over-voltage and shorting before a stable emission point was reached. Inconsistent device-

to-device operation (turn-on voltage, overall emission, discharge threshold) complicated

matters further. The 9th generation overcame the device-to-device inconsistencies through a combination of wire bonding, ballast resistors, and optimized HPMS operation, opening a window to measure device lifetimes under conditions that would be seen in a handheld mass spectrometer application.

Field emission lifetime was evaluated by monitoring the ionization pulse of a Gen 9.1 microionizer. The device was used as a field emission-based EI source for the HPMS and held at 0.77 Torr (limited by the EMT). A -80 V pulse was applied for 0.9 ms, generating a 0.8 MV/cm electric field biased to -86 V. The duty cycle was 4% (0.9/22.55 ms). The results of a five-hour field emission lifetime test are shown in Figure 5.4, where each data point represents the integrated ionization pulse of 500 averaged mass spectra; as such they are spaced approximately 20 seconds apart. The analyte, o-xylene, was periodically introduced at the atmospheric inlet to correlate the ionization pulse intensity to a mass spectral signal strength, as shown in the inset of Figure 5.4. For the first hour, an erratic signal from point-to-point with an overall decay occurred during the ionization pulse. At 1 hour, signal intensity recovers (with no external intervention) and continues a similar decay seen in the first hour, only with a slower overall decay rate. At no point during the five hours does the signal drop to zero, however from the inset showing the mass spectra, it is obvious the ionization pulse decay negatively impacts the mass spectral performance of the device.

In terms of lifetime, this particular device was operated at various field strengths (between 0.7 and 1.0 MV/cm) for a total of 9.3 h of instrument time (data not shown). Each field strength produced a similar pattern – a general decay over the course of hours with erratic point-to-point reproducibility. At a 4% duty cycle, this corresponds to only 22 minutes of emitter lifetime, but it is spread over 730,000 individual mass spectra. While this

lifetime would not be feasible for a portable HPMS operating in a continuous monitoring mode, it could be used in an instrument that operates on an infrequent basis by spending the 730,000 mass spectra as-needed.

The most concerning feature of Figure 5.4 is the inconsistent nature of the ionization pulse from point-to-point. Field emission intensity is a strong function of emitter tip geometry.[9] Tip geometry is subject to change over time for two main reasons: ion bombardment and field desorption.[10] Electron impact ionization can occur anywhere along the electron beam's path; ions generated within a mean free path length (order of 100 μm at 1 Torr).[11] of the emission site will gain energy equivalent to the total potential (pulse plus bias), which for the data shown in Figure 5.4 was 166 eV. At these energies, ion bombardment can result in physical sputtering of the tips.[12] This sputtering is unpredictable and can either serve to enhance emission by sharpening the emission site or degrade it by erosion. Moreover, thermal runaway at the sharpened tips is a concern where Joule heating promotes electrons into the conduction band, leading to further field emission and higher intensities. This process, however can feedback until temperatures are sufficient for the tip to desorb, destroying the emission site and can occur over the nanosecond to microsecond timeframe.[10] Given the 0.9 ms pulse duration of the microionizer, thermal runaway could account for both the erratic signal from random activation of emission sites and signal decay from reductions in emission sites across the device. Conversely, working at high pressure may have increased the ionizer's lifetime by slowing ions formed in the vicinity of the ionizer. Most field emission sources operate at pressures below 10^{-6} Torr, where the mean free path length is greater than 10 mm. Thus, an ion will experience little or no collisional cooling and impact with the surface will likely yield sputtering damage. However, at 1 Torr,

ions must be generated within 100 μm to avoid collisional cooling. Given the mean free path for electrons is 2.5 mm[13] at this pressure, the rate of ion generation within the 100 μm threshold is low. But, even a low probability event when spread across the entire microionizer could be enough to cause erratic signal intensity.

As higher field strengths should lead to improved performance, the microionizer was operated at a field strength of 1.0 MV/cm (data not shown). After 35 min of operation, the device suffered insulator breakdown that proved consistent with other tested microionizers. The breakdown consisted of several bursts of significant instantaneous signal intensity (100 to 1000 times typical signal level) followed by a short circuit across the insulating layer. Depending upon preparation, silicon dioxide thin films should breakdown near 11 ± 2 MV/cm.[14] The observed field strength at breakdown was only 1.0 MV/cm. This discrepancy was attributed to surface flashover at the vacuum-insulator interface.[15-16]

The ability to generate mass spectra for an extended time period is paramount for an ion source. Field emission devices, particularly for display technologies have 10,000+ hour lifetimes, defined as the time-to-half emission intensity, however these devices require pristine vacuum environments to achieve these lifetimes.[17-18] Field emission mode with the Gen 9 microionizers generated HPMS with impressive lifetimes with low power consumption at 1 Torr of air.[19] However, the utility of the microionizer in field emission mode is ultimately limited by two factors: the inconsistent scan-to-scan signal and the overall signal decay.

5.3.2 Field Ionization HPMS Characterization

The 9th generation delivered low-power field emission-based mass spectrometry in a high pressure air environment. While this was encouraging, the inconsistency of the signal

intensity limits its use in potential analytical applications so its use as a field ionization source was explored. Previous attempts at field ionization with Gen 1 through 8 produced device failure before ionization was detected. This was attributed to insulator breakdown due to thermal contributions from the leakage current.[20] Having reduced the leakage current by four orders of magnitude, positive mode operation was demonstrated with the Gen 9 microionizer using a gate aperture discussed in Chapter 4. It was shown in Chapter 2 that external ion injection into the ion trap at high pressure is a balancing act. The ion must have enough energy to transit from the source-to-trap without scattering, however with not so much energy that collisional cooling cannot reduce its energy below the potential well depth of the ion trap. Experimentally, ion injection is dependent upon the ion kinetic energy as well as the buffer gas pressure. In addition, the high pressures involved in HPMS provide a wide window of acceptable kinetic energies for successful ion injection.

The experience gained from external ion injection experiments was utilized to couple the microionizer in positive mode with the HPMS to generate mass spectra. A Gen 9.5 microionizer (300 nm insulating layer) was mounted 400 μm from a full-size SLIT trap. The field strength was pulsed at 1.63 MV/cm for 1 ms and biased to +50 V. Mass spectra of several volatile organic compounds (VOC) introduced at the atmospheric inlet needle valve are plotted in Figure 5.5. Overall, the signal intensities and fragmentation patterns are very similar to those seen with the microionizer acting as a field emission source. However, the scan-to-scan signal fluctuations that were observed in field emission mode are not present (see lifetime results, Figure 5.10). At this point, the ionization mechanism behind positive mode was thought to be field ionization but not proved conclusively based on the experiments performed. The aperture experiments documented in Chapter 4 showed the

microionizer is indeed a source of positive charge. However, these experiments could not discriminate between localized field emission-induced EI and direct field ionization. HPMS offers a powerful tool to examine the ions generated in positive mode to determine their origins.

Evidence for distinguishing field emission and positive mode operation includes comparing the relative intensities of the ionization pulses. A Gen 9.1 microionizer was operated in field emission (0.91 MV/cm and -150 V_b) mode followed by positive mode (1.12 MV/cm and 0 V_b) without breaking vacuum. Mesitylene was leaked at a constant rate for both ionization modes and the signal intensities during the ionization pulse and resulting mass spectra are plotted in Figure 5.6. The ionization pulses are 3 ms in duration (between t = 3 and 6 ms), while the mass spectra are also 3 ms in duration (between t = 14.5 and 17.5 ms). The ion kinetic energy was adjusted in positive mode such that the mass spectral signal intensity was similar to field emission mode. Performance can be compared with integrated mass spectra and ionization pulse signals. The integrated mass spectrum for field emission mode is 0.55 V*ms, while for positive mode it is 0.47 V*ms. The corresponding integrated ionization pulses are 205.35 and 5.87 V*ms, respectively. There is a significant difference in the charge generation efficiency seen for a field emission mass spectrum vs. a positive mode spectrum. Field emission mode clearly generated more ions than positive mode. However, only 0.3% of those ions were trapped and detected versus 8.0% for positive mode. This is further evidence that field ionization is the mechanism behind the positive mode operation. Field ionization has a threshold behavior; i.e. neutrals with too great an ionization potential will not ionize[21] whereas field emission generates electrons for subsequent electron impact ionization. EI also does not discriminate between buffer gas and

168

analyte(s) as it will ionize both.[22] This is an inefficient process at high pressures when one

considers that analyte concentrations range in the ppb to 100 ppm levels and the buffer gas

comprises over 99% of the neutral molecules in a sample.   Therefore, the ionization pulse is

mainly comprised of ionized buffer gas in field emission mode, explaining the discrepancy

between the magnitudes of the ionization pulse and mass spectrum. Consequently, field

ionization generates less wasted charge and targets analytes with lower ionization potentials

than the buffer gas.

Targeted field ionization was demonstrated with a mixture of DMA and benzene

introduced at the atmospheric inlet of the HPMS and various microionizer field strengths.

These compounds were chosen because of the large spread between their ionization

potentials, 7.1 (DMA) and 9.2 eV (benzene) respectively and because of their mass range

(molecular ions at 121 and 78 m/z) and lack of interfering fragments. A series of mass

spectra are shown in Figure 5.7 using a Gen 9.5 device where the electric field was increased

from 1.17 to 1.80 MV/cm. A sample container was wafted at the inlet and the pulse voltage

was slowly increased. When the field strength was 1.17 MV/cm, it is below the ionization

threshold of benzene and near that of DMA so only a slight peak was observed at 121 m/z.

As the field strength increased, the DMA peak at 121 m/z increased in intensity. Benzene

(m/z 78) began to ionize as the field strength approached 1.67 MV/cm with a slight peak

evident. By 1.80 MV/cm the field strength exceeded both analytes' ionization potentials and

both showed SNR > 50. This ionization field strength dependence is further proof this mode

of operation is field ionization. The benzene spectra in Figure 5.7 add an additional piece of

evidence. HPMS of benzene with EI-based ionization sources are typically dominated by a

fragment peak at 63 amu.[23] The benzene mass spectrum at 1.80 MV/cm is clearly dominated

by the molecular ion peak at 78 amu. The lack of fragmentation suggests that the ionization mechanism behind positive mode is softer than EI, further supporting field ionization.[24]

The emission intensity of a field ionization source is directly proportional to the partial pressure of the analyte. A typical field ionizer is operated in an environment where the signal intensity is dominated by the analyte such as in high vacuum[25] or in a controlled atmosphere.[26] However, HPMS operates in ambient air, where the analyte represents only a small fraction of a complex mixture of small molecules. Fortunately, the mass spectrometer offers a tool to gain insight into the microionizer's field ionization as a function of partial pressure. A Gen 9.1 microionizer was used in field ionization mode under optimal conditions with a constant field strength of 2.4 MV/cm and +35 V bias. Mesitylene concentrations between 520 and 2080 ppm were achieved by leaking saturated air (2600 ppm) into the vacuum chamber from 0.4 to 1.0 Torr, while a second atmospheric inlet was adjusted to maintain 1.0 Torr total pressure. The SNR of the mesitylene mass spectra recorded between 520 and 2080 ppm are plotted in Figure 5.8a. The SNR linearly increases between 500 and 1300 ppm, above which it plateaus. The plateau is most likely due to space charge limitations in the ion trap. Further insight can be gained by looking at the total integrated ionization signal, the ion pulse plus mass spectral intensity. This information is plotted in Figure 5.8b with the total signal increasing linearly by 21% over a 4-fold increase in mesitylene concentration. Extrapolating a linear fit to 0 ppm mesitylene reveals a y-intercept at 21.3 au. Assuming this accounts for field ionization of the buffer gas, then the mesitylene ionization can be determined by subtracting this baseline from the points in Figure 5.8b. The increase in mesitylene signal is 4.4-fold, which is close to the increase in mesitylene concentration, demonstrating a linear response to concentration. The mass

spectral results in Figure 5.8a did not reveal the presence of an unknown due to the ionized buffer gas, however the low mass cutoff at this frequency is near 60 m/z, so smaller constituents are observable during the ionization pulse but not in the mass spectrum.[27] Of the major ambient air components (nitrogen, oxygen, argon, carbon dioxide, and water vapor), oxygen has the lowest ionization potential at 12.1 eV.[28] With oxygen making up 21% of air, if the field strength were sufficient for oxygen ionization, a discharge would likely be observed thereby setting the maximum high end field strength. This extends the microionizer's usable range beyond typical UV ionization sources with 10.6 eV limits.[29]

Having determined that positive mode operation is in fact field ionization, it was used to study external ion injection with the SLIT ion trap, specifically the ion kinetic energy (KE) effect on HPMS performance at 0.5 and 1.0 Torr. A Gen 9.1 device was trap-mounted 125 μm from a full-size SLIT. Mesitylene partial pressure was held constant along with a field ionization strength of 2.1 MV/cm and ranging the bias from -200 to -12 V (low to high KE). The ion KE was calculated from the addition of the V_{pulse} and V_{bias} and was limited by electric discharge. The total integrated ionization (ion pulse plus mass spectrum) is plotted in Figure 5.9a with the integrated mass spectra plotted in Figure 5.9b. In Figure 5.9a, a linear increase in total ionization intensity is seen for both pressures as ion kinetic energy is increased. Moreover, the intensities nearly overlap with 0.5 Torr having a slightly higher signal intensity that diminishes at higher kinetic energies. A hard sphere approximation determines the mean free path for mesitylene at 1.0 Torr to be 160 μm and 320 μm at 0.5 Torr.[30] Since both path lengths are shorter than the spacing between the microionizer and trap, we expect similar signal intensities for each pressure. However, the mean free path at 1.0 Torr is similar to the ionizer/trap spacing, so losing a small percentage of the ions to

171

scattering collisions is expected. This difference should diminish as the ions gain enough kinetic energy to overcome the scattering effect due to the buffer gas.

Interestingly, the same scattering mechanism that is responsible for this difference improves ion trap operation. The integrated mass spectral portions of the total ionization are plotted in Figure 5.9b. Below 30 eV, signal is essentially zero because ions do not have sufficient KE to traverse the field between the ionizer and ion trap. As KE increases, mass spectral signal does as well with a unique optimal energy, 50 and 150 eV at 0.5 and 1.0 Torr, respectively with the peak signal at 1.0 Torr 3.5-fold greater than the peak observed at 0.5 Torr. Between 30 and 200 eV, the mass spectral intensity at 1 Torr is 40 to 350% greater than the peak intensity at 0.5 Torr. This data reinforces the conclusions reached in Chapter 2: external ion injection is dependent upon both pressure and ion KE where it is more effective at higher pressure because the increased collisional frequency acts to cool the ions into the ion trap's potential well depth. This trend was previously observed at the mTorr level with helium buffer gas in a QITMS.[31] Chapter 2 extended these results to miniature CIT's operated at 1 Torr buffer gas and this data extends it to SLIT-based mass analyzers.

The last characteristic evaluated for field ionization mode of operation is lifetime. Field emission mode with the 9th generation microionizer utilized a short duty cycle to produced devices with cumulative lifetimes approaching 25 minutes which were used to achieve HPMS instrument times near 10 h of continuous scanning. Overall, the scan-to-scan stability in field emission mode was difficult to control and likely contributed to the short lifetime. This shortened lifetime was attributed to ion bombardment, which is inevitable due to the negative potentials required to generate and extract negative charge. The results of field ionization mode lifetime stand in stark contrast. A Gen 9.1 microionizer was trap mounted

400 μm from a full-size SLIT with critical dimensions $x_0 = 500$ μm and $z_0 = 645$ μm operated at 8.86 MHz. The microionizer electric field was 2.06 MV/cm, set by a 10 ms, 206 V pulse. The device was biased to -100 V for optimal mass spectral signal strength at 1.05 Torr of ambient air. Mesitylene was leaked at constant partial pressure via UHV leak valve. Mass spectra were recorded with 1000 scan averaging yielding about 40 seconds between each spectrum. The instrument operated for nearly 500 h and was monitored in-person during the day and remotely overnight. The SNR of the nearly 500 h of continuous operation is plotted in Figure 5.10. The duty cycle was 44.4%, translating to 220 h of cumulative lifetime for the microionizer. Over the course of the experiment, the average current and power consumption never exceeded 3 μA and 0.8 mW, respectively. The discontinuities at 240 and 325 h were due to computer errors, where a DAQ hardware restart was required which could not be performed remotely. There was significant fluctuation in the signal over the course of the first 10 h of operation with SNR ranging from 50 to 145. Afterwards, the SNR varied in an envelope of about ±15 units around an average value. At about 10 h, the average SNR settled near 100 followed by an asymptotic decay. At 50 h, the SNR had decreased to 50, roughly 50% of its starting value. At the end of the test (t = 500 h), the device was operating on average at 20% of its original SNR though at no point did the microionizer cease field ionizing. While the overall lifetime figures may not be as impressive as other field ionization sources,[25] it is important to note that that the microionizer was tested under HPMS conditions. It operated for nearly 10 days of cumulative ionization at 1 Torr of air buffer gas with constant analyte introduction under much harsher conditions than most field ionization sources are tested.[26, 32] Moreover, it achieved this lifetime as both a low power and low voltage field ionizer – meeting the original project goals.

5.3.3 Modes of Failure

The cause of failure in field ionization mode also contrasted with field emission failures. While both modes suffered failures via insulator breakdown, the field strengths were different. In field ionization mode, breakdown typically manifested above 2.5 MV/cm, with some devices approaching 3.5 MV/cm; whereas, field emission mode showed signs of discharge and breakdown near 1.0 MV/cm. This difference was attributed to surface flashover – where trapped charges at the insulator-vacuum interface facilitate current flow along the surface. Surface flashover was observed in field emission mode because of charge enhancement. Ions produced near the surface of the emission tip act to enhance the electric field,[10] which in turn increases field emission intensity, creating a positive feedback which enhances the conditions for flashover. In field ionization mode, the bias of the microionizer repels ions from the surface suppressing the conditions for surface flashover.

In terms of extended operation, signal decays for both field emission and field ionization as observed in Figures 5.4 and 5.10. However, the decay rate for field emission was much greater than for field ionization. In order to maintain adequate signal intensity with field emission, the field strength would have to be increased eventually leading to breakdown of the insulator and microionizer failure. Field ionization decay was much slower and similar to field emission, the field strength could be increased to maintain signal intensity as well. Also like the field emission source, it is possible for a device to bump up against the field breakdown strength (near 2.6 MV/cm) and display zero ionization intensity. The cause of breakdown was not thought to be due to ion bombardment. The next likely culprit considered was a thin film barrier preventing neutrals from accessing the field strengths necessary for ionization. Device recovery was attempted by operating in field emission

mode but without success (data not shown). Venting to atmosphere as well as pumping to low pressure ($\sim 10^{-5}$ Torr) also failed to recover field ionization as did rinses in mild organic solvents. Harsh chemical cleanings and etches were not possible due to the exposed wire bonds. As such the mechanism behind signal decay was undetermined, but is believed to be a thin film buildup.

5.4 Conclusions

Both field emission and field ionization sources were successfully developed for HPMS applications. Strong mass spectra were recorded with a field emission microionizer however signal fluctuations and lifetime issues reduce its efficacy as an ionization source. The longest lasting field emission device ran for an accumulated 9 h of instrument time – roughly 22 minutes of cumulative ionizer lifetime. After thorough testing, the positive ion mode was attributed to field ionization. Due to the more favorable electric field polarity and selective ionization of the analyte, field ionization displayed over a 50-fold increase in lifetime over field emission mode. The longest lasting device provided 20.6 days of instrument time and 9.1 days of cumulative ionization. Moreover, both modes were shown to operate with average currents draws on the order of microamps and average power consumption between 0.5 and 5.0 mW, depending upon insulating layer thickness. Overall, the 9th generation microionizers accomplished each goal set forth at the beginning of the project under the specified HPMS conditions for a portable instrument.

5.5 Figures
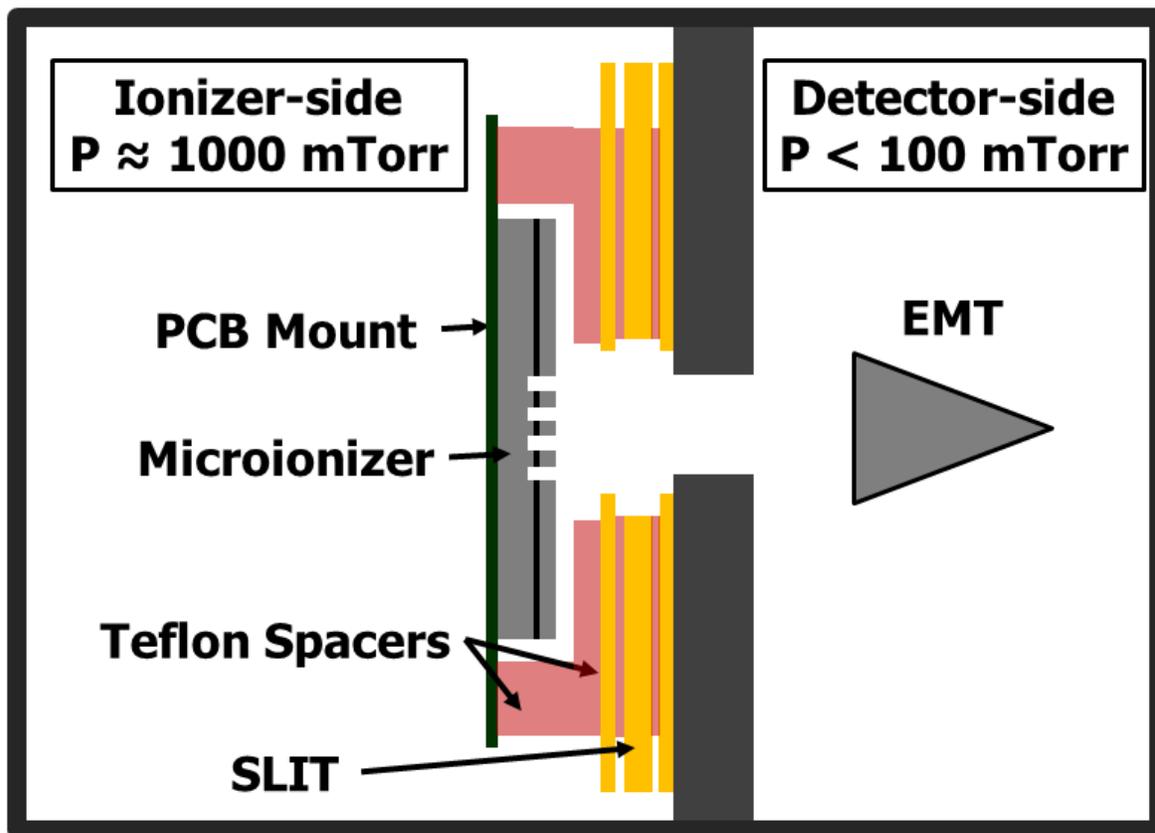
Figure 5.1: Cross sectional schematic of the mini-chamber HPMS with a trap mounted microionizer. The entire assembly fits into the trap chamber and is held at 1.0 Torr with the EMT on the Detector-side held a < 100 mTorr. In order to maximize signal, the active features of the microionizer are laid out to match the length of the SLIT. The microionizer is aligned and mounted with the same hardware as used to build the SLIT.
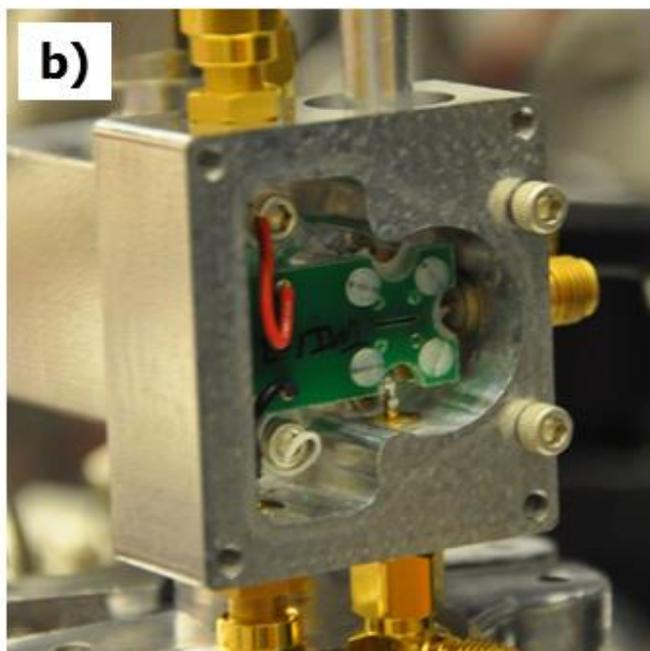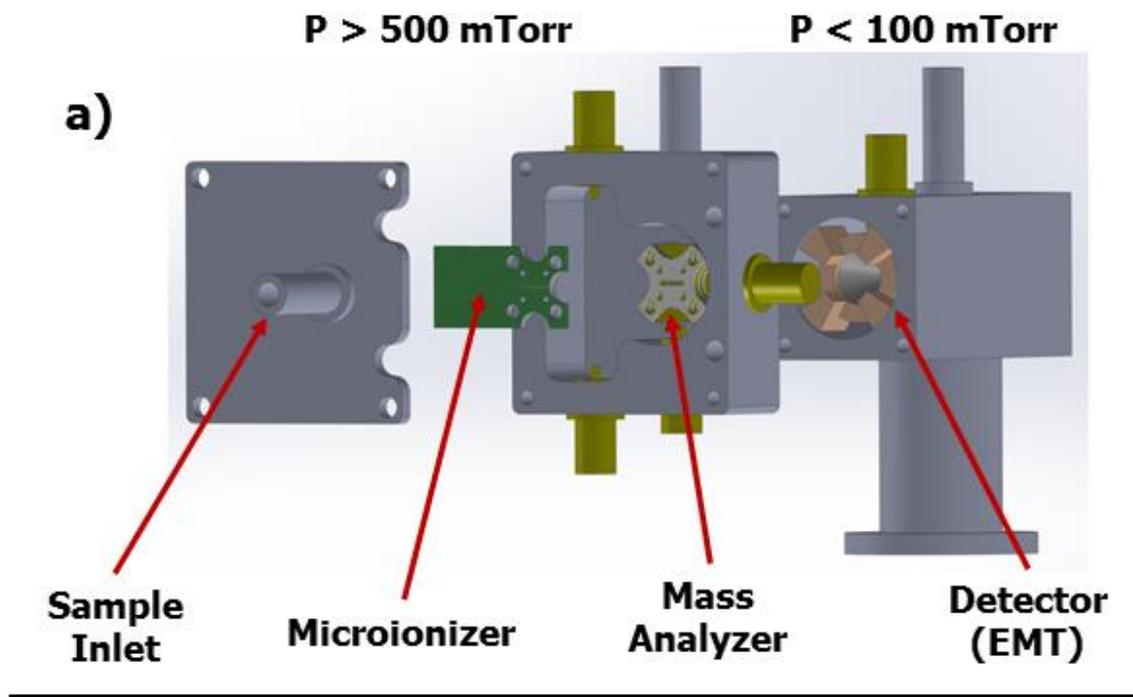
Figure 5.2: The mini-chamber HPMS adapted to work with the trap-mounted microionizer.
a) Solidworks schematic of the chamber showing the sample inlet, microionizer and detector
placement relative to the SLIT (mass analyzer). b) Image of the assembled vacuum chamber
with the sample inlet plate removed showing the mounted microionizer. The microionizer is
positioned about 400 μm from the SLIT.
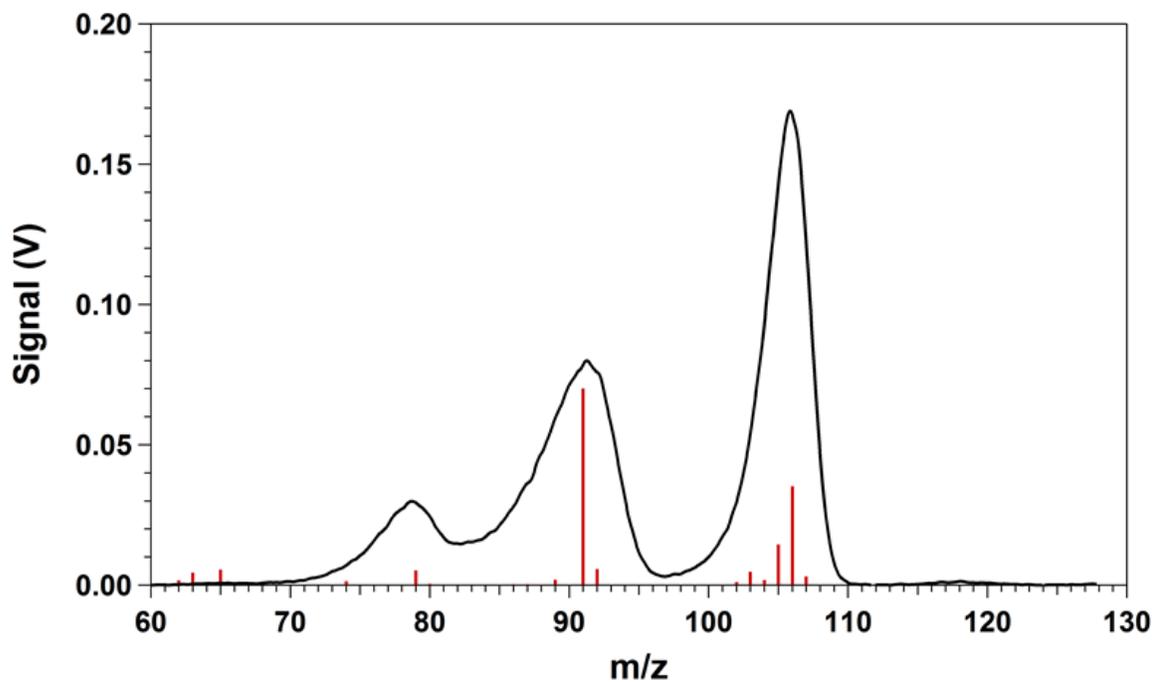
Figure 5.3: High pressure mass spectrum of *o*-xylene in field emission mode (▬) and NIST standard (■). The spectrum was taken in room air at 1.0 Torr with a $x_0 = 500$ μm and $z_0 = 645$ μm SLIT operated at 8.84 MHz drive RF. A series of five, 1 ms pulses (with 1 ms periodicity) were used for ionization. Gain on the current preamplifer was 1 μA/V.
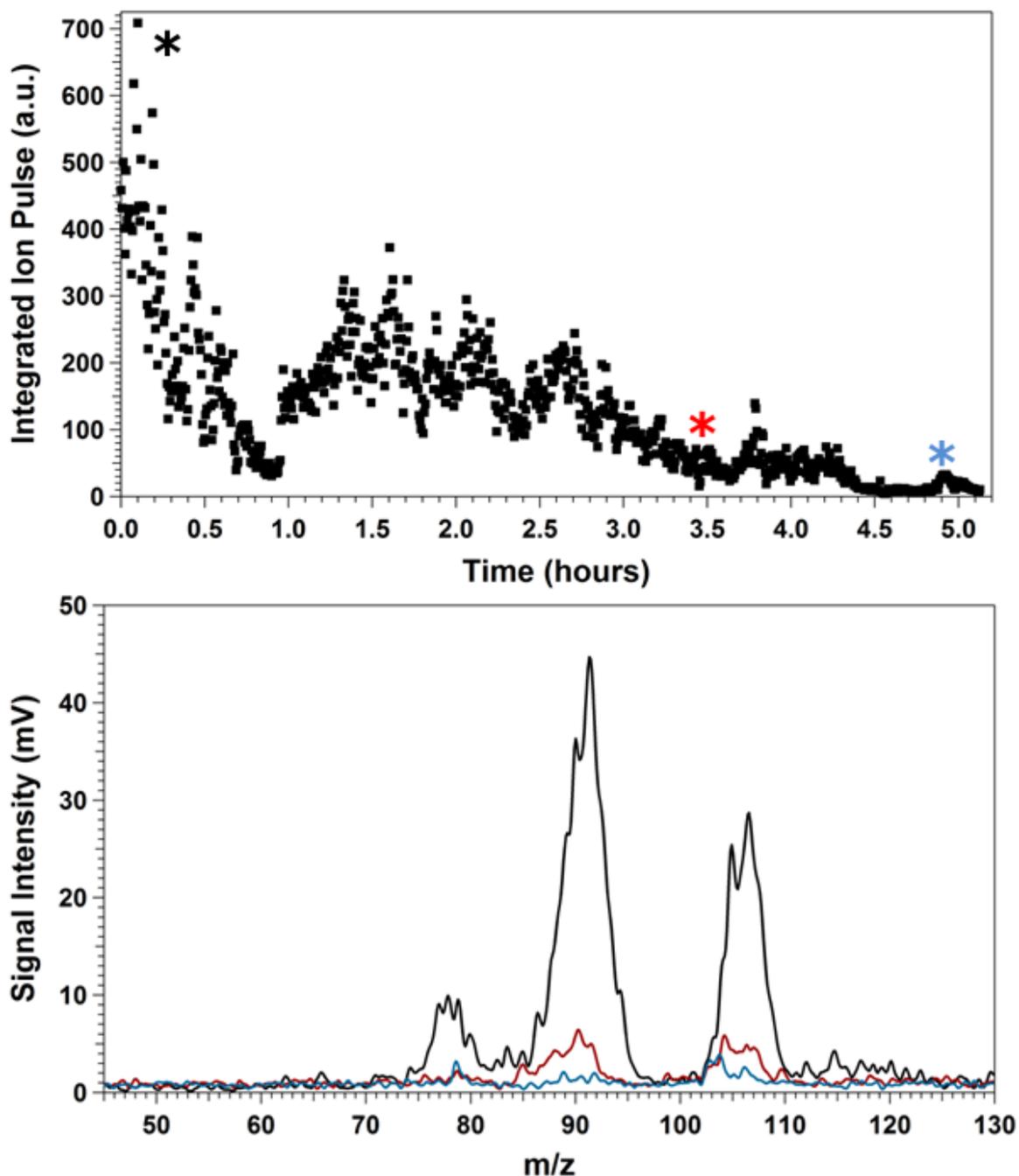
Figure 5.4: a) The lifetime of a Gen 9.1 microionizer operated in field emission mode was investigated by plotting the integrated ionization pulse as a function of time (■). Analyte was introduced at the atmospheric inlet. b)Three of the resulting mass spectra are shown from t = 0 (*), 3.4 (*), and 5.0 (*) hours. The electric field strength was 0.8 MV/cm, generated with a -80 V pulse applied for 0.9 ms (4% duty cycle). The average current never exceeded 1 μA for an average power of 80 μW.
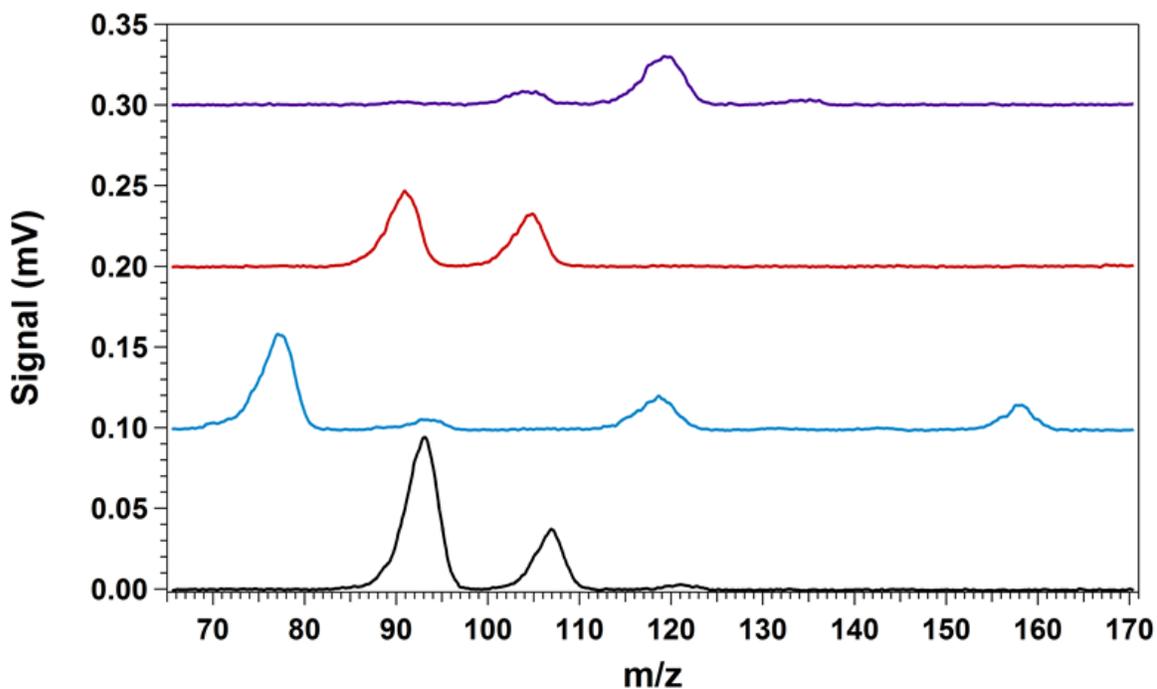
Figure 5.5: Offset high pressure mass spectra of several VOCs acquired in field ionization mode: mesitylene (—); toluene (—); benzene (—); and aniline, methylaniline, and dimethylaniline (—). HPMS pressure was 0.93 Torr of room air and the analytes were introduced by wafting from open containers. The field strength was 1.63 MV/cm, pulsed for 1 ms (4.5% duty cycle), and biased +50 V relative to the trap endcap. The SLIT (x_{0x0} = 500 μm and z_0 = 645 μm) was operated at 8.74 MHz using double resonance at 2.95 MHz.
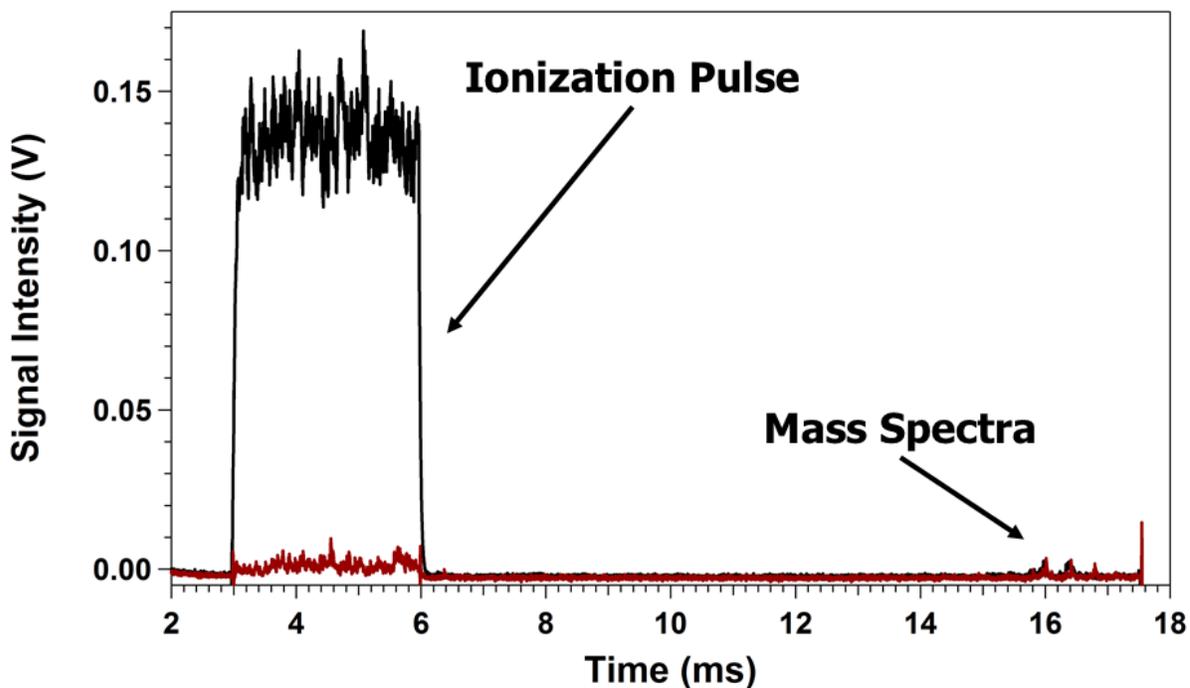
Figure 5.6: Overlay of mass spectra recorded in field emission (—) and positive mode (—) including both the ionization pulse and mass spectrum for each mode. The spectra were taken with the same ion trap, analyte concentration, and ion pulse length of 3 ms ionization pulse. The mass spectra were tuned near the same integrated signal intensity in order to demonstrate the difference in ionization pulses between the two modes.
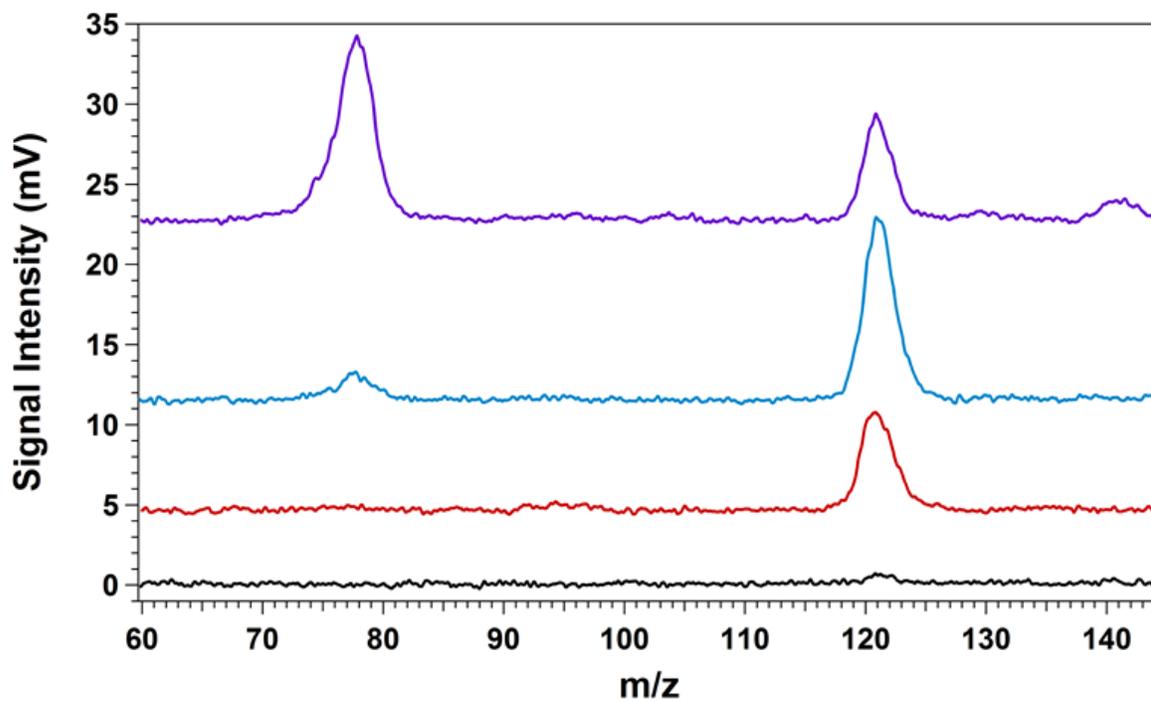
Figure 5.7: Mass spectra of a dimethylaniline and benzene mixture using field ionization with increasing field strengths of 1.17 MV/cm (━); 1.53 MV/cm (━); 1.67 MV/cm (━); and 1.80 MV/cm (━), the mass spectra are offset for clarity. Dimethylaniline has a m/z = 121 amu and ionization energy of 7.1 eV and benzene has a m/z = 78 amu and ionization energy of 9.2 eV.
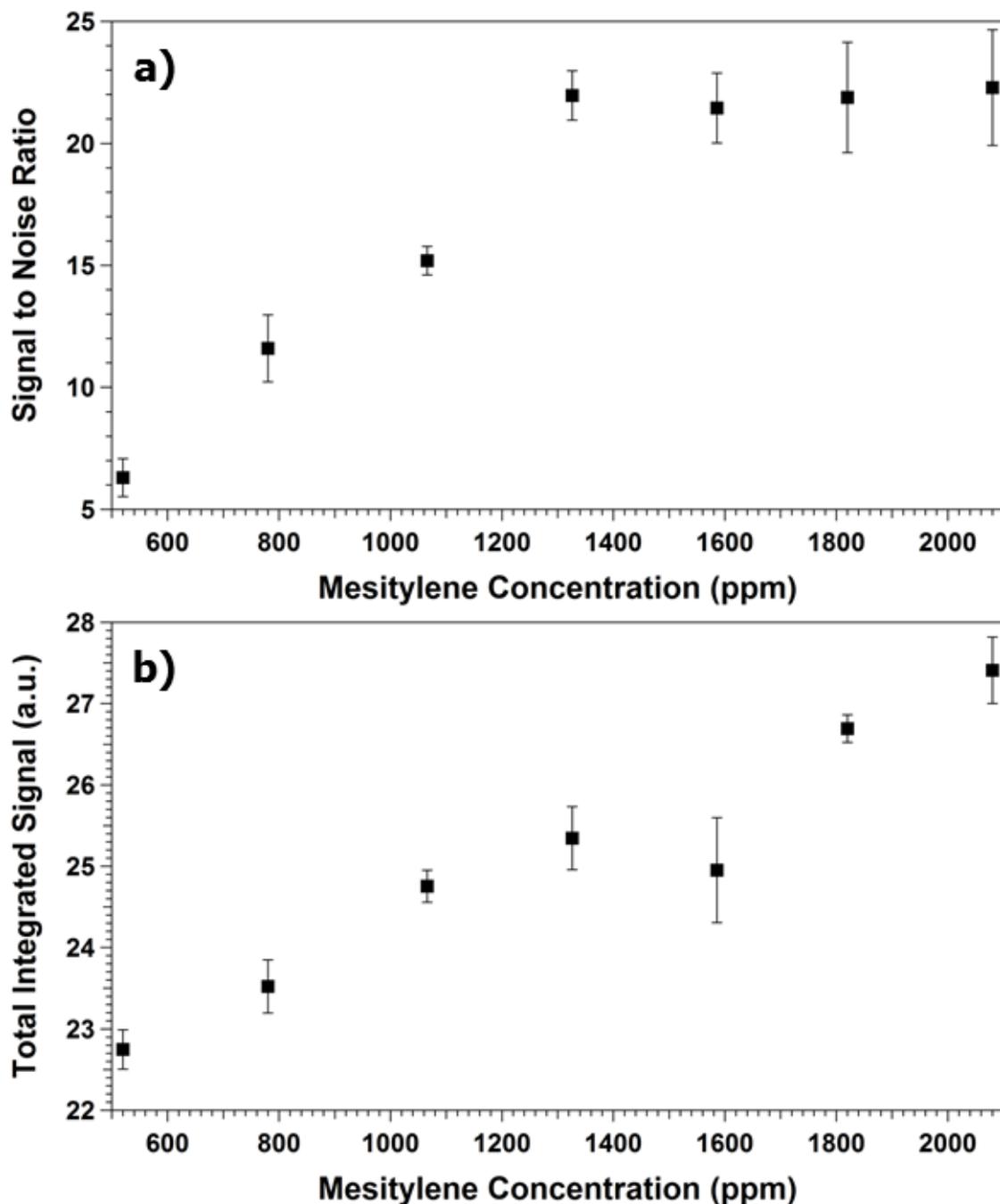
Figure 5.8: a) SNR of mass spectra taken in field ionization mode increasing concentrations of mesitylene at a constant 1 Torr total pressure. The HPMS response is linear between 520 and 1320 ppm, above which the ion trap appears to saturate. b) Total integrated ion signal (ion pulse plus MS ramp) for the same experiment, showing a linear response from the microionizer across the entire pressure range.
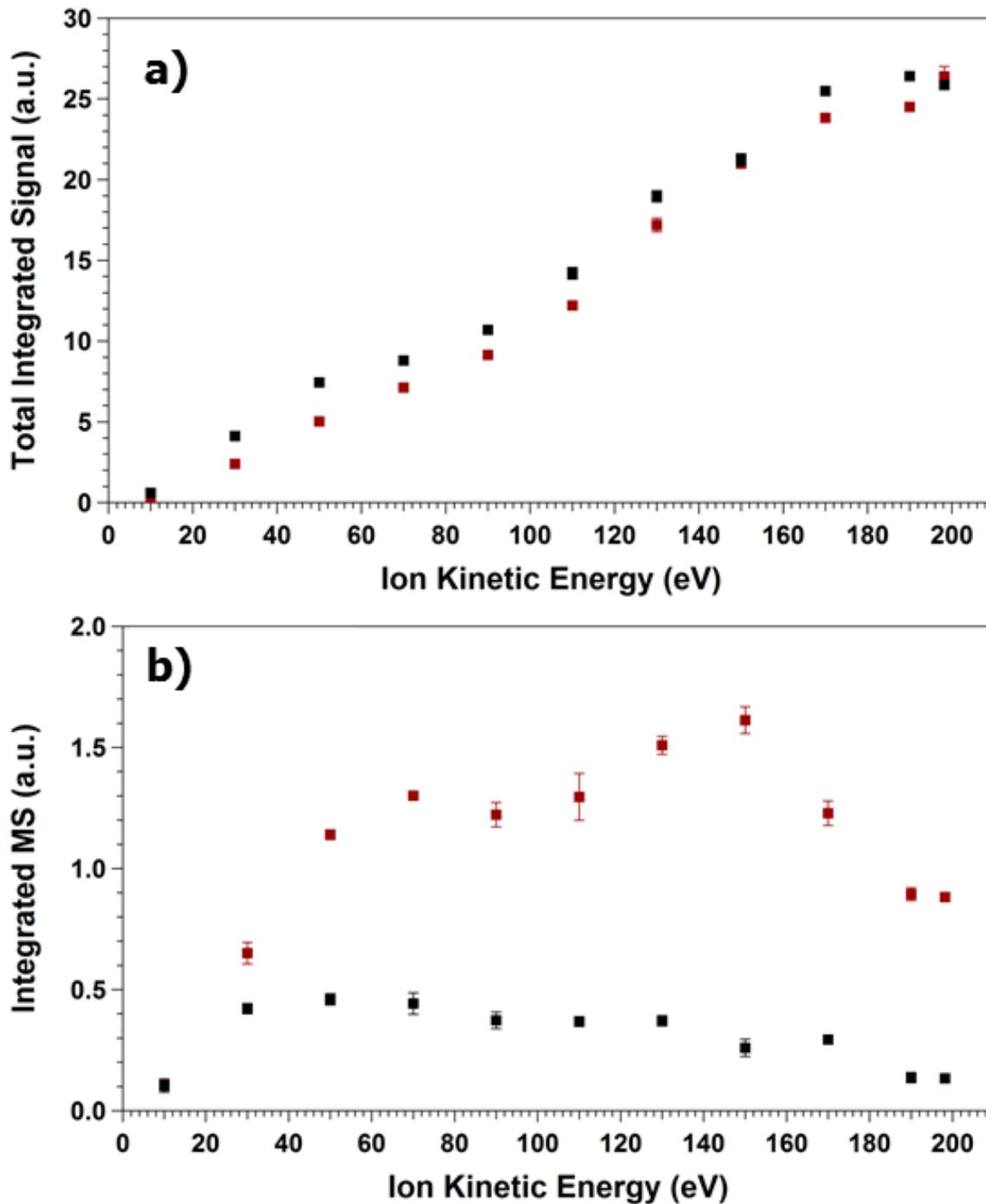
Figure 5.9: HPMS performance as a function of ion kinetic energy at 1.0 Torr (■) and 0.5 Torr (■). a) Total integrated signal (ion pulse plus MS) shows a linear increase in signal as ions overcome scattering between the microionizer and ion trap. b) Integrated mass spectra of the same data as a). At 1.0 Torr, the ion injection efficiency is higher, yielding stronger signal intensity than at 0.5 Torr. The electric field was set to 2.1 MV/cm and mesitylene was introduced via UHV leak valve.
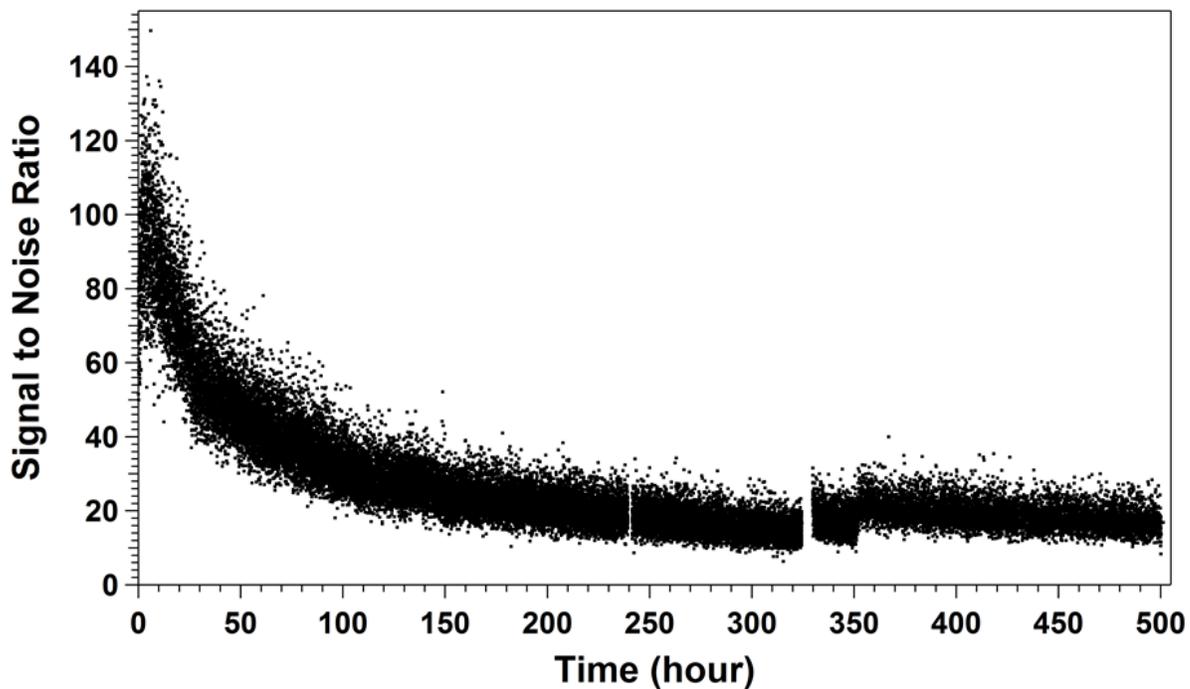
Figure 5.10: Signal to noise ratio of a single microionizer operated in field ionization mode. The Gen 9.1 device was pulsed for 10 ms with constant field strength at 2.06 MV/cm and biased to -100 V. The duty cycle was 44.4%. The discontinuities in the plot are due to computer errors which halted acquisition. The ionizer operated for approximately 220 h when corrected for duty cycle, and 495 h of HPMS total uptime.

5.6 REFERENCES

1.   Schultze, K. P. Advanced System Components for the Development of a Handheld Ion Trap Mass Spectrometer. Dissertation, University of North Carolina at Chapel Hill, Chapel Hill, NC, 2014.

2.   Blakeman, K. H.; Ramsey, J. M., High Pressure Mass Spectrometry in Nitrogen and Air. *Manuscript in preparation* **2014**.

3.   Ramsey, J. M.; Schultze, K., Miniature charged particle trap with elongated trapping region for mass spectrometry. Google Patents: 2014.

4.   Gilliland, W. M., et al., Coupling Microchip Electrospray Ionization Devices with High Pressure Mass Spectrometry. *Manuscript in preparation* **2015**.

5.   Miller, S., Personal communication. May 22, 2015.

6.   Jenkins, R. O., A Review of Thermionic Cathodes. *Vacuum* **1969,** *19* (8), 353-359.

7.   Smith, J. N., et al., Facility monitoring of chemical warfare agent simulants in air using an automated, field-deployable, miniature mass spectrometer. *Rapid Commun. Mass Spectrom.* **2011,** *25* (10), 1437-1444.

8.   Huq, S. E., et al., Field emitters for space application. *J Vac Sci Technol B* **2001,** *19* (3), 988-991.

9.   Fowler, R. H.; Nordheim, L., Electron Emission in Intense Electric Fields. *Proceedings of the Royal Society A: Mathematical, Physical and Engineering Sciences* **1928,** *119* (781), 173-181.

10. Fursey, G., *Field emission in vacuum microelectronics*. Kluwer Academic/Plenum Publishers: New York, 2005; p 205.

11. Borsdorf, H., et al., Atmospheric-pressure ionization studies and field dependence of ion mobilities of isomeric hydrocarbons using a miniature differential mobility spectrometer. *Analytica Chimica Acta* **2006,** *575* (1), 76-88.

12.   Madou, M. J., *Fundamentals of microfabrication and nanotechnology*. 3rd ed.; CRC Press: Boca Raton, FL, 2012.

13.   Hoffman, K. R., et al., Total-Cross-Section Measurements for Positrons and Electrons Colliding with H-2, N-2, and Co2. *Physical Review A* **1982,** *25* (3), 1393-1403.

14.   Ainger, F. W., The Formation and Devitrification of Oxides on Silicon. *J Mater Sci* **1966,** *1* (1), 1-13.

15.   Pillai, A. S.; Hackam, R., Surface Flashover of Solid Insulators in Atmospheric Air and in Vacuum. *J Appl Phys* **1985,** *58* (1), 146-153.

16.   Miller, H. C., Surface Flashover of Insulators. *IEEE T Electr Insul* **1989,** *24* (5), 765-786.

17.   Wei, Y., et al., Surface chemical changes on field emitter arrays due to device aging. *J Vac Sci Technol B* **1999,** *17* (1), 233-236.

18.   Talin, A. A., et al., Field emission displays: a critical review. *Solid-State Electronics* **2001,** *45* (6), 963-976.

19.   Charbonnier, F., Arcing and voltage breakdown in vacuum microelectronics microwave devices using field emitter arrays: Causes, possible solutions, and recent progress. *J Vac Sci Technol B* **1998,** *16* (2), 880-887.

20.   Osburn, C. M.; Weitzman, E. J., Electrical-Conduction and Dielectric Breakdown in Silicon Dioxide Films on Silicon. *Journal of the Electrochemical Society* **1972,** *119* (5), 603-609.

21.   Gomer, R., *Field emission and field ionization*. Harvard University Press: Cambridge, 1961; p 195.

22.   Märk, T. D.; Dunn, G. H., *Electron impact ionization*. Springer-Verlag: Wien ; New York, 1985; p 383.

23.   Blakeman, K. H.; Hampton, A. S., Personal Communication. 2015.

24.   Beckey, H. D., *Principles of field ionization and field desorption mass spectrometry*. 1st ed.; Pergamon Press: Oxford Eng. ; New York, 1977; p 335.

25.   Aberth, W.; Spindt, C. A., Characteristics of a Volcano Field-Ion Quadrupole Mass-Spectrometer. *International Journal of Mass Spectrometry and Ion Processes* **1977,** *25* (2), 183-198.

26.   Fomani, A. A., et al., Low-Voltage Field Ionization of Gases Up to Torr-Level Pressures Using Massive Arrays of Self-Aligned Gated Nanoscale Tips. *Ieee Transactions on Electron Devices* **2014,** *61* (5), 1520-1528.

27.   Blakeman, K. H., et al., High-Pressure Mass Spectrometry at Pressures Exceeding 1 Torr in a Microscale Cylindrical Ion Trap. *Manuscript in preparation* **2015**.

28.   Stein, S. E., "Mass Spectra". in *NIST Chemistry WebBook, NIST Standard Reference Database Number 69* [Online] Linstrom, P. J.; Mallard, W. G., Eds. National Institute of Standards and Technology, Gaithersbrug, MD, http://webbook.nist.gov, (accessed 10/2/2015).

29.   Sielemann, S., et al., IMS with non radioactive ionization sources suitable to detect chemical warefare agent simulation substances. *International Journal of Ion Mobility Spectrometry* **2002,** *5* (3), 143-148.

30.   Lin, S. N., et al., Dependence of Polyatomic Ion Mobilities on Ionic Size. *J Chem Phys* **1974,** *60* (12), 4994-4999.

31.   Louris, J. N., et al., Injection of Ions into a Quadrupole Ion Trap Mass-Spectrometer. *International Journal of Mass Spectrometry and Ion Processes* **1989,** *88* (2-3), 97-111.

32.   Johnson, B. B., et al., Field ionization characteristics of an ion source array for neutron generators. *J Appl Phys* **2013,** *114* (17).

CHAPTER 6: CONCLUSIONS AND FUTURE WORK

6.1 Conclusions

The development of the microionizer was undertaken to help develop and advance high pressure mass spectrometry (HPMS). The ultimate goal is to not only release mass spectrometry from the confines of the laboratory but also to reduce hardware costs. This would help make mass spectrometry a ubiquitous technique bringing its chemical informing power to as many toolboxes as possible. The research presented in this dissertation began in earnest in 2011. Since then, a low-cost, portable HPMS instrument has been commercialized[1] and used in the field to target volatile organic chemicals.[2] In this sense, the overall goal of producing a handheld mass spectrometer has been achieved. However, continued advancement and refinements are necessary to improve the performance of HPMS in terms of resolution,[3] sensitivity,[4] range of detectable analytes,[5] as well as cost-effective miniaturization.[6]

The project began with three, simple objectives:

1. Demonstrate HPMS with the microionizer in air.

2. Maximize microionizer lifetime under HPMS conditions.

3. Minimize overall microionizer/mass analyzer footprint.

At the outset of the project, HPMS was in its early stage of development. The tenets of HPMS – high-pressure, high-frequency, miniature ion trap-based mass spectrometry – had been shown to work in helium at relatively high pressures ($\approx$ 10 mTorr) of helium.[7-8] The goals of 1 Torr operation in helium,[9-10] nitrogen[3], and air[11] were achieved using proven

189

internal, electron impact ionization (EI) sources. As an external ion source, the microionizer was not guaranteed to be compatible with the miniature cylindrical ion trap (mCIT) under HPMS conditions due to potential well depth concerns of the mCIT relative to a standard QIT.[12-13] Thus, initial studies focused on coupling traditional, external ion sources with the mCIT under HPMS conditions to determine operational boundaries. Using both off and on-axis external ion sources, helium, nitrogen, and air were studied from 0.01 to 1.0 Torr. The trends in the signal intensity of mass spectra revealed several important points: the potential well depth and small trap dimensions of HPMS are indeed compatible with external ion injection. External ion trapping was shown to be dependent upon buffer gas composition and pressure, ion kinetic energy, and ion trap operation. The window of acceptable ion kinetic energies was widest at 1 Torr of air buffer gas; and under these conditions, it was shown that deeper well depth also aids external ion trapping. These studies provided operational boundaries for the microionizer. Deeper well depths, achieved by increasing the drive RF frequency and amplitude, provide the best opportunity for external ion injection. Buffer gas composition and pressure are both related to collisional cooling. Larger buffer gases (air or nitrogen vs. helium) can remove more energy per collision than lighter ones, while pressure controls the collisional frequency. Ion kinetic energy needs to be high enough to overcome collisional cooling and scattering between the source and trap, but not so large that the ion skips through the trap. Most importantly, it was found that increased pressure (1 Torr) provides the best trapping efficiency. While this must be balanced with ion trap resolution, it provides a wide range to tune the parameters relative to one another. Thus, source-to-trap spacing, ion kinetic energy, operational pressure, and RF drive frequency and amplitude can

be optimized based upon instrument design constraints as well as analyte properties (m/z, etc).

Studies of the microionizer began with first generation devices provided via collaboration with Dr. Pau at the University of Arizona. These devices were successfully coupled with HPMS and produced internal, EI-based mass spectra in both helium and air at pressures ranging from a few mTorr to 1 Torr. Field emission was achieved at field strengths below 1 MV/cm, but field ionization was never realized. Although successful in producing spectra, this generation of microionizer had high-current draw (current limited to 10 mA); a short lifetime (a few hours of instrument time); and poor field emission stability making it unsuitable for potential hand held use. These drawbacks were addressed with improvements in design, materials, fabrication, and operation procedures and culminated in a 9th generation microionizer.

The 9th generation devices utilized every advance in HPMS, fabrication, and microionizer operation learned throughout the course of this research project. The active features were designed to align with a stretched length ion trap (SLIT) to maximize signal intensity.[4, 6] The microionizer-to-ion trap spacing was minimized by the use of a printed circuit board (PCB) based microionizer mount. The result was an ion source capable of mounting within one, ionic mean free path length ($\approx$ 100 µm) of the ion trap. Optimal electrical contact to the silicon was achieved by combining metallized contact pads and wire-bonding. The current draw was reduced from milliamps to microamps yielding, sub-milliwatt average power. Moreover, both field emission and field ionization modes were possible: electric field strengths for field emission were less than 1.0 MV/cm while field ionization began near 1.5 MV/cm and was observed upwards of 3.0 MV/cm. A study of several variants using

different materials and geometries were compared using current draw, emission currents (both electron and ion), mass spectra, and lifetimes as the criteria. Two variants, bonded silicon-on-insulator (SOI) and metal-on-insulator substrates were the best performers. Both yielded emission currents (electron and ion) as well as mass spectra at 1 Torr of air buffer gas, with the longest observed lifetime to be over 20 days of HPMS instrument time for the SOI-based variant. Fabrication yield and HPMS performance showed SOI to be the better material, but metal-on-insulator is a lower-cost alternative and could be worth additional investigation.

The data gathered with the 9th generation microionizer brought the project around full-circle. Not only did the microionizer corroborate the initial conclusions regarding external ion injection under HPMS conditions; but in doing so, all three of the major objectives: air-based HPMS; maximum lifetime; and minimum footprint were achieved.

6.2 Future Work

While the microionizer has successfully demonstrated HPMS operation, there are several aspects including signal intensity, operational voltage, field emission mode and signal loss over time that could be addressed to improve on its strengths. In comparison to glow discharge, the microionizer displays both reduced power consumption and mass spectral signal intensity by about two orders of magnitude.[11] The microionizer does have a smaller footprint and hence a reduction in pumping capacity required for the smaller volume relative to the GD. However, the lower sensitivity may not be worth the power gains in a portable instrument designed for rapid chemical detection.[14] Improvement in sensitivity is an area in need of future research with three possible design changes that could improve sensitivity worth investigating: 1) use the microionizer as the atmospheric inlet of the MS; 2) combine

192

the microionizer and endcap of the ion trap; 3) further reduce the insulating layer thickness for reduced voltage operation.

6.2.1 Microionizer as Atmospheric Inlet

Many field ionization sources force the gas flow through their high field regions resulting in near 100% ionization of neutral analytes.[15-17] Combining this efficiency with the improved trapping of externally injected ions at 1 Torr (as demonstrated in Chapter 2) could increase signal intensity generated by the microionizer.

Preliminary studies using the microionizer as an atmospheric inlet were attempted where the gas flow was forced through the active regions of a Gen 9.6 microionizer. Figure 5.2a shows a cross-sectional diagram of the atmospheric inlet version of the mini-chamber and Figure 6.1b shows the microionizer mounted to the coverplate of the mass analyzer chamber. In this configuration, the microionizer was sealed to the PCB with epoxy ensuring all gas flow into the chamber passed through the high-field region of the microionizer. This configuration moved the microionizer away from the ion trap so a tube lens was incorporated to ensure maximum ion transmission into the ion trap.[5] The tube lens, 5 mm in length and 5 mm in diameter, was mounted on top of the ion trap endcap and spaced 140 μm from the endcap using a Teflon spacer. The focusing field was generated by a DC potential ranging from -135 to +135 V.

Pressure measurements on either side of the microionizer (14.6 Torr inlet side and 1 Torr outlet side) suggest the microionizer was indeed acting to limit conductance into the ion trap chamber. With the gas flow forced through the high-field region, both field emission and field ionization modes were tested. Field emission proved to be unstable, resulting in uncontrollable discharges. Field ionization mode with mesitylene as the test analyte

performed slightly better, generating mass spectra for nearly 1 hour of instrument time. A steady stream of field ionization was present, but it was generally masked by random discharges, similar to (but less frequent) than those observed in field emission mode. The discharges point towards the need to investigate thinner insulating layers as this would lower the voltages needed to create sufficient field strengths. The field strength for these experiments was near 3.0 MV/cm, requiring a 300 V pulse voltage, which approaches Paschen breakdown under these conditions.[18] While these preliminary studies showed limited success for the microionizer as an atmospheric inlet, the fact that any mass spectra under these conditions were produced is an encouraging first step down this path. Further pursuit is warranted, because of the possible gains in sensitivity. As the atmospheric inlet, virtually all of the analyte sampled from the air can be ionized and efficient ion injection at high pressure will ensure the analyte ions are retained. This would lead to either more signal at the existing atmospheric sampling flow rate, or the ability to reduce the flow rate and vacuum pump power consumption.

6.2.2 Microionizer as Ion Trap Endcap

A second method for potentially improving the sensitivity is to substitute the microionizer for one (or both) of the mCIT endcap(s). With this configuration, gas flow is forced through the microionizer/endcap (similar to the atmospheric inlet) with the ions exiting the microionizer directly into the ion trap. Because of the short travel distance (≤ 250 μm) between microionizer and trap, ion transmission losses should be minimized thereby maximizing sensitivity. Note the insulating layer thickness would need to be chosen such that the potential required for field ionization does not produce ions with too much kinetic energy for injection.

194

Additionally, this arrangement could reduce the vacuum volume and thus pumping requirements. The 'trap chamber' could consist of the internal volume of the mCIT which would reduce overall power consumption of the vacuum system. Finally, it could be used in tandem with an ambient source such as ESI with the ions sprayed through the microionizer/endcap into the ion trap. The same ion trap assembly could be used to sample both highly volatile compounds via atmospheric sampling or thermal desorption as well as less volatile compounds via ambient techniques.

6.2.3 Further Microionizer Development

Early development of the microionizer was plagued by high leakage current, which was combated with SOI wafers containing thick insulating layers (≈ 1 μm). Improvements in fabrication and wire bonding reduced the leakage current, and it is likely that SOI substrates with thinner insulating layers could be used. Insulating layers as thin as 300 nm in SOI-alternatives were able to generate field ionization with potentials near 50 V; about one-third the applied potential required for field ionization with thick, 1 μm insulators. Further thinning of the insulating layer could drop the potentials for field emission and field ionization even further, which would simplify the pulsing circuitry necessary for ionizer operation and reduce the risk of arc discharge. The latter benefit would also align very well in efforts to use the microionizer as an atmospheric inlet.

Decreasing the insulator thickness should offer better lifetime – both for field emission mode as well as field ionization signal intensity vs. time. Both modes showed a general decrease in signal intensity over time, with field emission mode decaying much faster than field ionization mode. For field emission mode, this was attributed to emitter tip erosion due to ion back streaming. For field ionization mode, the decay in signal intensity is most likely

the result of adsorbed neutrals on the microionizer. By reducing insulator thickness, field emission could be achieved with smaller potentials (e.g. 10 V or less). This would reduce the maximum possible kinetic energy of stray ions and limit damage due to back streaming. The end result would be a smooth, predictable field emission current. Moreover, short pulses of field emission mode can be used to clear the adsorbed layer off of the surface of field ionizers.[19] Thus, periodic field emission mode pulses or even alternating field emission and field ionization MS scans could reduce the rate of signal decay for field ionization mode – potentially increasing lifetime.

6.3 Applications Beyond HPMS

More traditional field effect devices rely upon Spindt cathodes (or similar geometries) and tend to require rather complicated fabrication processes.[20-21] The strength of the microionizer is its simple design and fabrication.[22] This should translate to lower costs upon scaling up fabrication. As such, the microionizer might find use beyond HPMS. Thus, it could prove to be a low cost alternative to other field effect devices that have been developed for applications ranging from RF amplifiers[23] to field effect transistors[24] and even microsatellite ion thrusters.[25] These applications would be best approached via collaborations, where proof of concept experiments could be achieved by tailoring the PCB mount to each application. Further development could then utilize more advanced designs similar to that proposed for the endcap-based microionizer.

6.4 Figures
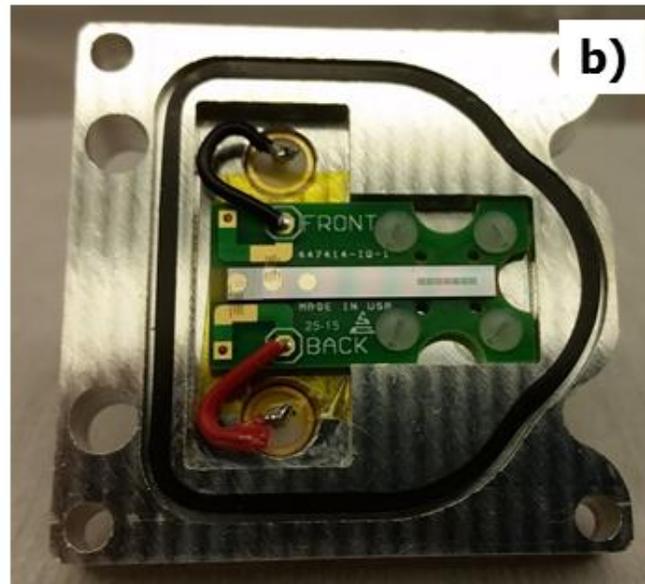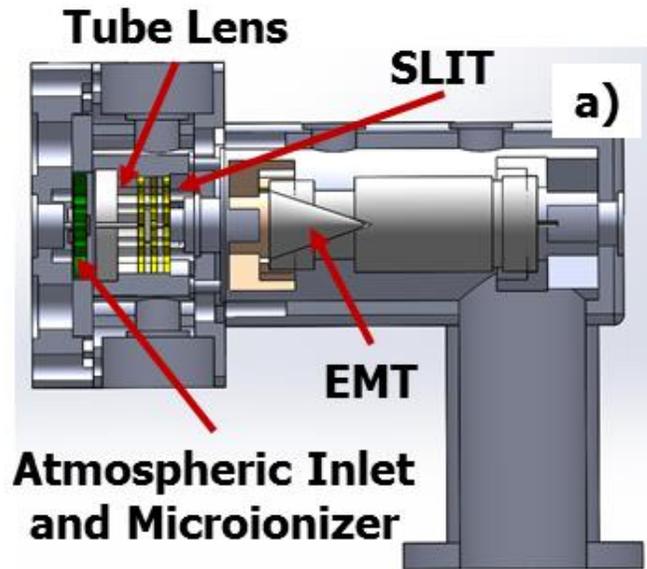
Figure 6.1: Solidworks schematic and images of the atmospheric inlet mini-chamber and coverplate. a) Cross-sectional view of the mini-chamber which highlights the inlet, microionizer, tube lens, and SLIT positions. b) An image of a microionizer mounted in coverplate ready for atmospheric inlet operation; the ionizer is sealed to the PCB with epoxy and a Viton o-ring (not shown) between the aluminum cover plate and PCB ensures gas flow through the high-field region.

6.5 REFERENCES

1.   M908 Spec Sheet. http://908devices.com/wp-content/uploads/2014/10/SpecSheet-908_2014_v21.pdf (accessed 11/3/2015).

2.   Nanos, J., 908 Devices has a hand-held approach to thwarting chemical attacks. *Boston Globe* 4/20/2015, 2015.

3.   Blakeman, K. H. Development of High Pressure Mass Spectrometry for Handheld Instruments. Dissertation, University of North Carolina at Chapel Hill, Chapel Hill, NC, 2015.

4.   Ramsey, J. M.; Schultze, K., Miniature charged particle trap with elongated trapping region for mass spectrometry. Google Patents: 2014.

5.   Gilliland, W. M., et al., Coupling Microchip Electrospray Ionization Devices with High Pressure Mass Spectrometry. *Manuscript in preparation* **2015**.

6.   Schultze, K. P. Advanced System Components for the Development of a Handheld Ion Trap Mass Spectrometer. Dissertation, University of North Carolina at Chapel Hill, Chapel Hill, NC, 2014.

7.   Goeringer, D. E., et al., Theory of high-resolution mass spectrometry achieved via resonance ejection in the quadrupole ion trap. *Analytical chemistry* **1992,** *64* (13), 1434-1439.

8.   Kornienko, O., et al., Micro ion trap mass spectrometry. *Rapid Commun. Mass Spectrom.* **1999,** *13* (1), 50-53.

9.   Blakeman, K. H., et al., High-Pressure Mass Spectrometry at Pressures Exceeding 1 Torr in a Microscale Cylindrical Ion Trap. *Manuscript in preparation* **2015**.

10.   Wolfe, D. W. High-Pressure Cylindrical Ion Trap Mass Spectrometry. Dissertation, University of North Carolina, Chapel Hill, 2012.

11.   Blakeman, K. H.; Ramsey, J. M., High Pressure Mass Spectrometry in Nitrogen and Air. *Manuscript in preparation* **2014**.

12. McLuckey, S. A., et al., Ion Trap Mass Spectrometry of Externally Generated Ions. *Analytical chemistry* **1994,** *66* (13), 689-696.

13. March, R. E., An Introduction to Quadrupole Ion Trap Mass Spectrometry. *Journal of Mass Spectrometry* **1997,** *32* (4), 351-369.

14. Lammert, S. A., Field Portable Mass Spectrometry. In *Detection of chemical, biological, radiological and nuclear agents for the prevention of terrorism : mass spectrometry and allied topics*, Banoub, J., Ed. Springer: New York, 2014; p 291.

15. Aberth, W.; Spindt, C. A., Characteristics of a Volcano Field-Ion Quadrupole Mass-Spectrometer. *International Journal of Mass Spectrometry and Ion Processes* **1977,** *25* (2), 183-198.

16. Fomani, A. A., et al., Low-Voltage Field Ionization of Gases Up to Torr-Level Pressures Using Massive Arrays of Self-Aligned Gated Nanoscale Tips. *Ieee Transactions on Electron Devices* **2014,** *61* (5), 1520-1528.

17. Ghodsian, B., et al., Gas Detector with Low-Cost Micromachined Field Ionization Tips. *IEEE Electron Device Letters* **1998,** *19* (7), 241-243.

18. Lisovskiy, V. A.; Yakovin, S. D., Experimental study of a low-pressure glow discharge in air in large-diameter discharge tubes: I. Conditions for the normal regime of a glow discharge. *Plasma Phys Rep+* **2000,** *26* (12), 1066-1075.

19. Beckey, H. D., *Principles of field ionization and field desorption mass spectrometry*. 1st ed.; Pergamon Press: Oxford Eng. ; New York, 1977; p 335.

20. Spindt, C., et al., Thermal field forming of Spindt cathode arrays. *J Vac Sci Technol B* **2015,** *33* (3).

21. Fomani, A. A., et al., Toward Amp-Level Field Emission With Large-Area Arrays of Pt-Coated Self-Aligned Gated Nanoscale Tips. *Ieee Transactions on Electron Devices* **2014,** *61* (7), 2538-2546.

22. Madou, M. J., *Fundamentals of microfabrication and nanotechnology*. 3rd ed.; CRC Press: Boca Raton, FL, 2012.

23.   Temple, D., Recent progress in field emitter array development for high performance applications. *Mat Sci Eng R* **1999,** *24* (5), 185-239.

24.   Lim, H. J., et al., Impact of the crystallization of the high-k dielectric gate oxide on the positive bias temperature instability of the n-channel metal-oxide-semiconductor field emission transistor. *Appl. Phys. Lett.* **2013,** *102* (23).

25.   Hartley, F. T., Miniature Free-Space Electrostatic Ion Thrusters. Stephens, J. B., Ed. NASA: NASA Technology Briefs, 2006; p 29.

APPENDIX 1: LIST OF MICROFABRICATION TECHNIQUES, TOOLS, AND GENERAL RESOURCES

A1.1 Tools and Techniques Used During Fabrication Development

Tool/Technique	Purpose	Location
Karl Suss MA6/BA6	Photolithography – Exposure	UNC/CHANL
Laurell WS-650 Spin Coater	Photolithography – Photoresist Application	UNC/CHANL
Kurt J Lesker PVD-75 Magnetron Sputter Coater	Thin Metallic Film Deposition	UNC/CHANL
Electron Beam Evaporator	Thin Metallic Film Deposition	UNC/CHANL
Tempress LPCVD Furnace	Si_3N_4 and Polysilicon Deposition	UA/TMNFC
Cricut Explore	Xerography	UNC
Furnace	Annealing	UNC
Alcatel AMS-100 DRIE	Anisotropic Etching and Plasma Cleaning	UNC/CHANL
Trion Mini-lock Phantom III RIE/ICP	Isotropic Etching and Plasma Cleaning	UNC
AGS RIE	Isotropic Etching	UA/TMNFC
Trion Phantom II RIE	Isotropic Etching	Duke/SMIF
SPTS Pegasus Deep Silicon Etcher	Anisotropic Etching	Duke/SMIF
Transene Chromium Etch 1020	Chrome Etch	UNC
Transene Buffered Oxide Etch	Isotropic SiO_2 Etching	UNC
Heated Phosphoric Acid	Si_3N_4 Etching	UNC
Scribe and Break	Dicing	UNC
Disco-XXX	Dicing	UNC
WestBond 7KE	Wire Bond	UNC
Cyantek Nanostrip 2X	Cleaning	UNC
SC1/SC2 (RCA Series)	Cleaning	UNC

Table A1.1: List of fabrication tools and techniques employed.

A1.2 Notes and Resources

The following information is a list of useful hints, tricks, and resources accumulated during the development of the process flow for microionizer fabrication. This list is not meant to be exhaustive but should be a good starting point for future deep, anisotropic etching with or without SOI substrates.

A1.2.1 General Resources

There are many resources for semiconductor (specifically silicon) theory and fabrication. This project relied heavily upon Madou's series on micro and nanofabrication for introductory information as well as citations for further research.[1] The classic book by Sze, *Physics of Semiconductors Devices,* was also very useful.[2] Several other books were used for more specific aspects of the project including metal-semiconductor contacts,[3] wire bonding,[4] and silicon-on-insulator technology.[5] There were also several research articles and reviews regarding insulating layers that are worth mentioning: conduction in insulators;[6-8] silicon dioxide characteristics and breakdown;[9-11] and materials for field emission devices.[12] Finally two articles by Williams, *et al* were crucial for practical microfabrication. These articles report the etch rates of many common semiconductors, metals, and polymers under different etch and cleaning processes.[13-14]

A1.2.2 Cleaning and Wet Etches

Photoresist removal is best done with oxygen plasma or Nanostrip 2X (Cyantek Corporation). 150 mm wafers do not fit into either of the oxygen plasma cleaners at UNC; the DRIE and RIE can substitute but will leave behind resist along the edge. Nanostrip 2X is a stabilized piranha solution (sulfuric acid + hydrogen peroxide + peroxymonosulfuric acid), and it is less likely to result in explosive hydrogen outgassing than standard piranha. It

is best for removing organics, certain metals, and photoresists. If heated to $\approx 75\ ^{o}C$, it can even remove stubborn negative resists such as KMPR or SU-8. Heating will significantly deplete the strength of the solution and it is not recommended to be reused afterwards.

The SC1/SC2 cleaning series, developed by Kern at RCA, should be used whenever the surface of the substrate needs to be pristine.[15-16] Examples of when it would be appropriate are to prep a wafer that is no longer 'prime' for spin coating (e.g. double-sided processing) or for a thin film deposition where adhesion and/or electrical contact are important (e.g. wire bonding pad deposition).

A typical cleaning series:

- Nanostrip 2X at 75 ^{o}C for 10 min (for photoresist and organics)

- SC1 at 70 ^{o}C for 10 min (for organics)

- 2% HF Dip for 30 s (strips oxide left behind by SC1)

- SC2 at 65 ^{o}C for 10 min (for metal ion removal)

Times and temperature can vary within reason (except the HF dip, where 15 to 30 sec is sufficient). The wafer should be rinsed with deionized water between steps and thoroughly dried with N_2 gas after cleaning. And as always, make sure you use containers appropriate to the solution. Certain glasses (pyrex and borosilicates) can release potassium ions into solution which can affect insulator behavior. PTFE and PFA beakers were used for nearly every cleaning (just make sure the hotplate is pre-heated!). Quartz is an acceptable, but expensive alternative for SC1 and SC2 (but not HF).

Silicon dioxide etching via buffered oxide etch solution (BOE, 5:1) was the most successful wet etch employed at UNC. For small features (< 50 μm), surface tension can be

an issue and a short oxygen-plasma cleaning is suggested to ensure wetting at the bottom of etch trenches.

Heated phosphoric acid (85% at 125 to 180 °C) for silicon nitride requires careful control of the temperature and concentration, if either gets out of range the etch rate of silicon and silicon dioxide become non-neglible.[17]

Silicon can be wet etched with several solutions including potassium hydroxide in isopropyl alcohol (KOH); tetramethyl ammonium hydroxide (TMAH); and hydrofluoric/nitric/acetic acid (HNA).[1] KOH and TMAH yield anisotropic etches because they selectively etch crystal planes at different rates, while HNA is an isotropic etchant.[1, 18]

A1.2.3   AZ-9260 Guidelines

AZ-9260 (MicroChem GMBH) became the workhorse photoresist for microionizer fabrication. It is a thick, positive resist which can be spin coated upwards of 24 µm thick. A typical recipe for 6.5 to 7.0 µm was:

- Dehydrate wafer in oven for 10 min

- Spin at 3k RPM for 30 s (004 acceleration)

- Softbake on hotplate for 3 min at 115 °C

- Cool to RT (≈ 1 min)

- Soak in H_2O for 5 min (rehydration step)

- Rinse and Dry

- Expose for 19.5 s (same for silicon, SOI, and chromed silicon)

- Develop in AZ-400K (1:3 dilution) for 1 to 2 min

- Rinse and Dry

This thickness was adequate for silicon and SOI (up to 1 μm insulator) DRIE for at least 200 μm total depth (provided dead time cooling steps were included). When working with AZ-9260 (or any thick, positive resist), it is good to use a rehydration time between the softbake and exposure.[19]

A1.2.4   Thin Metallic Films

Metallic thin films can be used for electrical contact and/or etch masks. Electrical contacts for wire bonding were exclusively deposited using the e-beam evaporator, which was always given an overnight pumpdown to ensure high quality thin films. The sputter coater (Lesker PVD 75) was used for solderable contacts and masking layers.

Titanium is a great, all-purpose base-layer for silicon metallization; typically a thin flashing of 5 to 25 nm. It acts as a getter for the deposition chamber, helping to remove residual gases such as oxygen (often you will see chamber pressure decrease after titanium deposition has started). Moreover, it adheres to silicon (and silicon oxide) as well as most metals (such as gold and chromium). If annealed, it will form an Ohmic contact with either n- or p-type silicon.[3]

Chromium and aluminum were both used as masking materials for DRIE. Chromium was preferred for the microionizer because it is compatible with Nanostrip 2X which was used to strip the photoresist used to transfer mask patter into the chromium layer. Compared to photoresist, chromium demonstrated a strong tendency to micro-mask, which increased surface roughness for both sidewalls and trench bottoms. For masking, a 25 nm of titanium followed by 100 to 250 nm of chromium were used.

In the early days of microionizer fabrication development, electrical contact was overlooked. This was a mistake which lead to inconsistent results (one device would work

fairly well while others would not even turn on) and slowed progress. Electrical contact to silicon is difficult to achieve, because an insulating layer of native oxide forms in seconds.[20-21] Metallic pads for electrical contact are the most reliable way to overcome the oxide.[3] There are many methods to produce high quality pads and many are sensitive to the doping of the silicon. The two processes highlighted should work most of the time; one is for soldering and the other is for gold wire bonding.

- Solderable Pads (also good for aluminum wire bonding)[22]

    o 25 nm Titanium (adhesion)

    o 250 nm Copper (solder bond)

- Wire bondable Pads (for gold wire bonding)[23-24]

    o 50 nm Titanium (adhesion)

    o 65 nm Palladium (diffusion barrier)

    o 250 nm Gold (wire bond)

- Anneal at 450 $^{\circ}$C for 30 minutes under forming gas (95% N_2, 5% H_2)

Thicker copper will allow for multiple solder attempts (the copper dissolves on each attempt). For wire bonding, this recipe is close to the minimum – usually a thicker gold layer (closer to 400 nm) is recommended for strong bonds.[4] The last reference, by Harman is also a good guide for other bonding systems. Other electrical contacts include indium soldering[25] as well as direct wire bonding to silicon.[26] These were attempted for the microionizer, but proved inferior to gold wire bonding.

A1.2.5   Dry Etching

There are many resources for dry etching (both standard RIE and DRIE), however every tool and process is a little different, so there is no substitute for experience and a working

knowledge of plasma/reactive ion chemistry. Some good resources to get started are Madou,[1] the back silicon process,[27-29] as well as the following review articles.[18, 30-31] Several articles were useful for specific aspects of DRIE such as aspect ratio dependent etch rate;[31] notching at an insulating layer;[32-33] and deep, anisotropic etching.[18, 34] Ideas for etch recipes were found at:

- BYU Cleanroom website: http://www.cleanroom.byu.edu/rie_etching.phtml
- Trion Technology: http://www.triontech.com/applications.htm
- Etch Rates for Micromachining[13-14]

The Alcatel AMS-100 was the main tool used for DRIE. It relies upon the Bosch process[35] to generate deep, anisotropic etches by alternating an isotropic etch with a passivation step. The AMS-100 etches between 6 and 15 μm/min depending upon etch conditions. During continuous etching, it was found the substrate heated significantly (worse at higher etch rates) and mask selectivity was an issue (even for chromium and thick resists). This was overcome by adding a cooling step between short etch times, typically 30 s of etch time + 35 s of cool time. Note, the AMS-100 requires a minimum of 35 s to reestablish the plasma. Using this looped recipe, anistotropic etches up to 250 μm in depth were achieved with 6.5 μm of AZ-9260 photoresist.

A1.3 REFERENCES

1.   Madou, M. J., *Fundamentals of microfabrication and nanotechnology*. 3rd ed.; CRC Press: Boca Raton, FL, 2012.

2.   Sze, S. M.; Ng, K. K., *Physics of semiconductor devices*. 3rd ed.; Wiley-Interscience: Hoboken, N.J., 2007; p 815.

3.   Rhoderick, E. H., *Metal-semiconductor contacts*. Clarendon Press: Oxford, 1978; p 201.

4.   Harman, G. G.; Harman, G. G., *Wire bonding in microelectronics*. 3rd ed.; McGraw-Hill: New York, 2010; p 426.

5.   Cristoloveanu, S.; Li, S. S., *Electrical characterization of silicon-on-insulator materials and devices*. Kluwer Academic: Boston, 1995; p 381.

6.   Chiu, F. C., A Review on Conduction Mechanisms in Dielectric Films. *Adv Mater Sci Eng* **2014**.

7.   Bachhofer, H., et al., Transient conduction in multidielectric silicon-oxide-nitride-oxide semiconductor structures. *J Appl Phys* **2001,** *89* (5), 2791-2800.

8.   Swaroop, B.; Schaffer, P. S., Conduction in Silicon Nitride and Silicon Nitride-Oxide Films. *J Phys D Appl Phys* **1970,** *3* (5), 803-806.

9.   Osburn, C. M.; Ormond, D. W., Dielectric Breakdown in Silicon Dioxide Films on Silicon: II Influence of Processing and Materials. *Journal of the Electrochemical Society* **1972,** *119* (5), 597-603.

10.   Osburn, C. M.; Weitzman, E. J., Electrical-Conduction and Dielectric Breakdown in Silicon Dioxide Films on Silicon. *Journal of the Electrochemical Society* **1972,** *119* (5), 603-609.

11.   Osburn, C. M.; Ormond, D. W., Dielectric Breakdown in Silicon Dioxide Films on Silicon: I Measurement and Interpretation. *Journal of the Electrochemical Society* **1972,** *119* (5), 591-597.

12. Xu, N. S.; Huq, S. E., Novel cold cathode materials and applications. *Mat Sci Eng R* **2005,** *48* (2-5), 47-189.

13. Williams, K. R.; Muller, R. S., Etch Rates for Micromachining Processing - Part II. *Journal of Microelectromechanical Systems* **2003,** *12* (6), 761-778.

14. Williams, K. R.; Muller, R. S., Etch Rates for Micromachining Processing. *Journal of Microelectromechanical Systems* **1996,** *5* (4), 256-269.

15. Kern, W., The Evolution of Silicon-Wafer Cleaning Technology. *Journal of the Electrochemical Society* **1990,** *137* (6), 1887-1892.

16. Kern, W.; Puotinen, D. A., Cleaning Solutions Based on Hydrogen Peroxide for Use in Silicon Semiconductor Technology. *RCA Review* **1970,** *31* (2), 187.

17. Vangelde.W; Hauser, V. E., Etching of Silicon Nitride in Phosphoric Acid with Silicon Dioxide as a Mask. *Journal of the Electrochemical Society* **1967,** *114* (8), 869-872.

18. Wu, B. Q., et al., High aspect ratio silicon etch: A review. *J Appl Phys* **2010,** *108* (5).

19. Lehar, O. P., et al. In *Resist Rehydration During Thick Film Prcessing*, SPIE Proceedings, 2001.

20. Morita, M., et al., Growth of Native Oxide on a Silicon Surface. *J Appl Phys* **1990,** *68* (3), 1272-1281.

21. Morita, M., et al., Control Factor of Native Oxide-Growth on Silicon in Air or in Ultrapure Water. *Appl. Phys. Lett.* **1989,** *55* (6), 562-567.

22. Lum, I., et al., Footprint study of ultrasonic wedge-bonding with aluminum wire on copper substrate. *J Electron Mater* **2006,** *35* (3), 433-442.

23. Nicolet, M. A., Diffusion Barriers in Thin-Films. *Thin Solid Films* **1978,** *52* (3), 415-443.

24.   Poate, J. M., et al., Thin-Film Interdiffusion .1. Au-Pd, Pd-Au, Ti-Pd, Ti-Au, Ti-Pd-Au, and Ti-Au-Pd. *J Appl Phys* **1975,** *46* (10), 4275-4283.

25.   Belser, R. B., A Technique of Soldering to Thin Metal Films. *Review of Scientific Instruments* **1954,** *25* (2), 180-183.

26.   Hirshberg, A.; Elata, D. In *Direct Wire-Bonding of Silicon Devices Without Metal Pads*, Proceedings of the IEEE, 2009.

27.   Jansen, H. V., et al., Black silicon method X: a review on high speed and selective plasma etching of silicon with profile control: an in-depth comparison between Bosch and cryostat DRIE processes as a roadmap to next generation equipment. *Journal of Micromechanics and Microengineering* **2009,** *19* (3).

28.   Jansen, H., et al., The Black Silicon Method - A Universal Method for Determining the Parameter Setting of a Fluorine-based Reactive Ion Etcher in Deep Silicon Trench Etching with Profile Control. *Journal of Micromechanics and Microengineering* **1995,** *5* (2), 115-120.

29.   Jansen, H., et al., The Black Silicon Method 2 - The Effect of Mask Material and Loading on the Reactive Ion Etching of Deep Silicon Trenches. *Microelectronic Engineering* **1995,** *27* (1-4), 475-480.

30.   Jansen, H., et al., A survey on the reactive ion etching of silicon in microtechnology. *Journal of Micromechanics and Microengineering* **1996,** *6* (1), 14-28.

31.   Yeom, J., et al., Maximum achievable aspect ratio in deep reactive ion etching of silicon due to aspect ratio dependent transport and the microloading effect. *J Vac Sci Technol B* **2005,** *23* (6), 2319-2329.

32.   Kim, C. H.; Kim, Y. K., Prevention method of a notching caused by surface charging in silicon reactive ion etching. *Journal of Micromechanics and Microengineering* **2005,** *15* (2), 358-361.

33.   Chang, J. P.; Sawin, H. H., Notch formation by stress enhanced spontaneous etching of polysilicon. *J Vac Sci Technol B* **2001,** *19* (5), 1870-1873.

34.   Bower, C. A., et al., Microfabrication of fine-pitch high aspect ratio Faraday cup arrays in silicon. *Sensors and Actuators, A: Physical* **2007,** *A137* (2), 296-301.

35.   Laermer, F.; Schilp, A., Method of anisotropically etching silicon. Google Patents: 1996.